Fall 2015

# Metallurgical optimization of high strength cast steels with stage I tempering

Terrell Owen Webb Jr.

# METALLURGICAL OPTIMIZATION OF HIGH STRENGTH CAST STEELS WITH STAGE I TEMPERING

by

TERRELL OWEN WEBB, JR.

A DISSERTATION

Presented to the Faculty of the Graduate School of the

MISSOURI UNIVERSITY OF SCIENCE AND TECHNOLOGY

In Partial Fulfillment of the Requirements for the Degree

DOCTOR OF PHILOSOPHY
in
METALLURGICAL ENGINEERING
2015

Approved by

David C. Van Aken, Advisor
Ronald J. O'Malley
Von L. Richards
Wayne Huebner
Jason Baird

## PUBLICATION DISSERTATION OPTION

This dissertation is compiled in the format that consists of one paper for publication in a peer-reviewed journal, one paper published in the proceedings of the 118th Metal Casting Congress of the American Foundry Society, and four papers published in various years of Technical and Operating Conference proceedings for the Steel Founders Society of America. A statement of research objective and a review of the background are included as a foreword. A statement on the impact of the work, suggestions for future work, and supporting data and papers are included as an afterword. The first paper (pages 13 - 45), "An Innovative Heat Treatment to Improve the Ductility of High Strength Steels", the second paper (pages 46 - 85), "Grain Refinement Strategies in High Strength Cast Steel", and the third paper (pages 86 - 112), "Porosity and Cleanliness Limitations on High Strength Steel" have been submitted and/or published as proceedings under the Steel Founders Society of America. The fourth paper (pages 113 - 166), "Normalization of High Strength Steels to Improve Homogeneity and Mechanical Properties" will be submitted for publication with in the International Journal of Metalcasting. Finally the fifth paper given as supporting data in Appendix B, "Evaluating Chemical Homogeneity in the Performance of Eglin Steel," was published as a proceeding under the American Foundry Society.

## ABSTRACT

Eglin steel was developed by the U.S. Air Force and Ellwood National Forge Company as a cost-effective, ultrahigh strength steel for use in armament, aerospace, and commercial applications. Eglin steel has been successfully substituted for high alloy steels, such as AF1410 and HP-9-4-20/30, to produce the casing for "bunker buster" bombs where penetration of concrete barriers and rock at high velocity (>1000 ft/sec) is desired. Unlike AF1410 and HP-9-4-20/30, Eglin steel is low nickel (nominal 1 wt.%) and contains no cobalt. Given the successful performance of Eglin steel in the casings applications, the Department of Defense has directed that further development of Eglin steel as a cast product should be conducted.

The goal of the research reported here was to use existing knowledge and practices of producing Eglin steel as a basis and to advance the science and the physical metallurgy of cast Eglin steel to produce a more consistent material that meets current performance requirements by optimizing chemical homogeneity, and thermal processing.

A novel heat treatment was designed which reduced the prior austenite grain size from 283 ± 74 μm to 58 ± 17 μm, and increased Charpy impact energy at -40° F/C from 34 ± 4 ft-lbs to 40 ± 11 ft-lbs. Porosity and Cleanliness Limitations were investigated, and it was found porosity must be restricted to less than 0.05% to obtain elongations to failure of 10% or greater. A general model for the notch effect of a large pore was formulated and shows that shrinkage pores must be restricted to less than 400 μm in length to eliminate brittle behavior induced by porosity. Finally elevated temperature normalization at 2250°F for up to 11 hours was explored in which it was concluded that for Eglin steel, homogeneity is a secondary consideration to casting porosity, cleanliness, and martensitic substructure.

## ACKNOWLEDGEMENTS

This work has been supported under the Steel Founders' Society of America (SFSA) program on Casting and Advanced Steel Technology that has been funded by the Army Research Laboratory under the provisions of cooperative agreement W911NF-12-2-0033.

I would like to thank my advisor, Dr. David Van Aken for his patience, love of teaching, and tireless support. My success is directly linked to his motivation and tutelage for which I am deeply grateful.

This work would not have been possible without the help of an entire team of professors, graduate students, and undergraduates, all of whom I thank. Specifically I would like to thank my advisory board, the members of the CES research team assembled by SFSA, Dr. Laura Bartlett, Scott Pisarik, Daniel Field, Marc Harris, Seth Rummel, Zachary Henderson, Sonya Snyder, Elaina Hodges, Anna Bretzke, and Josh Green.

Finally, I'd like thank my entire family, most especially my wife, for the endless love and support, as well as their sacrifice in helping me reach my goals.

## TABLE OF CONTENTS

SECTION

## LIST OF ILLUSTRATIONS

SECTION Page

PAPER II

PAPER III

PAPER IV

SECTION

## LIST OF TABLES

PAPER III



PAPER IV

# 1. RESEARCH OBJECTIVE

In today's ever changing economic environment, all facets of industry require advances in technology to stay competitive and meet consumer needs. As such industrial leaders continuously push their resources and equipment to operate for longer times and in more extreme environments, which in turn creates a need for advancement in material understanding and performance. The demand for higher toughness levels in ultrahigh-strength steels has driven the evolution from alloy steels similar to AISI 4340 to high nickel-cobalt steels such as HP 9-4-20, HP 9-4-30, and AF 1410; however, the higher nickel contents drive up cost and drive down profits. Eglin steel was developed by the U.S. Air Force and Ellwood National Forge Company as a cost-effective, ultrahigh strength steel to meet the demand for high toughness.

The goal of the research reported here was to use existing knowledge and practices of producing Eglin steel as a basis and to advance the science and the physical metallurgy of cast Eglin steel to produce a more consistent material that meets current performance requirements by optimizing chemical homogeneity, and thermal processing. Furthermore, establishment of any metrics that may be used to gauge casting performance prior to use and or further processing to reduce cost and increase efficiency was envisioned.

# 2. BACKGROUND INFORMATION

## 2.1. ARMAMENT STEELS

The development of armament steels can be sufficiently debated to begin well back to the B.C. time frame when chariots and ships began cladding their vessels with iron or other metals for the protection against penetration during combat. Further development throughout the years has established great changes in the actual production and even classification of armament steel; however, the modern day armament steel can be argued in that its greatest developments have only been achieved since World War II (WWII) in which the culmination of world dominance was established by the numerous battles of tanks. Although many armors currently exist from steel, to ceramic to composites, the generic standard by which most armor is generally compared is that of Rolled Homogenous Armor (RHA) of which many tanks were made of during WWII until the development of armor piercing rounds, shape charges, and kinetic energy penetrators. [1,2]

Prior to WWII and until 2006, the United States has historically tracked as well as improved upon the scientific correlations of armor performance at Watertown Arsenal in Massachusetts, and this organization was considered to be one of the world's foremost leaders in armor development. Review of numerous documents can be made describing in detail not only the historical but scientific undertakings of that organization with respect to armor, and due to an increased demand during WWII for production in armor similar to RHA the birth of industrial cast armor was established in September of 1940 by the forming of the Subcommittee for Cast Armor of the Ordnance Department. [3]

Initial reports from the subcommittee correlated ballistic properties to Brinell hardness and thickness of cast armor plates, ranging from 3/8" to 3". By 1941 metallurgical testing of cast armor, "consisted of radiographic examination, chemical analysis, Brinell hardness, tensile tests,

macroscopic examination, and microscopic examination", and high alloy contents for Carbon, Manganese, Nickel, Chromium, Molybdenum, and Vanadium were being used to gain requisite hardenability as thickness increased.

With the continued cost of the ongoing war a restriction on the amount of alloy was imposed in the beginning of 1942, which brought about the development of low alloy cast armor. Additionally, demand for castings continued to rise and full ballistic testing was now being performed on castings including resistance to penetration. Resistance-to-Penetration testing, as defined by TOP 2-2-710 the "Ballistic Tests of Armor Materials" [4], "measures the ability of armor to withstand attack by Kinetic Energy (KE) projectiles or simulated projectile fragments." The expression of ballistic protection under this test is given by the V50 Ballistic Limit, in which thickness and obliquity of the armor are held constant while varying the velocity of the projectile until an equal amount of probability to defeat or not defeat the armor is completed, i.e. it resists penetration 50% of the time and the other 50% it does not. Further use of the V50 may be given in estimation of armor protection requirements through the equation:

$$V_{penetrator} = 2t\sqrt{\frac{\pi\sigma_0 e_f r_p}{M}} \qquad (1)$$

Where $t$ is target thickness, $\sigma_0$ is flow stress, $\varepsilon_f$ is the true strain to failure, $r_p$ is the projectile radius, and M is mass of the projectile.

Successful testing of many castings was completed through 1943; however, as munitions became larger and the need for increased armor thickness grew, a matter of hardenability began to become apparent in ballistic testing failure. Lower alloy contents did not allow for sufficient through hardening and non-homogenous microstructures were noted as the cause for failure in many thick castings. Additionally testing performed in cold weather environments during this period showed a significant decrease in performance by which the same armor tested at room temperature or above successfully passed all testing. Correlations of this performance and

metallurgical properties were obtained using the previously mentioned testing procedures, as well as the then newly developed Charpy V-notch impact test, see Figure 2.1.

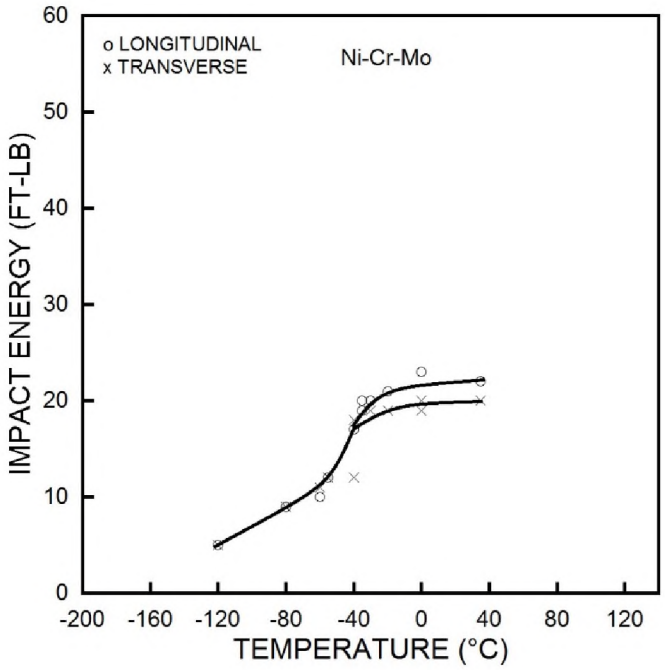


Figure 2. 1 Reproduction of graph from W.P. Hatch [10] showing V-NOTCH impact transition curves for H-plate armor base metals.

Driven even more by the tactical situation in 1944, heavy section castings of 4 inches to 6 inches thick were needed for gun shields and tank protection. Compositional restrictions were loosely imposed on the thick section castings based on the previous testing in thinner section castings identifying the need for higher alloy contents to reach the requisite hardenability; thus, compositions ranging from as high as 2.5% Cr, .5% Mo, 1.0% Ni, 1.5%Mn and .1% V were all being used with great hardship to achieve toughness requirements. Ultimately thick section

castings showed inferior ballistic performance attributed to manufacturing difficulties and a need for basic research was established, furthermore, the adoption of impact testing for armor specification was officially accepted.

With the establishment of modern test specifications for armament steel countless research efforts have been made in improving armor to continue meeting increased threat requirements; however, one key concept which has undoubtedly continued to this day from the WWII development is that armor castings generally do not provide adequate ballistic performance compared to wrought products. This notion has been acceptable to metallurgists and Department of Defense officials from a cost perspective, as wrought product can simply be welded and layered on modern day vehicles to increase protection without the necessity of developing new or improved casting technologies. However, the ever increasing threat from Improvised Explosive Devices (I.E.D.'s), Explosively Formed Penetrators (E.F.P.'s), and KE penetrator weapon systems which produce significantly high strains (~300%) and strain rates (~ $10^4$ $s^{-1}$ ), have demanded that this notion be put aside as armor is failing at welds and geometries for welded vehicles are limited which has been shown to reduce blast damage. [5]

The Army Research Laboratory's (ARL) Weapons and Materials Research Directorate (WMRD) who is one of the DoD organizations charged with developing materials and materials processing to mitigate this threat has directed under Cooperative Agreement W911NF-12-2-0033 research with the specific objectives of creating stronger lighter weight steel alloys that can economically compete with other more expensive metals for higher end applications, and developing advanced melting and processing capabilities to reduce manufacturing cycle time and cost.

## 2.2. EGLIN STEEL (ES-1)

The material researched under this investigation was specifically directed by the cooperative agreement noted in the previous section; however, a review of this material and why it was specifically directed by that agreement is well worth mentioning. Eglin steel was developed by the U.S. Air Force and Ellwood National Forge Company as a cost-effective, ultrahigh strength steel for use in armament, aerospace, and commercial applications. Eglin steel has been successfully substituted for higher alloy steels, such as AF1410 and HP-9-4-20/30, to produce the casing for "bunker buster" bombs where penetration of concrete barriers and rock at high velocity (>1000 ft/sec) is desired. [7,8,10] A comparison of Eglin Steel to similar high alloy steels with respect to Charpy impact and yield strength is given below in Figure 2.2. Unlike AF1410 and HP-9-4-20/30, Eglin steel is low nickel (nominal 1 wt.%) and contains no cobalt and therefore cost is significantly reduced to around $2.70 per pound compared to $15.00 per pound. Eglin steel is a Stage I tempered steel consisting of a lath martensitic microstructure (see Figure 2.3) with intra-lath ε-carbides. [9] In the Stage I tempered condition, Eglin steel will produce a yield strength ranging from 170 to 190 ksi and an ultimate tensile strength of 230 to 250 ksi. The low ratio of yield to ultimate strength indicates extensive work hardening during plastic deformation and this contributes to the toughness of the steel under impact conditions. Eglin steel is designated as ES-1 when produced as a wrought product and CES when it is cast. Although primarily used as a wrought product, successful casting of Eglin steel has also been achieved as bomb casing material and is slowly gaining support for continued use as a penetrator material.

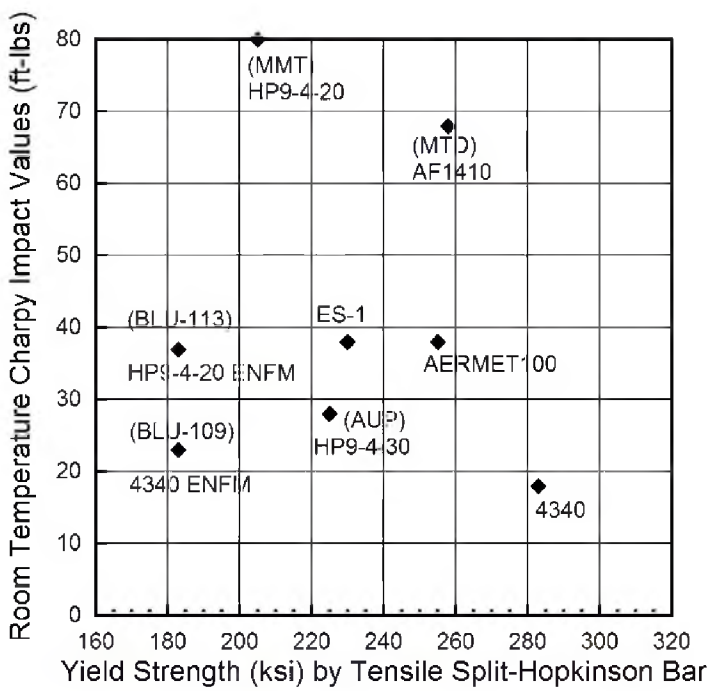


Figure 2. 2 Reproduction of graph from Dilmore et al. [8] showing ES-1 compared to similar high alloy penetrator steels with respect to Charpy impact and yield strength.

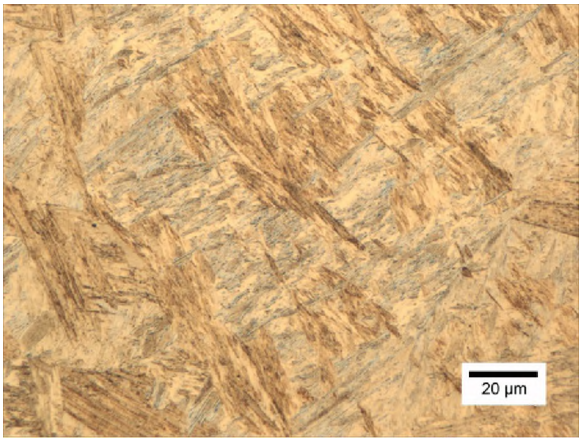


Figure 2. 3 Optical image of the Stage I tempered lath martensitic microstructure of ES-1.

## 2.3. CAST EGLIN STEEL (CES)

Given the Success of Eglin steel in the wrought form and more importantly its success in the cast form as a penetrator, ARL selected Eglin steel as a viable candidate to meet the needs of mission requirements in producing future vehicles requiring protective armor. Introducing this material as a casting for main structural components, which allows for more complex geometries to help defeat threats as opposed to bolting or welding on additional armor protection, allows for significant weight reduction in vehicle systems and reduces fuel costs.

As part of the cooperative agreement noted in section 2.1, a group of researchers from multiple universities and industry partners were assembled in 2010 to begin investigating CES. Initially, efforts were focused on utilizing current practices for the wrought product and obtaining a general metallurgical understanding of the material and its mechanical properties. Some success had been gained in the wrought product using Hot Isostatic Pressing (HIP) to reduce internal porosity and thus both the cast and HIP'ed conditions of CES were explored after heat treatment. Based on studies by Abrahams, Lynch and Voigt [12,13], the heat treatment of that time was a normalization at 2000°F for 1 hour, austenitization for 1 hour at 1900°F with a brine water quench, and then temper for 4 hours at 375°F. Similar heat treatment was given for the HIP'ed material after the HIP process of 2125°F at 15 ksi for 4 hrs. Mechanical testing by O'Loughlin et al. [14] using this heat treatment produced the properties listed in Tables 2.1 and 2.2. Statistical measurement of the inclusions and microporosity were reported for that study, and are given in Table 2.3.

Table 2. 1 Tensile properties in heat treated ES-1 Product 1 for the cast and the HIP conditions tested at room temperature reported by O'Loughlin et al. [11,14]

| | | **0.2% Yield Strength Y.S. (ksi)** | **Ultimate Tensile Strength U.T.S. (ksi)** | **Elongation (%)** | **Reduction in Area R.A. (%)** | **Modulus (Msi)** |
|---|---|---|---|---|---|---|
| **ES-1 Cast** | Test 1 | 179.7 | 239.1 | 9.5 | 41 | 29.2 |
| | Test 2 | 180.4 | 239.1 | 8.5 | 48 | 29.6 |
| | Test 3 | 179.8 | 233.6 | 3.0 | 33 | 29.5 |
| | **Average** | **180.0** | **237.3** | **7.0** | **40.7** | **29.4** |
| **ES-1 HIP** | Test 1 | 179.8 | 238.8 | 14.0 | 63 | 27.9 |
| | Test 2 | 183.0 | 239.5 | 13.0 | 60 | 27.7 |
| | Test 3 | 182.1 | 237.6 | 13.0 | 61 | 29.1 |
| | **Average** | **181.6** | **238.6** | **13.3** | **61.3** | **28.2** |

Table 2. 2 V-Notch Charpy impact energy in heat treated ES-1 Product 1 for the cast and the HIP conditions tested at -40°F (-40°C), reported by O'Loughlin et al. [11,14]

| | | **V-Notch Charpy Impact Energy tested at -40°F (-40°C) (ft-lbs)** | | | |
|---|---|---|---|---|---|
| | | Test 1 | Test 2 | Test 3 | **Average** |
| **ES-1** | **Cast** | 17 | 20 | 22 | **19.7** |
| | **HIP** | 27 | 26 | 28 | **27.0** |

Table 2. 3 Statistical measurement of inclusions and microporosity in heat treated ES-1 Product 1 for the cast and the HIP conditions tested at room temperature reported by O'Loughlin et al. [11,14]

| | | Population Density # per mm$^2$ | Average Diameter µm | Average Surface Area µm$^2$ | Coverage ppm (µm$^2$ per mm$^{2)}$ | Av. Min. Particle Spacing µm | Min P.S. StDev µm |
|---|---|---|---|---|---|---|---|
| **ES-1 Product #1 Cast** | **Inclusions** | 34.7 | 2.8 | 8.6 | 296.7 | 59.7 | 48.8 |
| | **Porosity** | 13.1 | 4.2 | 36.2 | 491.1 | | |
| | **Both** | 47.8 | 3.2 | 16.4 | 787.8 | | |
| **ES-1 Product #1 HIP** | **Inclusions** | 65.9 | 2.1 | 4.3 | 286.1 | 52.4 | 35.5 |
| | **Porosity** | 10.1 | 1.6 | 5.7 | 56.7 | | |
| | **Both** | 76.0 | 2.0 | 4.5 | 342.8 | | |

Conclusions drawn from that study, significant to this research, were that "inclusions were predominantly Mn-rich oxides made up primarily of $MnSiO_3$ inclusion with some MnS and MnO" and the inclusions in two heats of the ES-1 product were similar; however, the ladle refined and vacuum degased product contained many more $Al_2O_3$ inclusions and smaller sized $MnSiO_3$ inclusions. Additional conclusions that the HIP process "provided an effective densification of the microporosity," lowering "the total microporosity in ES-1 by 88.5% (491.1 to 56.7 ppm), reduced the average pore diameter from 4.2 to 1.6 µm, and the number of pores per mm$^2$ from 13.1 to 10.1" were helpful in understanding the processing of CES; however, using the process is not viable for castings of the size intended for end use in this research.

Preliminary un-published studies by Webb et al., transitioning from O'Loughlin to the research reported in this dissertation, focused on chemical composition, dynamic fracture toughness, and prior austenite grain size. As part of those studies CES and 8 alloy modifications of Eglin steel were examined with respect to austenite grain structure and austenitization temperature.

Most of the cast steels had aluminum contents below 0.01 wt.% and produced a minimum limiting prior austenite grain diameter ($L_3$) of 400μm as measured by the Heyn intercept method. In general, the prior austenite grain diameter decreased with increasing austenitizing temperature up to 2200°F. Prior austenite grain diameters up to 1400μm were obtained when austenitized at temperatures between 1700°F and 1900°F. It had been suggested that the anomalous grain coarsening at low temperatures was related to an inhomogenous distribution of persistent alloy carbides that go into solution above 1900°F, which produced a few large grains that coarsen during austenitization at temperatures below 1900°F. The aluminum content of the high nickel variant of Eglin steel was 0.043wt.% and produced an average grain diameter of 200 μm over the entire austenitizing temperature range from 1700°F to 2200°F.

Dynamic fracture toughness testing during preliminary studies was conducted on CES ballistic test plates and a series of 9 Eglin steel chemistries that were modified by addition of Nb and Co or modified by changes in the standard ES-1 chemistry, i.e. high Ni, W-free, low W, low Mn, low carbon, and one chemistry with all alloy additions made leaner. Relative to the standard CES composition, a higher normalization temperature (2200°F vs. 2000°F) produced better toughness results (107 $MPa\sqrt{m}$ vs. 81 $MPa\sqrt{m}$). Addition of Nb produced eutectic carbides, which resulted in lower toughness (64 $MPa\sqrt{m}$) and the toughness exhibited evidence of anisotropy relative to the direction of solidification. For Eglin-based steels normalized at 2200°F for two hours, austenitized at 1900°F for one hour, water quenched, and aged 375°F for 4 hours, the highest average dynamic fracture toughness (107 $MPa\sqrt{m}$) was observed in the standard CES composition. However, the low tungsten alloy and the 5 wt.% Ni alloy merited further investigation with average toughness values greater than 100 $MPa\sqrt{m}$.

The goal of the research reported here was to use existing knowledge and practices of producing Eglin steel as a basis and to advance the science and the physical metallurgy of casting it to produce a more consistent material that meets current performance requirements by optimizing chemical composition, pouring process, and thermal processing.

# PAPER

## I. AN INNOVATIVE HEAT TREATMENT TO IMPROVE THE DUCTILITY OF HIGH STRENGTH STEELS

**AUTHORS:**

T.O. Webb
D.C. Van Aken

Missouri University of Science and Technology
401 W. 16th St.
Rolla, MO
65409

**ABSTRACT**

A new heat treatment schedule designed to refine the prior austenite grain size and improve the lath martensitic microstructure was evaluated on a cast Argon, Oxygen, Decarburized (AOD) refined high strength steel used in applications requiring high toughness. Grain refinement was documented using orientation image mapping produced by an electron back-scatter detector. Elevated temperature normalization to eliminate persistent $M_{23}C_6$ carbides and heat treatment produced a prior austenite grain size of 283 ± 74 μm whereas the new heat treatment described here produced a grain diameter of 58 ± 17 μm. Lath martensite plate misorientation was also quantified and the new heat treatment produced a higher boundary per volume misorientation frequency at approximately 10°, 35°, 45°, and 60°, which likely accounts for the increase in Charpy impact energy at -40° F/C from 34 ± 4 ft-lbs to 40 ± 11 ft-lbs. Hydrogen damage was also apparent in this high strength steel; hydrogen was measured to be 7 ppm in the liquid. The grain refining heat treatment increased the elongation to failure from 3% to 8% and the percent reduction in area from 7% to 21%.

# 1. INTRODUCTION

High strength steels are defined here as exhibiting yield strength greater than 150 ksi and ultimate tensile strengths greater than 200 ksi. Lath martensitic microstructures as shown in Figure 1. are required to obtain adequate ductility as measured by either elongation to failure greater than 8% or reduction in areas greater than 30%. In addition, a Charpy V-notch (CVN) impact energy greater than 40 ft-lbs (54 J) at -40°F/C is often desirable for applications requiring high toughness. There are three basic pathways to obtain high strength and toughness: (1) nickel steels where secondary hardening (Stage IV tempering) is used to precipitate semi-coherent $Mo_2C$, (2) high nickel and cobalt steels where secondary hardening is used to precipitate coherent intermetallic phases, and (3) low carbon alloys where Stage I tempering precipitates semi-coherent, metastable epsilon carbide. In general, any feature (carbide, intermetallic, nonmetallic inclusion, or porosity) that appears on a fracture surface must be eliminated by improved melting practice, casting practice or heat treatment to obtain the best ductility and notch toughness for a given steel chemistry. Prior austenite grain size can also be used to increase strength, ductility, and notch toughness. Controlling the prior austenite grain size is most often accomplished by aluminum additions to prevent normal grain growth and multiple austenitization treatments to refine the austenite grain size. However, both AlN and $Al_2O_3$ can negatively affect ductility and notch toughness. This paper will examine the heat treatment of argon, oxygen decarburized (AOD) refined high strength steel with low aluminum that relies upon Stage I tempering to obtain the desirable properties.

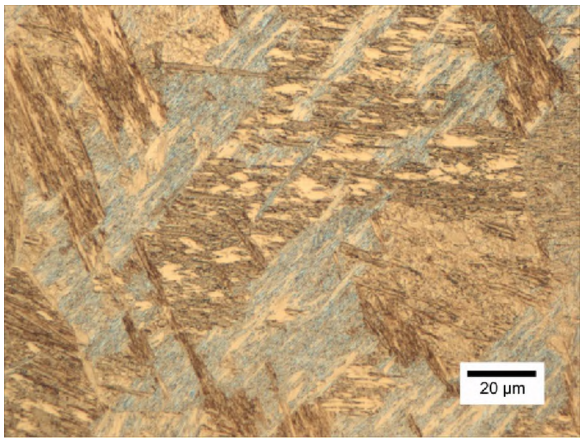


Figure 1. Optical micrograph of lath martensitic microstructure. Lath Packets are differentiated by color where a series of bundles of alternating color are parallel within the packet.

Thick section castings require a more highly alloyed steel to obtain the requisite hardenability to produce a lath martensitic microstructure throughout the cast section. Additions of manganese, chromium, and molybdenum are the most common additions with vanadium and tungsten added to improve Stage I tempering response. High austenitizing temperatures (>1800°F or 982°C) are often required to dissolve persistent alloy carbides and this may lead to austenite grain growth when the steels are designed for -40°F/C notch toughness by reducing the aluminum content. For example it can be shown for high chromium cast steel that temperatures in excess of 2100°F may be required to dissolve the persistent, interdendritic $M_{23}C_6$ carbides. Segregation will result in regions that are lean and rich in solute concentration. Persistent carbides will be difficult to remove if the austenitization temperature is chosen using the nominal steel composition as shown in Figure 2(a). Homogenization of the carbon content is impossible until the persistent carbides are dissolved, see Figure 2(b). Carbon content in the two-phase region is fixed by the solvus temperature and the flux of carbon out of the two phase region is

determined by the dissolution of carbide along the periphery of the segregated region. Carbides near the center of the segregated region coarsen rather than dissolve. Increasing the austenitization temperature to above the solvus temperature of the most segregated region is the only recourse, but this is at the expense of rapid austenite grain growth at the higher temperatures. Again it should be emphasized that these $M_{23}C_6$ carbides are often associated with void nucleation during fracture and should be eliminated to obtain the best ductility of the high strength steel.

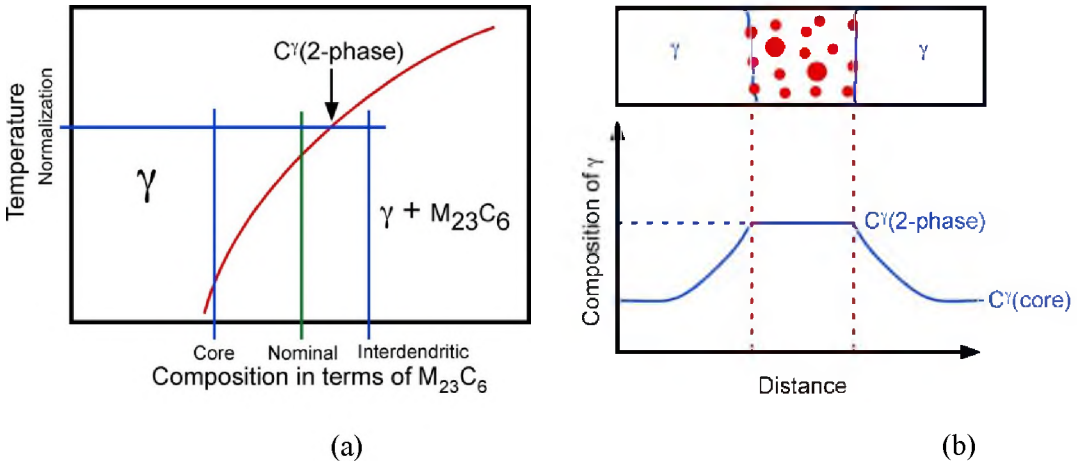


Figure 2. A schematic illustration of how the redistribution of solute is affected by (a) a two-phase equilibrium in the alloy rich interdendritic region and (b) the effect of the two-phase equilibrium restricting the composition of the austenite (γ).

Fracture ductility of steel is dependent upon the volume fraction of void nucleating second phases and that includes porosity. The true strain at fracture ($\varepsilon_f$) is related to the reduction in area ($RA$) as shown by equation (1). The true fracture strain is the sum of the true strain to

nucleate a void ($\varepsilon_{nucleate}$) and the true strain to grow ($\varepsilon_{grow}$) the void to critical size for shear failure. Brown and Embury related $\varepsilon_{grow}$ to the volume fraction ($V_f$) of void nucleating second phase particles. [1] Negating the strain to nucleate is appropriate with respect to porosity, since the void is already present. Garrison and Wojcieszynski performed careful analysis of matching fracture surfaces and showed that only a small fraction of the microvoids contain the initiating inclusion [2]. This may suggest that the nonmetallic inclusions are poorly bonded and that the strain to nucleate the void ($\varepsilon_{nucleate}$) is negligible. In contrast, nanometer-sized carbides may require the addition of a nucleating strain, since they are observed with a much higher frequency on the fracture surface. [3] These carbides would still lower the overall strain to fracture, since the carbides initiate the microvoids and the voids grow to fracture as described by the Brown-Embury equation.

$$\varepsilon_f = \ln\left(\frac{1}{1-RA}\right) = \varepsilon_{nucleate} + \varepsilon_{grow} = \varepsilon_{nucleate} + \frac{1}{2}\ln\left[\left(\frac{\pi}{6V_f}\right)^{\frac{1}{2}} - \left(\frac{2}{3}\right)^{\frac{1}{2}}\right] \quad (1)$$

In contrast, the low temperature fracture (cleavage) is dependent upon the lath martensitic structure, which is characterized as having a packet size containing three possible crystallographic bundles, and each bundle contains two crystallographic variants of the lath plates that are nearly parallel with only 10.53° of misorientation. [4] Lath packets are differentiated by multiple parallel bundles as shown in Figure 1 where these bundles have varying colors. The cleavage strength or the energy of fracture is related to the size of microstructural feature resisting the crack propagation, which is the lath bundle size for lath martensite. Increasing the low temperature fracture resistance is most often accomplished by refining the prior austenite grain size, which reduces both the lath martensite packet size and lath bundle size; and, increases the number per unit volume of high angle boundaries greater than 15°. The cleavage strength would

be inversely proportional to the square root of the lath bundle width. Thus, the prior austenite grain size becomes important with respect to CVN toughness at -40°F/C.

Thermal cycling steel through the critical temperatures is a traditional method of refining the austenite or ferrite grain structure using the ferrite to austenite to ferrite polymorphic phase transformation. Experience indicates; however, that the grain size reduction is exhausted after 2-3 thermal cycles as a result of austenite grain growth at the austenitizing temperature. The limitations of particle pinning to prevent normal grain growth or crystallographic considerations also limit the effectiveness of the polymorphic phase transformation.

The crystallography of the polymorphic transformation is dominated by the Kurdjumov-Sachs (K-S) orientation relationship. These same crystallographic considerations are important with respect to lath martensite. Figure 3(a) shows the types of boundaries created as austenite transforms to ferrite to produce blocky ferrite. The ferrite nucleates at the prior austenite grain boundary and is related by the K-S orientation relationship to one austenite grain only. Two possibilities of grain misorientation will be observed when the ferrite grains impinge upon growing together: either the boundaries will be random or they will meet as variants determined by the K-S orientation relationship. Figure 3 (b) shows the expected grain distributions based upon these two possibilities.

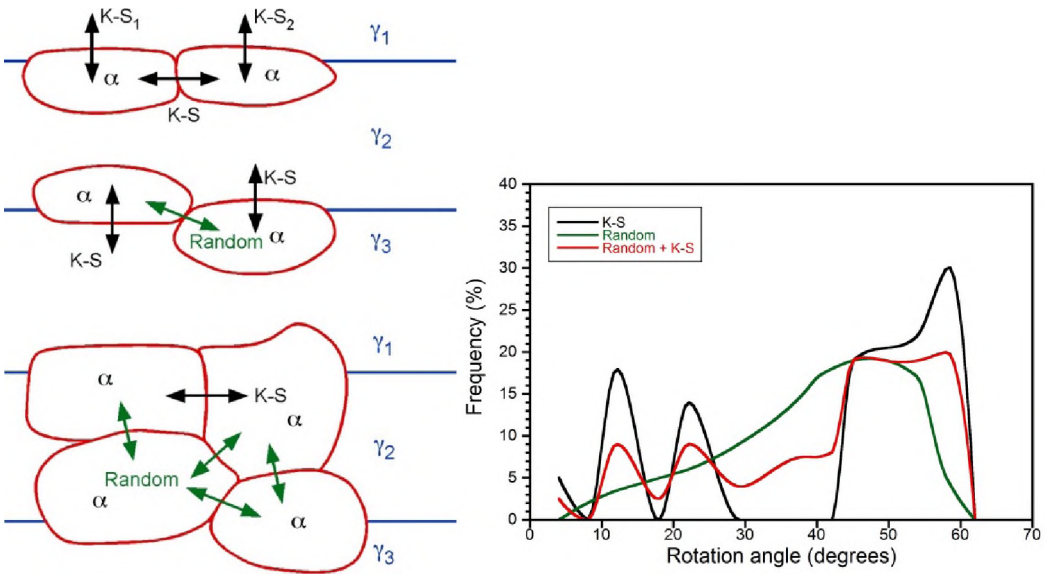


(a) (b)

Figure 3. Reproduction of graph from Novillo et al. [5] showing grain misorientation distribution for ferrite grains produced during cooling transformation. A similar distribution may be expected upon quenching to form martensite.

Upon reheating, there is the distinct possibility that the K-S related grains may return to austenite with exactly the same crystallography, i.e. 2 ferrite grains become one austenite grain and thus limit the amount of refinement achieved during the polymorphic phase transformation. Furthermore, upon cooling, the transformation may produce the same two previous ferrite grains.

A study by Novillo et al. [5] demonstrated that recrystallization prior to the austenite to ferrite transformation increases the grain misorientation frequency resulting from polymorphic phase transformations. The same should be true also when the ferrite is deformed and recrystallization occurs upon heating to form austenite. Taking advantage of prior plastic deformation to improve cast steel would appear problematic at first thought; however, quenched martensite is known to exhibit a highly dislocated microstructure. Tempering martensite at

temperatures greater than 1100°F (600°C) will induce recrystallization and a heat treatment consisting of (1) quench hardening, (2) tempering, and (3) quench hardening may produce the desired grain refinement and an improvement in ductility and toughness. Similar strategies have been used by Morris et al. [6] in modifying the fracture resistance of cryogenic steels.

The difficulty with processing high strength steel will be the elimination of persistent carbides during austenitization. The high temperatures necessary to dissolve $M_{23}C_6$ carbides are likely to promote grain growth. The grain refinement study presented here utilizes a quench after normalization to form martensite, which is a microstructure that approximates a cold worked material. Upon tempering the lath martensite it is expected to recrystallize and induce a refined austenite grain structure upon heating to the hardening temperature. The tempering temperature and time were chosen to precipitate alloy carbides ($M_{23}C_6$), which may persist up to the austenitization temperature and serve as a temporary pinning agent to resist austenite grain coarsening. Application of this grain refinement technique is expected to improve the strength and ductility of a cast high strength steel which is used in high impact applications such as ground engaging tools, armor and penetrator type projectiles.

# 2. EXPERIMENTAL METHODS

## 2.1. CHEMICAL ANALYSIS

The steel for this study was refined using Argon, Oxygen, Decarburization (AOD) and the resulting steel was expected to yield relatively clean steel with minimal inclusions. Melt chemistry was closely controlled to minimize aluminum content to reduce alumina and aluminum nitride inclusions. Carbon content was lowered in an effort to improve ductility and low temperature notch toughness.

A hybrid chemical analysis is provided in Table I where American Cast Iron Pipe Co. (ACIPCo) provided optical emission spectrometry results for the metallic elements. Carbon and sulfur were measured using a LECO CS6000; oxygen and nitrogen were measured using a LECO TC 500 by Missouri University of Science & Technology.

Table I- Chemical analysis for high strength steel.

| Element (wt%) | C | Mn | Si | Cr | Ni | Mo | W | V | Cu | P | S | Ca | N | Al | O |
|---|---|---|---|---|---|---|---|---|---|---|---|---|---|---|---|
| High Strength Steel | 0.25 | 0.77 | 0.88 | 2.64 | 1.03 | 0.425 | 0.92 | 0.097 | 0.12 | 0.006 | 0.004 | - | 0.009 | 0.008 | 0.022 |

## 2.2. HEAT TREATMENT

The standard heat treatment for this steel consisted of a hydrogen bake at 600°F (315°C) for 16hrs, to remove hydrogen that may cause a phenomena known as hydrogen embrittlement, a normalization at 2125°F (1163°C) for 8 hours with an air fan cool, austenitization at 1950°F

(1066°C) for 4 hours with a water quench, and a temper at 380°F (193°C) for 5 hours. The new heat treatment consisted of a hydrogen bake at 600°F (315°C) for 7 hours, a nonstandard normalization at 2100°F (1149°C) for 2 hours with an oil quench to produce a martensitic microstructure, an intermediate temper at 1200°F (649°C) for 4 hours, an austenitization at 1900°F (1038°C) for 1 hour with a water quench, and a temper at 375°F (190°C) for 4 hours. Austenitization temperatures for the new heat treatment were chosen by modeling the solidification of the high strength steel with FactSage version 6.4 with the FSstel database and using a Scheil-Gulliver solidification model to predict the chemistry of the last liquid then using an equilibrium solidification model based on that chemistry to determine the expected weight percent of the $M_{23}C_6$ carbide, see Figure 4. At 2100°F (1149°C), all of the $M_{23}C_6$ is expected to go into solution whereas at 1900°F (1038°C) up to 1.8% $M_{23}C_6$ carbide is possible in the interdendritic regions.

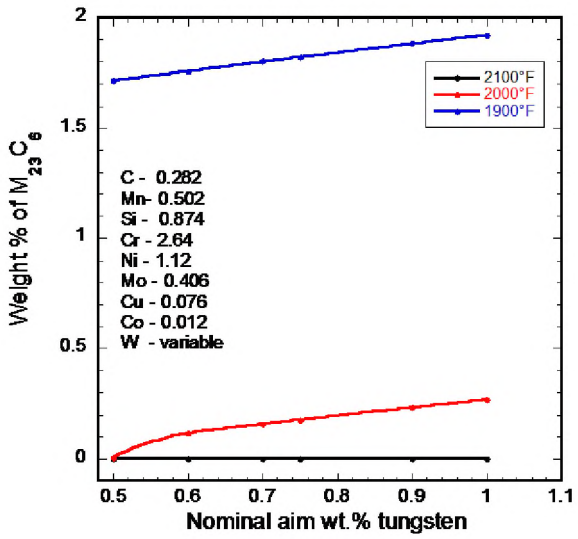


Figure 4. The plot shows the weight percent of carbide predicted for a composition of the last 15-20% liquid predicted using the nominal high strength steel composition shown as the original input in FactSage Version 6.4 with the FSstel database and a Scheil-Gulliver segregation model followed by equilibrium cooling from the predicted segregated chemistry. The nominal tungsten composition was used as the independent variable (x-axis).

## 2.3. MECHANICAL TEST PROCEDURES

Materials for testing were removed by waterjet cutting from 15"x7.5"x2" cast weld plates, and allowed for 3 specimens each of tensile testing, 4 specimens each for Dynamic Fracture Toughness (DFT) testing at room temperature and 4 specimens each for CVN impact testing at -40°F/C. Finish machining of specimens and tensile testing was conducted by Westmoreland in accordance with ASTM E8-13 at a rate of 0.005in/in/min. Ground and notched CVN bars received from Westmoreland were fractured in accordance with section 8 of ASTM E23-12 at a temperature of - 40°F/C using a Tinius Olson model 84 Charpy pendulum impact machine outfitted with an MPM instrumented striker. Ground DFT bars received from Westmoreland were notched using a 0.012in (0.31mm) thick diamond-wafering blade and pre-cracked in 3-point bending (R = 0.1) to a total initial crack length ($a_0$) of between 0.18in and 0.22in (4.5mm and 5.5mm) as per ASTM E1820-11, section 7.4.2. Fatigue loading was incrementally reduced during pre-cracking, as per section 7.4.5 of ASTM E1820-11, to avoid large plastic strain fields that might affect measurement of the fracture toughness. Finished DFT bars were fractured at room temperature using a Tinius Olson model 84 Charpy pendulum impact machine outfitted with an MPM instrumented striker. The load vs. displacement data was used to estimate the dynamic fracture toughness ($K_{ID}$) using the single specimen technique developed by Schindler [7]. All specimens behaved in an elastic-fracture manner. The maximum load recorded during impact was used as $P_Q$ and the crack length, a, was measured after fracture using optical microscopy. The average crack length was determined by using the nine point method described in section 8.5.3 of ASTM E1820-11 with the exception that the original crack length was not heat tinted prior to fracture. The toughness, $K_Q$, was calculated using section A3.5.2 of ASTM E399-08. The reported value of $K_{ID}$ is the calculated value $K_Q$.

# 3. RESULTS

## 3.1. MECHANICAL TEST RESULTS

Test results shown in Table II indicate an improvement in all mechanical properties using the new heat treatment with an average tensile strength of 230 ksi, average yield strength of 176 ksi, average reduction in area of 21%, average instrumented CVN energy of 40 ft-lbs, and average Dynamic Fracture Toughness of 110 MPa√m compared to the standard heat treatment with an average tensile strength of 184 ksi, average yield strength of 175 ksi, average reduction in area of 6.7%, average instrumented CVN energy of 34 ft-lbs, and average Dynamic Fracture Toughness of 111 MPa√m. Mechanical test results for individual specimens are given below in Tables II, III, and IV.

Table II- Mechanical test results of high strength steel with standard and new heat treatments. Uncertainty reported is sample standard deviation.

| Condition | Bar | UTS (ksi) | Condition Average | .2% YS (ksi) | Condition Average | Reduction in Area (%) | Condition Average | Elongation (%) | Condition Average |
|---|---|---|---|---|---|---|---|---|---|
| Standard Heat Treatment | B1 | 179 | 184 ± 12 | 177 | 175 ± 2.8 | 9.0 | 6.7 ± 2.3 | 1.9 | 2.7 ± 0.61 |
| | B2 | 173 | | 171 | | 7.5 | | 3.2 | |
| | B3 | 201 | | 176 | | 3.7 | | 3.2 | |
| New Heat Treatment | M1 | 229 | 230 ± 0.67 | 175 | 176 ± 0.74 | 16.0 | 21 ± 8.3 | 7.5 | 8.3 ± 1.9 |
| | M2 | 230 | | 177 | | 33.0 | | 11.0 | |
| | M3 | 230 | | 176 | | 15.0 | | 6.5 | |

Table III- Charpy V-notch impact energies (-40°F) for four specimens each of standard and new heat treated steel.

| | CVN min ft-lb (J) | CVN max ft-lb (J) | Average ±95%CL | Hardness HRC±95%CL |
|---|---|---|---|---|
| **Standard Heat Treatment** | 33 (44) | 36 (48) | 34 ± 4 (46 ± 5) | 48 ± 1.4 |
| **New Heat Treatment** | 35 (48) | 43 (58) | 40 ± 11 (55 ± 15) | 49 ± 1.7 |

Table IV- Dynamic Fracture Toughness at RT for three specimens each of standard and new heat treated steel.

| | DFT min $K_{ID}$ MPa√m | DFT max $K_{ID}$ MPa√m | Average ±95%CL | Hardness HRC±95%CL |
|---|---|---|---|---|
| **Standard Heat Treatment** | 115 | 108 | 111 ± 9 | 46 ± 0.3 |
| **New Heat Treatment** | 117 | 106 | 110 ± 15 | 44 ± 0.8 |

### 3.2. OPTICAL AND SCANNING ELECTON MICROSCOPY

Optical micrographs of the cast steel after receiving the standard heat treatment and the new heat treatment are shown in Figure 5. Some segregation as noted by light etching of interdendritic regions is still evident in the optical images; however, a fully martensitic structure can also be seen. A modified Marbles reagent that had been cut by 50% with Glycerin to etch less aggressively was used to highlight the prior austenite grain boundaries and the Heyn intercept grain counting method was used to determine the mean intercept length ($L_3$) of the prior austenite grain diameter. The reported uncertainty ($\Delta L_3$) is at a 95% confidence level. A prior austenite grain size of 283 ± 74 μm was measured for Figure 5(a), which received the standard heat treatment, and a

prior austenite grain size of 58 ± 17 μm was measured for Figure 5(b) which received the new heat treatment.

Orientation Image mapping (OIM) using Electron Backscatter Diffraction on a FEI Quanta 200F Scanning Electron Microscope was conducted and is shown in Figure 6, images were subject to a cleanup procedure, setting the minimal confidence index to 0.1 and matching orientation of data points that are within 5 degrees of 4 of its closest neighboring data points. The Heyn intercept grain counting method was used to determine the mean intercept length ($L_3$) of the prior austenite grain diameter with a reported uncertainty ($\Delta L_3$) at a 95% confidence level. A prior austenite grain diameter of 265 ± 88μm was measured for the image in Figure 6(a), which received the standard heat treatment; and, a prior austenite grain diameter of 56 ± 12μm was measured for the image in Figure 6(b), which received the new heat treatment. Both measurements show good agreement with measurements made by optical microscopy. Higher magnification OIM of the same areas in Figure 6 are shown in Figure 7. A distribution of the misorientation angles between crystallographic directions in the OIM's from Figure 6 are shown in Figure 8. Higher frequencies of grain misorientations per unit area at approximately 10°, 35°, 45°, and 60° help explain the observed increases in ductility and notch toughness for the new heat treatment.

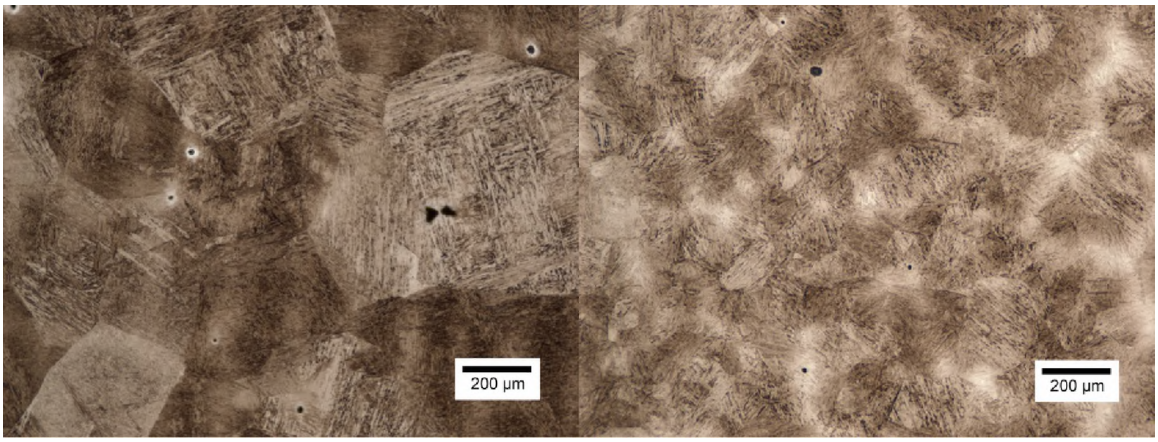


(a) (b)

Figure 5. Optical microscope images of high strength steel. (a) Optical image of the standard heat treatment, and (b) Optical image of the new heat treatment. Modified Marble etch.

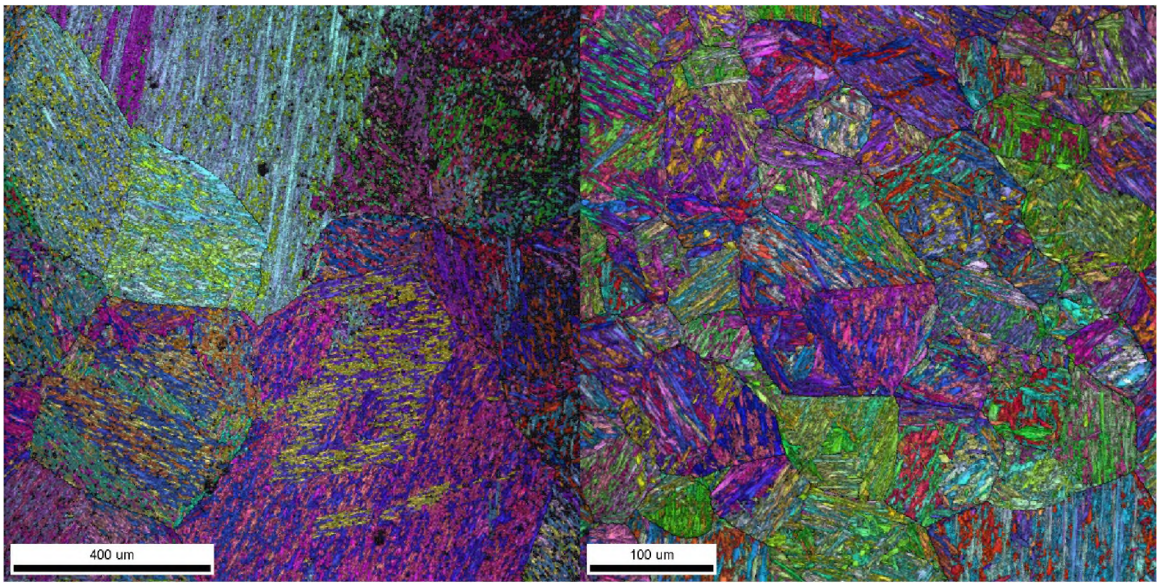


(a) (b)

Figure 6. Orientation Image Map (OIM) using Electron Backscatter Diffraction (EBSD). (a) OIM of the standard heat treatment, and (b) OIM of the new heat treatment. Colors are randomly generated to show differences in crystallographic orientation, and boundaries between 15° and 50° are highlighted in black to highlight prior austenite grain size.

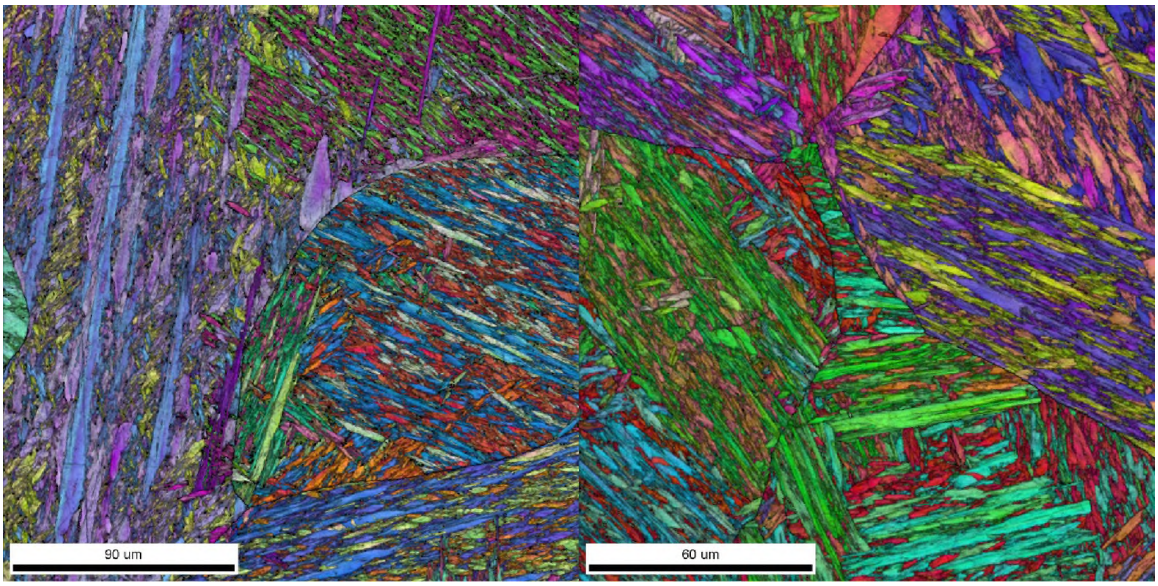


(a) (b)

Figure 7. Orientation Image Map (OIM) using Electron Backscatter Diffraction (EBSD). (a) OIM of the standard heat treatment, and (b) OIM of the new heat treatment. Colors are randomly generated to show differences in crystallographic orientation, and boundaries between 15° and 50° are highlighted in black to highlight prior austenite grain size.

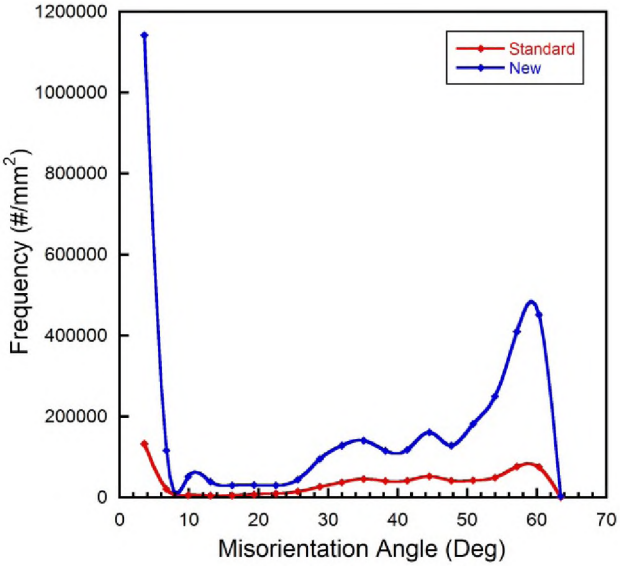


Figure 8. Distribution of misorientation angles between crystallographic directions within the Orientation Image Maps shown in Figure 6. Increases at approximately 10°, 35°, 45°, and 60° indicate a possible increase in ductility and correlate well to increases in -40 CVN energies for specified heat treatments.

As stated earlier the cleavage strength or the energy of fracture is related to the size of microstructural feature resisting the crack propagation, which is the lath martensite bundle size. Increasing the low temperature fracture resistance is most often accomplished by refining the prior austenite grain size, which reduces both the lath martensite packet size and lath bundle size while increasing the number per unit volume of high angle boundaries greater than 15°. Physical measurements of the martensite features shown in Table V indicate a reduction in packet length and width, as well as lath length and width; however, an anomalous increase in bundle width was observed. Evaluation of misorientation within an individual grain is shown in Figure 9 in which it can be seen that intermediate angles are limited to prior austenite grain boundaries; and thus, increases in toughness and ductility are likely due to grain refinement during the polymorphic phase transformation.

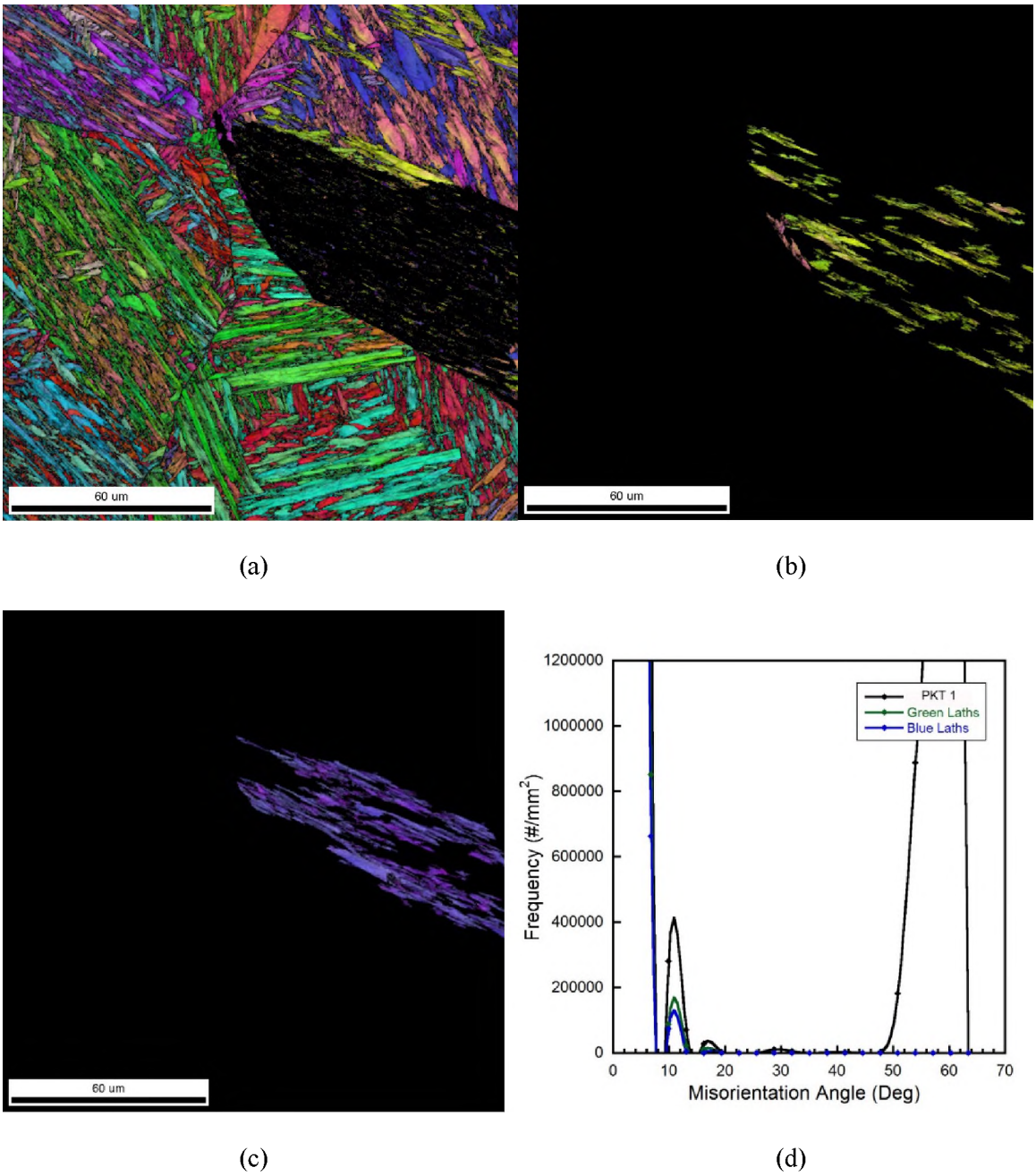


Figure 9. Orientation Image Map (OIM) using Electron Backscatter Diffraction (EBSD) for the new heat treatment. (a) Individual packet location with in grain from Figure 7(b), (b) green laths of similar orientation within 9(a), (c) blue laths of similar orientation within 9(a), and (d) distribution of misorientation angles within the individual packet.

Table V- Physical measurements of martensite structures for high strength steel with standard and new heat treatment.

| Condition | Prior Austenite Grain Size (μm) ± 95%CL | Packet Length (μm) ± 95%CL | Packet Width (μm) ± 95%CL | Bundle Length (μm) ± 95%CL | Bundle Width (μm) ± 95%CL | Lath Length (μm) ± 95%CL | Lath Width (μm) ± 95%CL |
|---|---|---|---|---|---|---|---|
| **Standard Heat Treatment** | 265 ± 88 | 291 ± 59 | 185 ± 71 | 291 ± 59 | 3.1 ± 0.67 | 55 ± 19 | 1.5 ± 0.22 |
| **New Heat Treatment** | 56 ± 12 | 50 ± 7.1 | 34 ± 12 | 50 ± 7.1 | 3.6 ± 0.45 | 50 ± 7.1 | 1.0 ± 0.13 |

OIM was also used to identify retained austenite (see Figure 10) for the sampled areas shown in Figure 7. Small amounts of retained austenite are clearly present and are located along lath boundaries in the original heat treatment whereas the retained austenite is more randomly located in the new heat treatment. An attempt to quantify the retained austenite in each microstructure was conducted using X-ray diffraction and is shown in Figure 11. Large intensity peaks at approximately 44.8°, 64.6°, and 81.8° represent reflections about the {110}, {200}, and {211}, respectively for BCC martensite. Small intensity peaks at approximately 50.8, and 74.3° represent reflections about the {200}, and the {220} for FCC austenite. Greater intensity for the {220} than the {200} for austenite indicates the large grain size of the standard heat treatment introduces a diffraction preference specific to the individual grain(s) as shown in Figure 11(b). Peak intensities for retained austenite were large enough to identify the presence of retained austenite; however, the low intensities and texturing prevented quantification. A simple comparison of the OIM images in Figure 10 would suggest a higher volume fraction of retained austenite in the standard heat treatment.

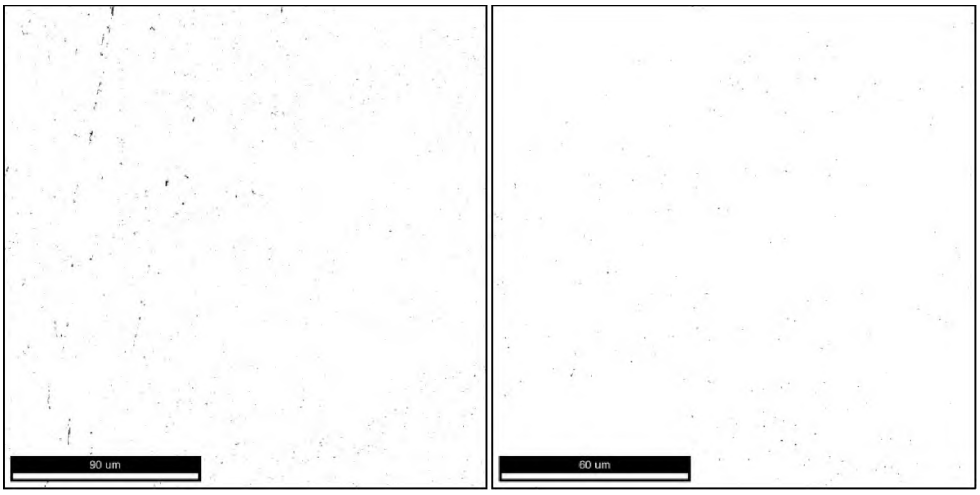


(a) (b)

Figure 10. Orientation Image Map (OIM) using Electron Backscatter Diffraction (EBSD) of retained austenite. (a) OIM of the original heat treatment and (b) OIM of the new heat treatment. Location of retained austenite is clearly along lath boundaries in (a) and is more randomly distributed in (b).

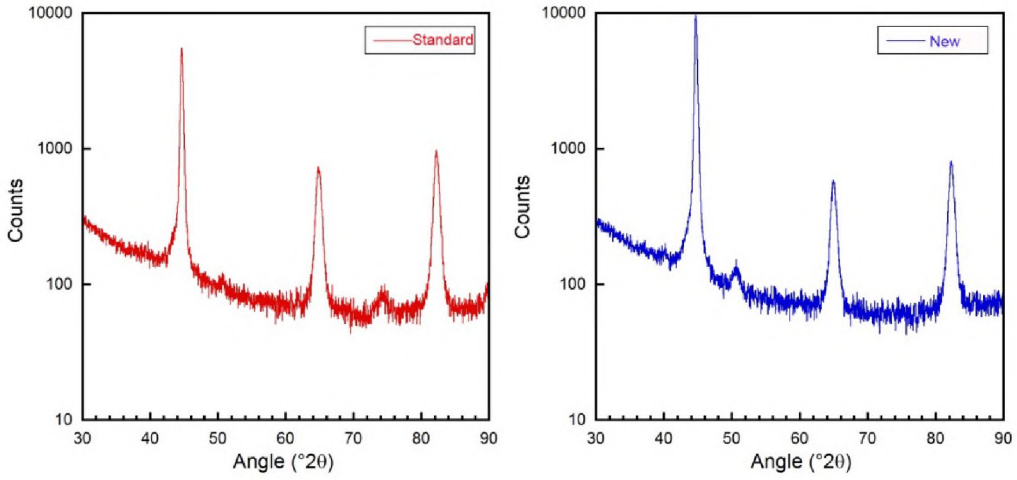


(a) (b)

Figure 11. X-Ray diffraction intensity peaks of retained austenite. (a) of the original heat treatment and (b) of the new heat treatment. Larger second peak at (220) reflection in standard heat treatment indicates more texture for retained austenite.

### 3.3. INCLUSION ANALYSIS AND FRACTOGROPHY

Inclusion and porosity measurements of the two heat treatmented materials were performed using an ASPEX SEM with PICA 1020 automated feature analysis software. Results for each of the tensile bars are shown in Figure 12 and in Figure 13. The dominant inclusion types in both heat treatments were $Al_2O_3$, MnS and complex $MnO\text{-}Al_2O_3\text{-}SiO_2$ with varying amounts of porosity between the tensile bars.

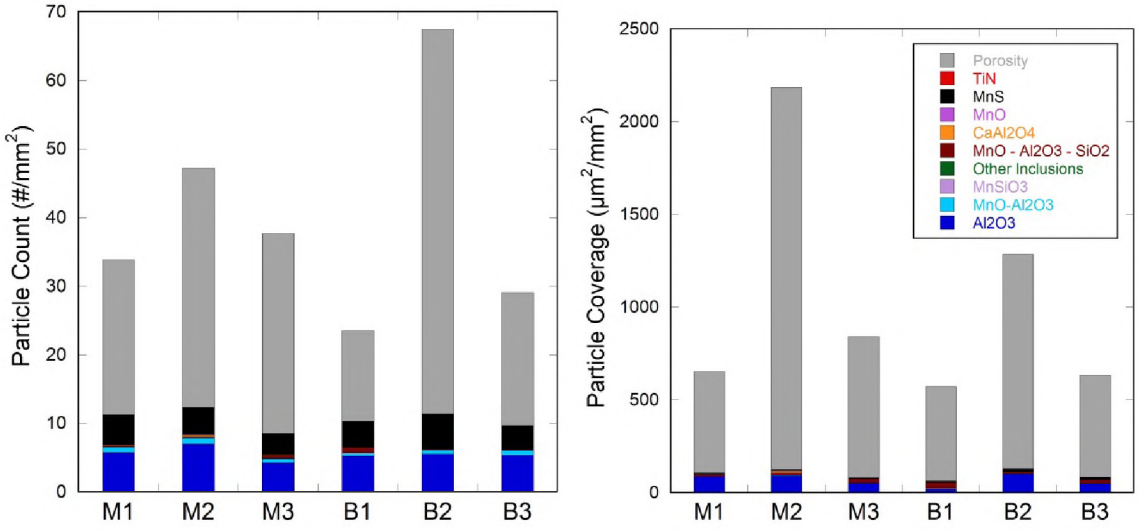


(a) (b)

Figure 12. Automated feature analysis for tensile bars of each tensile bar. (a) Density of inclusions and pores measured as an areal density. (b) Area fraction of inclusions and pores.

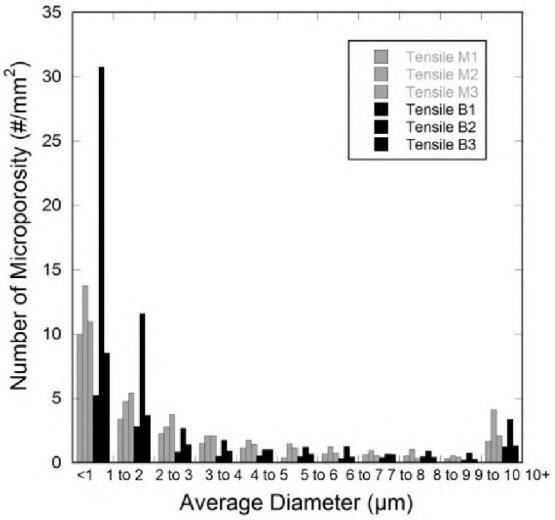


Figure 13. Frequency histogram of porosity diameter showing similar porosity density distribution between all of the tensile bars.

Fractography was performed on the tensile bars listed in Table II using scanning electron microscopy. Figure 14 shows an image of the standard heat treated tensile bar B1, which shows an intergranular fracture with microvoid coalescence on the grain surfaces. This type of fracture is typical of steel embrittled by overheating; however, this fracture mode was not representative and only observed in one of the test bars. Overheating is a result of elevated temperature solution of MnS and precipitation of the MnS along prior austenite grain boundaries during subsequent thermal processing. The MnS nucleate voids and the cohesion of the prior austenite grains is lost and fracture follows the embrittled grain boundaries. Figure 15 shows a reduced magnification image of the fractured tensile bar showing a plateau fracture feature that was associated with porosity and cleavage fracture near shrinkage pores as shown in Figure 16. Cleavage fracture of the lath martensite microstructure is shown in Figure 17, which is typical of hydrogen damage in high strength steels. Fracture by mircovoid coalescence was observed elsewhere on the fracture surface as shown in Figure 18.

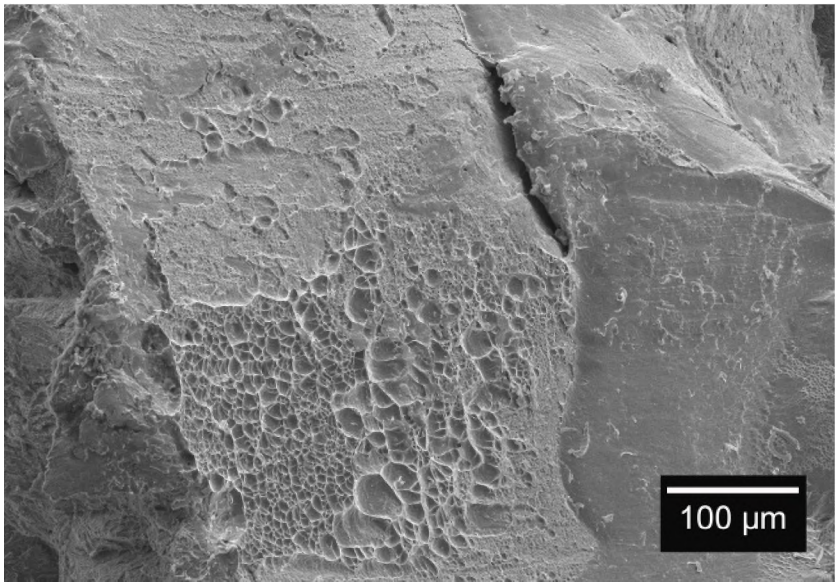


Figure 14. Secondary electron image of standard heat treated B1 tensile bar showing intergranular like fracture as might be expected for embrittlement by overheating.

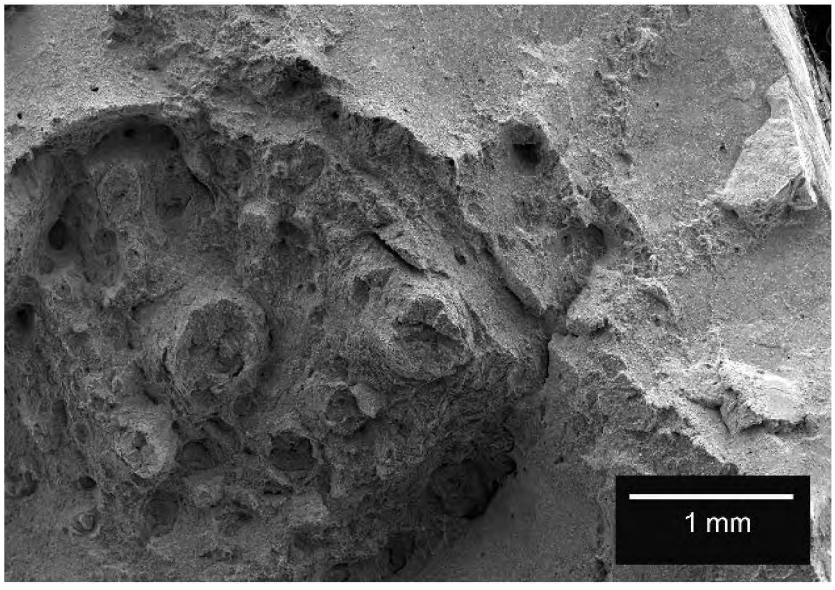


Figure 15. Secondary Electron image of tensile bar B1 with standard heat treatment showing large circular plateaus at shrinkage pores with brittle cleavage facets at the edge of the pore and microvoid coalescence in between plateaus.

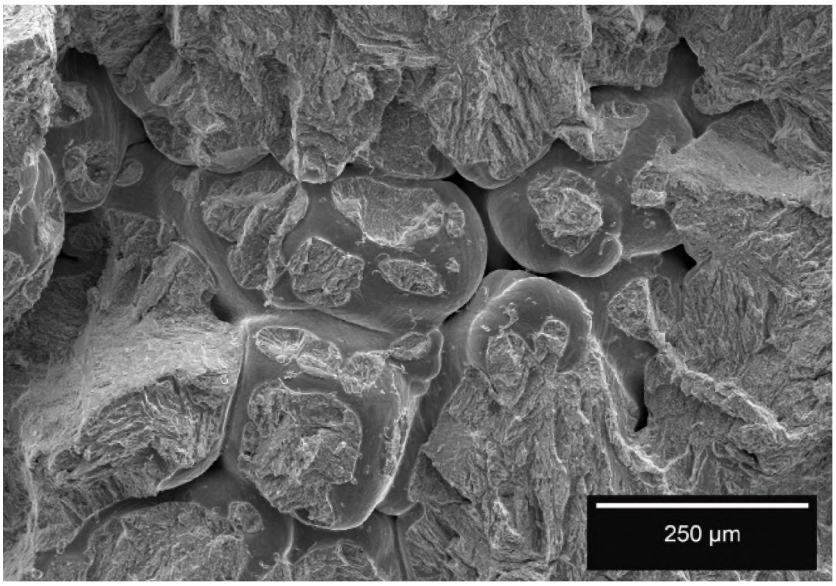


Figure 16. Secondary Electron image of tensile bar with new heat treatment showing a shrinkage pore with the majority of the fracture surface exhibiting brittle cleavage facets, which indicate hydrogen damage.

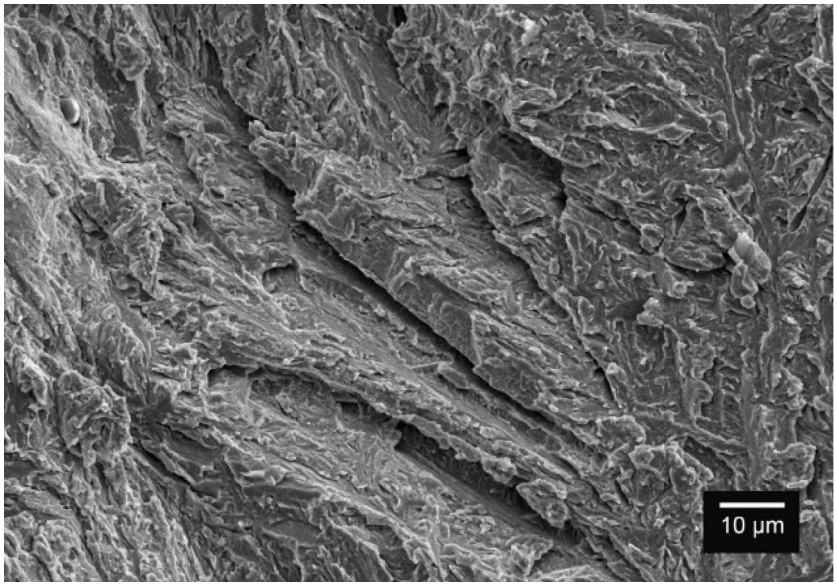


Figure 17. Secondary Electron image of the edge of the pore in Figure 16 showing brittle cleavage facets which is likely due to hydrogen embrittlement.

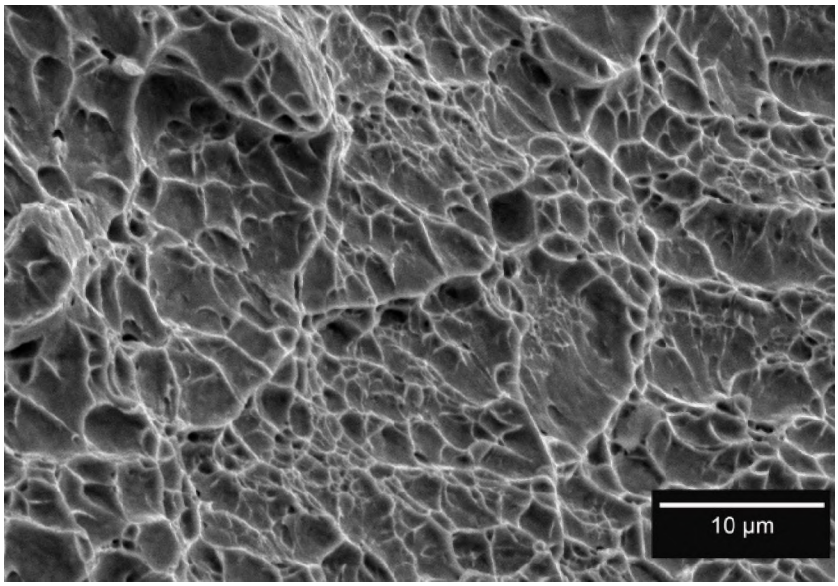


Figure 18. Secondary Electron image of tensile bar with new heat treatment showing fracture by microvoid coalescence. Image was taken in areas between the plateaus showing hydrogen damage.

Shrinkage porosity serves as a strong hydrogen trap and under tensile loading (slow strain rates) typical of ASTM E8 testing the pores can produce a significant stress concentration. The close proximity of a hydrogen source can then produce damage and cleavage fracture similar to that shown in Figure 16 and 17. Hydrogen embrittlement will significantly impact both elongation and reduction in area; however, hydrogen damage is unlikely to occur at higher strain rates such as those encountered in CVN or DFT tests. Given the low elongation to failure, the apparently unaffected CVN and DFT results, and the fractographic evidence it is likely that the low ductility of the standard heat treatment may be accounted for as a combination of overheating, porosity, and hydrogen damage. Hydrogen damage was also evident in the steel processed by the new heat treatment as well.

# 4. DISCUSSION

The new heat treatment for this high strength steel clearly shows a smaller prior austenite grain structure; however, some question may arise as to the nature of the mechanism by which this has occurred. The rationale of quenching from the typical normalization temperature and then tempering at 1200°F (649°C) was two-fold. First, lath martensite is known to be heavily dislocated with dislocation densities on the order of $10^{14}$ $m^{-2}$. [8] The work of Novillo et al. [3] might suggest that a recrystallization of the martensite has the potential to produce a higher frequency of grain misorientations in the newly formed austenite upon heating to the hardening temperature. Recrystallization during tempering is typically observed in alloyed steels above 1100°F (600°C). Second, tempering at 1200°F will produce secondary hardening or Stage IV tempering as a result of alloy carbide precipitation such as the $M_{23}C_6$. These carbides may act as Zener pinning agents, which prevent austenite grains from growing during the subsequent austenitization for hardening. As indicated in Figure 4, the interdendritic regions may have more than 1.8 wt.% of stable $M_{23}C_6$ carbides. Thus differentiation of both mechanisms is necessary in order to understand which mechanism provides for the grain refinement in this steel.

Evidence of recrystallization in the 1200°F tempered steel was explored using EBSD/OIM. Nuclei of recrystallizing grains may be identified by grain boundary misorientation angles greater than 15° as described by Rios et al. [9]. A comparison of the as-cast, normalized and quenched, tempered, and quench hardened microstructures is shown in Figure 20. No increase in grain misorientation frequency was observed after tempering at 1200°F, but recrystallization upon heating to the 1900°F hardening temperature cannot be excluded. It should be noted; however, that austenite formation should begin at temperatures above 1200°F as shown in Table VI and compete with recrystallization. Thus, it is doubtful that recrystallization plays an important role in the observed grain refinement. The transformation temperatures shown in Table VI are from a review of literature on steels of similar chemistry and by thermodynamic

calculation using FactSage software. Thermodynamic calculations predict austenite (γ), carbide ($M_{23}C_6$), and ferrite (α) will be present below 1481°F. Leister and Dupont [10] report austenite (γ), ferrite (α), and carbide (θ) will be present below 1488°F based upon dilatometry results, which shows good correlation between calculated and experimental results assuming the carbide is actually $M_{23}C_6$. The dilatometry results were based upon curves for a cooling rate of 0.01 C°/s, which approximates equilibrium cooling. FactSage calculations assumed the nominal composition of the high strength steel as reported in Table 1.

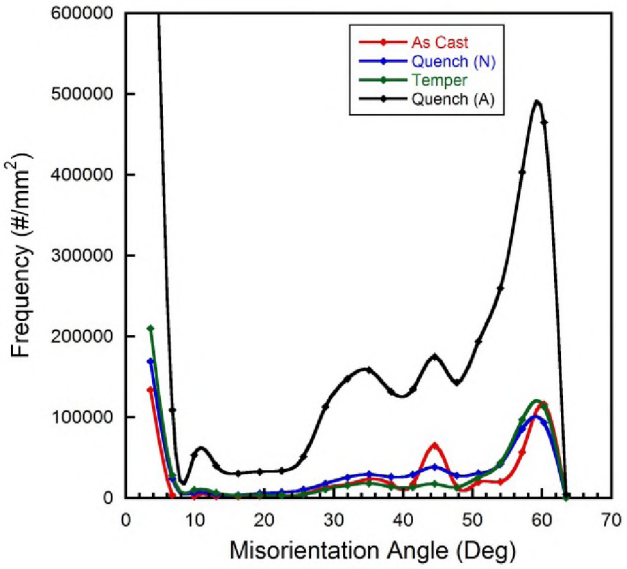


Figure 19. Distribution of misorientation angles between crystallographic directions within Orientation Image Maps of specimens through the microstructural evolution of the new heat treatment.

Table VI- Equilibrium reaction start temperatures for cooling: calculated equilibrium using FactSage and measured [10] by dilatometry (0.01C°/s)

| Phases | Calculated °F (°C) | Reported °F (°C) |
|---|---|---|
| $\gamma + M_{23}C_6$ | 1634 (890) | - |
| $\alpha+\gamma+M_{23}C_6$ | 1481 (805) | 1488 (809) |
| $\alpha + M_{23}C_6$ | 1202 (650) | 1197 (647) |

Upon heating to 1900°F for quench hardening, the austenite would begin to nucleate and grow above 1202°F (650°C). Growth of the austenite would be in the presence of persistent carbides and these carbides may provide Zener pinning and restrict the austenite grain growth. Automated feature analysis was performed using the ASPEX SEM equipped with PICA 1020 software to characterize the carbide distribution (see Figure 21) and carbide chemistry (see Figure 22) in the 1200°F tempered steel. It should be noted that Figure 21 depicts the location of each carbide detected, but does not indicate the size. Clusters of carbides are located in the interdendritic regions of the microstructure and the secondary spacing is on the order of 100μm. A microstructure of austenite and $M_{23}C_6$ is expected above 1634°F (890°C) and growth of the austenite grain is controlled by the coarsening and dissolution of the $M_{23}C_6$ carbide. These carbides will persist in the segregated regions as shown in Figure 4 and will continue to resist grain coarsening during austenitization. It may thus be concluded that the persistent carbides behave as Zener pining agents and provide sufficient retardation of normal grain growth at 1900°F to maintain a finer prior austenite grain structure for the new heat treatment.

Future work will examine the necessity of quenching the high strength steel from the normalization temperature. Air cooling these highly alloyed steels would most probably produce a bainitic microstructure, which may also be tempered to produce the desirable $M_{23}C_6$ carbides.

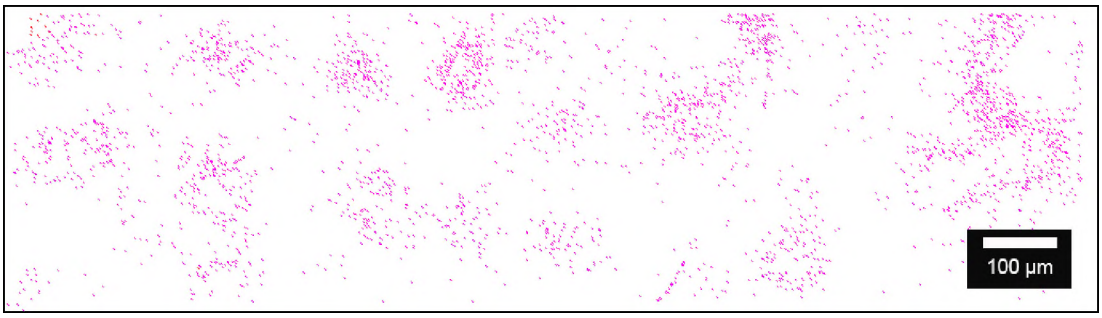


Figure 20. Carbide distribution map generated using the ASPEX PICA 1020 automated feature analysis software showing distribution of small (<2µm) bright Cr, W, Mo rich $M_{23}C_6$ carbides in matrix. Carbides appear to be distributed into interdendritic areas.

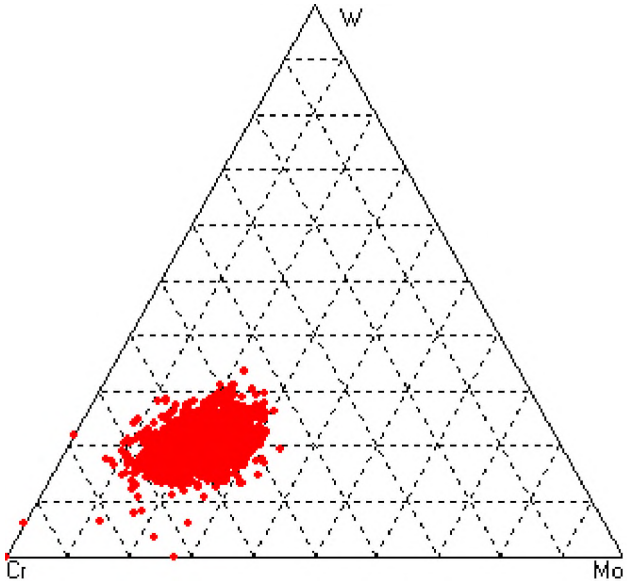


Figure 21. Mo, W, Cr ternary phase diagram generated using the ASPEX PICA 1020 automated feature analysis software showing distribution of small (<2µm) bright Cr, W, Mo rich $M_{23}C_6$ carbides in matrix.

# 5. CONCLUSIONS

Addition of an elevated temperature tempering operation at 1200°F (649°C) was used to precipitate $M_{23}C_6$ carbides and these carbides acted as Zener pinning agents to retard normal grain growth during austenitization for quench hardening. The quenched steel demonstrated a finer prior austenite grain size, greater ductility and increased Charpy V-notch toughness at -40°F (-40°C). No evidence of recrystallization was observed using EBSD/OIM of the 1200°F tempered microstructure.

## 6. ACKNOWLEDGEMENTS

This work has been supported under the Steel Founders' Society of America (SFSA) program on Casting and Advanced Steel Technology that has been funded by the Army Research Laboratory under the provisions of cooperative agreement W911NF-12-2-0033. The authors are grateful for steel castings supplied by Bradken-Atlas LP., and for optical emission spectroscopy results provided by Mr. Don Denney at American Cast Iron Pipe Co. (ACIPCo). The authors also gratefully acknowledge the Army Research Office Defense University Research Instrumentation Program (award number W911NF-08-1-0267) for financial support in buying the ASPEX-PICA 1020 SEM that was used for automated feature analysis, as well as the Air Force Research Laboratory at Eglin AFB in providing support for conducting Orientation Image Mapping.

## REFERENCES


[1] L.M. Brown and J.F. Embury, The microstructure and design of alloys: proceedings of the third International Conference on the Strength of Metals and Alloys (Cambridge) The Institute of Metals, vol. 1, p. 164 (1973).

[2] W.M. Garrison and J.L. Wojcieszynski, "A discussion of the spacking of inclusions in the volume and of the spacing of inclusion nucleated voids on the fracture surface of of steels," Mater. Sci. Eng., vol. A505, pp. 52-61, (2009).

[3] J.R. Paules, M.F. Dilmore, and K.J. Handerhan, "Development of Eglin Steel -- A new, Ultrahigh-strength Steel for Armament and Aerospace Applications," in Ferrous Physical Metallurgy of Highly Alloyed Steels, Proceedings of a Symposium sponsored by Materials Science & Technology, Pittsburgh, 2005.

[4] S. Morito, H. Tanaka, R. Konishi, T. Furuhara, and T. Maki, "The morphology and crystallography of lath martensite in Fe-C alloys," Acta Materialia vol. 51 (2003) pp. 1789–1799.

[5] E. Novillo, D. Hernandez, I. Gutierrez, and B. Lopez "Analysis of ferrite grain growth mechanisms during $\gamma-\alpha$ transformation in a niobium alloyed steel using EBSD," Materials Science and Engineering A vol. 385 (2004) pp. 83–90.

[6] M. Niikura, and J.W. Morris, Jr., "Thermal Processing of Ferritic 5Mn Steel for Toughness at Cryogenic Temperatures," Metallurgical Transactions A, vol. 11A, pp. 1531-1540, 1980.

[7] H.J. Schindler, "Estimation of the Dynamic J-R Curve from a Single Impact Bending Test". Mechanisms and Mechanics of Damage and Failure: proceedings of the 11th ECF, (1996).

[8] S. Morito, J. Nishiaka and T. Maki, "Dislocation Density within Lath Martensite in Fe-C and Fe-Ni Alloys," ISIJ International, vol. 43, no. 9, pp. 1475-1477, 2003.

[9] P.R. Rios, S. Fulvio Jr., H.R.Z. Sandim, L. Ronald, and A.F. Padilha, "Nucleation and Growth During Recrystallization," Materials Research, vol. 8, no. 3, pp. 225-238, 2005.

[10] B.M. Leister and J.N. Dupont, "Phase transformation and welding of Eglin Steel" Steel Founders of America Technical and Operating Conference, paper 3.7, Chicago, IL, December 14, 2012.

[11] R.O. Richie ASM conference proceedings, What Does the Charpy Test Really Tell Us? , (1978) pp. 54-73.

[12] L.N. Bartlett, A. Dash, D.C. Van Aken, V.L. Richards, and K.D. Peaslee, Dynamic Fracture Toughness of High Strength Cast Steels," AFS Trans vol.120, (2012) pp. 469-486.

[13] G.E. Hale and J. Nutting, "Overheating of low alloy steels," International Metals Reviews vol. 29 (1984), pp.273-298.

[14] S.P. Lynch, Hydrogen-embrittlement (HE) phenomena and mechanisms, Stress corrosion cracking: theory and practice, Raja VS, Shoji T. (Eds), Cambridge, UK: Woodhead Publishing, pp 90-130, 20114.

[15] S. Morito, J. Nishiaka and T. Maki, "Dislocation Density within Lath Martensite in Fe-C and Fe-Ni Alloys," ISIJ International, vol. 43, no. 9, pp. 1475-1477, 2003.

[16] D. Kolesnikov; A. Belyakov; A. Kipelova; V. Dudko; R. Kaibyshev, and D. Molodov, "Zener pinning pressure in tempered martensite lath structure" Materials Science Forum, vol. 715-716, pp. 745-750, 2012

[17] A.F. Gourgues, H.M. Flower, and T.C. Lindley, "Electron backscattering diffraction study of acicular ferrite, bainite, and martensite steel microstructures" Materials Science and Technology, vol. 16, 2000

# II. GRAIN REFINEMENT STRATEGIES IN HIGH STRENGTH CAST STEEL

## AUTHORS

D.C. Van Aken
T.O. Webb
J.D. Green

Missouri University of Science and Technology
401 W. 16th St.
Rolla, MO
65409

## ABSTRACT

This paper reviews the physical metallurgy of grain refinement produced by standard heat treatment practices. Grain refinement by normalization is shown to be dependent upon the starting microstructure. High alloy steels with as-cast microstructures that are bainitic are shown to be problematic with respect to standard normalization practices. These as-cast bainitic microstructures contain remnant austenite that is stable during heating, which subsequently grows during austenitization and upon grain impingement reproduces the original parent austenite grain. Subcritical annealing at 649°C (1200°F) for high alloy steels such as Eglin steel and potentially 4320 is shown to eliminate the austenite and increase grain multiplication upon heating. Lower alloy steels such as 8620, 8630 and 4140, can also benefit from subcritical annealing although the effects are not as dramatic. The addition of a subcritical anneal for the lower alloy steels may affect grain size uniformity.

# 1. INTRODUCTION

A novel heat treatment for grain refinement of a high strength W-steel casting was presented at the 2014 SFSA T&O conference by Webb and VanAken. [1] Improved tensile ductility as measured by either elongation to failure or reduction in area and higher Charpy V-notch impact energy was obtained by this grain refinement heat treatment. A prior austenite grain size of 56 μm was obtained in the quenched and tempered steel and a comparison of the mechanical properties is shown in Table I. This new heat treatment required quenching the steel from the normalizing temperature in oil and the incorporation of a 649°C (1200°F) subcritical anneal prior to the hardening heat treatment. The resulting quenched and tempered steel exhibited a prior austenite grain diameter of 56 μm and a refined lath martensitic microstructure with increased frequency of martensite lath boundary misorientation angles, which produced improvement in both tensile ductility and Charpy V-notch impact energy. The exact mechanism of grain refinement was not determined, but the authors hypothesized that recrystallization during tempering or grain pinning by alloy carbides upon heating to the hardening temperature may have contributed to producing a smaller prior austenite grain size.

Table I- Mechanical properties for W-steel with respect to grain size.

| Prior austenite grain size | 0.2% offset yield strength MPa (ksi) | Ultimate tensile strength MPa (ksi) | Elongation to fracture | Reduction in area | V-notch Charpy impact at energy (-40°C) | Dynamic fracture toughness $K_{ID}$ |
|---|---|---|---|---|---|---|
| **265±88 μm** | 1207 (175) | 1269 (184) | 2.7% | 6.7% | 48J (36 ft-lb) | 111 MPa√m |
| **56±12 μm** | 1210 (176) | 1586 (230) | 8.3% | 21% | 58J (43 ft-lb) | 110 MPa√m |

To fully understand the evolution of grain structure when steel is heat treated, the investigator must know how the prior microstructure affects grain multiplication during phase transformation, the kinetics of grain growth, and how second phase particles pin the growing austenite grains. In wrought alloys grain refinement can be produced by recrystallization and grain pinning with AlN, NbC, VN, etc. Smaller grain diameters are produced when plastic deformation exceeds 20-30% and grains grow to the pinning diameter. Grain refinement in plain carbon and low alloy steels is obtained exclusively by thermal processing in the foundry industry. Polymorphism in iron is responsible for grain refinement in steels when thermally processed at elevated temperatures. The following paragraphs will review some basic concepts related to grain refinement and build simple models that can be used to estimate grain multiplication factors associated with phase transformation upon heating and cooling.

Grain multiplication during a polymorphic transformation ($\alpha \rightarrow \gamma$) will occur in pure iron as the steel is heated above 912°C (1674°F). Nucleation of new grains ($\gamma$) will typically occur at grain corners and grow until impingement. Grain coarsening will occur after complete transformation and the growth of the average grain diameter ($L_3$) follows parabolic time dependence, i.e. $L_3 \propto \sqrt{t}$. Here we use the measure of $L_3$, as determined by the Heyn intercept method, to describe the grain size, see ASTM E112. [2] A simple model of grain multiplication can be built using a grain structure of space filling Kelvin tetrakaidecohedrons as shown in Figure 1. Each individual tetrakaidecohedron has 14 faces, 36 edges, and 24 corners. The volume (V) of a single tetrakaidecohedron can be calculated [3] based upon $L_3$ as

$$V=1.767(L_3)^3 \qquad (1)$$

Close examination of Figure 1(a) reveals 4 grains share each corner; thus, there are 6 corners for each grain and a grain multiplication factor of 6 may be inferred during polymorphic

phase transformation. It should be noted that grain multiplication should occur upon both heating and cooling. Using this same argument of grain multiplication the heating and cooling cycle will transform a single parent grain into 36 new grains assuming grain coarsening at the elevated temperature is ignored. Figure 1(b) shows the effect of two heating and cooling cycles to produce 1296 new grains from a single parent grain and a final grain diameter ($L_3$) of 9.3μm will result if the starting grain diameter was 100μm.

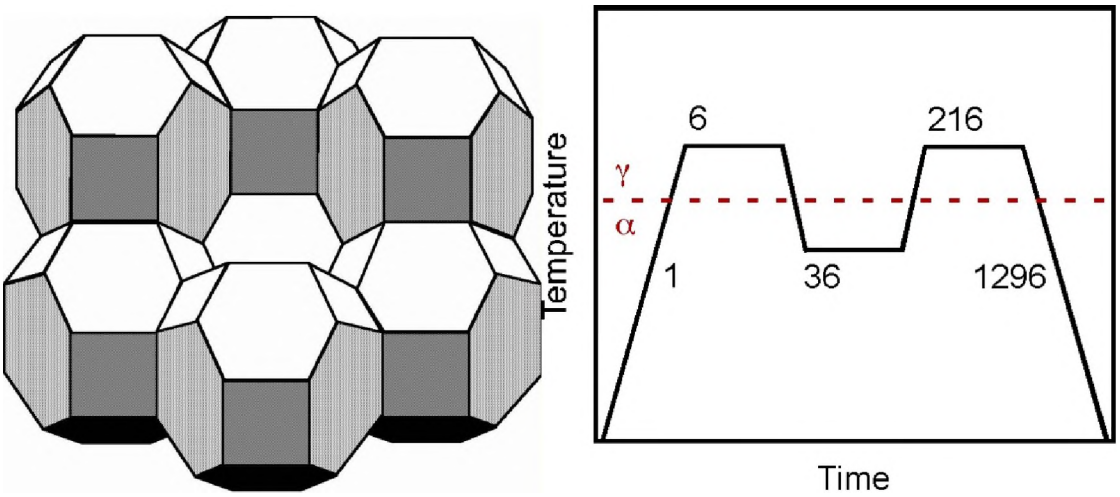


(a) (b)

Figure 1. (a) A cluster of tetrakaidecahedron shaped grains. (b) An illustration of grain multiplication assuming that each polymorphic phase transformation produces a grain multiplication of 6.

Refinement by grain multiplication is more complicated in mixed microstructures of ferrite, carbide, and potentially austenite. A very nice study of austenite formation in Fe-$Fe_3C$ microstructures was reported by Roberts and Mehl [4] and the time-temperature transformation diagram for austenite formation in 1080 steel is shown in Figure 2. It should be noted from this diagram that carbide and carbon chemical inhomogeneities persist for times in excess of an hour above the A1 critical temperature and that austenite nucleation is delayed near the $A_1$ critical temperature.

Grain multiplication during heating of multiphase microstructure will be dependent upon the distribution of ferrite and the carbon source to obtain austenite of the appropriate composition. Work of Vilella as reported by Grossman and Bain [5] shows nucleation of austenite at spheroidal $Fe_3C$ carbides in plain carbon steel. A similar observation is shown in Figure 3 for ductile iron having a "bullseye" microstructure that has been partially austenitized. The austenite formed during heating has transformed to martensite (brownish contrast) upon quenching as is observed around the graphite nodule and in areas that were previously pearlitic.

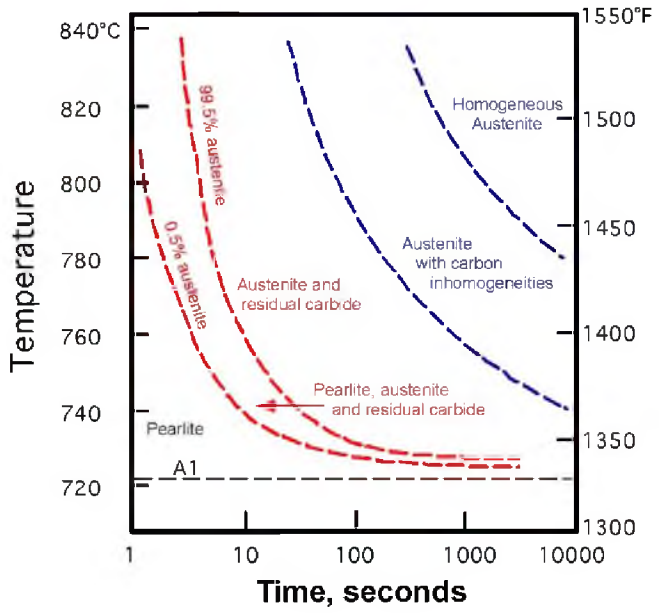


Figure 2. A time-temperature transformation diagram for the formation of austenite in a 1080 steel. The A1 temperature is the eutectoid reaction where α-ferrite and $Fe_3C$ react to form γ-austenite. Figure adapted from reference [4].

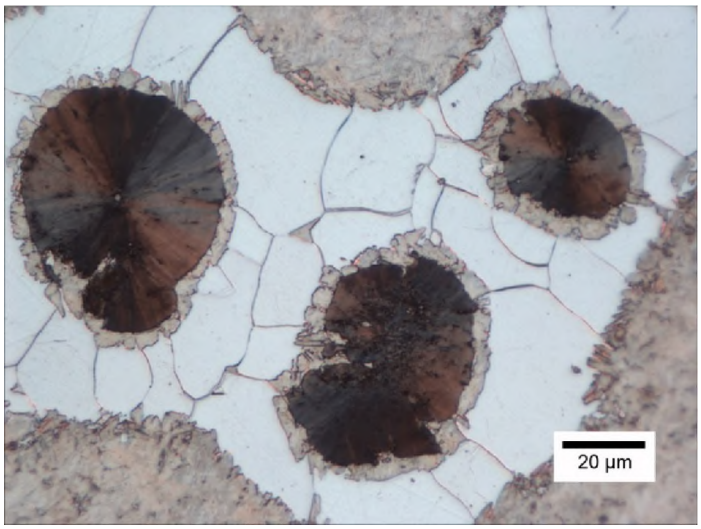


Figure 3. Austenite formation in a ductile iron that was rapidly heated above the A1 critical temperature and quenched. The microstructure before heating consisted of graphite nodules surrounded by free ferrite or "bullseye" microstructure with a pearlitic matrix. Upon heating the pearlite transformed to austenite and was subsequently quenched to martensite. Austenite (now martensite) was also formed adjacent to the graphite nodules, which supplied the necessary carbon to form the austenite.

In plain carbon steels, the austenite forms first in the pearlitic microstructure and these new austenite grains grow into the remaining ferrite. Upon cooling, proeutectoid ferrite might be expected to form at austenite grain corners and grain edges. Thus, multiplication factors greater than 6 might be expected. An example of grain multiplication is shown in Figure 4 for cast 1524 steel. The initial ferrite grain size $L_3$ is approximately 200 μm and upon a single normalization cycle the ferrite grain structure is reduced to approximately 30 μm. The resultant grain multiplication ($n$) for this heating and cooling cycle can be calculated using eq. (1) as

$$1.767(200\,\mu m)^3 = n1.767(30\,\mu m)^3$$

$$n = \frac{(200\,\mu m)^3}{(30\,\mu m)^3} = 296$$

where 296 new grains occupy the volume of the original 200μm diameter grain.

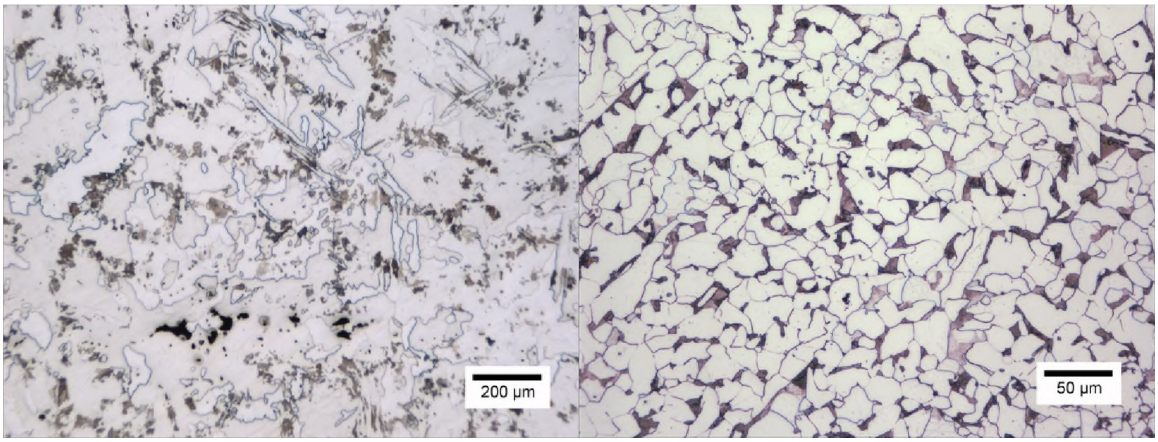


(a) (b)

Figure 4. Microstructures of 1524 (a) as cast and (b) normalized at 925°C (1700°F). Each microstructure consists of ferrite grains and pearlite. Etched with 2% nital.

Grain multiplication can be reduced by crystallographic factors during the polymorphic phase transformation and by grain growth during the elevated temperature hold. Quite often the new grain nucleated will have a specific orientation relationship to one of the adjacent parent grains. A random boundary is established with the other parent grains. The Kurjumov-Sachs orientation relationship describes the most commonly observed relationship between ferrite and austenite in steel where close packed planes and close packed directions are parallel. The Kurjumov-Sachs orientation relationship is written as follows using the standard Miller index notation:

$$\langle 1\bar{1}0\rangle_\gamma // \langle 1\bar{1}1\rangle_\alpha \; and \; \{111\}_\gamma // \{110\}_\alpha \qquad (2)$$

If two adjacent corners to the same parent grain nucleate with the same orientation relationship to the parent grain then the two new grains will coalesce upon impingement to a single grain and the multiplication factor will be reduced. As a result it is often easier to determine the grain multiplication factors by experiment as shown above for the normalization of the 1524 steel.

Grain growth at elevated temperature will also reduce the extent of grain refinement by increasing the volume of the average grain and thus reducing the number of grain corners per unit volume upon cooling. Figure 5 shows a schematic double normalization process where grain growth is incorporated and the multiplication factors for heating are

$$n_1 = \left(\frac{L_3(t_0)}{L_3(t_1)}\right)^3 \text{ and } n_2 = \left(\frac{L_3(t_2)}{L_3(t_3)}\right)^3 \qquad (3)$$

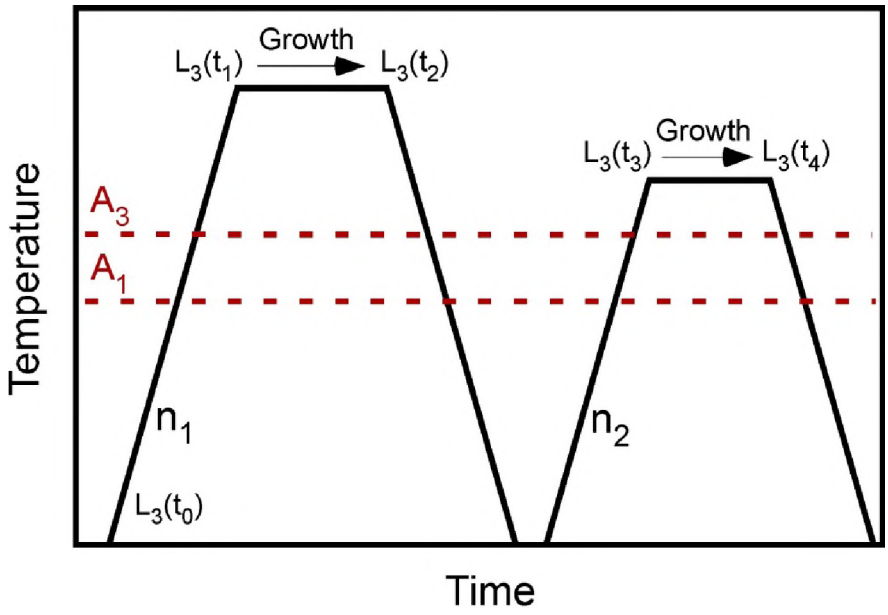


Figure 5. Schematic showing a double normalization heat treatment. The prior austenite grain size of the casting is $L_3(t_0)$. At the end of the first and second normalization cycles the prior austenite grain diameters would be measured as $L_3(t_2)$ and $L_3(t_4)$. Calculation of the grain multiplying factors, $n_1$ and $n_2$, requires that the austenite grain diameter at the beginning of the austenitization cycle be determined by estimating the grain growth at temperature.

The prior austenite grain diameters $L_3(t_2)$ and $L_3(t_4)$ can be measured after each heating and cooling cycle. However, to determine $L_3(t_1)$, $L_3(t_3)$ and the grain multiplication factors $n_1$ and $n_2$ requires knowledge about the grain growth kinetics of austenite. A comparison of the prior austenite grain diameters, $L_3(t_4)$ shown in Table I might be explained by either a difference in grain growth or the increase in the grain multiplication factor. The 285 μm prior austenite grain diameter was produced by normalizing for 8 hours at 1163°C (2125°F) and quench hardened after 4 hours at 1066°C (1950°F) whereas the 56 μm prior austenite grain diameter was produced by normalizing for 2 hours at 1149°C (2100°F) and quench hardened after 1 hour at 1038°C (1900°F). Likewise, addition of the quench from the normalization temperature or the

introduction of the 649°C (1200°F) subcritical anneal may have increased the grain multiplication factor. Thus, the purpose of the study presented here is to clarify the role of grain growth, determine if the introduction of quenching from the normalization temperature or adding a subcritical anneal produces a change in grain multiplication factor, and if so determine the mechanism responsible for that change.

## 2. EXPERIMENTAL PROCEDURE

Several steels have been examined in the course of this investigation and the steel chemistries are listed in Table II. The W-steel from Foundry 3 is the same steel previously studied in the paper by Webb and Van Aken [1] in developing the grain refinement heat treatment. This same steel was used here to study grain growth and grain multiplication. Low alloy steel chemistries were determined by optical emission spectrometry by the providing foundry. American Cast Iron Pipe Co. (ACIPCo) provided optical emission spectrometry results for W-steels. Carbon and sulfur were measured using a LECO CS6000; oxygen and nitrogen were measured using a LECO TC 500 by Missouri University of Science & Technology. The low alloy steels were provided as legs from keel blocks and the W-steel supplied as 2 inch thick weld plates.

Table II- Steel chemistry and foundry designation.

| Alloy | C | Mn | Si | Cr | Ni | Mo | W | V | Cu | P | S | Ca | N | Al | O | Fe |
|---|---|---|---|---|---|---|---|---|---|---|---|---|---|---|---|---|
| **8620 Foundry 1** | 0.19 | 0.71 | 0.44 | 0.50 | 0.50 | 0.22 | | 0.005 | 0.14 | 0.007 | 0.001 | | | 0.013 | | Bal. |
| **8620 Foundry 2** | 0.20 | 0.74 | 0.51 | 0.57 | 0.53 | 0.19 | 0.01 | 0.009 | 0.22 | 0.014 | 0.025 | | 0.02 | 0.032 | | Bal. |
| **8630 Foundry 2** | 0.29 | 0.75 | 0.55 | 0.66 | 0.57 | 0.21 | 0.01 | 0.017 | 0.18 | 0.013 | 0.019 | | 0.02 | 0.036 | | Bal. |
| **4140 Foundry 2** | 0.51 | 0.88 | 0.57 | 1.04 | 0.13 | 0.21 | 0.01 | 0.001 | 0.34 | 0.001 | 0.011 | | | 0.08 | | Bal. |
| **4320 (AOD) Foundry 1** | 0.20 | 0.83 | 0.44 | 0.86 | 2.18 | 0.30 | | 0.006 | 0.11 | 0.019 | 0.006 | | | 0.004 | | Bal. |
| **W-Steel (AOD) Foundry 3** | 0.25 | 0.77 | 0.88 | 2.64 | 1.03 | 0.425 | 0.92 | 0.097 | 0.12 | 0.006 | 0.004 | - | 0.009 | 0.008 | 0.022 | Bal. |
| **W-Steel (AOD) Foundry 1** | 0.26 | 0.63 | 1.02 | 2.72 | 1.03 | 0.45 | 0.75 | 0.092 | 0.07 | 0.009 | 0.004 | | 0.013 | 0.022 | 0.015 | Bal. |

Grain growth kinetics were studied using the W-steel from Foundry 3. The steel was first grain refined by heating to 1049°C (2100°F), holding for 4 hours to dissolve alloy carbides, and water quenching. A second austenitization was conducted at 1038°C (1900°F), held for one hour and water quenched. A prior austenite grain diameter of 100 μm was measured after heat treatment and this heat treatment appears later in the paper as QQ in Table III. These steel coupons were then heated to 1093°C (2000°F), 1121°C (2050°F), 1149°C (2100°F), and 1177°C (2150°F) for varying lengths of time and then subsequently water quenched to produce martensite. Grain growth specimens were double bagged in treated stainless steel for each heat treatment to inhibit decarburization. Each specimen was etched with a Marbles reagent that was modified by adding an equal volume of glycerin. The modified Marbles reagent sufficiently highlighted the prior austenite grain boundaries to permit grain size measurement. Grain diameters were measured in accordance with ASTM E112 [2] using the Heyn intercept method and diameters are reported as the mean linear distance, $L_3$, and reported with a 95% confidence level for the measurement.

Studies involving the formation of austenite were conducted by heating the steel into the intercritical temperature range at either 760°C (1400°F) or 800°C (1472°F) and holding for varying times to determine the rate of austenite formation. Each experiment was conducted using 6 specimens cut to a thickness of approximately 10 mm (3/8 inch) and welding a thermocouple to one of the coupons. Time at temperature was recorded after the temperature was within 2°C of the test temperature. Specimens were stood-up in the furnace to allow free convection between each specimen. Specimens were removed at 5 minute intervals starting as soon as the test temperature was within 2°C of the test temperature, i.e. 0, 5, 10, 20, 30, 40 minutes etc, and then quenched in water. Rockwell C-scale hardness measurements were taken on each coupon after surface grinding to remove potential decarburization and to make the surfaces flat and parallel. A

total of ten measurements were taken on each specimen and the reported uncertainty represents the 95% confidence level of the mean value.

Standard metallographic techniques were used to prepare specimens for optical microscopy. Specimens used for orientation image mapping using electron backscatter diffraction (OIM-EBSD) were vibratory polished using 0.02 μm colloidal silica. OIM-EBSD was performed on a FEI Quanta 200F Scanning Electron Microscope and images were subject to a cleanup procedure, setting the minimal confidence index to 0.1 and matching orientation of data points that are within 5 degrees of 4 of its closest neighboring data points. The electron beam was operated at an accelerating voltage of 20.0 kV and an emission current of 11 nA with a 0.025 μm step size during mapping. Quantification of retained austenite was performed using X-ray diffraction and calculated utilizing the Rietveld refinement described by Martin et al. [6]

# 3. RESULTS

Optical images of the as-cast steels are shown in Figure 6. The as-cast prior austenite grain size was typically on the order of millimeters. The 8620 (Foundry 1) and 8630 (Foundry 2) had a microstructure of acicular ferrite and pearlite, the 8620 (Foundry 2) was allotriomorphic (blocky) ferrite and pearlite, the 4140 was nearly all pearlite, and both the 4320 and W-steel were 100% bainitic.

Austenite grain growth was studied using the W-steel supplied by Foundry 3. Grain growth data was assumed to follow a parabolic time dependence (normal grain growth) and described by the following kinetic equations:

$$\left[L_3(t)\right]^2 - \left[L_3(0)\right]^2 = kt \tag{4}$$

$$k = k_0 \exp\left(\frac{-Q}{RT}\right) \tag{5}$$

where $L_3(t)$ is the grain diameter measured after time t, $L_3(0)$ is the initial grain diameter, k is the rate constant determined from eq. 5 at absolute temperature T, R is the universal gas constant, $k_0$ and Q are kinetic constants for the steel. A plot of the square of the measured grain diameters versus time is shown in Figure 7. Continuous grain growth was observed at 1149°C (2100°F) and 1177°C (2150°F) and the data could be fit to a linear trendline indicating normal grain growth as shown in Figure 7(a). At temperatures below 1149°C (2100°F) the linear portion of the grain coarsening was restricted to short times. After 2 hours at 1121°C (2050°F) the grain diameter remained constant at approximately 230 μm. After 6 hours at 1093°C (2000°F) the grain diameter reached 230 μm and no further grain growth was observed. The 230μm grain diameter is consistent with the secondary dendrite arm spacing of the W-steel casting and the presence of persistent carbides could explain grain pinning. An initial austenite grain size of 100 μm upon heating the W-steel to the coarsening temperature was assumed when determining the rate

constants. Rate constants, k in $mm^2/hr$, were determined from the slopes of the linear trend lines. An Arrhenius plot of the rate constants is shown in Figure 7 (b). An activation energy (Q) of 537 kJ/mole and $k_0$ equal to $2.96x\ 10^{18}\ mm^2/hr$ was determined from the Arrhenius plot. Grain coarsening behavior can now be calculated using the kinetic data and is presented in tabular form in Appendix A for the W-steel. The grain growth data shown in Table III will likely under predict grain coarsening for plain carbon steels and over predict grain size when grain pinning occurs during coarsening such as might be observed in Al-killed steel.

Grain multiplication factors ($n_1$ and $n_2$) as shown in Figure 5 can now be calculated for various heat treatments (see Table IV) conducted on the W-steel. An OIM-EBSD study of the previous heat treatment (labeled QTQ in Table IV) reported by Webb and Van Aken is shown in Figure 8. The measured grain diameters of the as-cast (1800 μm) and that resulting from the first austenitization cycle (1454 μm) indicate little to no grain refinement. Austenite grain growth may now be calculated to determine the size of the austenite after the initial heating using the kinetic results above. The measured prior austenite diameter of 1454 μm would have grown from an initial austenite grain diameter of 1414 μm and the grain multiplication factor of 2.1 for $n_1$ is calculated from $(1800/1414)^3$. Grain growth and multiplication factors are summarized in Table V for the heat treatments listed in Table IV. It should be noted that the uncertainty in the measured grain size is quite large for grain diameters greater than 200 μm; however, order of magnitude changes in the multiplication factor may indicate substantial changes in the mechanism of austenite formation.

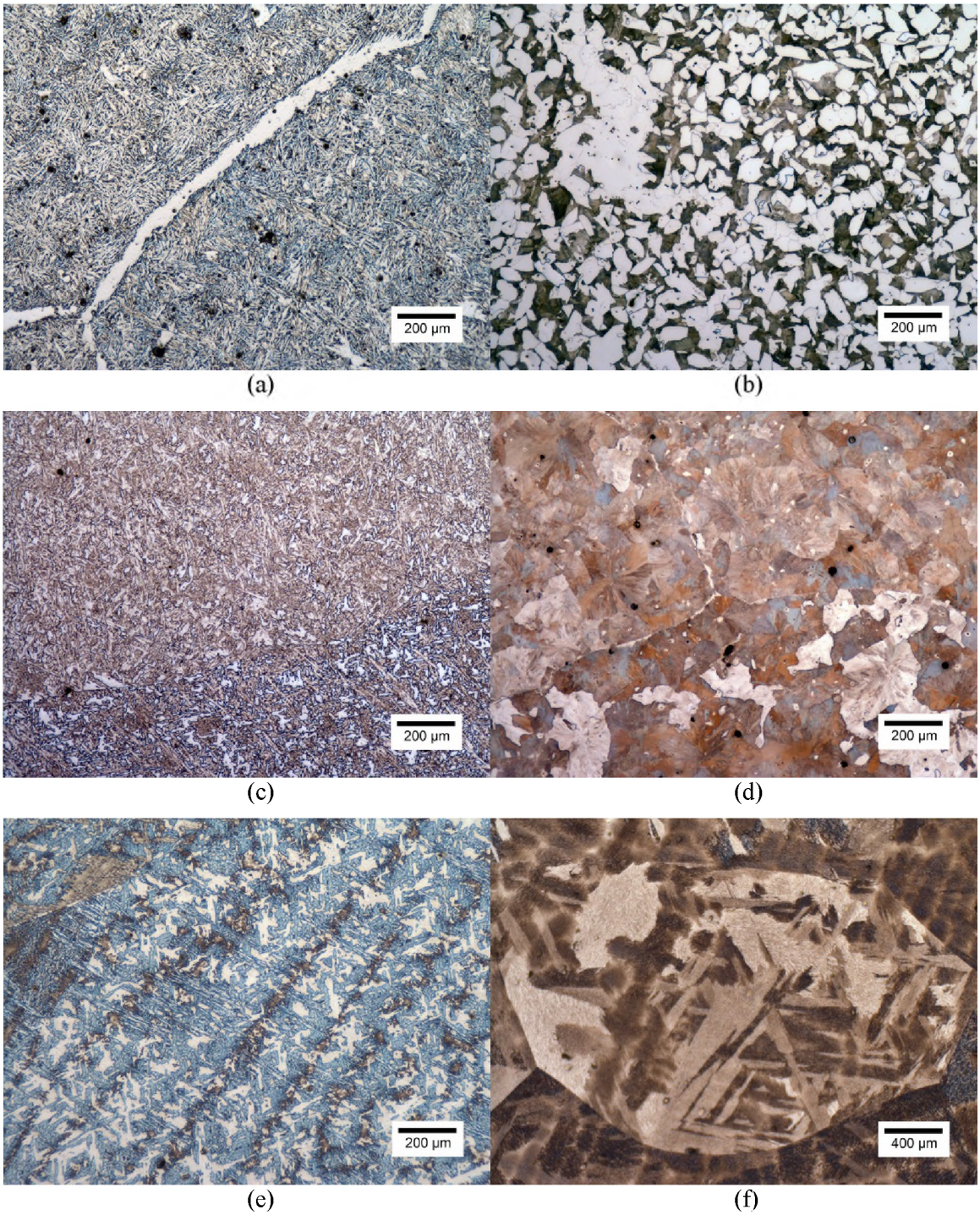


Figure 6. As cast microstructures of (a) 8620-Foundry 1, (b) 8620-Foundry 2, (c) 8630 (d) 4140 (e) 4320, and (f) W-steel. Figures (a) through (e) were etched with 2% nital and (f) was etched with modified Marbles reagent.

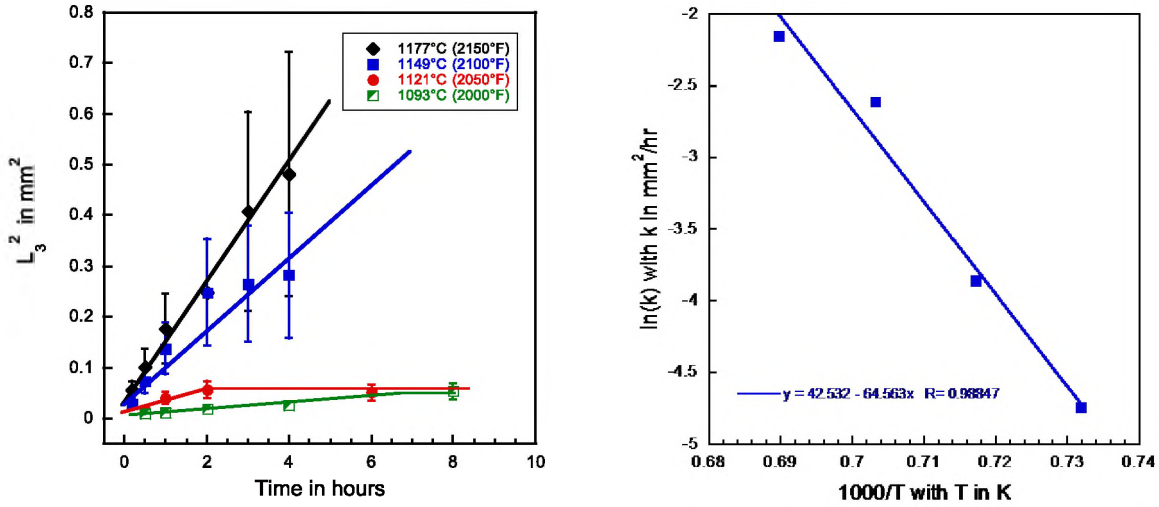


(a) (b)

Figure 7. (a) Normal grain growth is observed for the W-steel in 3 of the 4 (b) Arrhenius plot of rate constants determined from the slope of the lines shown in (a). The slope of the Arrhenius plot is equal to -Q/R and the y-intercept is ln($k_0$).

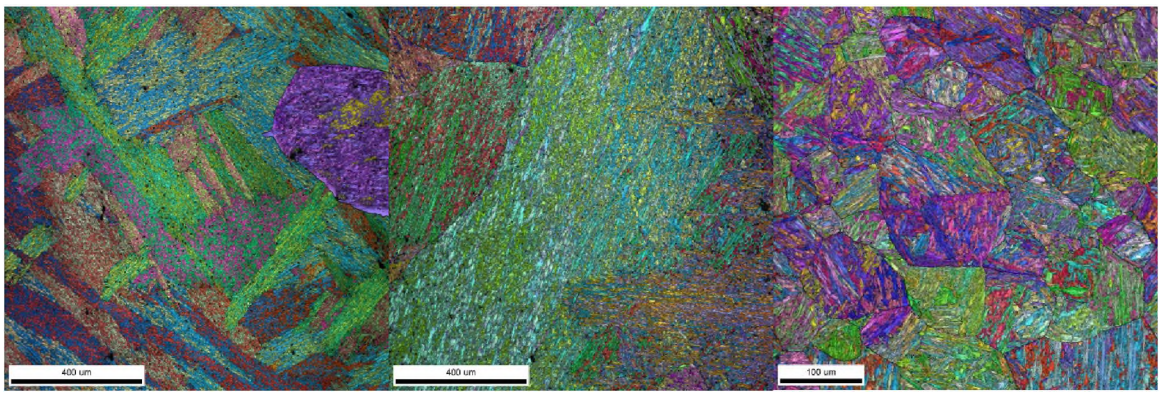


(a) (b) (c)

Figure 8. OIM-EBSD images from various stages of heat treatment from the same W-steel specimens as reported by Webb and Van Aken. [1] (a) As-cast microstructure with starting grain diameter of 1800µm. (b) Oil quenched microstructure of the steel austenitized for 2 four hours at 1149°C (2100°F) with measured grain diameter of 1454µm. (c) Water quenched microstructure of the W-steel after hardening from 1038°C (1900°F) and holding one hour producing a prior austenite grain diameter of 50µm.

Table III - Grain growth data derived for the W-steel

| Temperature (°F) | Temperature (°C) | k in $\mu m^2/hr$ | $L_3(t_0)$ in µm | 1 hr | 2 hr | 4 hr | 8 hr |
|---|---|---|---|---|---|---|---|
| **1750** | **954** | 42.71 | 10 | 11.9 | 13.6 | 16.5 | 21.0 |
| | | | 25 | 25.8 | 26.7 | 28.2 | 31.1 |
| | | | 50 | 50.4 | 50.8 | 51.7 | 53.3 |
| | | | 100 | 100.2 | 100.4 | 100.9 | 101.7 |
| | | | 200 | 200.1 | 200.2 | 200.4 | 200.9 |
| **1800** | **982** | 136.7 | 10 | 15.4 | 19.3 | 25.4 | 34.6 |
| | | | 25 | 27.6 | 30.0 | 34.2 | 41.5 |
| | | | 50 | 51.3 | 52.7 | 55.2 | 59.9 |
| | | | 100 | 100.7 | 101.4 | 102.7 | 105.3 |
| | | | 200 | 200.3 | 200.7 | 201.4 | 202.7 |
| **1850** | **1010** | 416.3 | 10 | 22.7 | 30.5 | 42.0 | 58.6 |
| | | | 25 | 32.3 | 38.2 | 47.9 | 62.9 |
| | | | 50 | 54.0 | 57.7 | 64.5 | 76.4 |
| | | | 100 | 102.1 | 104.1 | 108.0 | 115.5 |
| | | | 200 | 201.0 | 202.1 | 204.1 | 208.2 |
| **1900** | **1038** | 1209 | 10 | 36.2 | 50.2 | 70.3 | 98.9 |
| | | | 25 | 42.8 | 55.2 | 73.9 | 101.5 |
| | | | 50 | 60.9 | 70.1 | 85.7 | 110.3 |
| | | | 100 | 105.9 | 111.4 | 121.8 | 140.3 |
| | | | 200 | 203.0 | 206.0 | 211.7 | 222.9 |
| **1950** | **1066** | 3360 | 10 | 58.8 | 82.6 | 116.4 | 164.2 |
| | | | 25 | 63.1 | 85.7 | 118.6 | 165.8 |
| | | | 50 | 76.5 | 96.0 | 126.2 | 171.4 |
| | | | 100 | 115.6 | 129.3 | 153.1 | 192.0 |
| | | | 200 | 208.2 | 216.1 | 231.2 | 258.6 |
| **2000** | **1093** | 8955 | 10 | 95.2 | 134.2 | 189.5 | 267.8 |
| | | | 25 | 97.9 | 136.1 | 190.9 | 268.8 |
| | | | 50 | 107.0 | 142.9 | 195.8 | 272.3 |
| | | | 100 | 137.7 | 167.1 | 214.1 | 285.7 |
| | | | 200 | 221.3 | 240.6 | 275.4 | 334.1 |
| **2050** | **1121** | 22950 | 10 | 151.8 | 214.5 | 303.2 | 428.6 |
| | | | 25 | 153.6 | 215.7 | 304.0 | 429.3 |
| | | | 50 | 159.5 | 220.0 | 307.1 | 431.4 |
| | | | 100 | 181.5 | 236.5 | 319.1 | 440.0 |
| | | | 200 | 250.9 | 293.1 | 363.1 | 472.9 |
| **2100** | **1149** | 56720 | 10 | 238.4 | 336.9 | 476.4 | 673.7 |
| | | | 25 | 239.5 | 337.7 | 477.0 | 674.1 |
| | | | 50 | 243.3 | 340.5 | 478.9 | 675.4 |
| | | | 100 | 258.3 | 351.3 | 486.7 | 681.0 |
| | | | 200 | 311.0 | 391.7 | 516.6 | 702.7 |

Table IV- Heat treat schedules for determining grain multiplication factors.

| | Standard Practice NQ (T&O) | S&T QTQ (T&O) | QQ | TNTQ |
|---|---|---|---|---|
| **Subcritical anneal (T)** | None | None | None | 8 hrs at 1200°F |
| **1st austenitization** | 8 hrs at 2125°F | 2 hours at 2100°F | 4 hrs at 2100°F | 4 hrs at 2100°F |
| **Cooling** | Air (N) | Oil quench (Q) | Water Quench (Q) | Air (N) |
| **Subcritical anneal (T)** | None | 4 hrs. at 1200°F | None | 4 hrs at 1200°F |
| **2nd austenititization** | 4 hrs. at 1950°F | 1 hr at 1900°F | 1 hr at 1900°F | 1 hr at 1900°F |
| **Cooling** | Water quench (Q) | Water quench (Q) | Water quench (Q) | Water quench (Q) |

Table V- Prior austenite grain diameters and calculated multiplication factors.

| Heat Treatment | Measured $L_3(t_0)$ in µm | Calculated $L_3(t_1)$ in µm | Grain multiplier $n_1$ | Measured $L_3(t_2)$ in µm | Calculated $L_3(t_3)$ in µm | Grain multiplier $n_2$ | Measured $L_3(t_4)$ in µm |
|---|---|---|---|---|---|---|---|
| **NQ** | 1,800* | 1,414* | 2.1 | 1,756* | 259 | 311 | 283 |
| **QTQ** | 1,800 | 1,414 | 2.1 | 1,454 | 36 | 65,900 | 50 |
| **QQ** | 1,800* | 1,414* | 2.1 | 1,492* | 94 | 4000 | 100 |
| **TNTQ** | 1,979 | 226 | 671 | 226 | 87 | 17.5 | 94 |

Differences in multiplication factors appear to be influenced by the subcritical annealing for both the as-cast and steels quenched directly after the first heating cycle. Initial heating of the as-cast W-steel has a much smaller grain multiplication factor ($n_1$=2.1) upon heating than the same steel that has been subjected to an 8-hour subcritical anneal at 649°C (1200°F) as for the TNTQ process where $n_1$ is 670. A comparison of the QQ and QTQ processes also indicate that

the multiplication factor, $n_2$, increases from 4000 to 66,000 when a subcritical anneal of 4 hours at 1200°C is added prior to austenitization to harden the steels. It should also be noted that the prior austenite grain size after normalization in the TNTQ process is the pinned diameter as reported in the grain growth study. Also apparent is that the multiplying factors are quite different between the air-cooled (N) bainitic and quenched (Q) martensitic microstructures.

An OIM-EBSD examination of a normalized W-steel is shown in Figure 9 and reveals that the steel transforms to bainitic ferrite laths when air-cooled, see Figure 9 (a) and (b), with remnant austenite between the ferrite laths as shown in Figure 9(c). The crystallography of the remnant austenite indicates a single parent austenite grain as shown by the FCC crystal orientation distribution shown in Figure 9(e).

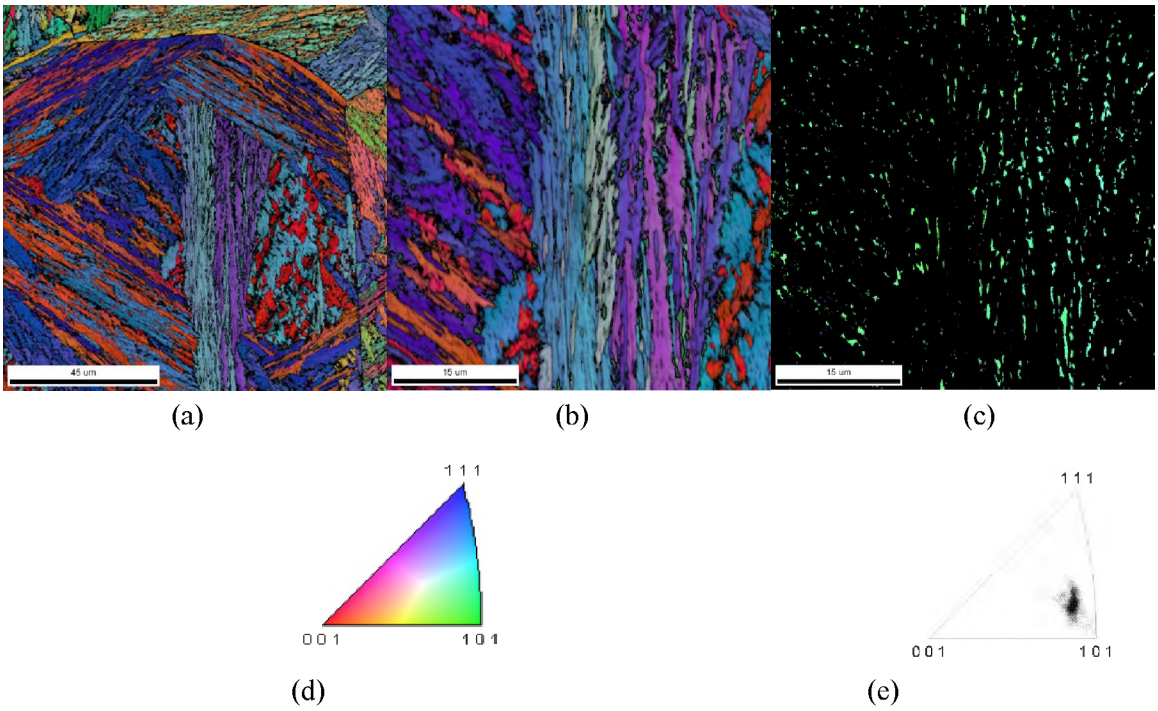


Figure 9. EBSD-OIM of normalized W-steel showing a bainitic microstructure of ferrite in (a) and (b) with remnant austenite in (c), and a colored inverse pole figure (d) highlighting the crystallographic orientation by color. It should be noted that each highlighted austenite portion shown has the exact same crystallographic orientation, as shown by the same distribution (e), and reflects the crystal orientation of the parent austenite grain from which the laths of ferrite formed.

X-ray diffraction patterns for the bainitic microstructure produced by a first stage normalization and then after a subcritical anneal are shown in Figure 10. Quantification of the austenite in the normalized steel was performed utilizing the Rietveld refinement described by Martin et al.[6] The normalized steel contains 13.2% austenite by volume, and 0.6% austenite was detectable after subcritical annealing. Some carbide is apparent in both conditions but cannot be identified from the single diffraction peak at approximately 2θ equal to 42.2°.

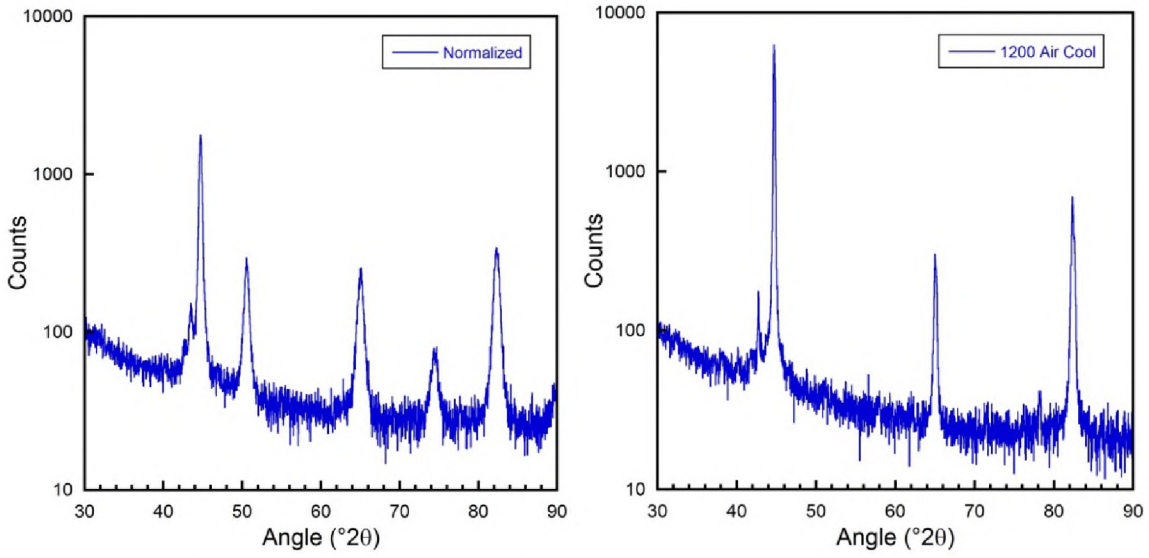


(a) (b)

Figure 10. Diffraction patterns for normalized W-steel. (a) Air cooled from 2100°F with microstructure as shown in Figure 9. (b) Same steel as in (a) but after a 4 hour, 649°C (1200°F) subcritical anneal. Diffraction peaks for austenite are found in (a) at 43° for {111}, 50.8° for {200} and 74.3° for {220}. Variation in the background counts produced a value of 0.6% austenite after the 4 hour subcritical anneal.

A series of intercritical annealing experiments were conducted at 800°C in an effort to understand the role of starting microstructure (bainite versus martensite) and the role of the subcritical anneal prior to heating in the formation of austenite. The martensitic microstructures were produced by first heating to 2100°F, holding 4 hours, and quenching in water. Each of the six specimens were heated to 800°C using a thermocouple attached to one of the specimens. Upon reaching 798°C the first specimen was removed and quenched in water, i.e. time zero. Additional specimens were removed and quenched in water after an additional 5, 10, 20, 30, and 40 minutes. The thermocoupled specimen was quenched last. Quenched hardness using a C-scale Rockwell test as a function of time is shown in Figure 11. In general, the hardness increased with time at temperature indicating that the volume of austenite was increasing with time. Upon quenching the austenite transforms to martensite and the measured hardness is proportional to the volume fraction of martensite. It should be noted that the as-cast bainitic microstructure appears to reach the maximum hardness in the time zero specimen whereas the other three conditions show that the hardness increases with time indicating a slower rate of austenite formation.

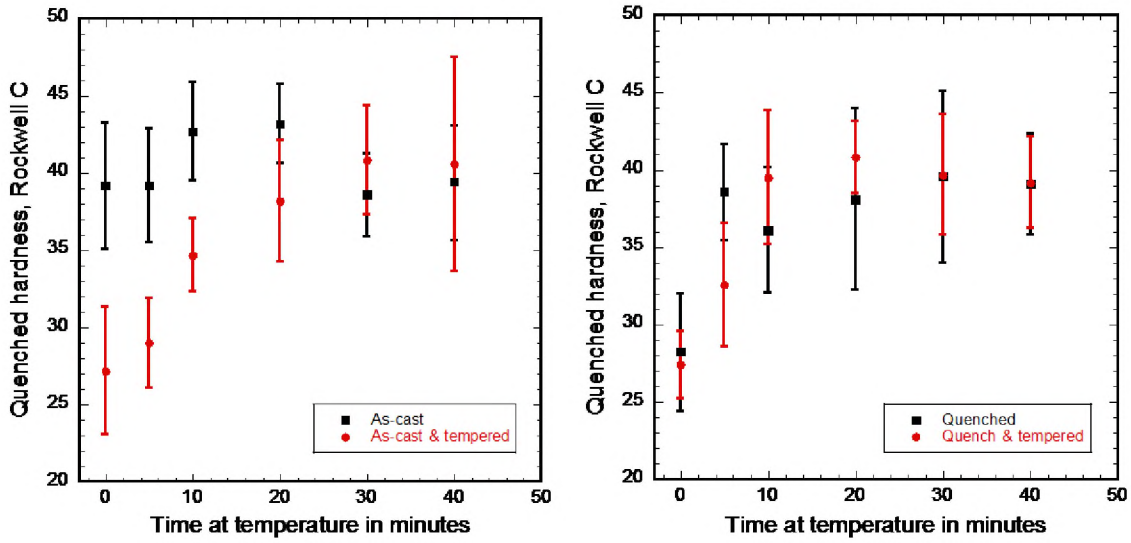


Figure 11. As-quenched hardness for steel heated to and held at 800°C for varying lengths of time. (a) A comparison of an as-cast microstructure of bainite versus bainite tempered at 650 °C. (b) A comparison of quenched martensite versus martensite tempered at 6549°C (1200°F) for 4 hours.

A microstructural study was conducted on select specimens from the intercritical heating study. Figure 12 shows a comparison of the as-cast bainitic microstructures with and without the prior subcritical anneal. A nearly fully martensitic microstructure is observed after 10 minutes at 800°C when heating the as-cast bainitic microstructure as shown in Figure 12 (a). The dark etching features shown in Figure 12(a) are more easily discerned in Figure 12(b), which shows a martensite, carbide, and ferrite microstructure. The ferrite appears as thin remnant laths (white contrast) between the regions of martensite (brown contrast). The convex nature of the martensite interface indicates a diffusional growth of austenite into the ferrite. Some carbide precipitation is evident at these boundaries and within the ferrite as might be expected for a 3-phase intercritical region for the W-steel. The subcritical annealed bainitic structure is shown in Figure 12(c) and 12(d). Carbide precipitation is evident throughout the microstructure and the martensite appears

as small islands. Growth of the austenite is crenulated as the austenite grows through the carbides rather than being lenticular and parallel to the previous ferrite laths.

Austenite formation in the martensitic microstructures, with and without subcritical annealing, is shown in Figure 13. Surprisingly, the resulting microstructures are very similar to each other and to the as-cast, W-steel without subcritical annealing as shown in Figure 12(b). Regions of the subcritically annealed martensitic structure as shown in Figure 13(d) show a more equiax growth of the newly formed austenite which is similar to the subcritically annealed bainitic microstructure shown in Figure 12(d).

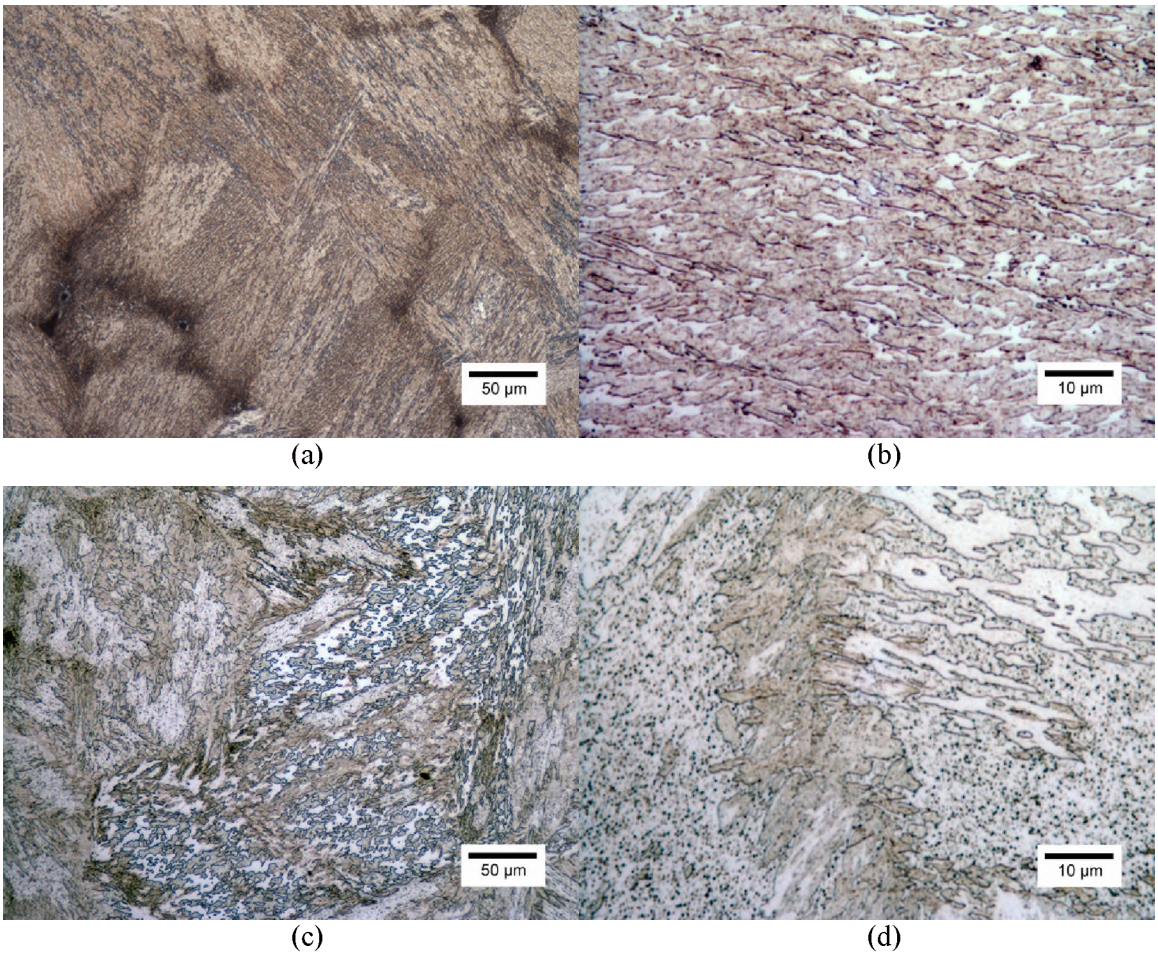


Figure 12. Austenite formation at 800°C ( 1472°F) in the as-cast microstructure of bainite is shown in (a) and (b) and for the subcritically annealed cast material in (c) and (d). Each was held for 10 minutes at 800°C and quenched into water. Nearly complete transformation to austenite was observed in the as-cast bainitic microstructure. Figure (b) shows the austenite formed in long laths with remnant ferrite inbetween these laths. Persistent carbides are discernible in the ferrite. The ferrite appears as dark etching features in (a). In contrast, substantial carbide precipitation has occurred in the subcritical annealed specimen and the regions of transformed austenite appear more irregular as shown in (d).

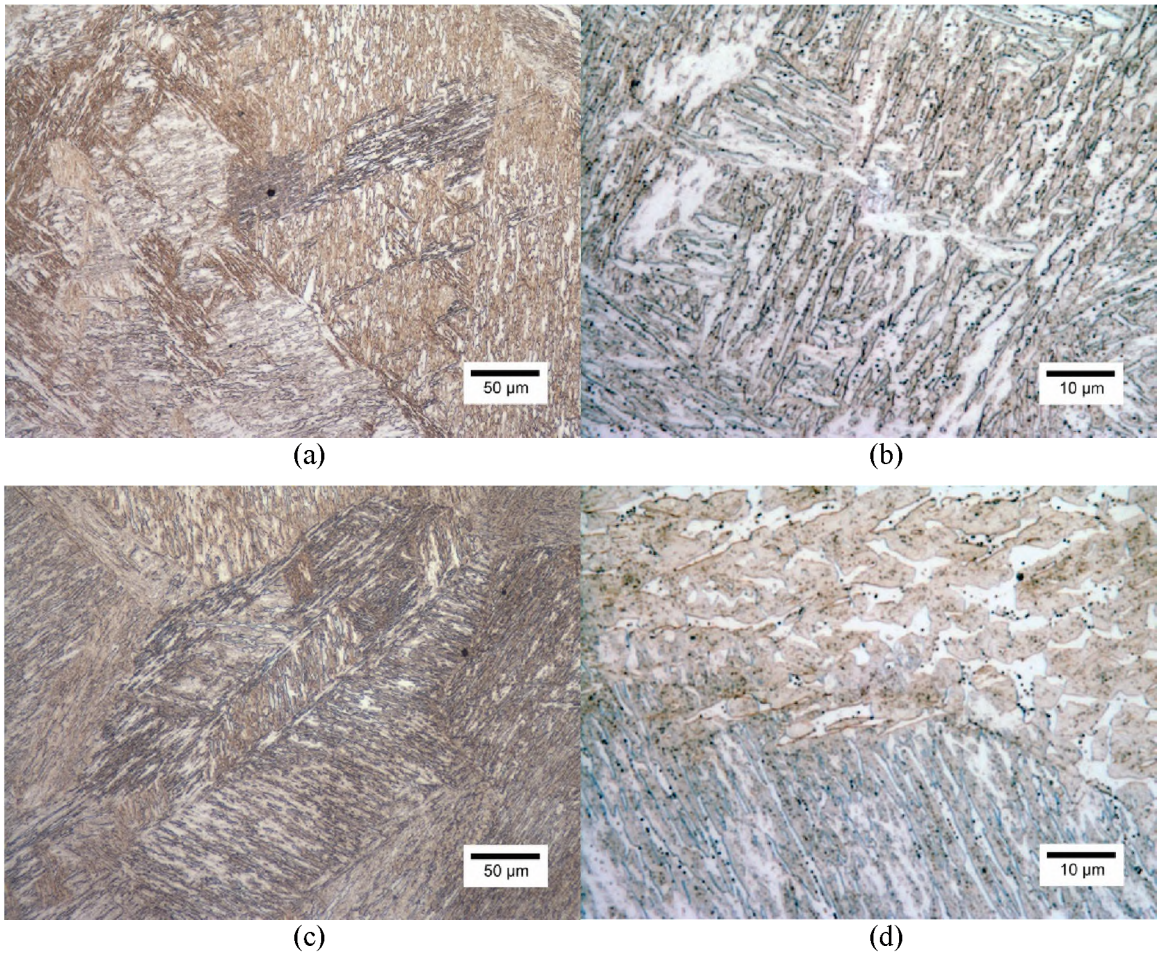


Figure 13. Austenite formation after 10 minutes at 800°C ( 1472°F) is shown in (a) and (b) for an initial microstructure of quenched martensite and for the subcritically annealed martensite after 20 minutes in (c) and (d). Both the quenched martensite and the subcritically annealed martensite have similar microstructures after the intercritical hold at 800°C.

# 4. DISCUSSION

Any discussion of phase transformation in steel must sta

rt with an understanding of the Kurdjumov-Sachs orientation relationship, see eq. (2). Manifestation of this crystallographic relationship are often displayed in both bainitic and martensitic microstructures. This relationship will produce distinct spatial relationships between lath packet variants. For example, the image of the as-cast W-steel shown in Figure 6(f) shows three ferrite lath packets forming equilateral triangles within a single prior austenite grain. These shapes result from the basic crystallography of a cubic parent phase where there are 4 independent {111} planes. Thus, a maximum of 4 lath packets will be observed in any single prior austenite grain for either bainite or lath martensite. Additional examples of this crystallographic relationship is shown in Figure 14 for both a bainitic microstructure in 4320 and a martensitic microstructure observed in the W-steel. Each lath packet (bainite or martensite) has a common {111}, but there can be up to three different variants with crystallographic directions of the ferrite lath aligned with different austenite directions. This difference is best demonstrated using the OIM-EBSD shown for bainite in Figure 9(a). Parallel ferrite laths with two different colors within a packet represent two different variants of the Kurdjumov-Sachs orientation relationship. Upon transformation back to austenite these different variants are capable of transforming to different austenite grains producing grain multiplication or to the same austenite grain with no refinement in the grain structure.

Large volumes of remnant austenite in the bainitic structures, as shown in Figure 9(c), suggest another explanation for low grain multiplication factors when these microstructures are heated. Upon heating there will be no incubation time to nucleate austenite and this may explain the rapid hardening shown in Figure 11(a) for the as-cast microstructure of the W-steel. Growth of this prior austenite upon heating may simply grow to consume the ferrite laths and reform the original parent austenite grain. A mechanism of preexisting austenite growth explains the low

grain multipliers of 2.1 calculated for the QTQ heat treatment shown in Table V. It needs to be emphasized that the remnant austenite within these bainitic microstructures is exactly the same in each of the different lath packets as shown in Figure 9(c) and 9(e).

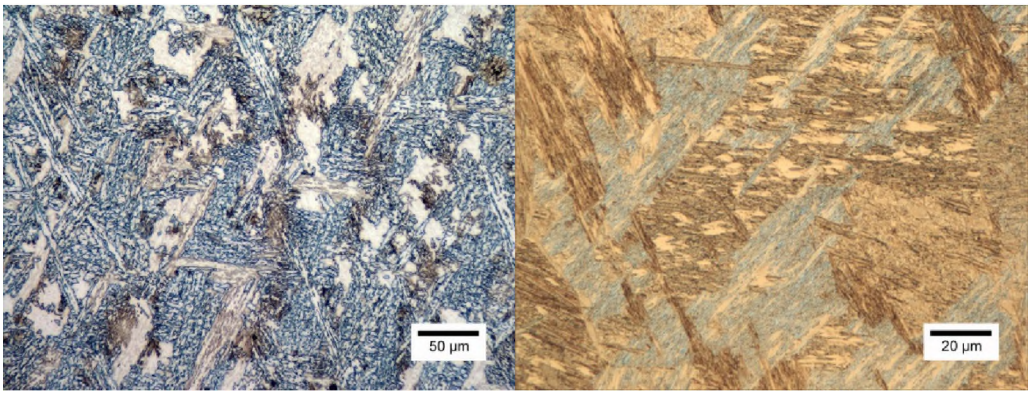


(a) (b)

Figure 14. Optical images of (a) cast 4320 with a bainitic microstructure and (b) a quenched and tempered W-steel showing a martensitic microstructure. Each photograph shows the microstructure within a single prior austenite grain, which is oriented to show three possible austenite {111} intersecting the metallographic plane of polish. The three packet variants combine to produce equilateral triangles.

Time dependent nucleation and growth of austenite is observed when the starting microstructure is martensitic or a subcritical anneal is performed prior to heating to austenitize the steel as shown in Figure 11. For the subcritical annealed bainite, the grain multiplier, $n_1$, increased to 671 for the first austenitization cycle of the TNTQ heat treatment. The second heating cycle of the TNTQ heat treatment appears to be much less effective ($n_2$= 17.5) and to

explain these differences we must consider how these bainitic microstructures develop during cooling.

In Cr-Mo steels there is a phenomenon of incomplete transformation [7], which is responsible for the development of an austenite bay in the time-temperature transformation diagrams of these steels. Metallurgists erroneously divide the transformation of the steel into a pearlitic transformation above the bay and a bainitic transformation below the bay. In fact, the development of the austenite bay results from a phenomenon of solute drag at the ferrite and austenite interface.[7] Carbon is partitioned to the austenite during the transformation to ferrite and growth of the ferrite eventually comes to a halt producing a condition of incomplete transformation or "growth stasis." Precipitation of carbide may break the stasis and allow further transformation of the austenite. The rate of transformation will be dependent upon the diffusivity and diffusion distance of the alloy to grow the $M_xC_y$ carbide. As a result, the scale of the microstructure might be expected to influence the effectiveness of the subcritical anneal in removing the remnant austenite and as a result the grain multiplication factor. In general, the dimension of the bainitic ferrite lath should be proportional to the prior austenite grain size; and as a result, the dimension of the remnant austenite should also scale with the prior austenite grain size. The consequence of austenite scale may manifest itself as a time dependence in complete removal of the remnant austenite during the subcritical anneal, i.e. coarse bainitic microstructures as observed in cast microstructures may require longer subcritical annealing cycles. A bainitic microstructure is also expected in the normalized microstructures for steels with high alloy content and the scale of the remnant austenite will be dependent upon both casting size, prior austenite grain size and application of forced air cooling. A fast cooling rate will decrease the size of the remnant austenite and may allow for shorter times during the subcritical anneal. Also, a slow heating rate upon the second austenitization cycle may be sufficient to remove the remnant austenite and eliminate the need for the subcritical anneal. The fine scale of the remnant austenite

combined with a slow heating rate may explain the larger grain multiplication factor ($n_2$) of 311 in the NQ heat treatment. Retained austenite in martensitic microstructures exists in sub-micron layers between the laths of martensite. The thin retained austenite in martensite may thus be consumed during heating or during the subcritical anneal and this may explain the high grain multiplication factors, $n_2$, for the QQ and QTQ heat treatments.

The order of magnitude increase in the multiplication factor with the addition of the subcritical anneal in the martensitic microstructure is both difficult to ignore and explain. In the previous paper by Webb and Van Aken [1] it was suggested that recrystallization of the martensitic microstructure during the subcritical anneal may enhance the nucleation of additional grains, but a significant difference in how austenite nucleates and grows in the two martensitic microstructures is not obvious in Figure 13. There is some evidence that the forming austenite is more globular in the subcritical annealed microstructure. This may indicate a deviation from the Kurdjumov-Sachs orientation relationship and the early development of more equiax austenite grains as shown in Figure 13(d). However, the majority of the new austenite forms as laths with remnant ferrite in between indicating that the Kurjumov-Sachs orientation relationship constrains the growth of the new austenite. Further work will be required to fully understand these details; however, the results presented here can be used to develop robust heat treatments to develop improved grain refinement, e.g. TNTQ.

The addition of the subcritical anneal to other Cr-Mo steels might be expected to yield similar benefits in grain refinement. A quick review of the cast microstructures in Figure 6(e) and Figure 14(a) show that 4320 steel produces a bainitic microstructure as well. Again, using OIM-EBSD the lath packet microstructure and the remnant austenite is observed in the bainitic microstructures as shown in Figure 15.

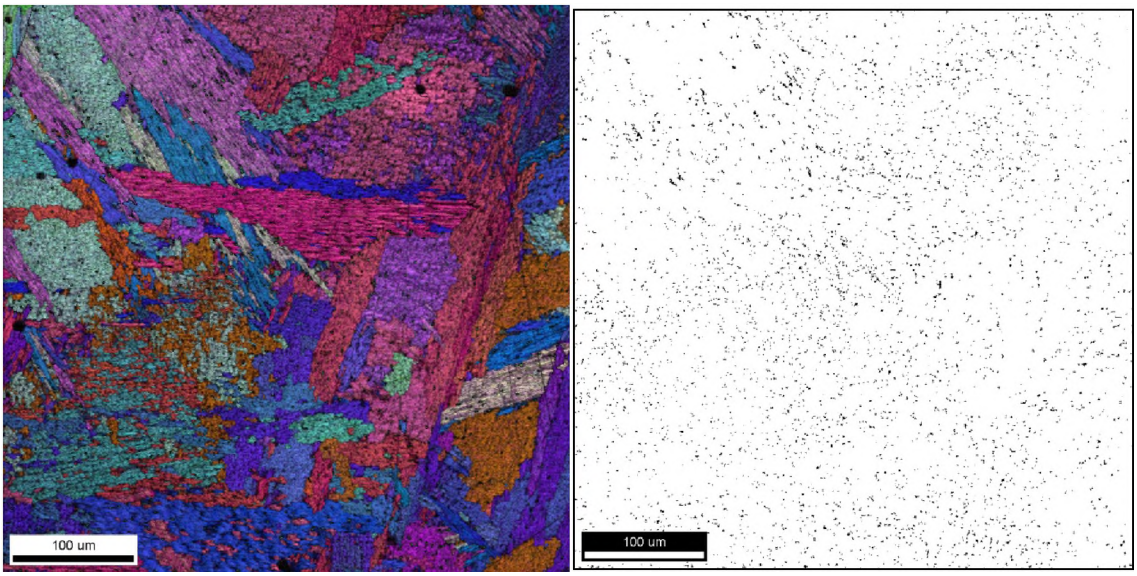


Figure 15. EBSD-OIM of an as-cast 4320 steel. (a) OIM image of the bainite showing lath packets of ferrite. (b) An inverted image to highlight the remnant austenite in the bainitic microstructure.

In contrast, the cast 4140 steel has a pearilitic microstructure as shown in Figure 6(d) and when heated to an intercritical temperature of 760°C (1400°F), the austenite that forms grows in a more equiax fashion to consume the ferrite and carbide (pearlite) microstructure as shown in Figure 16. A distribution in the austenite grain size might be expected as a result of a time dependent nucleation of austenite. Normal grain growth would eliminate the smaller austenite grains in favor of the larger grains, which nucleated at the beginning of the transformation, i.e. normal grain growth.

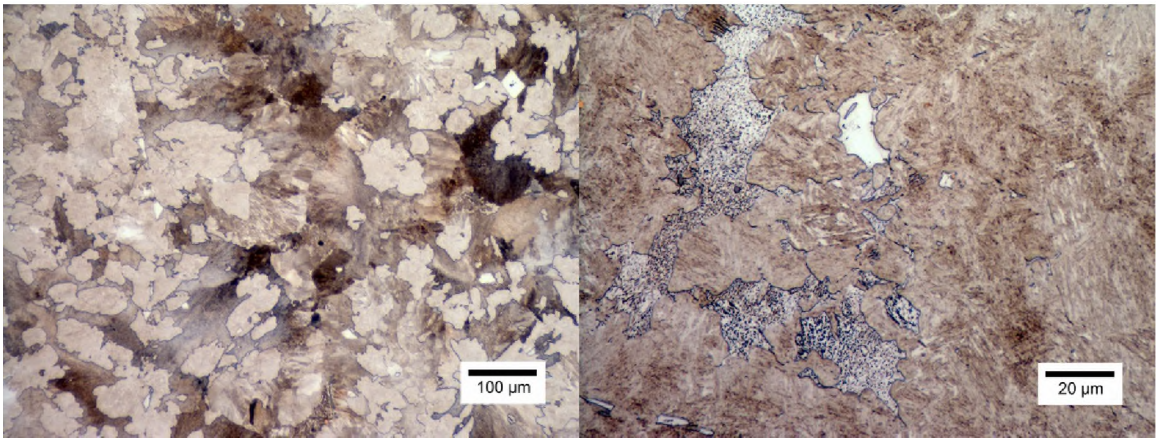


(a) (b)

Figure 16. Optical images showing the formation of austenite at 760°C (1400°F) in a pearlitic microstructure of 4140 after (a) 10 minutes and (b) 20 minutes. In (a) a large number of new austenite grain have nucleated and appear as globular shapes with a light tan contrast. After 20 minutes at temperature these new grains of austenite have begun to impinge and small remnant areas of pearlite have become spheroidized. The carbide pinning of the growing austenite is evident by the crenulated shape of the austenite.

Austenite formation requires a source of carbon as shown in Figure 3 by the formation of austenite adjacent to the graphite nodule within the "bullseye" ductile iron microstructure. Microstructures as shown for 1524 in Figure 4 and 8620 in Figure 6(b) would be expected to show a uniform distribution of new austenite grains as each region of pearlite transforms to austenite. A more interesting study is to consider the more acicular ferrite microstructures exhibited by the cast 8620 and 8630 steels as shown in Figure 6(a) and Figure 6(c). Upon heating, the austenite first forms in the regions containing carbide between the ferrite laths as shown in Figure 17 for the 8620 steel. The 8630 shows a similar response during the 760°C (1400°F) intercritical heat treatment. Two morphologies of the austenite are apparent in Figure 17: larger more globular regions of austenite and lath-like regions of austenite between the remnant ferrite laths. Eventually the lath-like regions coalesce to form larger austenite grains.

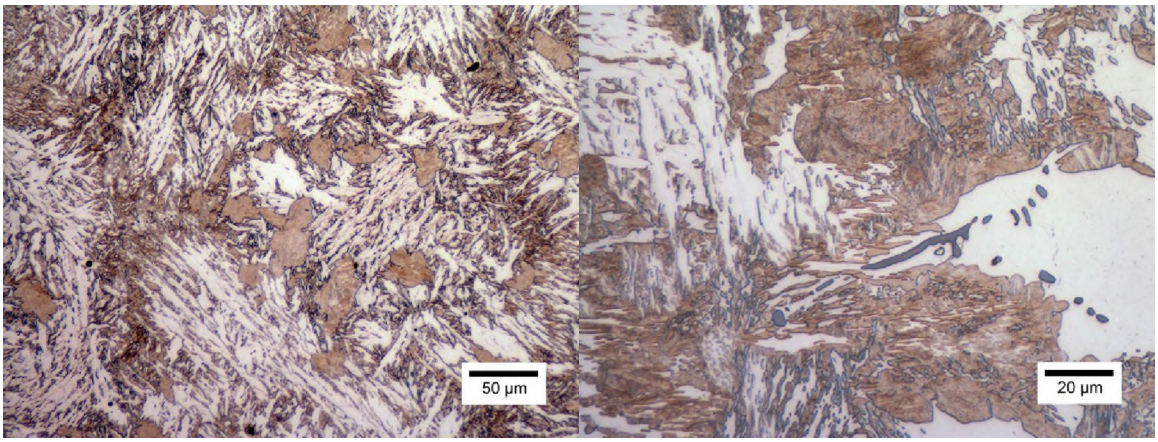


(a) (b)

Figure 17. Optical images showing austenite formation at 760°C (1400°F) in 8620-Foundry 1. (a) After 5 minutes at temperature globular regions of austenite have formed randomly throughout the acicular ferrite microstructure. Some austenite has also formed in the regions between the ferrite laths. (b) After 20 minutes at temperature the austenite begins to coalesce, but remnant ferrite remains as thin laths similar to what was observed in the martensitic microstructures of the W-steel during intercritical annealing. Type II MnS is evident in (b).

Grain refinement heat treatments were applied to the 8620 (Foundry-2), 8630 and 4140 steels. Normalization heat treatments were conducted at 925°C for the 8620 steel and 900°C for the 8630 and 4140 steels. Portions of keel block legs were double wrapped in chemically treated stainless steel bags, austenitized, removed from the furnace and immediately wrapped in an additional layer of kaowool to simulate the cooling of larger castings. The results of a single normalize (N) and a double normalize heat treatment (NN) are shown in Figure 18. Grain refinement after each normalization treatment is evident for these low alloy steels. However, some evidence of bainite, degenerate ferrite, [8] and martensite is apparent in the alloy-segregated, interdendritic regions as shown in Figure 19. These would be manifested as hard spots during machining and may affect the overall tensile ductility in the normalized condition, i.e. heat treatments TN and TNTN. Grain refinement in these interdendritic regions may also be

affected by the bainitic microstructures and this was explored by applying a four hour subcritical anneal at 649°C (1200°F) prior to each normalization heat treatment. The results are shown in Figure 20. A comparison of the grain structures between the results shown in Figure 18 without the subcritical anneal and the results shown in Figure 20 with the addition of the subcritical anneal suggests there may be some additional benefit with respect to grain refinement and refining the interdendritic microstructure. There is little evidence of the bainitic structure for the TNTN treated 8620 steel and the amount of bainite in the 8630 and 4140 steels has been reduced and partially broken up by the appearance of ferrite grains nucleated within the segregated regions.

Grain multiplication factors have not been calculated for the normalization heat treatments since the formation of and size of the ferrite will be dependent upon undercooling below the $A_3$ temperature. Generally speaking for a fixed cooling rate and a larger prior austenite grain size the steel will be undercooled to a greater amount. The undercooling below the critical temperatures was sufficient to produce a microstructure that was nearly all pearlite in the case of as-cast 4140 steel. As the grain size is reduced upon heating, during the polymorphic phase transformation, the finer grained austenite shifts the transformation curve to shorter times and nucleation occurs upon cooling at a higher temperature. Every effort was made to keep the cooling rates after normalization the same, but some variation is to be expected. It is; however, obvious that the overall size and the scale of the internal structure of the bainitic regions observed in the TNTN treated 8630 have been reduced as shown by a comparison of Figure 18(d) with Figure 20(d). These heat treatments appear to be less effective for the 4140 steel. These results suggest that future work be conducted to determine the effect of subcritical annealing on tensile and V-notch impact properties of steels given NQ and TNTQ heat treatments. Grain refinement using the subcritical anneal might be expected to increase both measures of ductility and increase Charpy V-notch energy.

# 5. CONCLUSIONS

The mechanism responsible for grain refinement of W-steel is associated with a bainitic microstructure containing more than 13% austenite. Upon heating this remnant austenite grows to reform the original parent austenite grain and little to no grain refinement occurs during the normalization heat treatment. Application of a subcritical anneal of four hours at 649°C (1200°F) can be used to remove the remnant austenite and enhance grain refinement during subsequent austenitization. Subcritical annealing for grain refinement should find good application to higher alloy steels such as 4320 and 4340 to improve mechanical properties in quenched and tempered castings. Application of subcritical annealing to lower alloy steels such as 8620, 8630 and 4140 to improve grain refinement and grain size uniformity may be of some limited benefit.

## 6. ACKNOWLEDGEMENTS

This work has been supported under the Steel Founders' Society of America (SFSA) program on Casting and Advanced Steel Technology that has been funded by the Army Research Laboratory under the provisions of cooperative agreement W911NF-12-2-0033. The authors are grateful for steel castings supplied by Spokane Industries, Bradken-Atlas LP, and Bradken-Tacoma. The authors wish to thank Mr. Don Denney at American Cast Iron Pipe Co. (ACIPCo) for optical emission spectroscopy of the W-steels. Richard Harris and Rachel Abrahams, Air Force Research Laboratory at Eglin AFB, are gratefully acknowledged in providing support for conducting Electron Backscattered Electron Diffraction Orientation Image Mapping. The authors also acknowledge the support of the Materials Research Center and in particular Dr. Eric Bohannan for guidance and training in using the FIB and performing the XRD work.

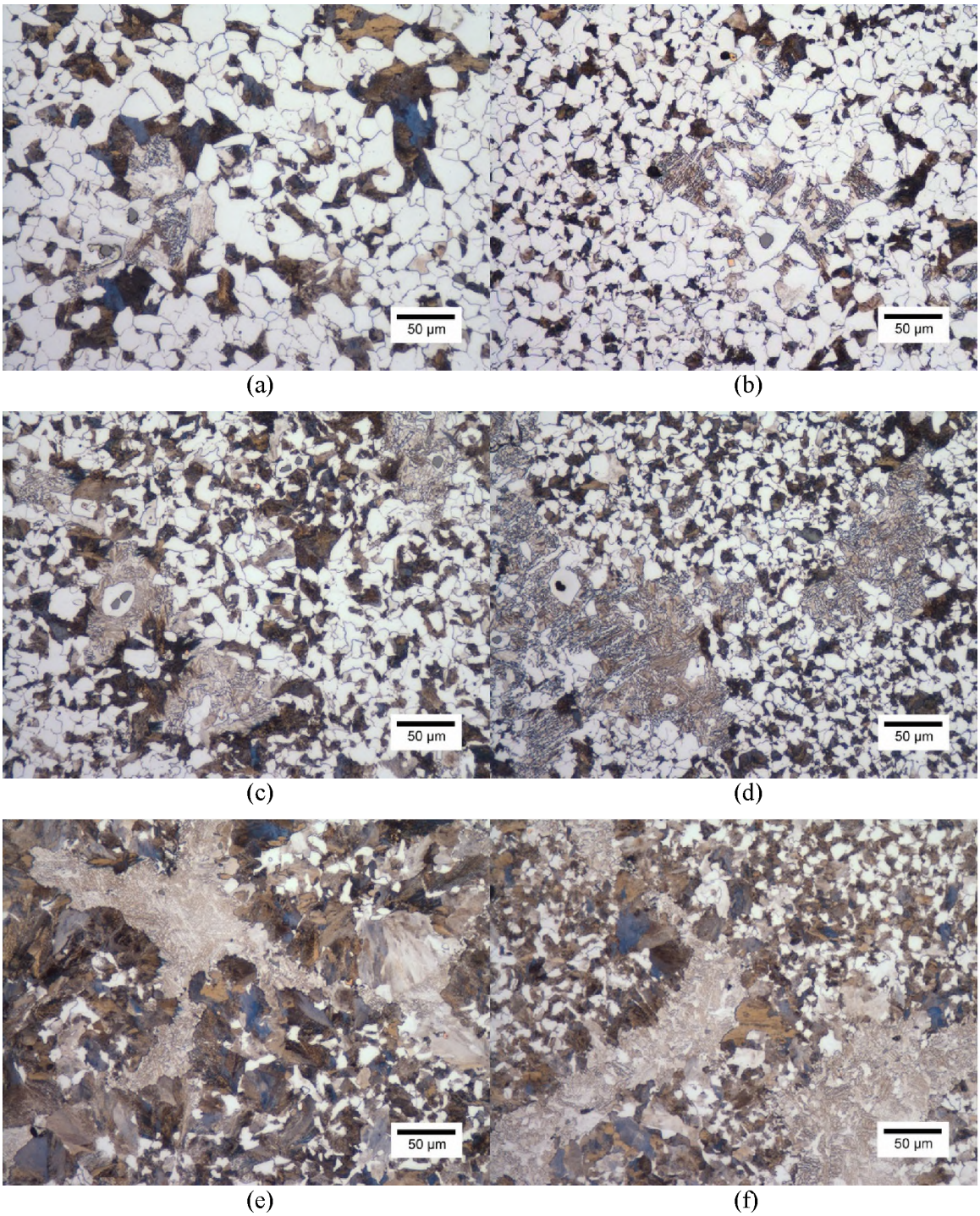


Figure 18. Normalization study of cast alloy steels 8620, 8630 and 4140. (a) single normalization of 8620, (b) double normalization of 8620, (c) single normalization of 8630, (d) double normalization of 8630, (e) single normalization of 4140, and (f) double normalization of 4140. All three alloys show grain refinement during standard normalization practices, but an intergranular microstructure is evident in each, which is more bainitic in nature.

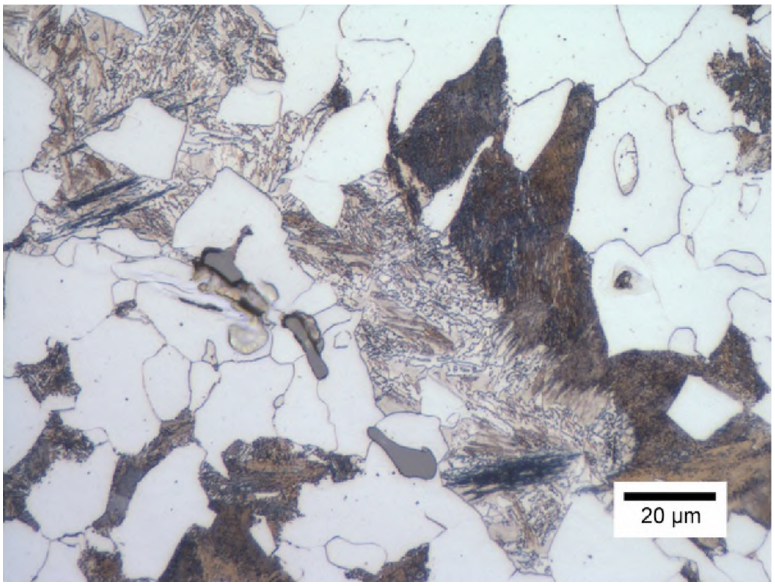


Figure 19. An optical image of 8620 after the first normalization cycle showing the microstructure of the interdendritic region that is alloy rich as a result of segregation during solidification. A combination of upper bainite, degenerate ferrite (crenulated), and martensite is observed. Etched with 2% nital.

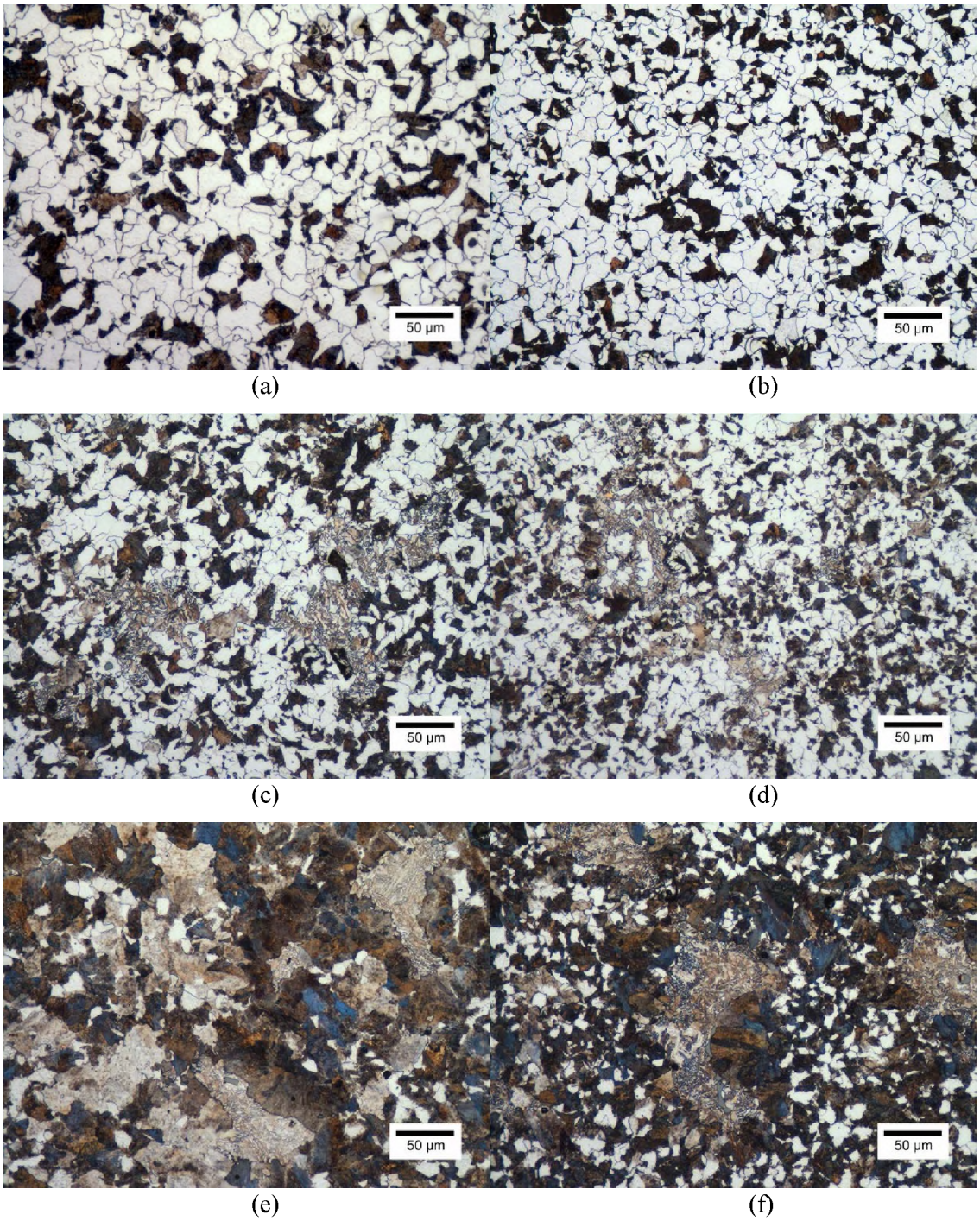


Figure 20. Normalization study of cast alloy steels 8620, 8630 and 4140 with the addition of a subcritical anneal prior (T) to the austenitization (N) of the steel. (a) single normalization (TN) of 8620, (b) double normalization (TNTN) of 8620, (c) single normalization (TN) of 8630, (d) double normalization (TNTN) of 8630, (e) single normalization (TN) of 4140, and (f) double normalization (TNTN) of 4140. All three alloys show grain refinement during standard normalization practices, but an intergranular microstructure is evident in each, which is more bainitic in nature.

## REFERENCES

[1] T.O. Webb and D.C. Van Aken, "An Innovative Heat Treatment to Improve the Ductility of High Strength Steels," Steel Founders' of America Technical and Operating Conference paper 2.1, Chicago, IL, December 13, 2014.

[2] ASTM E112-13, Standard Test Methods for Determining Average Grain Size.

[3] W.F. Hosford, Physical Metallurgy, CRC Taylor & Francis, NY (2005) pp. 476-477.

[4] G.A. Roberts and R.F. Mehl, Trans. ASM vol. 31 (1943) pp. 613-650.

[5] M.A. Grossman and E.C. Bain, Principles of Heat Treatment, 5th ed. ASM, Metals Park, OH (1971) pp. 38-39.

[6] S. Martin, C. Ullrich, D. Simek, U. Martin, and D. Rafaja, J. Appl. Crystallogr., vol. 44, (2011) pp. 779-787.

[7] H.I. Aaronson, W.T. Reynolds, and G.R. Purdy, "The Incomplete Transformation Phenonmenon in Steel," Metall. Mater. Trans. A, vol. 37A, (2006) pp. 1731-1745.

[8] H.I. Aaronson, G. Spanos, and W.T. Reynolds, "A progress report on the definitions of bainite," Scripta Mater. Vol. 47 (2002) pp. 139-144.

# III. POROSITY AND CLEANLINESS LIMITATIONS ON HIGH STRENGTH STEEL

**AUTHORS**
D.C. Van Aken
T.O. Webb

Missouri University of Science and Technology
401 W. 16th St.
Rolla, MO
65409

R.D. Foley
J.A. Griffin

University of Alabama at Birmingham
501 12th St. S
Birmingham, AL
35294

## ABSTRACT

Six steel heats of a high strength steel were examined to determine the ductility limitations induced by porosity and non-metallic inclusions. Maximum pore length as measured on a fracture surface produced the best correlation to ductility as measured by percent elongation to failure and the percent reduction in area. Measurement of porosity on metallographic specimens demonstrated that porosity must be restricted to less than 0.05% to obtain elongations to failure of 10% or greater. A general model for the notch effect of a large pore was formulated and shows that shrinkage pores must be restricted to less than 400 μm in length to eliminate brittle behavior induced by porosity. Brittle fracture may still be observed in high strength steels with smaller pore lengths, but the analysis suggests that these failures may be hydrogen related.

# 1. INTRODUCTION

High strength cast steels with yield strengths greater than 150 ksi (1030 MPa) and tensile strengths in excess of 200 ksi (1380 MPa) often exhibit limited ductility as measured by either elongation to failure or reduction in area. Measured ductility of high strength steels may be reduced by porosity, nonmetallic inclusions, and hydrogen. Harden and Beckermann [1] have shown that centerline shrinkage porosity in the range of 0.1 to 0.27 % by volume can reduce the elongation to failure in ASTM A216 grade WCB steel. In a sound casting the expected elongation to failure was 22% and the elongation to failure was decreased to a range of 19.6 to 12.8% with increasing amounts of porosity. Their work also demonstrated that finite element modeling could predict the tensile behavior of the cast WCB steel when experimental porosity distributions, mapped by radiographic methods, were appropriately meshed. The porous metal plasticity model within ABAQUS software was used to model the tensile behavior. It should be noted that WCB grade steels have a specified minimum yield strength of 36 ksi (250 MPa) and ultimate tensile strength of 70 ksi (485 MPa). Brittle fracture induced by a notch effect from porosity is unlikely to occur since the low yield strength of WCB grade steels will cause extensive plasticity and notch blunting.

It has been shown for cast aluminum alloys that the tensile properties of percent elongation to failure, yield strength, and ultimate tensile strength decrease with the maximum pore area. The decrease in yield strength with max pore area was linear while a logarithmic form was used to describe the decrease in percent elongation and ultimate tensile strength as shown by equation (1)

$$Y_{property} = B - A\ln(Pore\ Area) \tag{1}$$

where A and B are fitting parameters and pore area is a measure of the largest pore. Similar trends were observed by Avalle et al. [3] when the properties were plotted versus a

decreasing density, i.e. increasing porosity. More extensive work has been performed in relating fatigue life of aluminum castings with porosity, e.g. references [4-7]. Here again the fatigue property relationship is related to the area of the defect and the stress intensity calculations always follow a description introduced by Murakami and Endo [8] as shown in equation (2).

$$K_I = \alpha\sigma\sqrt{\pi\sqrt{area}} \qquad (2)$$

where $\alpha$ is 0.5 for an internal flaw or 0.65 for a surface flaw. The stress intensity factor was found to be less sensitive to the shape of the defect and the stress intensity varied by less than 10% with shape.

Ran and Zhou [9] performed a metallographic study of porosity in cast aluminum alloy A356-T6. A total of 5,600 pores in as-cast and 20,200 pores in hot isostatic pressed (HIPed) castings were measured for pore area, pore perimeter, and pore sphericity. The metallographic measurements were performed at a magnification of 50x. Some of Ran and Zhou's research is reproduced in Figure 1 showing the general relationship of pore area with pore length and pore perimeter with pore length. These authors also observed that the maximum pore area increased as the secondary arm spacing increased, but this observation was made in a relatively narrow range of 82 to 96 μm.

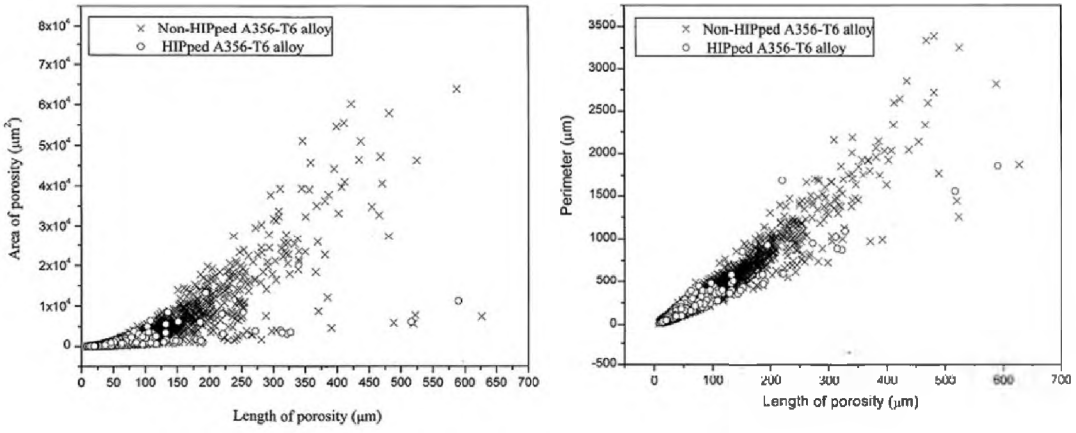


(a) (b)

Figure 1. Metallographic measurements of porosity from as-cast and HIP treated A 356-T6 castings. The length of porosity is the maximum length observed on the polished cross section. (a) area of porosity relative to the measured pore length shows considerable scatter whereas less scatter is observed for a measure of the perimeter of the pore relative to the maximum pore length.

Porosity is expected to play a more significant role in limiting the properties of high strength steels, since the plasticity of a quench hardened steel microstructure may be insufficient to blunt the notch effect of the pore and the fracture may be limited by the cleanliness of the steel. Bartlett et al. [10] have shown that the dynamic fracture toughness of HY130 can be reduced by 40% when titanium nitrides are present in the microstructure. Interestingly, a recent failure analysis of a duplex stainless steel casting related the fatigue failure to porosity and fast crack propagation facilitated by titanium nitrides. [11]

Fracture ductility of steel should depend upon the total volume fraction of both void nucleating second phases and porosity. Equation (3) shows the relationship between the true strain at fracture ($\varepsilon_f$) and the reduction in area ($RA$). The true fracture strain is the sum of the true

strain to nucleate a void ($\varepsilon_{nucleate}$) and the true strain to grow ($\varepsilon_{grow}$) the void to critical size for shear failure. Brown and Embury related $\varepsilon_{grow}$ to the volume fraction ($V_f$) of void nucleating second phase particles. [12] Negating the strain to nucleate is appropriate with respect to porosity, since the void is already present. Garrison and Wojcieszynski performed careful analysis of matching fracture surfaces and showed that only a small fraction of the microvoids contain the initiating nonmetallic inclusion. [13] This may suggest that the nonmetallic inclusions are poorly bonded and that the strain to nucleate the void ($\varepsilon_{nucleate}$) is negligible. The similarity of the logarithmic relationship of equation (1) is very similar to that of the Brown and Embury equation shown in equation (3).

$$\varepsilon_f = \ln\left(\frac{1}{1-RA}\right) = \varepsilon_{nucleate} + \varepsilon_{grow} = \varepsilon_{nucleate} + \frac{1}{2}\ln\left[\left(\frac{\pi}{6V_f}\right)^{\frac{1}{2}} - \left(\frac{2}{3}\right)^{\frac{1}{2}}\right] \tag{3}$$

Steels with yield strengths greater than 100 ksi (690 MPa) are also subject to hydrogen embrittlement and porosity will act as a strong trap for hydrogen. Upon tensile loading hydrogen assisted fracture may be observed in steels containing as little as 2 ppm hydrogen. [16] An example of hydrogen damage is shown in Figure 2 for a steel containing 7 ppm hydrogen, which failed at 180 ksi (1240 MPa) with less than 2% elongation to failure. The round fracture features shown in Figure 2(a) are a result of cleavage fracture emanating from shrinkage porosity as shown in Figure 2(b). This fracture is typical for steels damaged by hydrogen; however, this type of fracture may also be observed for notch-induced fracture near pores with large areas. Equation (2) would suggest that there should be a critical flaw size where the notch effect of the pore may induce fracture upon tensile loading. Figure 3 shows a similar steel where the fracture near the porosity is ductile; however, the hydrogen content for this steel is unknown.

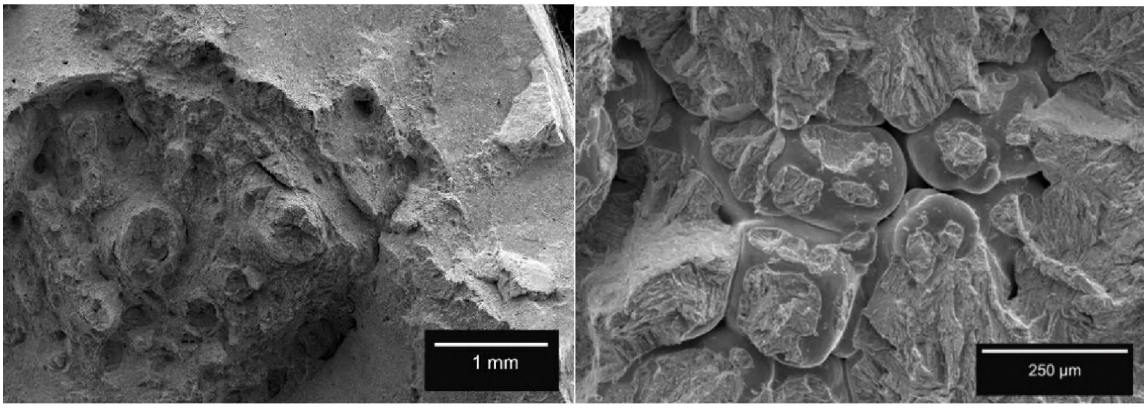


(a) (b)

Figure 2. Secondary electron image of high strength cast steel tensile bar showing (a) large circular plateaus at shrinkage pores and (b) brittle cleavage facets at the edge of the shrinkage pore.

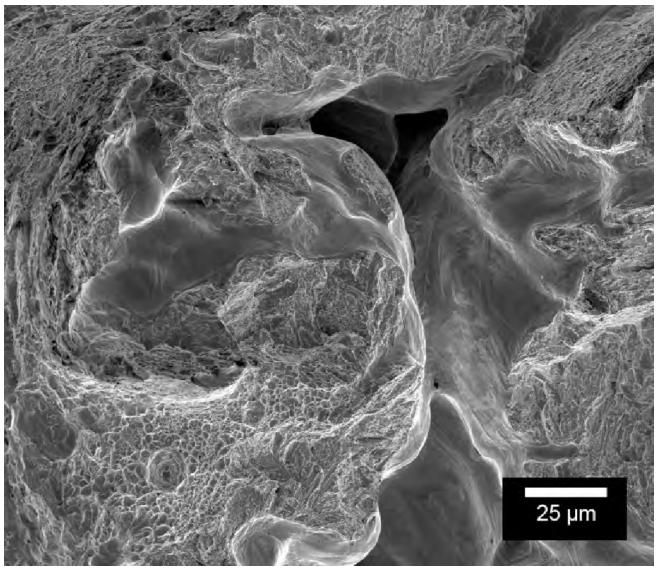


Figure 3. Secondary electron image of a high strength steel fracture surface near shrinkage porosity. A ductile fracture mode of microvoid coalescence is observed near the pore. This steel was induction melted using vacuum arc remelted forging stock and cast into preheated ceramic investment molds.

The goal of this paper is to examine the role of porosity and steel cleanliness in limiting the ductile behavior of high strength steel castings. All of the steels discussed in this paper have yield strengths in excess of 175 ksi (1205 MPa), and an ultimate tensile strengths greater than 230 ksi (1585 MPa) when not limited by porosity or hydrogen damage or both.

## 2. EXPERIMENTAL PROCEDURE

All of the high strength steels investigated here conformed to the chemistry ranges listed in Table I. Six different heats of steel were considered in this study. Most of the steels were cast in bonded sand, but a centrifugal process was used to cast one steel heat. Many of the steels investigated here were refined using Argon, Oxygen, Decarburization (AOD) and the melt chemistry was closely controlled to minimize aluminum content to reduce alumina and aluminum nitride inclusions.

Table I- Chemical range for high strength steel studied here.

| Element (wt%) | C | Mn | Si | Cr | Ni | Mo | W | V | Cu | P | S | Ca | N | Al | O |
|---|---|---|---|---|---|---|---|---|---|---|---|---|---|---|---|
| Chemistry range | 0.24 - 0.26 | 0.85 Max | 1.25 Max | 1.50 – 3.0 | 0.90 - 1.2 | 0.30-0.55 | 0.80 – 1.00 | 0.05 - 0.30 | 0.50 Max | 0.015 Max | 0.003 Max | 0.02 Max | 0.005 Max | 0.04 Max | 0.005 max |

Heat treatments for these steels varied, but the best ductility was obtained using the following heat treatment: a hydrogen bake at 600°F (315°C) for 7 hours, a nonstandard normalization at 2100°F (1149°C) for 2 hours with an oil or water quench to produce a martensitic microstructure, an intermediate temper at 1200°F (649°C) for 4 hours, an austenitization at 1900°F (1038°C) for 1 hour with a water quench, and a temper at either 375°F (190°C) for 4 hours or 380°F (193°C) for 5 hours. The resulting lath martensitic microstructure had a prior austenite grain size on the order of 50 μm. Tensile tests were conducted in accordance with ASTM E8-13.

Inclusion and porosity measurements using an ASPEX PICA 1020 automated feature analysis system was conducted in accordance with method 3 of ASTM E2142-08, and stereological data taken during analysis was computed as defined in Section 12 of ASTM E1245-03. Measurements were made using a combination of scans with the objective of quantifying both macroscopic porosity (10 μm to 320 μm) and microscopic porosity (<10 μm) and nonmetallic inclusions. Macroscopic measurements were made using a step size of 1.25 μm, and a magnification of 250X, while microscopic measurements were made using a step size of 0.2 μm, and a magnification of 750X. Standardization of fields scanned and area scanned is not required per ASTM E2142-08; however, multiple samples are scanned and included in measurements such that an area 60 $mm^2$ or greater is scanned. Field scanning is conducted using the non-randomized methodology and a nominal scan time of 1 second is used for collecting spectrums during EDS. Post-acquisition analysis rules for the steel using ASPEX PICA 1020 software are documented in Table II.

Table II- ASPEX PICA 1020 rule file used to characterize porosity and non-metallic inclusions.

| | Fe | Mn | S | Ca | C | Al | Si | Ti |
|---|---|---|---|---|---|---|---|---|
| **Porosity** | >= 80 | | | | | | | |
| **MnS** | | >30 | >15 | <20 | <10 | | | |
| **CaS** | | <20 | >20 | >30 | <10 | | | |
| **MnS-CaS** | | >15 | >20 | >15 | <10 | | | |
| **CaAl2O4** | | <20 | <20 | >15 | <10 | >20 | <20 | |
| **MnSiO3** | | >20 | <20 | <20 | <10 | <20 | >10 | |
| **MnAlSiO** | | >20 | <20 | <20 | <10 | >18 | >10 | |
| **CaSiO3** | | <20 | <20 | >20 | <10 | <20 | >10 | |
| **MnO-Al2O3** | | >25 | <20 | <20 | <10 | >25 | <20 | |
| **CaO-MnO** | | >25 | <20 | >25 | <10 | <20 | <20 | |
| **Complex** | | | | | <10 | >2 | >2 | |
| **Al2O3** | | | | | <10 | >25 | | |
| **MnO-Al2O3** | | >30 | <20 | | <10 | | | |
| **CaO** | | | <20 | >30 | <10 | | | |
| **TiN** | | | | | <10 | | | >40 |
| **Other Oxides** | | | <10 | | <10 | | | |
| **Other Oxisulfides** | | | >5 <10 | | <10 | | | |
| **Other Sulfides** | | | >10 | | <10 | | | |
| **Unclassified** | | | | | <10 | | | |
| **Diamond Paste** | | | | | >=40 | | | |

Accuracy of the ASPEX measurement can be demonstrated by comparing optical measurements and calculated measurements of the casting configuration shown in Figure 4(a). Figure 4(b) shows a comparison of porosity as measured by optical methods on metallographically prepared specimens and the volume percent porosity determined using MAGMAsoft casting simulation software to model the wedge shown in Figure 4(a). Figure 4(b)

was provided by Hardin and Beckermann. [14] Excellent agreement is found between the ASPEX measured porosity and those predicted by casting simulation. The discrepancy between optical measurements and those obtained by either ASPEX or simulation may be explained by an examination of pore size frequency as shown in Figure 5. A large number of submicron pores are observed closer to the chill surface and the ability to distinguish these small pores from nonmetallic inclusions becomes extremely difficult using optical methods.

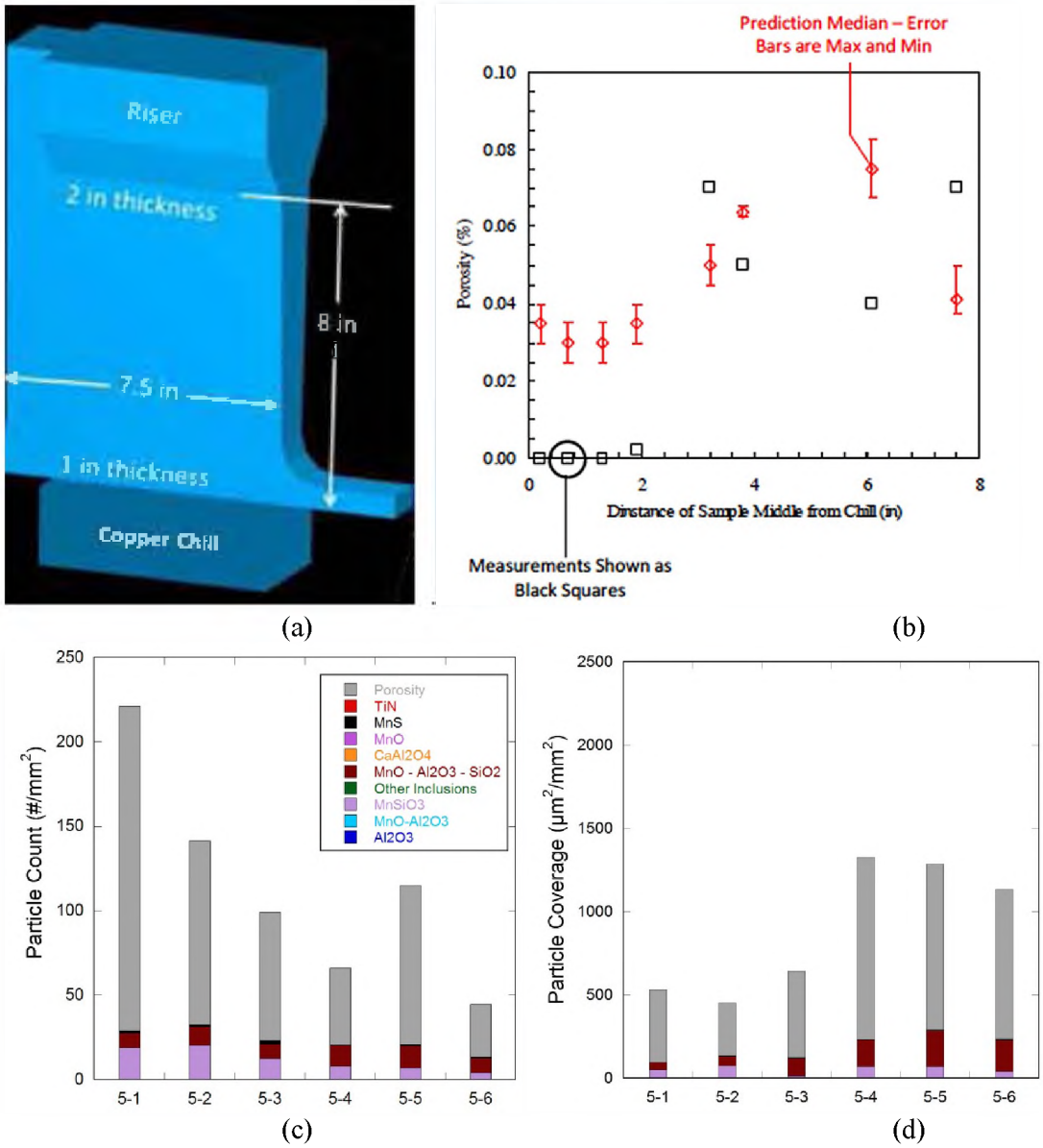


Figure 4. (a) Image of wedge casting on chill poured at the University of Alabama-Birmingham (UAB). (b) Composite graph provided by Harden and Beckermann [14] comparing the UAB optical measurements of porosity with the predicted porosity. ASPEX data is shown in (c) particle count per $mm^2$ and (d) particle coverage in $\mu m^2/mm^2$ which translates to ppm. The designations refer to casting/wedge # and approximate distance from the chill in inches. Porosity in (d) are 0.04%, 0.03%, 0.05%, 0.11%, 0.10%, and 0.09%. It should be noted that the ASPEX measurements were taken from tensile bars removed from the cast wedge that are located closer to the wedge center as compared to the measurements of UAB and the calculated predictions of Hardin and Beckermann.

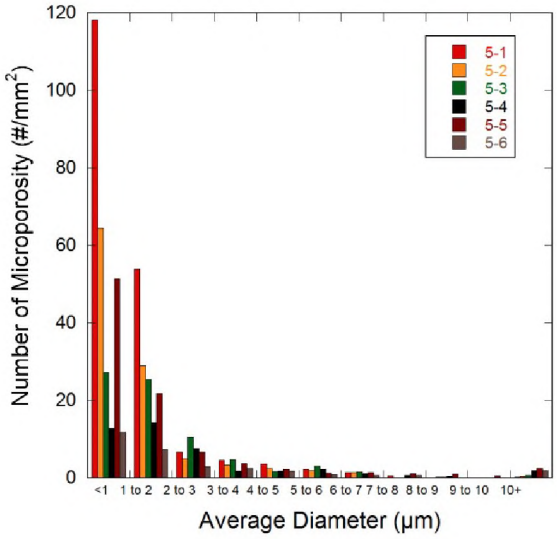


Figure 5. Frequency distribution of pore size for the wedge specimens shown in Figure 4. A large number of small pores are measured close to the chill as depicted by the frequency distribution for wedges 5-1 and 5-2.

# 3. RESULTS

Fracture surfaces from 46 tensile tests were examined using a stereo microscope and the porosity was carefully mapped on to an image of the fracture. Examples of the mapping are shown in Figure 6. The maximum length of the pore and the total pore area percentage were then determined. Figure 7 shows various mappings of these measurements and the measurements of percent elongation to failure and percent reduction in area. The strongest correlations exist between percent elongation to failure and percent reduction in area with max pore length as shown in Figures 7(c) and 7(d).

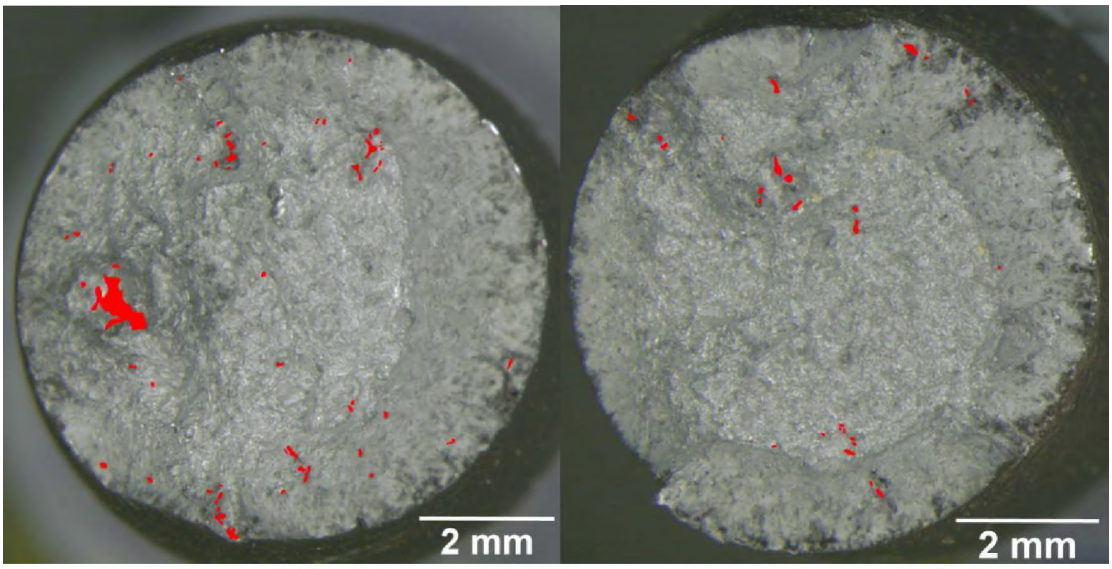


(a) (b)

Figure 6. Example of tensile fractures and optical measurement of porosity on the fracture surface. (a) Tensile specimen failed at 9.5% elongation and 29% reduction in area. (b) Tensile specimen failed at 11% elongation and 33% reduction in area.

Metallographic specimens were obtained from each tensile bar using the gage section exhibiting uniform elongation. Both porosity and non-metallic inclusions were measured. The low aluminum content of the steel resulted in a predominance of inclusions containing manganese listed here in decreasing measured area $MnO\text{-}Al_2O_3\text{-}SiO_2$, $MnSiO_2$, MnS and MnO. Porosity was the dominant feature measured and shows the strongest correlation to the measures of ductility. Figure 8 shows the measures of ductility relative to percent area coverage of porosity and a combination of both percent area coverage of pores and nonmetallic inclusions. One significant result that can be gleaned from Figure 8(a) is that to obtain an elongation to failure greater than 10% the porosity coverage must be less than 0.05%. As shown in Figure 4(b) optical measurements at these low concentrations are nearly impossible. A consideration of just nonmetallic inclusions is shown in Figure 9. No significant correlation is observed when all of the inclusions are considered together as shown in Figures 9(a) and 9(b). However, when MnS inclusions are considered separately a trend is observed and this makes sense considering the void nucleation at MnS inclusions is a common observance on fracture surfaces.

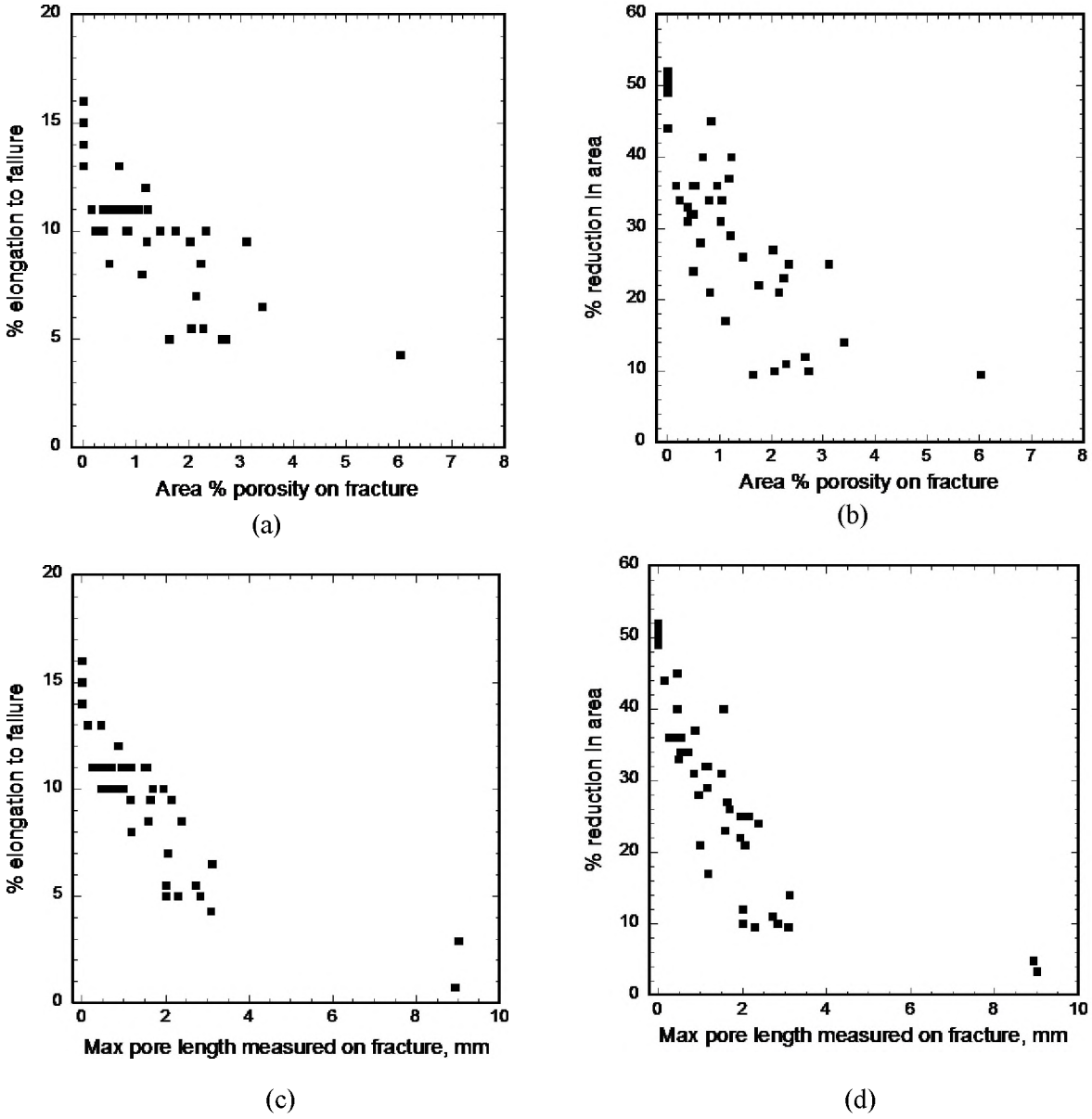


Figure 7. Measures of ductility with respect to stereoscopic measurements of percent area fraction of porosity and max pore length measured on the fracture surfaces of failed tensile bars. Results show the best correlation to the measure of max pore length.

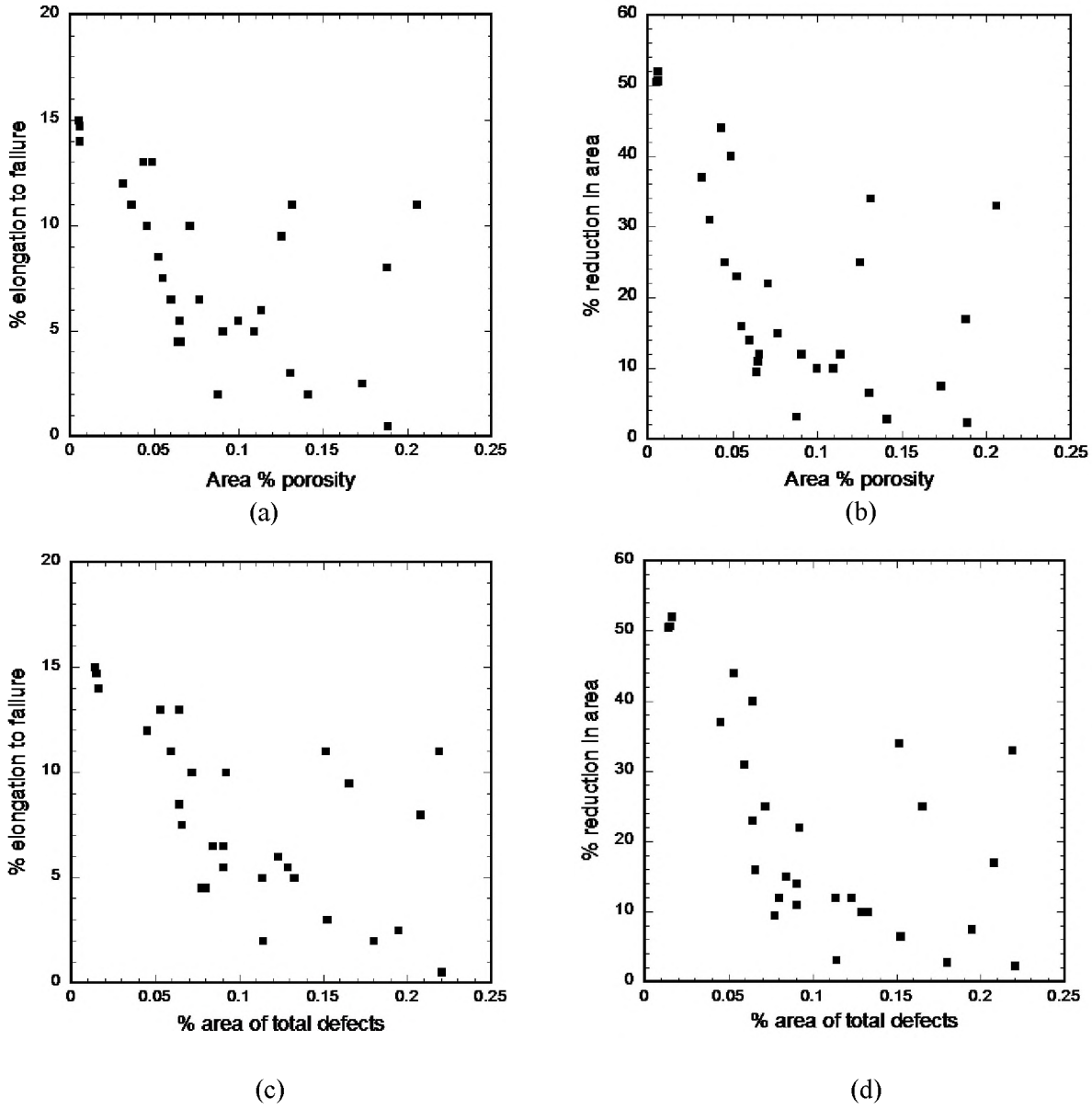


Figure 8. ASPEX measurements from metallographic specimens prepared from the gage section of the tensile bars. Figures (a) and (b) compare measures of ductility versus the % area of porosity. The area % was changed to include the contribution from nonmetallic inclusions in (c) and (d).

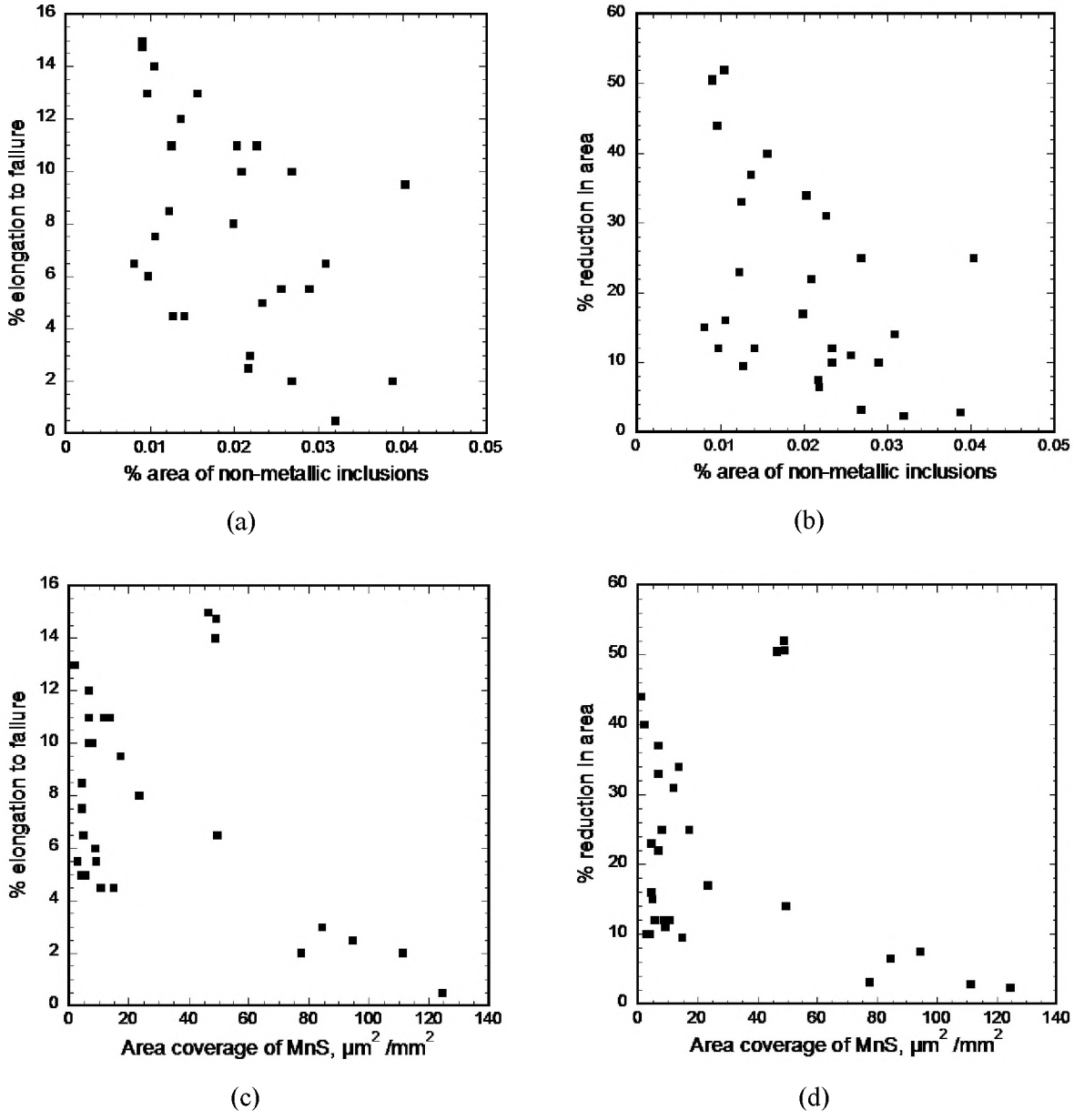


Figure 9. ASPEX measurements from metallographic specimens prepared from the gage section of the tensile bars. Figures (a) and (b) use the total area percent of nonmetallic inclusions and (c) and (d) restrict the analysis to measures of MnS content. The small grouping of data at the highest ductility is from the centrifugal cast steel tensile tests. Alumina shows a similar trend as MnS, although many of the steel heat tested in this study, as a result of very low aluminum contents, did not exhibit alumina in the microstructure.

# 4. DISCUSSION

Quality requirements for the production of high strength cast steel can now be formulated based upon the observations made here. If a minimum of 10% elongation to failure is required, the porosity must be less than 0.05% as shown in Figure 8(a) and the largest pore length should be less than 400 μm as demonstrated in Figure 7(c). Cleanliness of the steel must also be considered and sulfur must be restricted to keep the coverage of MnS to a minimum, which suggests that high strength steels should be made by an AOD process.

The measure of maximum pore length on the fracture surface appears to produce the best correlation to the measured ductility of high strength steel. Interestingly, the data in Figure 7(d) can be fit to equation (1) if the reduction in area is transformed into the true fracture strain using equation (3) and the max pore length is substituted for the max pore area. The substitution of max pore length for max pore area appears reasonable based upon the metallographic work of Ran and Zhou [9] as shown in Figure 1. The resulting plot of a trend line drawn through the data of Figure 7(d) is shown in Figure 10.

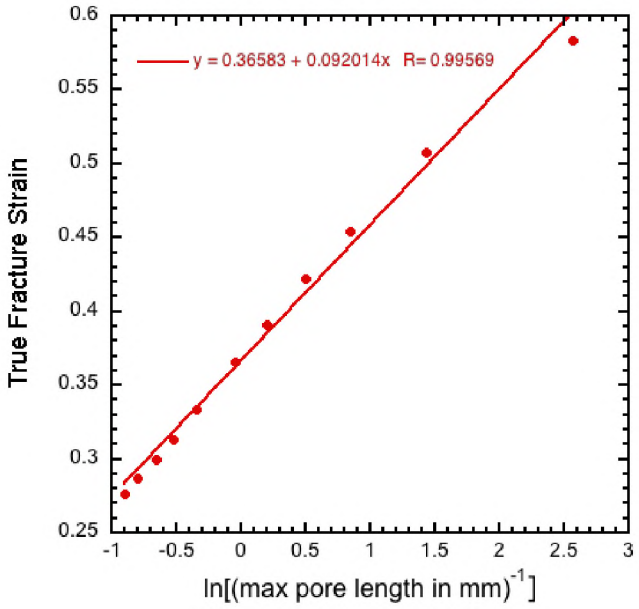


Figure 10. Linear regression analysis of the true fracture strain as a function of the max pore length in mm taken from Figure 7(d) and using equation (1).

The linear regression line from Figure 10 turns into the following

$$\varepsilon_f = 0.366 + 0.092 \ln\left(\frac{1}{\text{max } \textit{pore length}}\right) \tag{4}$$

where the reciprocal of the max pore length removes the negative sign proceeding the natural logarithm term shown in equation (1).

The strong relationship of max pore area to the fatigue properties of aluminum via the stress intensity calculation shown in equation (2) may suggest that there exists a correlation between max pore length and fracture of high strength steel. Richie et al. related the size of the critical fracture process zone ($r_c$) to the notch radius ($\rho$) using

$$r_c = \rho\left[\exp\left(\frac{\sigma_f}{\sigma_y} - 1\right) - 1\right] \tag{5}$$

where $\sigma_f$ is the true fracture strength and $\sigma_y$ is the yield strength. Equation (5) may be simplified by incorporating work hardening using

$$\sigma = K\left(\varepsilon_p\right)^n \tag{6}$$

where $\varepsilon_p$ is the true plastic strain. Using equation (6) the yield strength ($\sigma_y$) and the true fracture strength can be evaluated at a plastic strain of 0.002 and the true fracture strain ($\varepsilon_f$), which eliminates the materials constant *K*. A measure of the work hardening of the high strength steel studied here yields a work hardening exponent n=0.05. Incorporation of these terms and assumptions into the original equation yields

$$r_c = \rho\left\{\exp\left[\left(\frac{\varepsilon_f}{0.002}\right)^{0.05} - 1\right] - 1\right\} \tag{7}$$

Combining equations (4) and (7) yields the relationship of the critical plastic zone size with the max pore length that initiates failure as shown in equation (8).

$$r_c = \rho\left\{\exp\left[\left(\frac{0.366 - 0.092\ln\left(\max\ \textit{pore length}\right)}{0.002}\right)^{0.05} - 1\right] - 1\right\} \tag{8}$$

Fracture of the matrix in the critical process zone ($r_c$) is often associated with void nucleating inclusions such as MnS which are often observed on the fracture surface. Interestingly, Figure 9 shows a strong correlation to MnS. Inclusion spacing ($S$) is related to the areal density ($N_S$) of inclusions by

$$S = 0.5\left(N_s\right)^{-\frac{1}{2}} \tag{9}$$

A condition for fracture can now be developed by equating equations (8) and (9) and assuming the notch radius will be ½ the maximum pore length. The result is graphed in Figure 11 where the control of the tensile ductility is divided into two regimes: one controlled by steel cleanliness and one controlled by shrinkage porosity. Typical cleanliness ranges taken from the tensile bars of this study are mapped onto this relationship to show that AOD processed steel should be more tolerant of porosity, but the porosity must be limited to a maximum pore length less than 400μm.

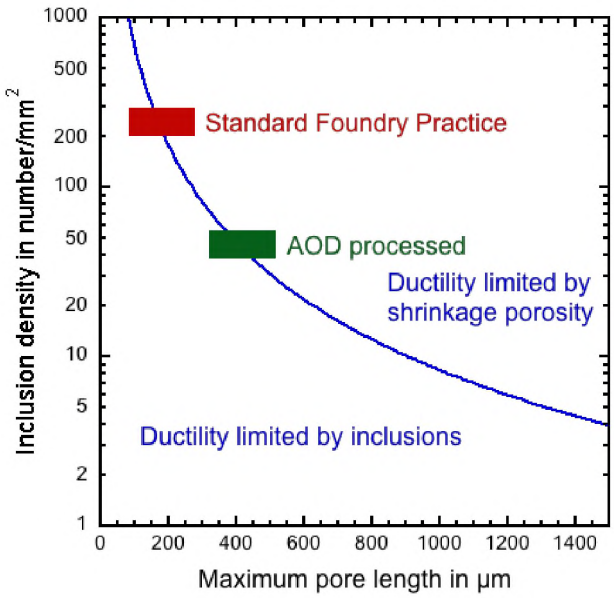


Figure 11. Ductility processing model with respect to inclusion density. Model leads to an intuitive conclusion that cleaner steels are more tolerant of shrinkage porosity.

Another interpretation of this result may be with respect to the observance of brittle fracture near porosity on the tensile fracture surface. For example, an AOD processed steel with a pore length less than 400 μm in length which exhibits cleavage fracture near the pores may be interpreted as having hydrogen embrittlement whereas an AOD processed steel may exhibit the same brittle cleavage fracture for pore lengths greater than 400 μm in the absence of hydrogen. The general applicability of this analysis has yet to be fully tested and the reader should be cautious in applying these results as a general rule. However, it might be expected that steels with even greater strength would shift the porosity limitations to even lower maximum pore lengths. The results presented here are not applicable to lower strength steels.

# 5. CONCLUSIONS

A combination of stereoscopic measurements of porosity on fracture surfaces and automated feature analysis using an SEM to measure porosity and cleanliness on metallographic specimens extracted for the same tensile bars were used to develop quantitative requirements for specifying ductility in high strength steels. Specifically, high strength steels as defined as having yield strengths greater than 175 ksi (1205 MPa) and ultimate tensile strengths greater than 230 ksi (1585 MPa) must have general porosity less than 0.05% and a maximum shrinkage pore length less than 400 μm to obtain elongations to failure greater than 10%. A model was developed to examine the synergistic effect of steel cleanliness and the notch effect of the pore. The results of this analysis suggest a method to differentiate brittle fracture induced by the notch stress concentration near the pore and brittle fracture induced by hydrogen damage near the porosity.

## 6. ACKNOWLEDGEMENTS

This work has been supported under the Steel Founders' Society of America (SFSA) program on Casting and Advanced Steel Technology that has been funded by the Army Research Laboratory under the provisions of cooperative agreement W911NF-12-2-0033. The authors also gratefully acknowledge Dr. Harden and Professor Beckermann for sharing their solidification modeling of the wedge casting and to the Army Research Office Defense University Research Instrumentation Program (award number W911NF-08-1-0267) for financial support in buying the ASPEX-PICA 1020 SEM that was used for automated feature analysis. Mr. Marc Harris at the University of Missouri Science & Technology is also acknowledged for helpful discussions and for the development of analysis tools for processing ASPEX data.

## REFERENCES


[1] R.A. Hardin and C. Beckermann, "Effect of Porosity on Deformation, Damage, and Fracture of Cast Steel," Metall. Mater. Trans. A44, (2013) pp. 5316-5332.

[2] Z. Ma, A.M. Samuel, F.H. Samuel, H.W. Doty, and S. Valtierra, "A study of tensile properties in Al-Si-Cu and Al-Si-Mg alloys: Effect of β-iron intermetallics and porosity," Mater. Sci. Eng. A490 (2008) pp. 36-51.

[3] M. Avalle, G. Belingardi, M.P. Cavatorta, and R. Doglione, "Casting defects and fatigue strength of a die cast aluminum alloy: a comparison between standard specimens and production components," Int. J. Fatigue 24 (2002) pp. 1-9.

[4] Q.G. Wang, C.J. Davidson, J.R. Griffiths, and P.N. Crepeau, "Oxide Films, Pores and the Fatigue Lives of Cast Aluminum Alloys," Metall. Mater. Trans. B37 (2006) pp. 887-895.

[5] J. Linder, M. Axelsson, and H. Nilsson, "The influence of porosity on the fatigue life for sand and permanent mould cast aluminum," Int. J. Fatigue 28 (2006) pp. 1752-1758.

[6] M. Mayer, M. Papakyriacou, B. Zettl, and S.E. Stanzl-Tschegg, "Influence of porosity on the fatigue limit of die cast magnesium and aluminum alloys," Int. J. Fatigue 25 (2003) pp. 245-256.

[7] H.R. Ammar, A.M. Samuel, and F.H. Samuel, "Porosity and the fatigue behavior of hypoeutectic and hypereutectic aluminum-silicon casting alloys," Int. J. Fatigue 30 (2008) pp. 1024-1035.

[8] Y. Murakami and M. Endo, "The area parameter model for small defects and nonmetallic inclusions in fatigue strength: experimental evidences and applications," Proc. Theoretical Concepts and Numerical Analysis of Fatigue, Birmingham, UK. Warley: Engineering Materials Advisory Services Ltd., Cradley Heath (1992) pp. 51–71.

[9] G. Ran and J. Zhou, "Metallographic Characterization of Porosity in a Cast Aluminum Alloy A356-T6," Materials Science Forum vol. 546-549 (2007) pp. 989-994.

[10] L.N. Bartlett, A. Dash, D.C. Van Aken, V.L. Richards, and K.D. Peaslee, Dynamic Fracture Toughness of High Strength Cast Steels," Int. J. Metalcasting Vol. 7, Issue 4, pp. 17-33 (2013).

[11] Mateo, F. Heredero, and G. Fargas, "Failure investigation of a centrifuge duplex stainless steel basket," Eng. Failure Anal. 18 (2011) pp. 2165-2178.

[12] L.M. Brown and J.F. Embury, The microstructure and design of alloys: proceedings of the third International Conference on the Strength of Metals and Alloys (Cambridge) The Institute of Metals, vol. 1, p. 164 (1973).

[13] W.M. Garrison and A.L. Wojcieszynski, "A discussion of the spacking of inclusions in the volume and of the spacing of inclusion nucleated voids on the fracture surface of of steels," Mater. Sci. Eng., vol. A505, pp. 52-61, (2009).

[14] R.A. Hardin and C. Beckermann, University of Iowa, SFSA research program communication.

[15] R.O. Richie, J.F. Knott, and J.R. Rice, "On the Relationship between critical tensile stress and fracture toughness in mild steel," J. Mech. Phys. Solids vol. 21, (1973) pp. 395-410.

[16] S.P. Lynch, Hydrogen-embrittlement (HE) phenomena and mechanisms, Stress corrosion cracking: theory and practice, Raja VS, Shoji T. (Eds), Cambridge, UK: Woodhead Publishing, pp 90-130, 2011

# IV. NORMALIZATION OF HIGH STRENGTH STEEL TO IMPROVE HOMOGENEITY AND MECHANICAL PROPERTIES

**AUTHORS**
T.O. Webb
D.C. Van Aken

## ABSTRACT

Elevated temperature normalization at 1232°C (2250°F) for up to 11 hours was explored in an effort to improve the chemical homogeneity, and toughness of a cast high strength steel. Additionally the effect of carbides on the ductility and toughness in this steel was evaluated through a comparison of the mechanical properties achieved using the heat treatment with a normalization temperature of 2100°F (1149°C) and those achieved on a similar heat treatment with a prolonged (up to 100 hour) subcritical anneal at 1300°F (704°C) designed to coarsen alloy carbides. Three key concepts and one supporting concept were concluded from this study, the first is that a normalization temperature above 2017°F (1103°C) in order to dissolve alloy carbide must be utilized for this steel, the second is that dissolution of carbides as well as coarsening of observed inclusions to increase the spatial distance between inclusions is necessary to improve notch toughness, and the third is that at the high austenitization/normalization temperatures necessary for this steel, homogeneity does not significantly improve mechanical properties. Finally, it was concluded that steel homogeneity is a secondary consideration to casting porosity, cleanliness, and martensitic substructure.

# 1. INTRODUCTION

High strength and high toughness steels, such as those exhibiting yield strength greater than 150 ksi (1034 MPa, ultimate tensile strengths greater than 200 ksi (1379 MPa), and Charpy V-notch (CVN) impact energy greater than 40 ft-lbs (54 J) at -40°F/C, rely on high alloy content to obtain the requisite hardenability to produce a lath martensitic microstructure throughout thick cast sections. Some steels of this nature which are designed for use in both military and commercial aerospace applications are AF1410, HP-9-4-20/30, and Eglin steel. Eglin steel is a low nickel alloy, which relies on additions of chromium, and molybdenum to increase hardenability and additions of vanadium up to 0.1wt% and tungsten up to 1wt% to improve Stage I tempering response. Figure 1 below shows the typical stage I tempered lath martensitic microstructure of cast Eglin steel.

Increased alloy content results in segregation where there are regions that are lean and rich in solute concentration, indicated by light etching regions in Figure 1, and this segregation will promote formation of both nonmetallic inclusions and alloy carbides. Previous work on wrought or forged Eglin steel has suggested that persistent alloy carbides lower the notch impact toughness. To remove these persistent carbides the austenitizing temperatures must be higher than the carbide solvus temperature of the alloy segregated regions. In a study by Webb et al. [8], the carbon content in segregated regions was predicted as high as 0.78wt% and tungsten contents were predicted as high as 1.83wt% for a steel of similar chemistry to Eglin steel. Dissolution of complex $M_{23}C_6$ carbide was predicted to be as high as 2012°F (1100°C). Chemistry of the liquid as a function of temperature for carbide forming elements is shown in Table I.

In general, any feature (carbide, intermetallic, nonmetallic inclusion, or porosity) that appears on a fracture surface must be eliminated by improved melting practice, casting practice or heat treatment to obtain the best ductility and notch toughness for a given steel chemistry. Both nonmetallic inclusions and alloy carbides contribute to void nucleation and fracture by microvoid coalescence, and porosity has been shown to decrease ductility and CVN impact energy [6,7].

Many investigations [1,4,5,23] have been performed to understand the role of heat treatment, steel cleanliness, and the role of persistent alloy carbides such as $M_{23}C_6$, $M_3C$, M(C,N), and $M_6C$ in the notched impact strength of steels of this and similar chemistries. In a study by O'Loughlin et al. [7] a weak correlation between the Charpy V-notch (CVN) energy at -40°F (-40°C) and steel cleanliness was obtained in which nonmetallic inclusion contents below 9 inclusions/ $mm^2$ and inclusion coverage less than 73 $\mu m^2/mm^2$ were reported as necessary in order to obtain CVN energies of at least 15 ft-lbs (20 J) in a similar steel. The same study also evaluated the effect of alloy carbides and found that samples with CVN energies greater than 15 ft-lbs (20 J) were those steels with less than 542 carbides/$mm^2$. It should be noted that the presence of these alloy carbides is dependent upon austenitization temperature and time at temperature prior to quench hardening. Paules et al. [1] and Abrahams et al. [5] reported that high austenitizing temperatures of 1850°F (1010°C) and greater were critical in the heat treatment of Eglin steel to prevent the loss of notch toughness resulting from persistent alloy carbides which were reported to include $M_3C$, M(C,N), and $M_6C$. Dupont et al. [23] also reported similar results with the exception that complex $M_{23}C_6$ carbides were also observed in microstructures of Eglin steel that had received a post weld heat treatment of 1292°F (700°C) for 4 hours; however, it was stated that that formation of $M_{23}C_6$ carbide is not detrimental to toughness.

Segregation of strong carbide forming elements such as chromium, molybdenum, vanadium, and tungsten are of particular importance with respect to carbide stability and these elements have diffusivities that require high temperatures and extended time during normalization to effectively homogenize the steel. As previously shown [8], persistent carbides in segregated regions will be difficult to remove if the austenitization temperature is chosen using the nominal steel composition as shown in Figure 2(a). If the chemistry of the segregated region is within a multiphase region at the austenitization temperature then even the homogenization of the carbon content is impossible until the persistent carbides are dissolved; see Figure 2(b). Carbon content in the two-phase region is fixed by the solvus composition and the flux of carbon out of the two phase region is determined by the dissolution of carbide along the periphery of the segregated region. Carbides near the center of the segregated region coarsen rather than dissolve. Increasing the austenitization temperature to above the solvus temperature of the most segregated region is the only recourse, but this is at the expense of rapid austenite grain growth at the higher temperatures. Again it should be emphasized that these carbides are often associated with void nucleation during fracture and should be eliminated to obtain the best notch and fracture toughness of the high strength steel.

Given the established formation of alloy carbides in this steel and the need to increase austenitization temperature to above the solvus temperature of the most segregated region, one might conclude that increasing the austenitization as high as possible might be the best recourse. However, this may lead to austenite grain growth when the steels are designed for -40°F/C notch toughness by reducing the aluminum content. Prior austenite grain size can be used to increase strength, ductility, and notch toughness through minimization of grain size as well as reduction of the resulting lath martensitic substructure. Controlling the prior austenite grain size is most often

accomplished by aluminum additions to prevent normal grain growth and multiple austenitization treatments to refine the austenite grain size. However, as aluminum is minimized in fracture resistant steels to prevent reduction in toughness due to the formation of angular AlN, heat treatment design is critical in ensuring the dissolution of carbides and inclusions as well as reducing the prior austenite grain size.[7,14,24,25]

Webb et al. [16] reported the design of such a heat treatment which utilized a quench after normalization to form martensite, subsequent tempering of which precipitated $M_{23}C_6$ carbides and these carbides acted as Zener pinning agents to retard normal grain growth during austenitization for quench hardening. The quenched steel demonstrated a finer prior austenite grain size and further improvement in ductility and toughness were also achieved in that study through the refinement of lath martensite sub-structure and increased misorientation of critical components with in that sub-structure.

Porosity is also detrimental to high strength cast steels and studies have shown that hot isostatic pressing (HIP) will improve ductility and CVN impact energy [6,7]. Both studies show that the average yield and ultimate strengths of cast high strength steel are unaffected by HIP, but elongation to failure, reduction in area, and Charpy V-notch energies are increased. O'Laughlin et al. [7] quantified the change in porosity with HIP treatment of (cast or wrought) Eglin steel and showed that as a result of HIP, the porosity as measured by particle coverage was lowered by 88.5% and the average diameter of pores was reduced to below 3 μm, which is approximately twice the size of pores observed in the wrought product. This reduction in porosity produced an increase in elongation to failure from 7% (40.7% reduction in area) to 13.3% (61.3% reduction in area) and improved -40°F (-40°C) CVN energy from 19.7 ft-lbs (26.7J) to 27 ft-lbs (36.6J).

The influence of cleanliness, segregation, persistent carbides, and porosity is extremely difficult to truly differentiate among these steels as each issue influences one or multiple other issues. Previous work by Webb et al. [8] attempted to investigate the role of elevated temperature homogenization on the toughness of cast steel with similar chemistry. The minimum austenitization temperature for homogenization was determined using FactSage version 6.4 thermodynamic software with the FSstel database to determine the solvus temperature for complex $M_{23}C_6$ carbide in the segregated microstructure and assuming the Scheil-Gulliver segregation model. The thermodynamic minimization algorithm predicted that 20 to 25% of the $M_{23}C_6$ carbides contained tungsten and the remainder were $(Cr, Fe)_{23}C_6$. Fluent computational fluid dynamics software was then used to model the casting process using parameters appropriate for both no-bake sand and investment casting of steel. From these studies the local solidification time was determined relative to the casting wall thickness. The secondary dendrite arm spacing was then determined using two different empirical models based upon local solidification time. A computational fluid dynamics model consisting of an assembly of close packed spheres with spacing based on the secondary dendrite arm spacing was then utilized, and diffusivity of Cr, W and Mo were used to calculate a homogenization rate. Tungsten was determined to be the limiting diffusion rate, and the predicted tungsten composition as a function of time for various homogenization temperatures was calculated as shown in Figure 3. Utilizing the minimum austenitization temperature at 2100°F (1149°C) and the calculated homogenization model to predict 90% homogenization at 11 hours, reasonable agreement with the homogenization model was obtained when applied to a one inch wall thickness casting.

Ultimately the presence of dendrite trunks in the microstructure of the specimen with the longest homogenization time provided sufficient evidence to specify a normalization temperature above

2100°F (1149°C) to fully homogenize the carbon content. Alloy homogeneity did not significantly improve either Charpy V-notch energy or dynamic fracture toughness. Normalization at temperatures above 2100°F (1149°C) were reported to promote MnS coarsening as a result of increased MnS solubility and upon cooling the MnS in solution precipitated as a fine dispersion along prior austenite grain boundaries. The steel examined during that study was of similar chemistry and molding process to the current study. However, melting practice was significantly different and as such had high inclusion count, inclusion coverage, and varying amounts of porosity contents, thus the effect of cleanliness, segregation, persistent carbides, and porosity could not be truly differentiated from each other.

The goal of the study presented here was to further the research previously conducted by the authors to examine the role of chemical homogeneity on mechanical properties by applying similar processing techniques and testing of a cast argon, oxygen decarburization (AOD) refined high strength steel of similar chemistry. The effect of inclusion content is expected to be reduced through the refinement of the steel using the AOD process to produce fewer inclusions and inclusion coverage as well as high temperature processing to increase spacing between inclusions. The adverse effect of persistent carbides is expected to be reduced through the use of the high temperature processing. Homogeneity is of particular importance with these steels as a more homogenous steel will lower persistent carbide solvus temperatures, thereby reducing the need for high temperature processing to remove those carbides and as well as prevent austenite grain growth. Additionally increased homogeneity will produce a more uniform distribution of strengthening particles such as epsilon carbide precipitated during the Stage I temper, which will in turn increase ductility.

# 2. EXPERIMENTAL PROCEDURE

The steel for this study was melted in an electric arc furnace, tapped into a transfer ladle and subsequently refined in an Argon, Oxygen, Decarburization (AOD) vessel. After refinement the steel was transferred to a pouring ladle and bottom poured at 2850°F (1566°C) into a sand mold 60in x 60in x 24in as shown in Figure 4(a), with 6 individual cast weld plates measuring 15in x7.5in x2in. Riser and gating removal was conducted by first preheating the casting to a temperature between 200°F (94°C) and 400°F (204°C) and then arc-air cutting. Further preparation of the casting prior to specimen removal was conducted by subcritical annealing at 1200°F (649°C) for 8 hours, and milling off the top .25in (6.4mm) of material directly under risers, in order to remove effects of arc-air cutting, using a vertical mill. Materials for tensile testing were removed using a band saw from a single cast weld plate, and this produced 3 specimens for each condition. Materials for impact testing were removed using a band saw from the same cast weld plate at approximately .75in (19mm) away from the in-gate, then waterjet cut to within +0.0393in (1mm) of the final dimensions to allow 3 specimens each for Dynamic Fracture Toughness (DFT) testing at room temperature and 3 specimens each for Charpy V-Notch (CVN) impact testing at -40°F/C at each condition. Approximate specimen removal location is depicted in Figure 4b.

## 2.1. CHEMICAL ANALYSIS

Melt chemistry was controlled to minimize aluminum content. Carbon content was lower than previous investigations in an effort to improve tensile ductility and low temperature notch toughness. A hybrid chemical analysis is provided in Table II where American Cast Iron Pipe Co. (ACIPCo) provided optical emission spectrometry results for the metallic elements. Carbon and

sulfur were measured using a LECO CS6000; oxygen and nitrogen were measured using a LECO TC 500 by Missouri University of Science & Technology.

## 2.2. HEAT TREATMENT

Test specimens were heat treated using the schedule shown in Table III. Each specimen was triple bagged in treated stainless steel for each normalization heat treatment, and double bagged for each austenitization heat treatment to inhibit decarburization. The minimum normalization temperature for homogenization was determined using FactSage version 6.4 thermodynamic software with the FSstel database to determine the solvus temperature for $M_{23}C_6$, $M_3C$, M(C,N), $M_6C$, and $M_7C_3$ in the segregated microstructure and assuming a Scheil-Gulliver segregation model as discussed in the results section below. Redistribution of carbon and alloy during the normalization hold is expected to lower the carbide solvus temperature, inhibit precipitation of new carbides during subsequent austenitization and hardening, and provide a more uniform distribution of strengthening particles. The length of time for the normalization hold was determined using computational fluid dynamic models to predict secondary dendrite arm spacing and subsequent homogenization times used from previous studies reported by Webb et al. [8]. Hydrogen baking at 600°F (315°C) for 16hrs, was used to remove hydrogen that may cause a phenomena known as hydrogen embrittlement; however, further discussion on this phenomena is not conducted in this paper as it outside the scope of this paper.

In an effort to validate the degree of homogenization obtained, a subcritical heat treatment at 1382°F (750°C) for 100 hours was used on test specimens after mechanical testing to evaluate carbide distribution relative to the normalization temperature and time at 2250°F (1232°C). Alloy carbides form during the subcritical anneal and serve as a proxy for the distribution of Cr,

W, and Mo, in which coarsening of size and a more even distribution is expected with increased homogenization. Alloy carbide distribution was evaluated using an ASPEX SEM with PICA 1020 automated feature analysis software using a step size of 0.2 μm, and a magnification of 750X.

### 2.3. MECHANICAL TEST PROCEDURES

Finish machining of tensile specimens and tensile testing was conducted by Westmoreland Mechanical Testing in accordance with ASTM E8-13 on 1.97in (50mm) gage length and .5in (12.5mm) diameter bars at a strain rate of 0.005 per minute. CVN and DFT bars were ground on each of the four waterjet surfaces to produce a final dimension of 0.39±0.002in (10±0.05mm) using a precision surface grinder. CVN bars were notched in accordance with section 7 of ASTM E23-12 using electrical discharge machining on a Hansvedt DS-2 Wire EDM with 0.01in (0.3mm) copper wire. CVN bars were then fractured in accordance with section 8 of ASTM E23-12 at a temperature of - 40°F/C using a Tinius Olson model 84 Charpy pendulum impact.

Ground DFT bars were notched using a 0.012in (0.31mm) thick diamond-wafering blade and pre-cracked in 3-point bending (R = 0.1) to a total initial crack length ($a_0$) of between 0.18in and 0.22in (4.5mm and 5.5mm) as per ASTM E1820-11, section 7.4.2. Fatigue loading was incrementally reduced during pre-cracking, as per section 7.4.5 of ASTM E1820-11, to avoid large plastic strain fields that might affect measurement of the fracture toughness. Finished DFT bars were fractured at room temperature using a Tinius Olson model 84 Charpy pendulum impact machine outfitted with an MPM instrumented striker. The load vs. displacement data was used to estimate the dynamic fracture toughness ($K_{ID}$) using the single specimen technique developed by Schindler[9]. All specimens behaved in an elastic-fracture manner. The maximum load recorded

during impact was used as $P_Q$ and the crack length, a, was measured after fracture using optical microscopy. The average crack length was determined by using the nine point method described in section 8.5.3 of ASTM E1820-11 with the exception that the original crack length was not heat tinted prior to fracture. The toughness, $K_Q$, was calculated using section A3.5.2 of ASTM E399-08. The reported value of $K_{ID}$ is the calculated value $K_Q$.

## 2.4. INCLUSION ANALYSIS AND MISCELLANEOUS TEST PROCEDURES

Inclusion and porosity measurements using an ASPEX PICA 1020 automated feature analysis SEM was conducted in accordance with method 3 of ASTM E2142-08, and stereological data taken during analysis was computed as defined in Section 12 of ASTM E1245-03. Measurements were made using a combination of scans with the objective of quantifying macroscopic porosity (10 μm to 320 μm), microscopic porosity (<10 μm), and nonmetallic inclusions. Macroscopic measurements were made using a step size of 1.25 μm, and a magnification of 250X, while microscopic measurements were made using a step size of 0.2 μm, and a magnification of 750X. Standardization of fields scanned and area scanned is not required per ASTM E2142-08; however, multiple samples are scanned and included in measurements such that an area 60 $mm^2$ or greater is scanned. Field scanning was conducted using the non-randomized methodology and a nominal scan time of 1 second was used for collecting spectrums during EDS. Post-acquisition analysis rules for the steel using ASPEX PICA 1020 software are documented in Table IV. Etching to reveal microstructure and prior austenite grain size was conducted using Marbles reagent that had been diluted by a 50% volume addition of Glycerin to etch less aggressively. This modified Marbles reagent highlighted prior austenite grain boundaries and the Heyn intercept grain counting method was used to determine the mean intercept length ($L_3$) of the prior austenite grain diameter.

# 3. RESULTS

## 3.1. THEMODYNAMIC MODELING

The minimum normalization temperature for homogenization was determined using FactSage version 6.4 thermodynamic software with the FSstel database to determine solvus temperatures for $M_{23}C_6$, $M_3C$, M(C,N), $M_6C$, and $M_7C_3$ in the segregated microstructure assuming a Scheil-Gulliver segregation model to determine the chemistry of the last 15% of liquid followed by equilibrium cooling from that chemistry. The thermodynamic minimization algorithm predicts that 20 to 25% of the carbides contain tungsten and molybdenum, while the remainder are rich in iron and chromium. Carbides of the type $M_{23}C_6$, MC, $M_3C_2$ and $M_7C_3$ were predicted to be present in the interdendritic regions while type M6C was not. Complete dissolution of the interdendritic carbides was predicted to occur at 2010°F (1099°C) as shown in Figure 5; subsequent solvus temperatures for the remaining carbide types are shown below in Table V. Solvus temperatures for carbides utilizing an equilibrium solidification model from the nominal chemistry are predicted at much lower temperatures and are also provided in Table V. It should be noted that $M_6C$ is predicted to form and $M_3C_2$ is not utilizing the equilibrium model, whereas the opposite is predicted to form utilizing the Scheil-Gulliver model.

## 3.2. CARBIDE EFFECTS

Prior to investigating the effect of homogeneity, the authors found it reasonable to truly establish the effect of persistent carbides in this specific steel as Paules et al., Dupont et al., Abrahams et al., O'loughlin et al., and Webb et al. [1,5,7,8,23] have all reported that segregation in this type of steel leads to the formation of persistent carbides of different types, and each of the results indicate removal is necessary to increase toughness. In an effort to establish this effect, a

modification to the baseline heat treatment was made as shown in Table VI, with the intent of growing massive carbides prior to austenitization and then varying austenitization temperatures to dissolve these massive carbides.

### 3.2.1 MICROSTRUCTURAL CHARACTERIZATION

Optical micrographs of the cast steel after receiving the baseline heat treatment and the carbide growth heat treatment for 50 hours followed by a 1900°F (1038°C) austenitization are shown in Figure 6. Some segregation as noted by light etching of interdendritic regions is evident in both optical images. A prior austenite grain size of 51 ± 10 μm was measured for Figure 6(a), which received the baseline heat treatment, and a similar prior austenite grain size was measured at 60 ± 13 μm for Figure 6(b), which received the carbide growth heat treatment. The reported uncertainty ($\Delta L_3$) is at a 95% confidence level in Table VII, for all heat treatments of this study.

Carbide distribution, as determined using a scanning electron microscope equipped with automated feature analysis software is presented in Figure 7(a) for a tensile bar that received the carbide growth heat treatment for 100 hours followed by a 1800°F (982°C) austenitization, and in Figure 7(b) for a tensile bar that received the carbide growth heat treatment for 50 hours followed by a 1900°F (1038°C) austenitization. Individual red dots within Figure 7 represent location of carbide within the scan but not size. It would seem logical at this point to compare carbide distribution in the baseline heat treatment to that with the longest carbide growth time, as well as the lowest austenitization temperature lending to largest growth and least dissolution of carbide; however, a scan of the baseline heat treatment using the same technique yields no carbide detection, as the heat treatment is designed, and thus would yield a blank scan to compare to. Furthermore, the major objective of this study is to understand the effect of carbides on toughness

and ductility in this steel, therefore the carbide distribution with the lowest toughness and ductility, Figure 7(a), is compared to that with the highest toughness and ductility, Figure 7(b). The distribution of Cr, Mo, and W for scanned carbides with in Figure 7(a) is shown in Figure 8 and indicates the presence of multiple carbide types.

### 3.2.2 INCLUSION ANALYSIS

Inclusion and porosity measurement results for 26 scans of the same material with small variations of the baseline heat treatment are shown in Figure 9, error bars shown are 68%CL for all inclusions and numerically listed at 95%CL for porosity. The dominant inclusion types though out all heat treatments were $Al_2O_3$, MnS and complex $MnO\text{-}Al_2O_3\text{-}SiO_2$ with varying amounts of porosity between the tensile bars. Inclusion and porosity measurement results for each of the carbide aged tensile bars are shown in Figure 10 compared to the average baseline measurements from Figure 9, particle count appears to be higher in the aged material; however, particle coverage appears to be the same with the exception of the specimen aged for 100 hours and then austenitized at 1800°F (982°C) which has both higher count and coverage. Individual measurements for tensile bars of each condition are also listed in Table VIII and Table IX.

### 3.2.3 MECHANICAL TEST RESULTS

Test results shown in Table X indicate a 1-2% improvement in ultimate tensile strength and yield strength, with an approximate tensile strength of 231 ksi (1593 MPa), and yield strength of 180 ksi (1241 MPa), compared to the baseline heat treatment with an average tensile strength of 230 ksi (1586 MPa), average yield strength of 176 ksi (1214 MPa). However, a large increase in reduction in area up to 37%, and elongation up to 11%, compared to the baseline heat treatment with an average reduction in area of 21%, and an average elongation of 8% was observed, and is

shown in Figure 11. CVN impact energy, shown in Table XI, dramatically dropped from 40 ft-lbs (54 J) for the baseline heat treatment to as low as 8 ft-lbs (11 J) for the carbide aged steel, and average Dynamic Fracture Toughness, Table XII, showed a similar trend dropping from 110 MPa√m (100 ksi√in) to as low as 56 MPa√m (51 ksi√in).

### 3.2.4 FRACTOGRAPHY

Fractography was performed on the tensile bars for both the baseline heat treatment and carbide aged heat treatments. Figure 12(a) shows an image of one of the baseline fractured tensile bars showing a plateau fracture feature that was associated with porosity and Figure 12(b) shows the same features in one of the fractured tensile bars with the 100 hour carbide aging and 1800°F heat treatment, similar features were found thorough out all tensile bars. Fracture by mircovoid coalescence was observed elsewhere on the fracture surface as shown in Figure 13 for the same tensile bars. It can be seen in in Figure 13(b) with the carbide aging that multiple carbides and inclusions are centered within microvoid dimples where Figure 13(a) with the baseline heat treatment does not have the same features. Figure 14 shows an image of one of these features with in the carbide aged material and Table XIII gives the composition of the feature from Figure 14, as taken from Energy Dispersive X-Ray Spectrometry, confirming the presence of carbide with in microvoids.

## 3.3. HOMOGENIZATION

### 3.3.1 MICROSTRUCTURAL CHARACTERIZATION

Optical micrographs of the cast steel after receiving the baseline heat treatment and the homogenization heat treatment are shown in Figures 15 and 16. Some segregation as noted by light etching of interdendritic regions is evident in the optical images for the baseline, 2 hour, and

4 hour heat treatments; however, the 6 hour and 11 hour heat treatment appear chemically homogeneous. The reported uncertainty ($\Delta L_3$) is at a 95% confidence level in Table XIV. A prior austenite grain size of 51 ± 10 μm was measured for Figure 15, which received the baseline heat treatment, and an increase in prior austenite grain size was measured with increasing homogenization time. Increases in prior austenite grain size may account for decreases in dynamic fracture toughness measurements reported due to increased martensitic substructure controlled by prior austenite grain size.

Although it appears optically that homogeneity has been achieved, a second evaluation of the degree of homogeneity is shown in Figure 17 where carbide distribution, as determined using a scanning electron microscope equipped with automated feature analysis software is presented. Individual red dots within Figure 17 represent location of carbide within the scan but not size. Although homogenization is seen at longer times with the dissolution of secondary dendrite arms, dendrite trunks are still present in Figure 17(d) and indicate full homogeneity was not reached. Figure 18 shows the carbide distribution relative to the elements Cr, W, and Mo and indicates the scanned carbides are rich in all three elements.

### 3.3.2 INCLUSION ANALYSIS

Inclusion and porosity measurement results for each of the homogenization tensile bars are shown in Figure 19 compared to the average baseline measurements from Figure 9, particle count appears to be slightly less with increased homogenization time; however, particle coverage does not appear to change indicating greater spacing of larger particles with increased homogenization

time. Individual inclusion measurements for tensile bars are also listed in Table XV and Table XVI below.

### 3.3.3 MECHANICAL TEST RESULTS

Test results shown in Table XVII and Figure 20 indicate a 1-2% improvement in all tensile mechanical properties with increasing homogenization time with an approximate tensile strength of 233 ksi (1606 MPa), yield strength of 179 ksi (1234 MPa), reduction in area of 26%, and elongation of 9%, compared to the baseline heat treatment with an average tensile strength of 230 ksi, average yield strength of 176 ksi, average reduction in area of 21%, and an average elongation of 8%. CVN impact energy remained unchanged at approximately 40 ft-lbs (54 J), and average Dynamic Fracture Toughness of 110 MPa$\sqrt{m}$ (100 ksi$\sqrt{in}$) slightly decreased to approximately 95 MPa$\sqrt{m}$ (87 ksi$\sqrt{in}$). Coarsening of prior austenite grains at elevated temperature resulting in larger martensitic substructure may account for the decrease in DFT values. Mechanical test results for individual specimens are given below in Tables XVII, XVII, and XIX, and are shown graphically in Figures 20 through 21. Tensile bars 2 and 3 from the heat treatment for 11 hours at 2250°F (1232°C) exhibited signs of quench cracking prior to tensile testing lending to the decrease in mechanical properties listed in Table XVII. Values shown in Figure 20 are representative of all tested values; however, trend lines are taken through tensile bar 1 of the 11 hour group as it did not exhibit signs of quench cracking and is likely a more valid interpretation of the results.

### 3.3.4 FRACTOGRAPHY

Fractography was performed on the tensile bars for both the baseline heat treatment and the homogenization heat treatment. Figure 22(a) shows an image of one of the fractured tensile bars

showing a plateau fracture feature, indicated by an arrow, which was associated with porosity greater than 5μm in diameter. Similar features were found throughout all tensile bars tested, and thus may be discounted as providing significant difference between specimens receiving either heat treatment. However, changes in fracture type around each of the features indicate a significant influence on fracture, which maybe expected with porosity of this size. Cleavage fracture of the lath martensite microstructure is also shown in Figure 22(b), which is typical of hydrogen damage or notch induced fracture in high strength steels. Fracture by mircovoid coalescence was observed elsewhere on the fracture surface as shown in Figure 23. No significant differences in fractography of the baseline and homogenized specimens were observed.

# 4. DISCUSSION

Thermodynamic modeling indicates segregation will occur regardless of using an equilibrium or Scheil-Gulliver solidification model used, as shown by Webb et al. [8] However, two distinct points of interest may be open for discussion when interpreting the given solidification results, predicted carbon content and carbide type. Predicted carbon content, which directly influences carbide formation [7], is significantly different in both the equilibrium solidification model and the Scheil-Gulliver solidification model [8,19]. It has been shown by Schafnitt et al. [19] that carbon solubility is affected with variation of fast diffusion elements within the solid phase; however, favorable results have been obtained using a Scheil-Gulliver solidification model through numerous studies. [8,18,19,20,21]. It may be argued that over estimation of the carbon content in segregated regions may have occurred; however, it could be further argued by the favorable results which led to the very development of the Scheil-Gulliver model that equilibrium or even more so nominal carbon content underestimates the carbon content in segregated regions where alloy carbides form. Furthermore it is clear by the results of this study alone that utilization of both the equilibrium model and the Scheil-Gulliver model leads to the prediction of different carbide types, and thus different solvus temperatures. Of particular note in the prediction of carbide type is that $M_6C$ is predicted to form and $M_3C_2$ is not utilizing the equilibrium model, whereas the opposite is predicted to form utilizing the Scheil-Gulliver model. A possible explanation for the lower solvus temperatures predicted by the equilibrium model might be that one of the major elemental constituents in the predicted $M_6C$ to form is tungsten which may take solute away from that available to form the predicted MC carbide which has the highest solvus temperature in both models. Discussion may also be necessary with respect to carbide type as the previous study by the authors considered the dissolution of complex $M_{23}C_6$ as opposed to MC carbide. Although MC carbide is predicted to have the highest solvus temperature in both models,

complex $M_{23}C_6$ is the largest contributor to Figure 5 with respect to weight percent, lending to longer dissolution times or higher temperatures to dissolve carbides of this type. The single most important prediction made by the thermodynamic results of this study is the necessity of a temperature above 2017°F (1103°C) in order to dissolve alloy carbide.

The effect of carbides on the ductility and toughness in this steel was of particular importance to the authors, to understand if gains in ductility and toughness were possible, and furthermore if elevated temperature homogenization is even necessary. It can be clearly identified through both CVN results, as well as DFT results, that the presence of carbides significantly drops toughness. Given the drop in toughness with carbides present compared to the baseline heat treatment in which carbides are not present, as shown in Figure 13, the elimination of carbides is imperative to increase toughness. It may further be concluded that regardless of the amount of carbide present, for example Figure 7(a) and (b), a significant drop in toughness is still experienced. The amount and size of the carbides present in the carbide aged material was expected to increase with time at 1300°F (704°C). Although size and type quantification may be more accurately obtained utilizing other methods, a general approximation of carbide size and type maybe taken from results given using the ASPEX pica 1020 SEM with automated feature analysis. Figure 24 indicates an increase in size and area fraction, as expected with the carbide aging treatment, and after 50 hours a maximum in size and coverage is achieved. It is therefore reasonable to expect that carbide size and density are relatively similar in both the 50 and 100 hour aging treatment. Comparison of Figure 7 (a) and (b) clearly indicates a significant drop in remaining alloy carbide, and it is reasonable to assume that if the steel is homogeneous, a higher austenitization temperature of 1900°F (1038°F) would dissolve all carbides within this same steel if the intermediate temper stage was not prolonged to specifically grow them. This theory may further be supported in a

comparison of the baseline heat treatment in which carbides are not found. Although toughness is severely impacted, the significant increase in ductility, as noted by 37% reduction in area and 11% elongation, is also necessary to be addressed. Carbide formation and subsequent growth, as noted previously in this discussion, is significantly impacted by carbon content. Carbon within the matrix is the only source from which carbides may form, and thus a decrease in matrix carbon would result in an increase in ductility. Support for this theory may also be seen in a drop in hardness of 5 HRC, also associated with carbon depletion, which is most apparent in the 100 hour carbide aged material. Although carbide effect was the specific focus during this portion of the study, it should be noted that during elemental analysis of materials within microvoid dimples, multiple inclusions of types listed in Table VIII were also found. Dissolution of carbides as well as these inclusions is necessary in notch toughness improvement.

With the establishment of the need to eliminate alloy carbide presence in order to increase toughness the role of homogeneity can now be truly discussed relative to dissolution of carbides as well in the investigation of ductility and toughness increases. Optical micrographs shown in Figure 16 indicate homogenization was achieved in that banding and light etching areas are no longer present; however, Figure 17 clearly shows the presence of dendrite trunks and even the presence of secondary dendrite arms. One might argue then that either modeling is incorrect or that heat treatment was not conducted properly thus not achieving homogenization. Homogenization modeling, as conducted by the authors, has two main components in determining the proper time and temperature to achieve homogenization, they are secondary dendrite arm spacing and solvus temperature of alloy carbides. Solvus temperature of carbides has been discussed in depth thus far and establishment of the 2100°F (1149°C) minimum should be clear; however, temperatures above this minimum should be evaluated in terms of

homogenization and balanced with reasonable industrial practices. Secondary dendrite arm spacing (SDAS) is of key concern as it establishes the distance across which solute must travel to complete homogenization, and furthermore, SDAS is directly related to solidification time which may be effected through mold properties such as mold medium and geometry. A thorough discussion on this relationship can be found through numerous historical documents such as that of Askeland and Wright [22]. The clear presence of secondary dendrite arms in Figure 17 allows a key opportunity to check validation of the homogenization model, and further establish reasoning behind the lack of homogeneity seen in this experiment. A quick measurement of SDAS in Figure 17(a) utilizing standard measurement techniques yields an approximate SDAS of 146μm, comparison of which to initial studies by Webb et al. [8] show an increase to approximately double the SDAS used in the original calculation of the homogenization model. Similar mold material was used in the production of the castings from this and the previous study thus eliminating effects from mold medium; however, mold geometry is somewhat different in that a thicker mold wall was utilized in the current study thus lending to longer solidification time and thus larger SDAS, which shows good agreement with the measured SDAS. As noted, SDAS establishes the distance across which solute must travel to complete homogenization, thus the effect of increased SDAS on homogenization would be an increase in time at the same temperature in order to achieve full homogenization. Therefore application of the homogenization model used in this study would suggest that a decrease in homogenization should be expected, as seen, since the 11 hour time at temperature was maintained, which would approximate 4 to 6 hours of homogenization in the original model. It may further be concluded that modeling and subsequent heat treatment results are accurate.

In light of the mechanical properties obtained in this study, further discussion as it relates to increases in those properties is warranted. It is generally accepted that increases in mechanical properties are expected with an increase in homogeneity. The slight increase of 1-2% in tensile properties is to be expected with a material that has received some homogenization; however, decreases in CVN and DFT are not expected. A possible explanation for these decreases might be seen in the work of Richie [13], who reports that the fracture toughness of 4340 steel increases and the CVN impact energy decreases with increasing austenitizing temperature (see Figure 25). Richie explains this divergent behavior between fracture toughness, either $K_{IC}$ or $K_{ID}$, and CVN impact energy with increasing austenitization temperature in terms of the notch acuity. For measures of fracture toughness, the sharp notch created by fatigue cracking has a plastic process zone comparable to the lath martensite bundle size and the tempered microstructure would control the ductile fracture. Cleavage fracture is controlled by the crystallographic misorientation of adjacent lath bundles. An increase in fracture toughness might be expected when the scale of these lath bundles are greater than the plastic process zone of the notch, which would be encouraged by grain growth at higher austenitizing temperatures. Grain growth from the baseline heat treatment to the homogenized heat treatment is clearly shown in Table XIV, in which it may be expected that increases in fracture toughness would be expected; however, Richie also indicates that a drop in fracture toughness is expected with increasing austenitization temperature above 2012°F (1100°C). Therefore, the observed drop in toughness might be explained by the baseline heat treatment being austenitized at a lower temperature than the homogenized heat treatment. A similar explanation might also be offered to explain the differences in CVN, in that Richie reports only a slight increase in CVN with increasing austenitization temperature above 2012°F (1100°C), while a decrease in CVN was observed for increasing austenitization below 2012°F (1100°C).

It seems reasonable that either grain size effects at such high temperatures may begin to play a role, or more importantly that statistically there is no change at these elevated temperatures. Certainly the statistical argument can be made for the present study.

# 5. CONCLUSIONS

Three key concepts and one supporting concept were concluded from this study, the first is that a normalization temperature above 2017°F (1103°C) in order to dissolve alloy carbide must be utilized, the second is that dissolution of carbides as well as coarsening of inclusions to increase the spatial distance between inclusions is necessary to improve notch toughness, and the third is that at the high austenitization/normalization temperatures necessary for this steel, homogeneity does not significantly improve mechanical properties. Finally, it was concluded that steel homogeneity is a secondary consideration to casting porosity, cleanliness, and martensitic substructure.

## 6. ACKNOWLEDGEMENTS

This work has been supported under the Steel Founders' Society of America (SFSA) program on Casting and Advanced Steel Technology that has been funded by the Army Research Laboratory under the provisions of cooperative agreement W911NF-12-2-0033. The authors are grateful for steel castings supplied by Bradken-Atlas LP., and for optical emission spectroscopy results provided by Mr. Don Denney at American Cast Iron Pipe Co. (ACIPCo). The authors also gratefully acknowledge the Army Research Office Defense University Research Instrumentation Program (award number W911NF-08-1-0267) for financial support in buying the ASPEX-PICA 1020 SEM that was used for automated feature analysis.

## TABLES AND FIGURES

Table I- Scheil-Gulliver segregation model prediction of liquid composition with solidification, taken from Webb et al. [8]

| Temperature | Liquid % | C wt.% | Cr wt.% | W wt.% | Mo wt.% | V wt.% |
|---|---|---|---|---|---|---|
| **2732°F (1500°C)** | 100 | 0.27 | 2.60 | 1.00 | 0.40 | 0.10 |
| **2696°F (1480°C)** | 100 | 0.27 | 2.60 | 1.00 | 0.40 | 0.10 |
| **2678°F (1470°C)** | 76 | 0.34 | 2.67 | 1.06 | 0.44 | 0.11 |
| **2660°F (1460°C)** | 55 | 0.42 | 2.76 | 1.20 | 0.50 | 0.12 |
| **2624°F (1440°C)** | 32 | 0.60 | 2.95 | 1.50 | 0.66 | 0.16 |
| **2588°F (1420°C)** | 21 | 0.78 | 3.11 | 1.83 | 0.81 | 0.20 |

Table II- Chemical analysis for high strength steel.

| Element (wt%) | C | Mn | Si | Cr | Ni | Mo | W | V | Cu | P | S | Ca | N | Al | O | Fe |
|---|---|---|---|---|---|---|---|---|---|---|---|---|---|---|---|---|
| **High Strength Steel** | 0.25 | 0.77 | 0.88 | 2.64 | 1.03 | 0.425 | 0.92 | 0.097 | 0.12 | 0.006 | 0.004 | - | 0.009 | 0.008 | 0.022 | BAL. |

Table III- Heat treatment schedule for homogenization study.

| Sample designation | Hydrogen Bake | Normalization | Intermediate Tempering | Austenitization | Tempering |
|---|---|---|---|---|---|
| **Baseline** | 16 hrs. at 600°F (315°C) | 4 hrs. at 2100°F (1149°C) | 4 hrs. at 1200°F (649°C) | 1 hr. at 1900°F (1038°C) | 4 hrs. at 375°F (191°C) |
| **2 hrs. at 2250°F** | 16 hrs. at 600°F (315°C) | 2 hrs. at 2250°F (1232°C) | 4 hrs. at 1200°F (649°C) | 1 hr. at 1900°F (1038°C) | 4 hrs. at 375°F (191°C) |
| **4 hrs. at 2250°F** | 16 hrs. at 600°F (315°C) | 4 hrs. at 2250°F (1232°C) | 4 hrs. at 1200°F (649°C) | 1 hr. at 1900°F (1038°C) | 4 hrs. at 375°F (191°C) |
| **6 hrs. at 2250°F** | 16 hrs. at 600°F (315°C) | 6 hrs. at 2250°F (1232°C) | 4 hrs. at 1200°F (649°C) | 1 hr. at 1900°F (1038°C) | 4 hrs. at 375°F (191°C) |
| **11 hrs. at 2250°F** | 16 hrs. at 600°F (315°C) | 11 hrs. at 2250°F (1232°C) | 4 hrs. at 1200°F (649°C) | 1 hr. at 1900°F (1038°C) | 4 hrs. at 375°F (191°C) |

Table IV- Post-acquisition analysis rules for inclusion and porosity analysis in Eglin Steel.

| Inclusion designation | Fe | Mn | S | Ca | C | Al | Si | Ti |
|---|---|---|---|---|---|---|---|---|
| **Porosity** | >= 80 | | | | | | | |
| **MnS** | | >30 | >15 | <20 | <10 | | | |
| **CaS** | | <20 | >20 | >30 | <10 | | | |
| **MnS-CaS** | | >15 | >20 | >15 | <10 | | | |
| **CaAL2O4** | | <20 | <20 | >15 | <10 | >20 | <20 | |
| **MnSiO3** | | >20 | <20 | <20 | <10 | <20 | >10 | |
| **MnAlSiO** | | >20 | <20 | <20 | <10 | >18 | >10 | |
| **CaSiO3** | | <20 | <20 | >20 | <10 | <20 | >10 | |
| **MnO-Al2O3** | | >25 | <20 | <20 | <10 | >25 | <20 | |
| **CaO-MnO** | | >25 | <20 | >25 | <10 | <20 | <20 | |
| **Complex (MnO-Al2O3-SiO2)** | | | | | <10 | >2 | >2 | |
| **Al2O3** | | | | | <10 | >25 | | |
| **MnO-Al2O3** | | >30 | <20 | | <10 | | | |
| **CaO** | | | <20 | >30 | <10 | | | |
| **TiN** | | | | | <10 | | | >40 |
| **Other Oxides** | | | <10 | | <10 | | | |
| **Other Oxisulfides** | | | >5 % <10 | | <10 | | | |
| **Other Sulfides** | | | >10 | | <10 | | | |
| **Unclassified** | | | | | <10 | | | |
| **Porosity with Diamond Paste** | | | | | >=40 | | | |

Table V- Solvus temperatures for interdendritic carbides predicted using both a Scheil-Gulliver segregation model and an equilibrium cooling model.

| Carbide Type | Scheil-Gulliver Solvus Temperature | Equilibrium Solvus Temperature | Major Chemical Constituents |
|---|---|---|---|
| **MC** | 2017°F (1103°C) | 1487°F (808°C) | W, Mo, C |
| **$M_7C_3$** | 2007°F (1097°C) | 1367°F (742°C) | Cr, Fe |
| **$M_{23}C_6$** | 1931°F (1055°C) | 1640°F (893°C) | Fe, Cr |
| **$M_6C$** | N/A | 1563°F (851°C) | W, Fe |
| **$M_3C_2$** | 779°F (415°C) | N/A | Cr, C |

Table VI- Heat treatment schedule for carbide effects study.

| Sample designation | Hydrogen Bake | Normalization | Intermediate Tempering | Austenitization | Tempering |
|---|---|---|---|---|---|
| **Baseline** | 16 hrs. at 600°F (315°C) | 4 hrs. at 2100°F (1149°C) | 4 hrs. at 1200°F (649°C) | 1 hr. at 1900°F (1038°C) | 4 hrs. at 375°F (191°C) |
| **Carbide 18-50** | 16 hrs. at 600°F (315°C) | 4 hrs. at 2100°F (1149°C) | 4 hrs at 1200°F/ 50 hrs at 1300°F (704°C) | 1 hr. at 1800°F (982°C) | 4 hrs. at 375°F (191°C) |
| **Carbide 18-100** | 16 hrs. at 600°F (315°C) | 4 hrs. at 2100°F (1149°C) | 4 hrs at 1200°F/ 50 hrs at 1300°F (704°C) | 1 hr. at 1800°F (982°C) | 4 hrs. at 375°F (191°C) |
| **Carbide 19-50** | 16 hrs. at 600°F (315°C) | 4 hrs. at 2100°F (1149°C) | 4 hrs at 1200°F/ 50 hrs at 1300°F (704°C) | 1 hr. at 1900°F (1038°C) | 4 hrs. at 375°F (191°C) |
| **Carbide 19-100** | 16 hrs. at 600°F (315°C) | 4 hrs. at 2100°F (1149°C) | 4 hrs at 1200°F/ 50 hrs at 1300°F (704°C) | 1 hr. at 1900°F (1038°C) | 4 hrs. at 375°F (191°C) |

Table VII- Prior Austenite Grain size measurements of tensile bars with varying homogenization times at 2250°F (1232°C).

| | Prior Austenite Grain Size (μm) ± 95%CL | Hardness HRC±95%CL |
|---|---|---|
| **Baseline** | 51 ± 10 | 46 ± 0.3 |
| **Carbide 18-50** | 62 ± 13 | 47 ± 1.9 |
| **Carbide 18-100** | 64 ± 14 | 46 ± 1.8 |
| **Carbide 19-50** | 60 ± 13 | 45 ± 5.6 |
| **Carbide 19-100** | 62 ± 13 | 44 ± 1.8 |

Table VIII- Porosity and inclusion density (#/mm) and spacing (μm) for varying amounts of carbide aging time and varying austenitization temperature.

| Inclusion Type/ Measurement | Baseline | Carbide 18-50 | Carbide 18-100 | Carbide 19-50 | Carbide 19-100 |
|---|---|---|---|---|---|
| **Al2O3 (#/mm)** | 3.61 | 3.94 | 4.09 | 4.02 | 4.86 |
| **MnO-Al203** | 0.64 | 0.72 | 0.27 | 0.65 | 0.90 |
| **MnSi03** | 0.01 | 0.00 | 0.00 | 0.00 | 0.00 |
| **Other Inclusions** | 0.01 | 0.00 | 0.00 | 0.00 | 0.00 |
| **MnO-Al2O3-SiO2 (complex)** | 0.81 | 1.06 | 0.96 | 0.92 | 0.83 |
| **CaAl2O4** | 0.07 | 0.08 | 0.12 | 0.00 | 0.10 |
| **MnO** | 0.03 | 0.00 | 0.04 | 0.08 | 0.00 |
| **MnS** | 3.51 | 4.62 | 2.67 | 5.84 | 3.74 |
| **TiN** | 0.00 | 0.00 | 0.00 | 0.00 | 0.00 |
| **Porosity** | 76.97 | 100.48 | 204.20 | 114.01 | 99.26 |
| **Spacing (μm)** | 49.07 | 34.48 | 34.22 | 38.97 | 40.72 |

Table IX- Porosity and inclusion area fraction (μm2/mm2) for varying amounts of carbide aging time and varying austenitization temperature.

| Inclusion Type/ Measurement | Baseline | Carbide 18-50 | Carbide 18-100 | Carbide 19-50 | Carbide 19-100 |
|---|---|---|---|---|---|
| **Al2O3** | 52.56 | 43.28 | 52.50 | 42.96 | 39.06 |
| **MnO-Al203** | 1.13 | 0.81 | 0.65 | 1.03 | 0.78 |
| **MnSi03** | 0.88 | 0.00 | 0.00 | 0.00 | 0.00 |
| **Other Inclusions** | 0.10 | 0.00 | 0.00 | 0.00 | 0.00 |
| **MnO-Al2O3-SiO2 (complex)** | 21.62 | 12.07 | 9.15 | 14.26 | 9.50 |
| **CaAl2O4** | 3.20 | 1.62 | 3.47 | 0.00 | 1.05 |
| **MnO** | 0.15 | 0.00 | 0.02 | 0.05 | 0.00 |
| **MnS** | 6.71 | 5.32 | 4.61 | 5.44 | 2.92 |
| **TiN** | 0.00 | 0.00 | 0.00 | 0.00 | 0.00 |
| **Porosity** | 1129.17 | 1140.61 | 2877.27 | 961.31 | 1058.26 |

Table X- Mechanical test results of high strength steel for varying amounts of carbide aging time and varying austenitization temperature.

| Condition | Bar | UTS (ksi) | Condition Average | .2% YS (ksi) | Condition Average | Reduction in Area (%) | Condition Average | Elongation (%) | Condition Average |
|---|---|---|---|---|---|---|---|---|---|
| **Baseline** | 1 | 229 | 230 ± 0.82 | 175 | 176 ± 0.90 | 16.0 | 21 ± 10 | 7.5 | 8.3 ± 2.4 |
| | 2 | 230 | | 177 | | 33.0 | | 11.0 | |
| | 3 | 230 | | 176 | | 15.0 | | 6.5 | |
| **Carbide 18-50** | 1 | 231.1 | 232.00±3.42 | 179.10 | 179.37±4.42 | 23.00 | 27.00±15.51 | 8.50 | 9.50±3.73 |
| | 2 | 232.6 | | 178.50 | | 30.00 | | 10.00 | |
| | 3 | 232.3 | | 180.50 | | 28.00 | | 10.00 | |
| **Carbide 18-100** | 1 | 230.5 | 231.77±8.00 | 181.30 | 181.53±8.86 | 15.00 | 19.00±19.72 | 6.50 | 7.17±3.29 |
| | 2 | 230.9 | | 179.60 | | 18.00 | | 7.00 | |
| | 3 | 233.9 | | 183.70 | | 24.00 | | 8.00 | |
| **Carbide 19-50** | 1 | 230.7 | 229.83±3.66 | 177.10 | 176.83±2.77 | 42.00 | 37.00±21.52 | 12.00 | 11.00±4.30 |
| | 2 | 229.0 | | 176.10 | | 37.00 | | 11.00 | |
| | 3 | 229.8 | | 177.30 | | 32.00 | | 10.00 | |
| **Carbide 19-100** | 1 | 234.4 | 232.97±5.68 | 181.60 | 179.87±6.47 | 41.00 | 35.67±21.66 | 13.00 | 11.33±6.57 |
| | 2 | 232.7 | | 179.10 | | 35.00 | | 11.00 | |
| | 3 | 231.8 | | 178.90 | | 31.00 | | 10.00 | |

Table XI- Charpy V-notch impact energies (-40°F) for high strength steel for varying amounts of carbide aging time and varying austenitization temperature.

| | CVN min ft-lb (J) | CVN max ft-lb (J) | Average ±68%CL | Hardness HRC±95%CL |
|---|---|---|---|---|
| **Baseline** | 35 (48) | 43 (58) | 40 ± 3.0 (55 ± 4.0) | 49 ± 1.7 |
| **Carbide 18-50** | 7.47 (10.12) | 11.47 (15.55) | 9.65 ± 8.72 (13.09 ± 11.83) | 47 ± 1.9 |
| **Carbide 18-100** | 7.09 (9.61) | 8.01 (10.86) | 7.68 ± 2.23 (10.42 ± 3.02) | 46 ± 1.8 |
| **Carbide 19-50** | 8.83 (11.97) | 14.32 (19.41) | 12.13 ± 12.53 (16.45 ± 16.99) | 45 ± 5.6 |
| **Carbide 19-100** | 6.98 (9.46) | 9.59 (13.00) | 8.08 ± 5.82 (10.96 ± 7.89) | 44 ± 1.8 |

Table XII- Dynamic Fracture Toughness at RT for high strength steel for varying amounts of carbide aging time and varying austenitization temperature.

| | DFT min $K_{ID}$ MPa√m | DFT max $K_{ID}$ MPa√m | Average ±68%CL | Hardness HRC±95%CL |
|---|---|---|---|---|
| **Baseline** | 106 | 117 | 110 ± 4.8 | 46 ± 0.3 |
| **Carbide 18-50** | 56 | 61 | 56 ± 2.5 | 48 ± 0.8 |
| **Carbide 18-100** | 55 | 60 | 59 ± 2.6 | 45 ± 5.4 |
| **Carbide 19-50** | 55 | 67 | 61 ± 4.8 | 48 ± 1.3 |
| **Carbide 19-100** | 55 | 64 | 60 ± 3.8 | 44 ± 2.2 |

Table XIII- Compositional results from Energy Dispersive X-ray Spectroscopy for alloy carbide present in microvoids of tensile bar aged for 100 hours at 1300°F (704°C) and then austenitized at 1800°F (982°C).

| Element | Wt % | At % |
|---|---|---|
| **C** | 10.46 | 37.75 |
| **Mo** | 3.54 | 1.6 |
| **V** | 0.75 | 0.64 |
| **Cr** | 17.31 | 14.43 |
| **Fe** | 54.69 | 42.45 |
| **W** | 13.24 | 3.12 |
| **Total** | 100 | 100 |

Table XIV- Prior Austenite Grain size measurements of tensile bars with varying homogenization times at 2250°F (1232°C).

| | Prior Austenite Grain Size (μm) ± 95%CL | Hardness HRC±95%CL |
|---|---|---|
| **Baseline** | 51 ± 10 | 46 ± 0.3 |
| **2 hour** | 76 ± 13 | 47 ± 0.3 |
| **4 hour** | 82 ± 14 | 46 ± 0.3 |
| **6 hour** | 89 ± 16 | 47 ± 0.5 |
| **11 hour** | 86 ± 15 | 47 ± 0.5 |

Table XV- Porosity and inclusion density (#/mm) and spacing (μm) for varying amounts of homogenization time.

| Inclusion Type/ Measurement | Baseline | 2 hour | 4 hour | 6 hour | 11 hour |
|---|---|---|---|---|---|
| **Al2O3 (#/mm)** | 3.61 | 3.22 | 3.10 | 2.94 | 2.02 |
| **MnO-Al203** | 0.64 | 0.07 | 0.05 | 0.00 | 0.00 |
| **MnSi03** | 0.01 | 0.00 | 0.00 | 0.00 | 0.00 |
| **Other Inclusions** | 0.01 | 0.00 | 0.05 | 0.04 | 0.04 |
| **MnO-Al2O3-SiO2 (complex)** | 0.81 | 0.68 | 1.13 | 0.87 | 0.74 |
| **CaAl2O4** | 0.07 | 0.07 | 0.21 | 0.12 | 0.08 |
| **MnO** | 0.03 | 0.00 | 0.00 | 0.04 | 0.00 |
| **MnS** | 3.51 | 0.20 | 0.09 | 0.04 | 0.00 |
| **TiN** | 0.00 | 0.00 | 0.00 | 0.00 | 0.04 |
| **Porosity** | 76.97 | 31.90 | 135.62 | 41.28 | 65.50 |
| **Spacing (μm)** | 49.07 | 66.89 | 25.17 | 68.86 | 48.54 |

Table XVI- Porosity and inclusion area fraction ($\mu m^2/mm^2$) for varying amounts of homogenization time.

| Inclusion Type/ Measurement | Baseline | 2 hour | 4 hour | 6 hour | 11 hour |
|---|---|---|---|---|---|
| **Al2O3** | 52.56 | 62.12 | 53.76 | 38.90 | 51.89 |
| **MnO-Al203** | 1.13 | 0.41 | 0.12 | 0.00 | 0.00 |
| **MnSi03** | 0.88 | 0.00 | 0.00 | 0.00 | 0.00 |
| **Other Inclusions** | 0.10 | 0.00 | 0.74 | 0.21 | 1.83 |
| **MnO-Al2O3-SiO2 (complex)** | 21.62 | 6.62 | 12.87 | 12.62 | 7.98 |
| **CaAl2O4** | 3.20 | 1.80 | 7.12 | 6.68 | 0.75 |
| **MnO** | 0.15 | 0.00 | 0.00 | 0.05 | 0.00 |
| **MnS** | 6.71 | 0.03 | 0.07 | 0.14 | 0.00 |
| **TiN** | 0.00 | 0.00 | 0.00 | 0.00 | 0.09 |
| **Porosity** | 1129.17 | 522.48 | 2154.62 | 1308.79 | 1312.15 |

Table XVII- Mechanical test results of high strength steel with varying homogenization times at 2250°F (1232°C).

| Condition | Bar | UTS (ksi) | Condition Average | .2% YS (ksi) | Condition Average | Reduction in Area (%) | Condition Average | Elongation (%) | Condition Average |
|---|---|---|---|---|---|---|---|---|---|
| Baseline | 1 | 229 | 230 ± 0.82 | 175 | 176 ± 0.90 | 16.0 | 21 ± 10 | 7.5 | 8.3 ± 2.4 |
| | 2 | 230 | | 177 | | 33.0 | | 11.0 | |
| | 3 | 230 | | 176 | | 15.0 | | 6.5 | |
| 2 hour | 1 | 232 | 233 ± 1.79 | 179 | 179 ± 0.50 | 26.0 | 26 ± 1.5 | 8.5 | 9.2 ± 0.8 |
| | 2 | 232 | | 179 | | 25.0 | | 9.0 | |
| | 3 | 235 | | 180 | | 28.0 | | 10.0 | |
| 4 hour | 1 | 234 | 232 ± 1.15 | 179 | 179 ± 0.25 | 29.0 | 26 ± 4.6 | 10.0 | 9.5 ± 1.8 |
| | 2 | 231 | | 179 | | 21.0 | | 7.5 | |
| | 3 | 232 | | 179 | | 29.0 | | 11.0 | |
| 6 hour | 1 | 233 | 232 ± 0.96 | 181 | 179 ± 1.37 | 32.0 | 28 ± 3.8 | 11.0 | 9.7 ± 1.2 |
| | 2 | 232 | | 179 | | 25.0 | | 9.0 | |
| | 3 | 231 | | 178 | | 26.0 | | 9.0 | |
| 11 hour* | 1 | 232 | 224 ± 8.45 | 181 | 175 ± 4.96 | 23.0 | 17 ± 5.6 | 10.0 | 7 ± 2.7 |
| | 2 | 216 | | 171 | | 12.0 | | 5.0 | |
| | 3 | 224 | | 175 | | 16.0 | | 6.0 | |

* 11 hour tensile bar 2 and 3 exhibited signs of quench cracking prior to tensile testing

Table XVIII- Charpy V-notch impact energies (-40°F) for high strength steel with varying homogenization times at 2250°F (1232°C).

| | CVN min ft-lb (J) | CVN max ft-lb (J) | Average ±68%CL | Hardness HRC±95%CL |
|---|---|---|---|---|
| **Baseline** | 35 (48) | 43 (58) | 40 ± 3.0 (55 ± 4.0) | 49 ± 1.7 |
| **2 hour** | 29 (39) | 37 (50) | 34 ± 3.7 (46 ± 5.0) | 47 ± 1.9 |
| **4 hour** | 41 (55) | 41 (56) | 41 ± 0.3 (56 ± 0.4) | 46 ± 1.6 |
| **6 hour** | 39 (52) | 42 (57) | 41 ± 1.6 (55 ± 2.2) | 47 ± 1.8 |
| **11 hour** | 37 (51) | 39 (53) | 39 ± 0.9 (52 ± 1.3) | 47 ± 2.1 |

Table XIX- Dynamic Fracture Toughness at RT for high strength steel with varying homogenization times at 2250°F (1232°C).

| | DFT min $K_{ID}$ MPa√m | DFT max $K_{ID}$ MPa√m | Average ±68%CL | Hardness HRC±95%CL |
|---|---|---|---|---|
| **Baseline** | 106 | 117 | 110 ± 4.8 | 46 ± 0.3 |
| **2 hour** | 73 | 114 | 94 ± 23 | 47 ± 0.3 |
| **4 hour** | 90 | 97 | 88 ± 3.8 | 46 ± 0.3 |
| **6 hour** | 92 | 111 | 95 ± 3.8 | 47 ± 0.5 |
| **11 hour** | 79 | 80 | 95 ± 3.3 | 47 ± 0.5 |

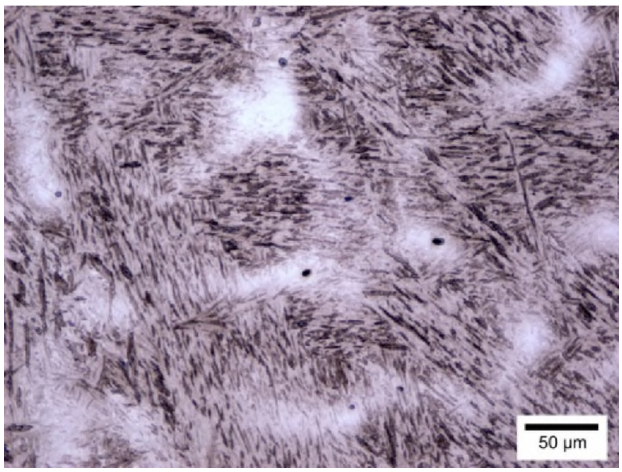


Figure 1. Optical microscope image of cast Eglin steel (CES) showing Stage I tempered lath martensitic microstructure. Remnant alloy segregation from solidification is visible in the light etching regions which are higher in chromium, tungsten and molybdenum. 2% nital etch.

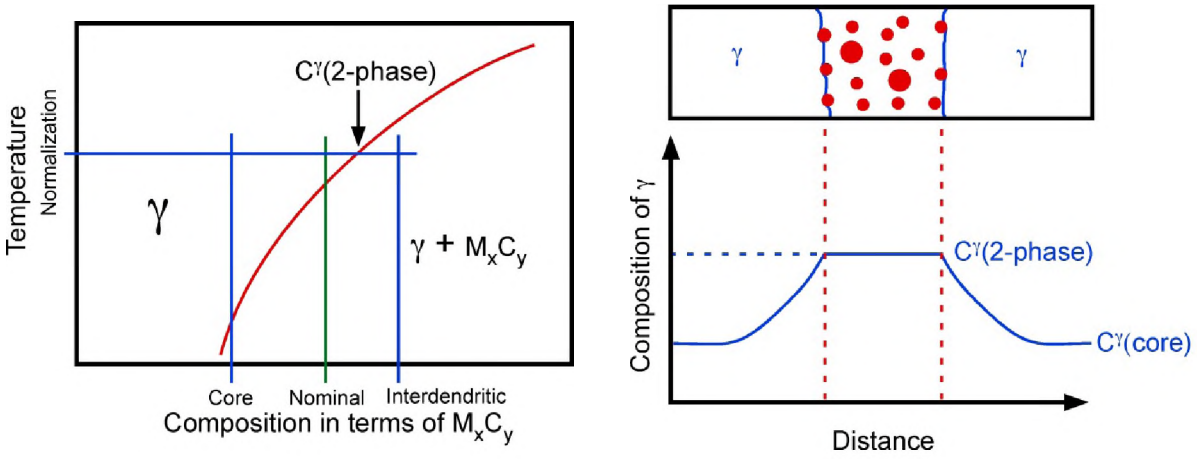


(a) (b)

Figure 2. A schematic illustration of how the redistribution of solute is affected by (a) a two-phase equilibrium in the alloy rich interdendritic region and (b) the effect of the two-phase equilibrium restricting the composition of the austenite (γ).

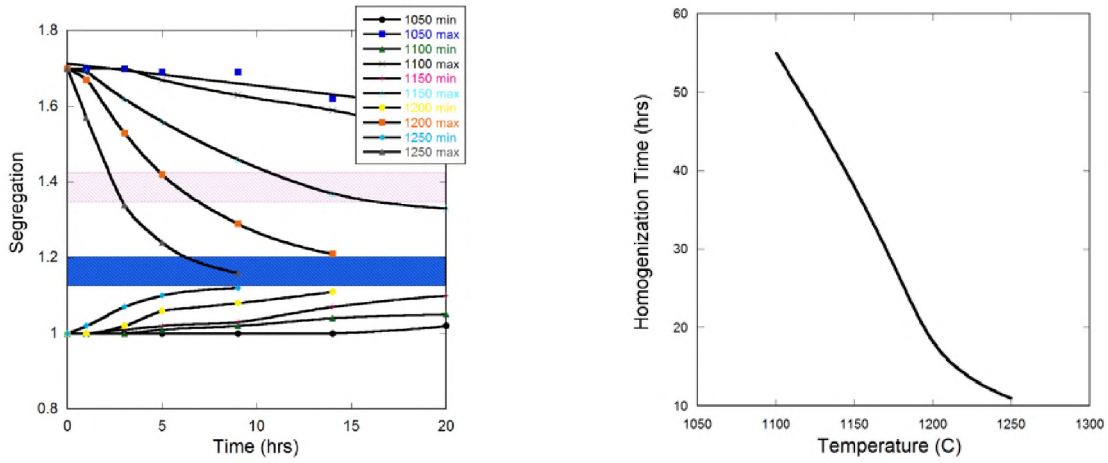


(a) (b)

Figure 3. (a) Homogenization of segregated tungsten based upon a secondary dendrite arm (SDA) spacing of 70μm. Pink and blue areas indicate partial (50%) and 90% homogenization. (b) Plot of times required to obtain 90% reduction in the interdendritic segregation. At 2280°F (1250°C) homogenization to 90% of the base chemistry would take more than 11 hours and a 50% reduction would take 2.75 hours. Results taken from reference. [8]

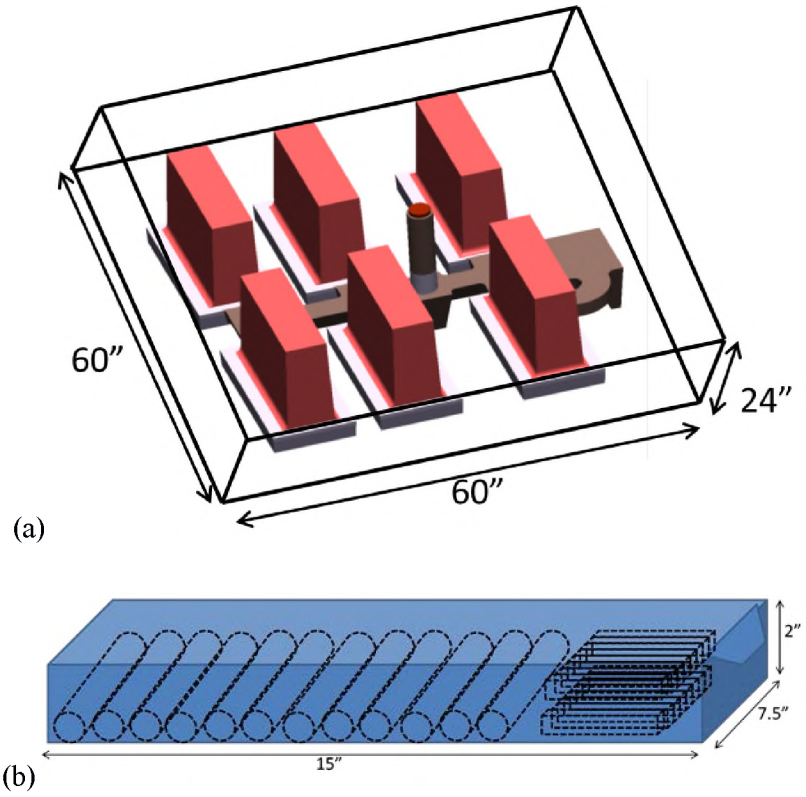


Figure 4. Schematic drawing of cast Eglin steel showing (a) mold configuration and (b) approximate specimen location within the individual cast weld plate.

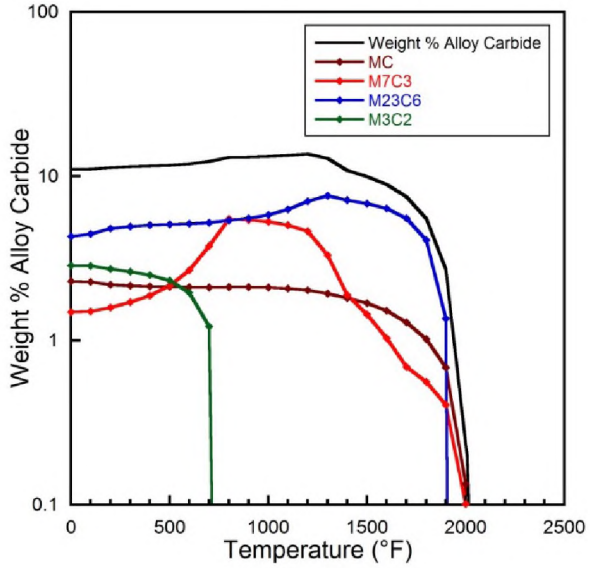


Figure 5. Weight percent of alloy carbide as a function of temperature for cast Eglin steel utilizing a Scheil-Gulliver segregation model in FactSage version 6.4 with the FSstel database. Solvus temperatures for individual carbide types are indicated along the total weight percent line.

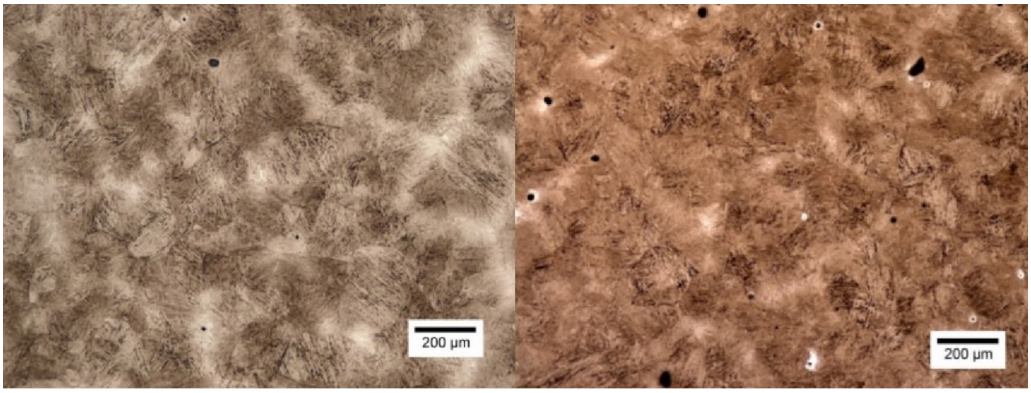


(a) (b)

Figure 6. Optical microscope image of cast high strength steel with (a) baseline heat treatment showing prior austenite grain size of 51 ± 10 µm, and (b) carbide growth heat treatment for 50 hours followed by a 1900°F (1038°C) showing a prior austenite grain size of 60 ± 13 µm. Prior austenite grains are highlighted using a modified marbles reagent.


Figure 7. Carbide particle maps obtained by automated feature analysis software showing the carbide distribution change with increased carbide aging time and decreased austenitization temperature. Red dots indicate position but not size within the scanned area. Figure (a) was intercritically tempered at 1300°F (704°C) for 100 hours and austenitized at 1800°F (982°C) for one hour. Figure (b) was intercritically tempered at 1300°F (704°C) for 50 hours and austenitized at 1900°F (1038°C) for one hour.

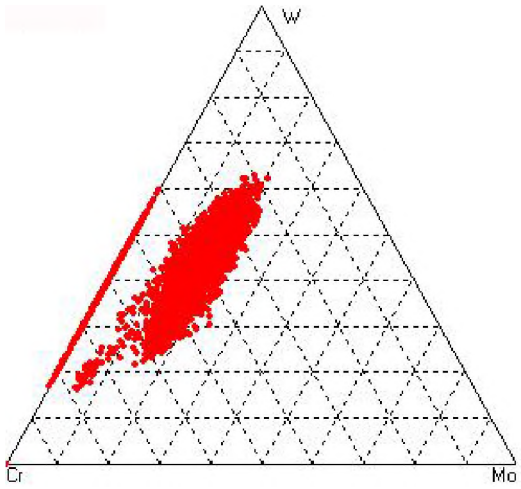


Figure 8. Ternary diagram obtained by automated feature analysis software for a tensile bar that was intercritically tempered at 1300°F (704°C) for 100 hours and austenitized at 1800°F (982°C) for one hour showing the distribution of Cr, W, and Mo for scanned alloy carbides. Multiple carbide types are indicated by the shift in distribution.

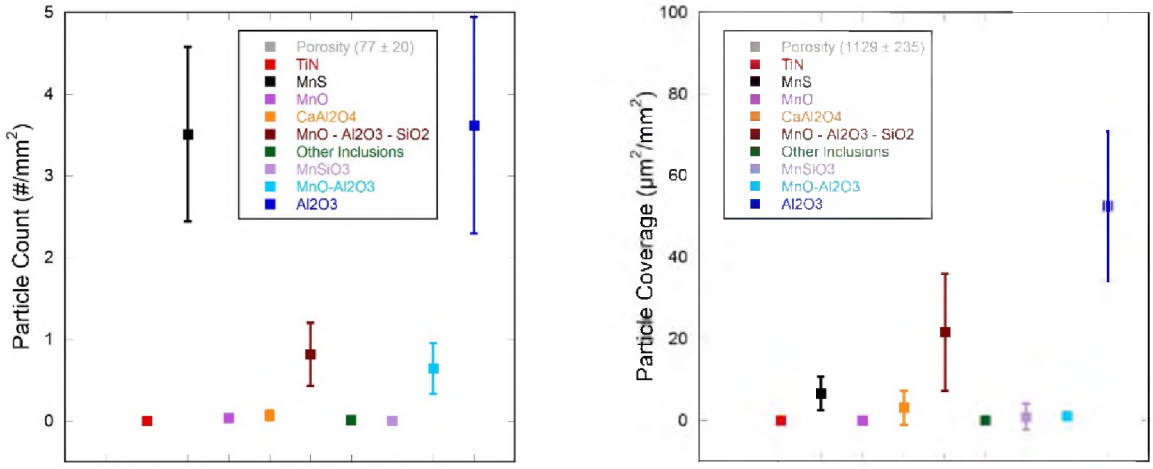


(a) (b)

Figure 9. Average (a) areal density of inclusions and pores, and (b) area fraction of inclusions and pores for homogenized tensile specimens and 26 scans of the same material with slight variations in the baseline heat treatment. Error bars shown are 68%CL for all inclusions and numerically listed at 95%CL for porosity.

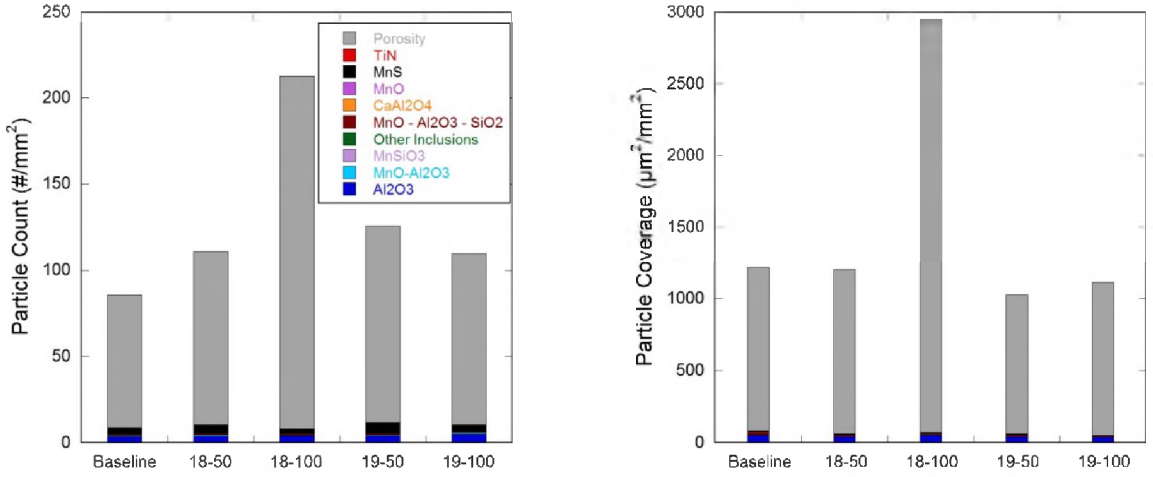


(a) (b)

Figure 10. Average (a) areal density of inclusions and pores, and (b) area fraction of inclusions and pores for tensile bars with varying amounts of carbide aging time and varying austenitization temperature.

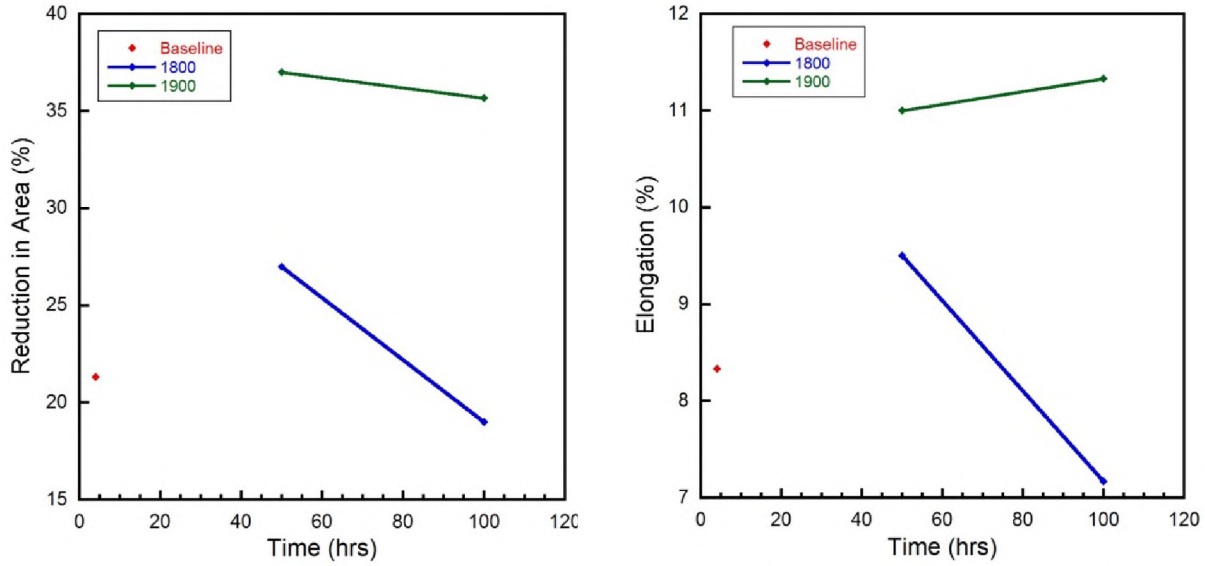


(a) (b)

Figure 11. Average (a) % reduction in area, and (b)% elongation vs carbide growth time at 1300°F (704°C) as a function of austenitization temperature for one hour on tensile bars of high strength steel.

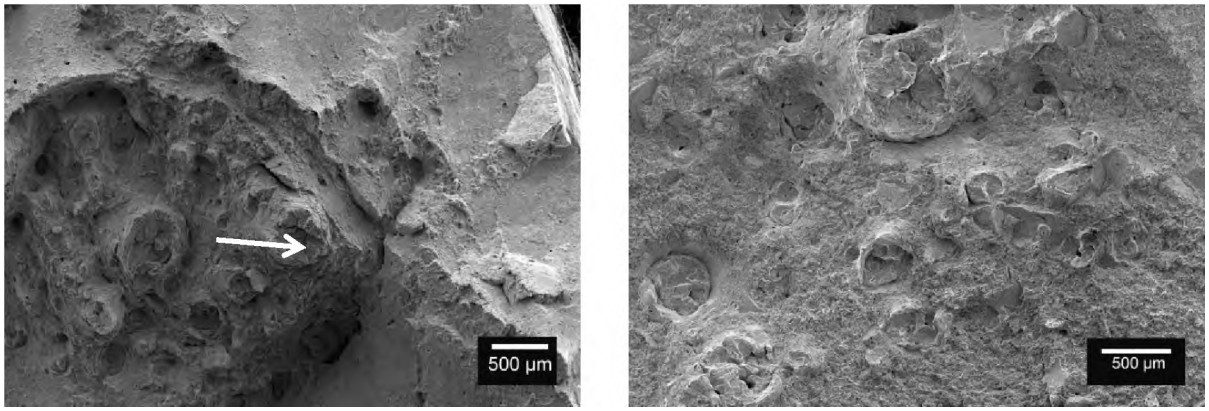


(a) (b)

Figure 12. Secondary electron images of tensile bar fracture surfaces for (a) baseline heat treatment, and (b) carbide aged material for 100 hours followed by 1800°F austenitization for one hour. White arrow indicates plateau feature associated with large porosity.

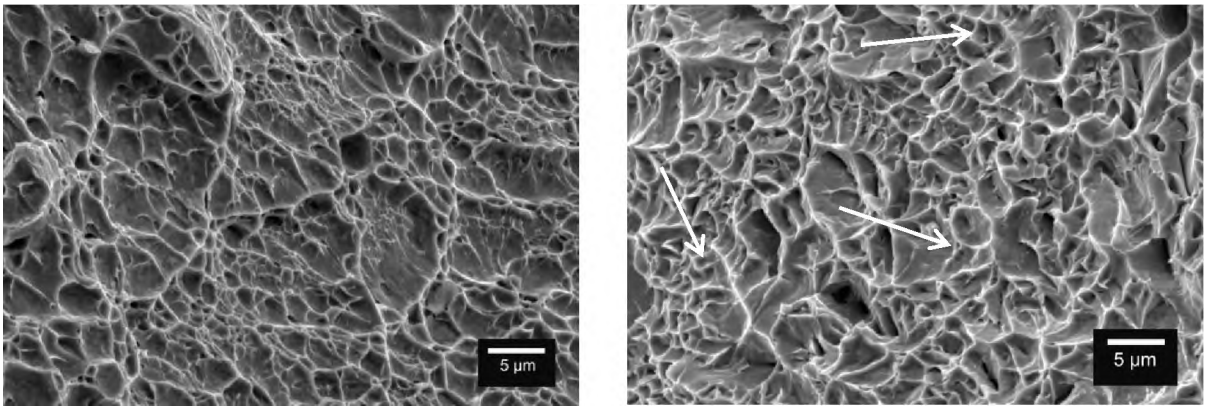


(a) (b)

Figure 13. Secondary electron images of tensile bar fracture surfaces for (a) baseline heat treatment, and (b) carbide aged material for 100 hours followed by 1800°F austenitization for one hour showing multiple carbides and inclusions, indicated with arrow, centered within microvoid dimples for the carbide aged material.

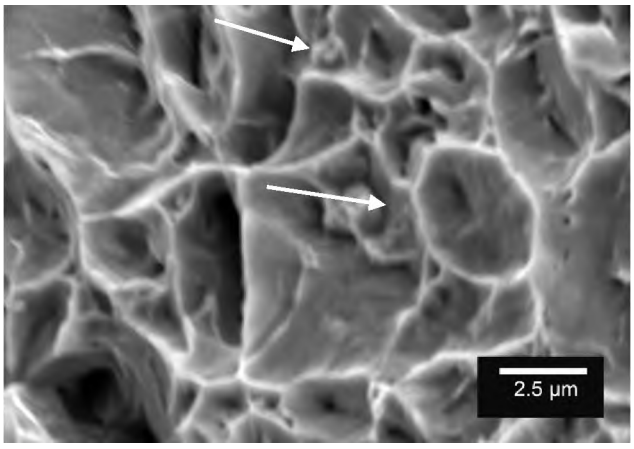


Figure 14. Secondary electron images of carbide in microvoid on fracture surface of carbide aged material for 100 hours followed by 1800°F austenitization.

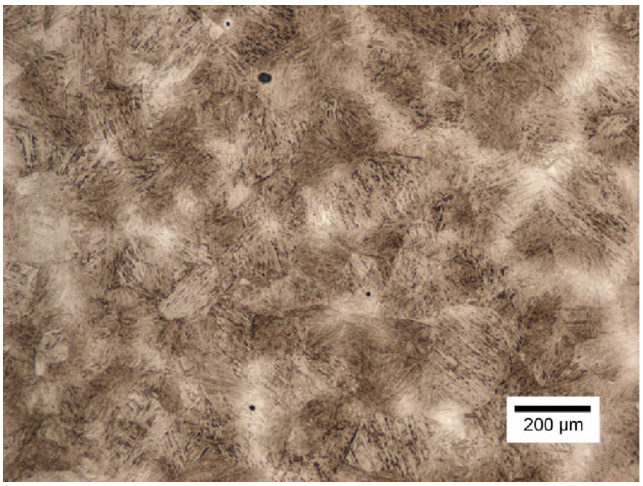


Figure 15. Optical microscope image of cast high strength steel with baseline heat treatment showing prior austenite grain size of 51 ± 10 µm highlighted using a modified marbles reagent.

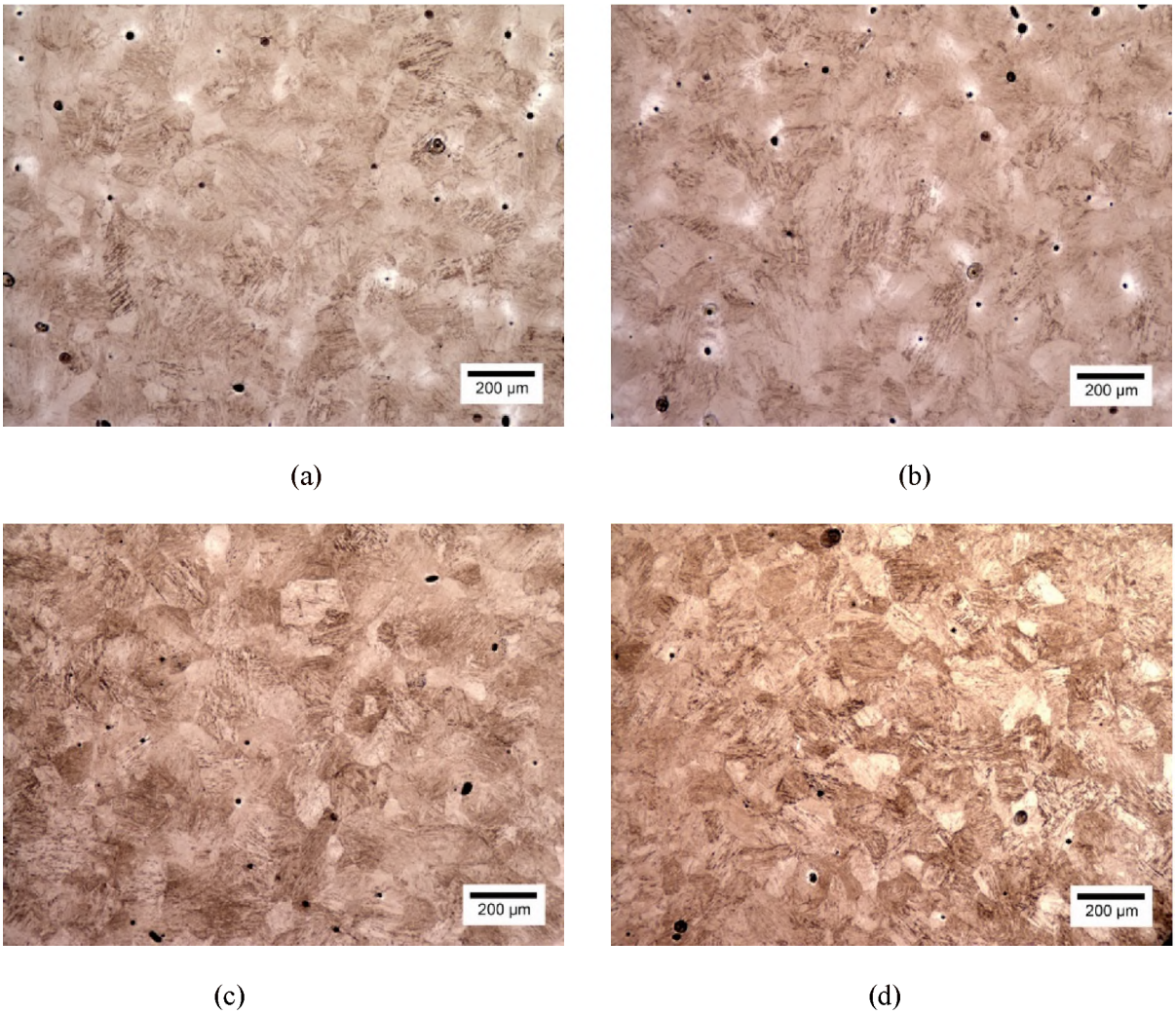


Figure 16. Optical microscope images of cast high strength steel with varying homogenization times of (a) 2 hours, (b) 4 hours, (c) 6 hours, and (d) 11 hours at 2250°F (1232°C) showing increase in prior austenite grain size highlighted using a modified Marbles reagent.

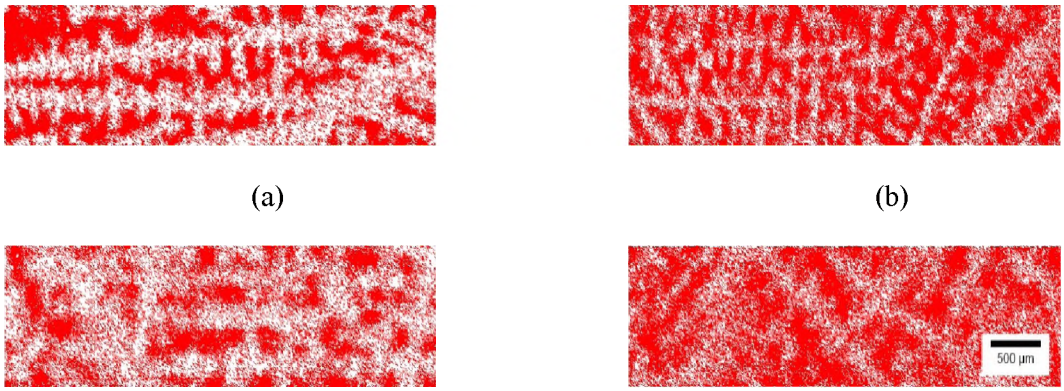


Figure 17. Carbide particle maps obtained by automated feature analysis software showing the carbide distribution change with homogenization heat treatment. Red dots indicate position but not size within the scanned area. Figure (a) was normalized at 2250°F (1232°C) for 2 hours Figure (b) was normalized at 2250°F (1232°C) for 4 hours, (c) 6 hours at 2250°F (1232°C) and (d) 11 hours at 2250°F (1232°C). All of the specimens were subsequently intermediately tempered at 1200°F (649°C), austenitized at 1900°F (1038°C) for one hour, quench hardened in water, tempered 4 hours at 375°F (191°C), and annealed for 100 hours at an intercritical temperature of 1382°F (750°C) to precipitate and coarsen the alloy carbides. All images were taken at the same magnification.

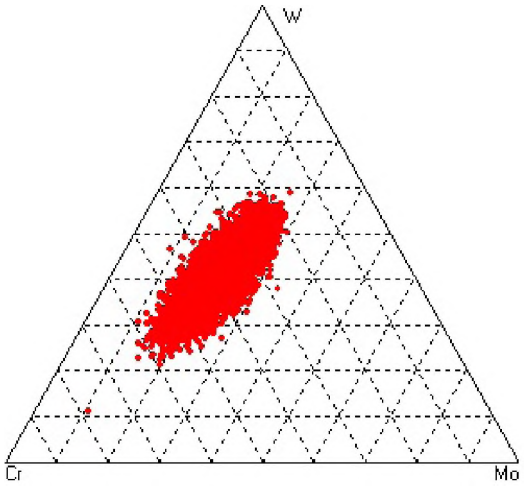


Figure 18. Ternary diagram obtained by automated feature analysis software showing the carbide distribution for a tensile specimen normalized at 2250°F (1232°C) for 11 hours, intermediately tempered at 1200°F (649°C), austenitized at 1900°F (1038°C) for one hour, quench hardened in water, tempered 4 hours at 375°F (191°C), and annealed for 100 hours at an intercritical temperature of 1382°F (750°C) to precipitate and coarsen the alloy carbides of type $M_{23}C_6$.

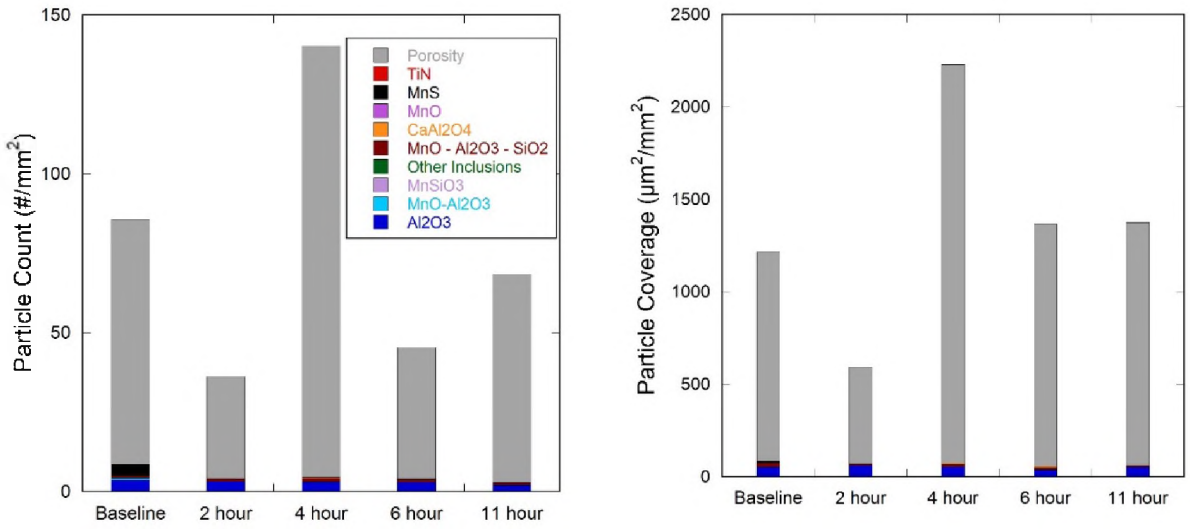


(a) (b)

Figure 19. Automated feature analysis for tensile bars in each condition. (a) Density of inclusions and pores measured as an areal density. (b) Area fraction of inclusions and pores.

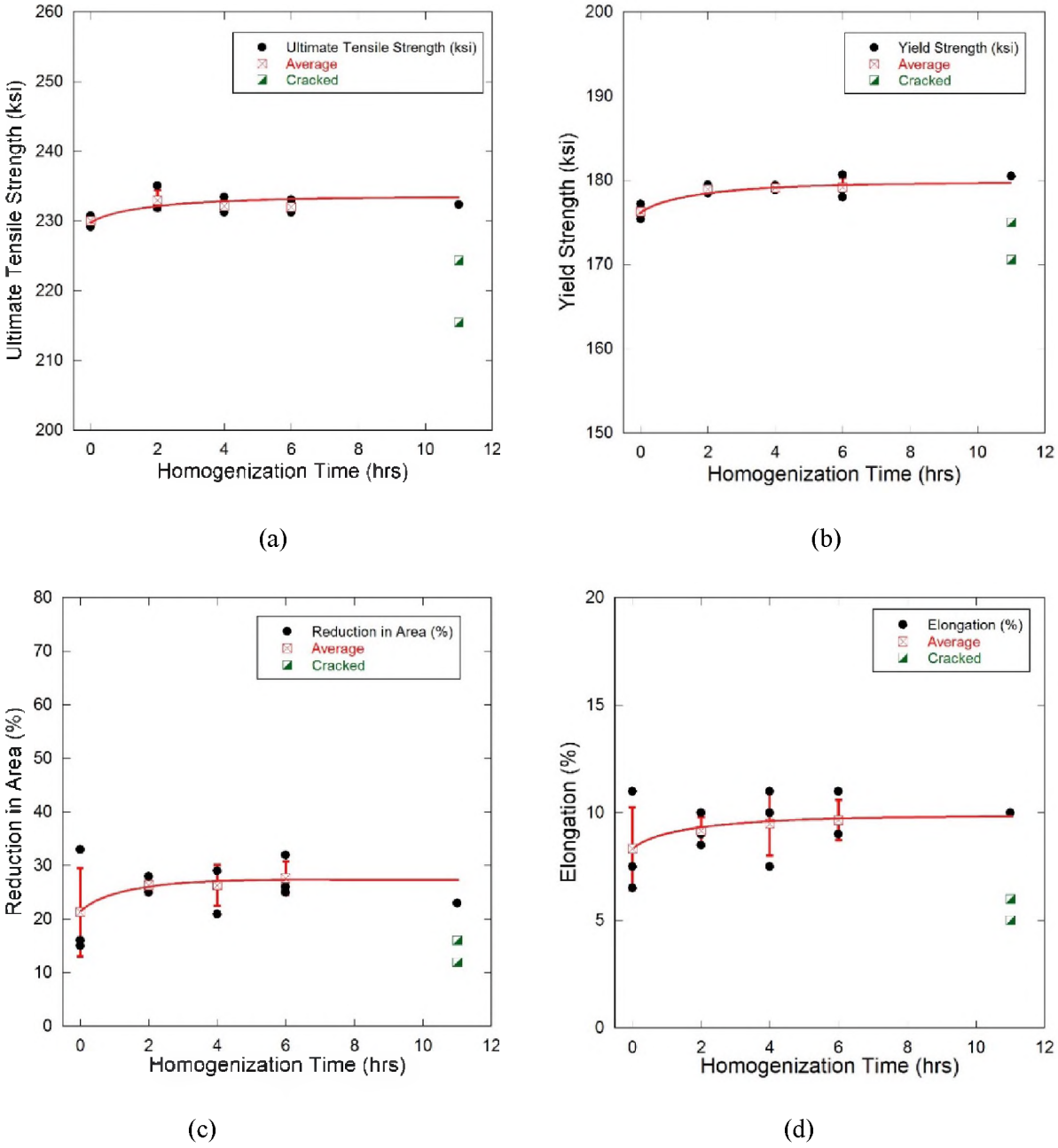


Figure 20. Mechanical test results of high strength steel with varying homogenization times at 2250°F (1232°C) showing (a) UTS, (b) YS, (c) reduction in area, and (d) percent elongation all increase with homogenization.

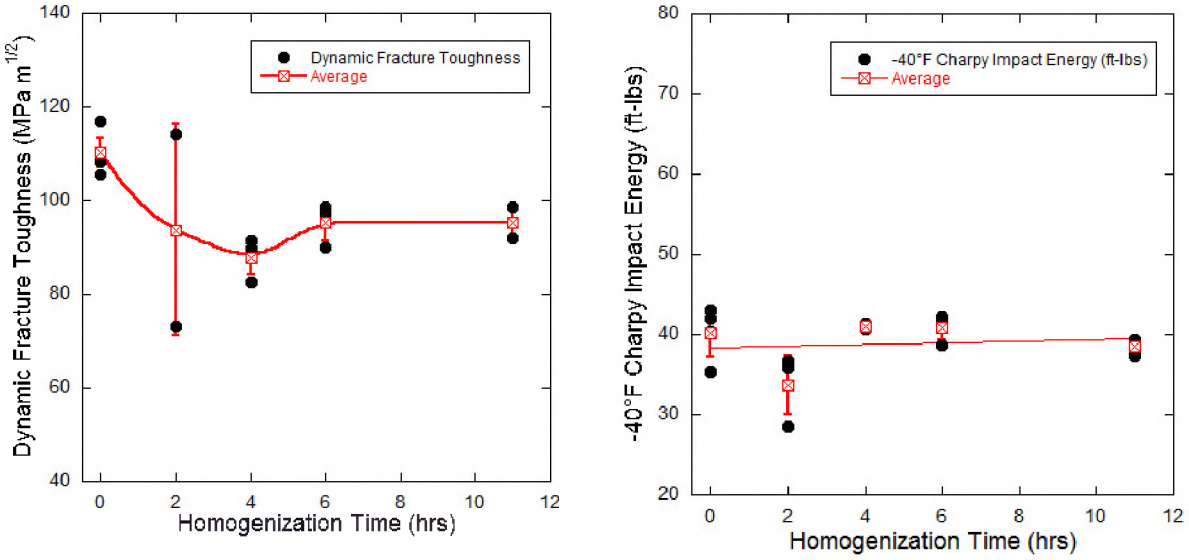


(a) (b)

Figure 21. Impact test results of high strength steel with varying homogenization times at 2250°F (1232°C) showing (a) Dynamic Fracture Toughness slightly decreases and (b) -40°F Charpy Impact Energy remains relatively unchanged with homogenization time.

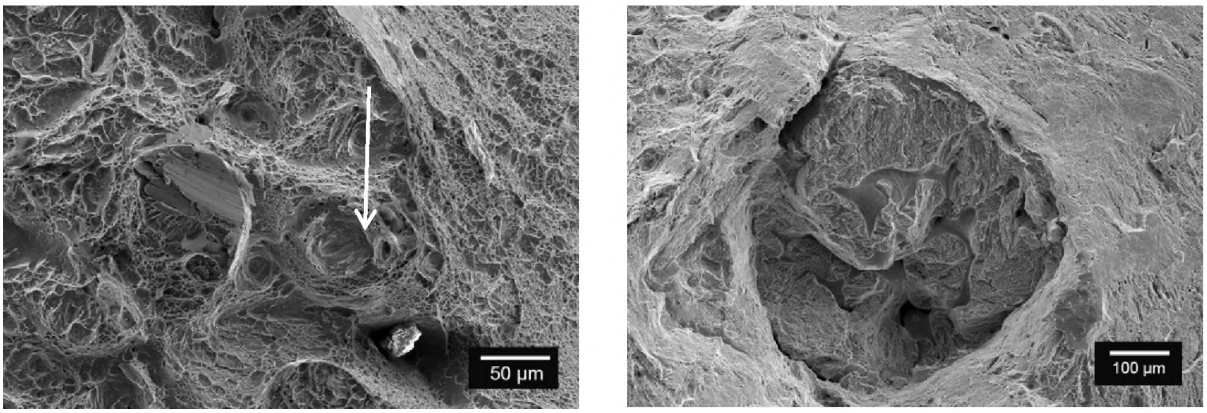


(a) (b)

Figure 22. Secondary electron images of homogenized tensile bar fracture surfaces normalized for (a) 11 hours, and (b) 4 hours. Low values for % elongation to failure and reduction in area may be explained by pores greater than 5µm. The white arrow in (a) indicates a plateau feature associated with this type of porosity.

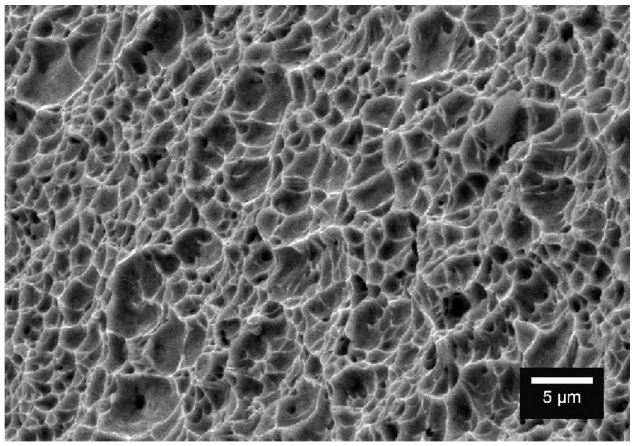


Figure 23. Secondary Electron image of tensile bar with the 4 hour homogenization heat treatment showing fracture by microvoid coalescence in areas between the plateaus with large shrinkage pores.

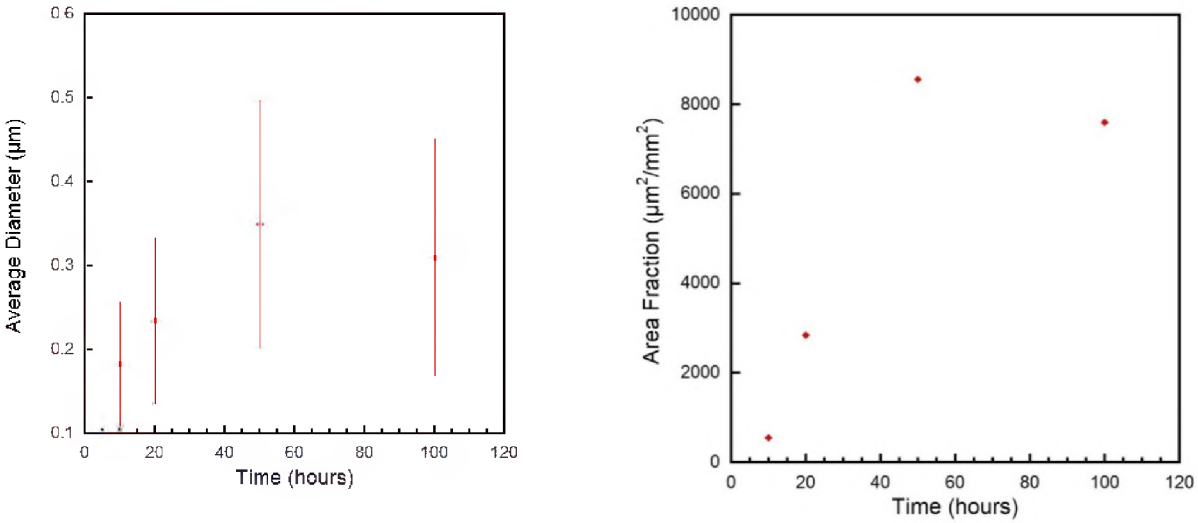


(a) (b)

Figure 24. Approximate interdendritic carbide (a) diameter, and (b) area fraction for Eglin steel as a function of time at 1300°F (704°C), where an apparent maximum is achieved at 50 hours. Error bars are reported as standard deviation.

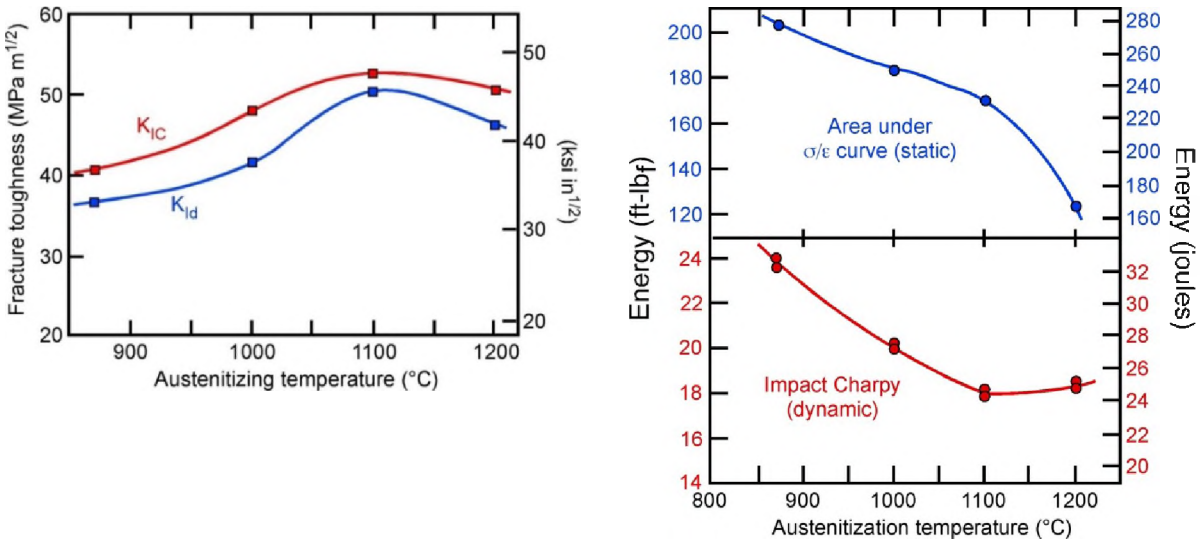


(a) (b)

Figure 25. A comparison of (a) fracture toughness and (b) CVN impact energy with austenitizing temperature showing that increasing the hardening temperature may increase the observed toughness, but decrease the notch toughness. This figure also shows that dynamic fracture toughness, $K_{ID}$, follows a similar trend as the quasi-static test for $K_{IC}$, but is lower. Figure redrawn from work presented by Richie. [13]

## REFERENCES


[1] J. Paules, M. Dilmore and K. Handerhan, "Development of Eglin Steel – A New, ultrahigh-Strength Steel for Armament and Aerospace Applications," Materials Science and Technology – AIST 2005 Vol. 2, pp 13-24.

[2] M. Dilmore and J.D. Ruhlman, Eglin Steel - A Low Alloy High Strength Composition. United States Patent Publication: US7537727.

[3] M.F. Dilmore, A.J. Armstrong, M.L. Green and M.L. Hughes, "Development of Eglin Steel for Hard Target Warhead Case Applications (U)," 6th Joint Classified Bombs/Warheads & Ballistics Symposium, Monterey, California, 2-5 June 2003.

[4] A. O'Loughlin, E. Martinez, K. Peaslee, and S. Lekakh, "Effects of Steel Processing on Property Variation in Eglin Steel (ES-1)" Materials Science &Technology 2010 Conference & Exhibition.

[5] R. Abrahams, P.Lynch, R.Voigt, "Processing & Composition of High Strength Cast Steel," 2009 SFSA Technical & Operating Conference.

[6] P. Lynch, R. Abrahams, R. Voigt, "Hot Isostatic Pressing and Homogenization of High Strength Steel Investment Castings," Investment casting Institute, 58th Technical Conference and Equipment Expo 2011.

[7] A. O'Loughlin, K. D. Peaslee and D. C. Van Aken, "Development of High Strength (200ksi) Cast Steel Alloy," 2011 SFSA technical & Operating Conference.

[8] T.O. Webb, D.C. Van Aken, S.N. Lekakh, "Evaluating Chemical Homogeneity in the Performance of Eglin Steel," AFS Proceedings 2014, Schaumburg, IL

[9] H.J. Schindler "Estimation of the Dynamic J-R Curve from a Single Impact Bending Test". Mechanisms and Mechanics of Damage and Failure: proceedings of the 11th ECF, (1996).

[10] T.F. Bower, H.D. Brody, and M.C. Flemings, "Measurement of Solute Solidification in Dendritic Solidification," Trans. AIME vol. 236 (1966) pp. 624-634.

[11] R. Pierer, and C. Bernhard, "On the influence of carbon on secondary dendrite arm spacing in steel," J. Mater. Sci. vol. 43 (2008) pp. 6938-6943.

[12] P.J. Alberry and C.W. Haworth, "Interdiffusion of Cr, Mo, and W in Fe," Metal Sci vol. 8 (Dec. 1974) pp. 407-412.

[13] R.O. Richie ASM conference proceedings, What Does the Charpy Test Really Tell Us? , (1978) pp. 54-73.

[14] L.N. Bartlett, A. Dash, D.C. Van Aken, V.L. Richards, and K.D. Peaslee, Dynamic Fracture Toughness of High Strength Cast Steels," AFS Trans vol.120, (2012) pp. 469-486.

[15] G.E. Hale and J. Nutting, "Overheating of low alloy steels," International Metals Reviews vol. 29 (1984), pp.273-298.

[16] T.O. Webb, D.C. Van Aken, "An Innovative Heat Treatment to Improve the Ductility of High Strength Steels," Steel Founders of America Technical and Operating Conference, paper 2.1, Chicago, IL, December 11, 2014.

[17] K. R. Santanu, "Effect of Phosphorus on Carbon Activity, Carbide Precipitation, and Coarsening in Ferritic Fe-C-P alloys," Metallurgical Transactions A, vol. 22A, (1991) pp. 35-43.

[18] D. Durinck, P.T. Jones, B. Blanpain, P. Wollants, "Slag Solidification Modeling Using the Scheil-Gulliver Assumptions," Journal of American Ceramic. Society, 90 (2007) pp. 1177-1185.

[19] P. Schaffnit, C. Stallybrass, J. Konrad, F. Stein, M. Weinberg, "A Scheil-Gulliver Model Dedicated to the Solidification of Steel," CALPHAD, vol. 48, (2015) pp.184-188.

[20] G.M. Gulliver, J. Inst. Metals 9 (1913) 120-157

[21] E. Scheil, Z. Metallkd., 34 (1942) 70-72

[22] D. R. Askeland, W. J. Wright, Essentials of Materials Science & Engineering, Stamford: Cengage Learning, 2014.

[23] B.M. Leister and J.N. Dupont, "Phase transformation and welding of Eglin Steel" Steel Founders of America Technical and Operating Conference, paper 3.7, Chicago, IL, December 14, 2012.

[24] C.E. Sims and C.W. Briggs, "A Primer on Deoxidation," Journal of Metals, 1959, pp. 815 – 822.

[25] W.C. Leslie. "The Physical Metallurgy of Steels", Hemisphere Publishing Co. (1981).

[26] W.M. Garrison and N.R. Moody, "The Influence of Spacing and Microstructure on the Fracture Toughness of Secondary Hardening Steel AF 1410," Met. Trans. A, Vol. 18A, 1987, pp. 1257-1263.

# SECTION

# 3. AFTERWORDS

This section provides a description of the impact this work as well as recommendations for future work.

Impact of work:

Given today's ever changing war time environment, the need for continuous improvement in armor is a daunting yet critical task. Additionally, the need for more lightweight and efficient armor to minimize cost and increase efficiency is constantly being demanded by the public whose tax dollars support the development of this technology, and moreover the continuing cost of global defense. This work has directly supported the Weapons and Materials Research Directorates mission for survivability as well as other DoD entities by opening an entirely new manufacturing process to a material that is already patented by the DoD and had considerable developmental funding applied to it. Casting of this metal which allows for more intricate and usable geometries with in the armor field not only increases the survivability of both the component and the individual war fighter, it also reduces the cost to increase the capability of the force.

From a more historical perspective, the development of a steel casting as a structural component has only recently (in the last 20 years) begun to gain momentum as prior attempts to apply steel castings as structural components have yielded less than desirable results. The success of casting this steel in the current applications can only help continue the momentum within industry and may help contribute to advancing both steel casting technology and the industry as a whole.

Recommendations for future work:

1. The first notion that needs to be dispensed with is that of isotropy. These castings will be engineered to limit shrinkage porosity and that means a directional solidification pattern that will produce anisotropy. The Eglin type steel produces very little delta ferrite with less than 33% predicted at the standard nickel content of 1wt%, see Figure 1. The resultant austenite texture produced in solidification will be a {100} in the plane of the plate as a combination of both <100> and <011> growth textures. A {100} crystallography is undesirable with respect to kinetic penetrators as it promotes spallation and lowers the Young's modulus in the <100> through thickness texture. [18]

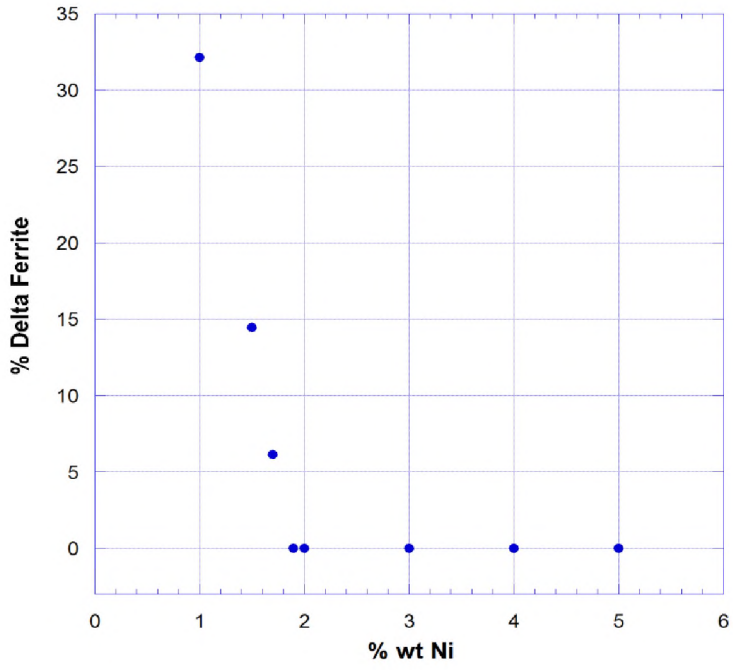


Figure 3. 1- FactSage prediction of % δ-ferrite for Fe-0.24C-0.77Mn-0.88Si-2.64Cr-0.42Mo-0.92W using a Scheil-Gulliver segregation model and variable nickel.

McGrath and Van Aken [15] have shown that the peritectic austenite crystallography is dependent upon the amount of delta ferrite formed. High volume fractions of delta ferrite favor the Kurdumov-Sachs orientation relationship, which should reduce the <100> texture of the peritectic austenite.

2. Problems and benefits of the peritectic reaction. The primary issue here is the solid fraction curve with respect to temperature and solidification. Beckermann [16] has established that steep solid fraction curves near the end of solidification are of benefit to reduction of shrinkage porosity and steels with this attribute may be solidified to produce lower shrinkage porosity at a lower Niyama number versus a steel with a kinetically inhibited solid fraction curve. Kinetically inhibited refers to a steel undergoing the peritectic reaction near the end of solidification where the solidification of the remnant liquid is kinetically inhibited by solid state diffusion through the peritectic austenite. Thus, improved ballistic performance of the texture produced by a late peritectic solidification is diminished by a higher level of shrinkage porosity. Proper engineering of the casting with appropriate use of risers and chills is the only viable approach to obtain the appropriate texture and reduction of shrinkage porosity.

3. Homogeneity of the casting also benefits from the polymorphic solidification. The initial delta-ferrite will be rich in bcc stabilizing elements and partition the fcc elements to the liquid, which encourages the formation of gamma austenite. The solid-state reaction of converting the ferrite to austenite will then redistribute the elements over a smaller length scale than either the secondary arm spacing or the primary dendrite trunk spacing.

4. Microporosity that is less than 2μm in size is often related to nitrogen. Nitrogen mitigation has been attempted with titanium; however, the formation of TiN reduces the notch toughness of the steel and excessive deoxidation with titanium results in the formation of eutectic MnS structures that reduce notch toughness. Zirconium is the current practice in many foundries

to reduce nitrogen, but ZrN is expected to behave in a similar fashion as TiN with respect to notch toughness. The advantages of using Zr are that its addition does not promote eutectic sulfides and the high density promotes settling in the furnace or ladle.

5. Boron is not normally considered for the reduction of nitrogen, but its addition to steel could be multi-beneficial. Boron readily reacts with nitrogen to form a low density BN compound that should float out of the steel. Excess boron left in the melt would inhibit nitrogen pick-up during casting and excess boron in solution would contribute grain boundary cohesive strength, i.e. more resistant to quench cracking. Benefits from hardenability will be marginal since these armor steels are already exceeding ideal diameters of 10 inches.

6. Quenching, tempering and retained austenite. Evidence in the wrought armor business has suggested that retained austenite of approximately 8% by volume is beneficial to high hardness armor steels. [18] Retained austenite is a function of the athermal nature of the martensitic reactions. A quench temperature that is above the finish temperature of the martensitic reaction will produce varying amounts of retained austenite. Stage I tempering will produce a partitioning of carbon to the austenite that will stabilize the austenite to lower temperatures. Segregation in thick walled castings may not provide an optimum distribution of austenite and has been to this point avoided. Eglin steel is designed for an Mf temperature above room temperature. However, it may be possible to eliminate this problem by controlling quench temperature in multiple stages. (1) Quench to above the average Mf temperature of the steel casting, (2) temper to carbon partition in the main dendritic structure, but not in the segregated regions, (3) quench to below room temperature to convert some of the austenite in the segregated regions, but not covert the previously stabilized austenite, and (4) final tempering that stabilizes the remaining austenite in the segregated regions.

7. Carbide formation in Eglin steel has been viewed mainly as being detrimental as massive carbides drop the toughness as shown in the first paper of this dissertation. Certainly Leslie [17] indicates steels of this type must avoid massive carbides; however, he also indicates the proper size, distribution, and shape of strengthening particles is necessary. Eglin steel utilizes a stage I temper to produce intralath ε-caribde which act as strengthening particles and thus should be looked at as beneficial. Furthermore, the first paper of this dissertation shows the formation of multiple types of carbide and those types are dependent on carbon segregation. Dupont [7] has provided an in-depth study of the carbide types in post weld heat treatments; however, it seems apparent that a more thorough understanding of the carbide types and their formation both during and after heat treatment may provide future gains in both mechanical properties and the manufacturability of Eglin steel.

## REFERENCES


[1] Directorate, Weapons and Materials Research, MIL-DTL-46177C Detail Specification for Armor Plate, Steel, Wrought, Homogeneous. Aberdeen Proving Ground: U.S. Army Research Laboratory (1998)

[2] W.S. de Rosset, "An Overview of Novel Penetrator Technology" Aberdeen Proving Ground: Army Research Laboratory (2001).

[3] M. Bolotsky, "Historical Review of the Correlation of Ballistic and Metallurgical Characteristics of Domestic Armor at Watertown Arsenal" Watertown: Ordnance Department of the United States Army (1945).

[4] US ARMY TEST AND EVALUATION COMMAND TEST OPERATIONS PROCEDURE "BALLISITC TEST OF ARMOR MATERIALS". ABERDEEN PROVING GROUND: US ARMY TEST AND EVALUATION COMMAND, (1984)

[5] J.Malamas, "Warhead Case for BLU-122X/B, 5000-lbs Penetrator Bomb Serial No. 9064." Aberdeen Proving Ground: US ARMY Research Laboratory, (2010)

[6] J.R. Paules, M. D, "Development of Eglin Steel -- A new, Ultrahigh-strength Steel for Armament and Aerospace Applications," Ferrous Physical Metallurgy of Highly Alloyed Steels, Proceedings of a Symposium sponsored by Materials Science & Technology (pp. 25-28). Pittsburgh: Materials Science & Technology (2005).

[7] B.M. Leister and J.N. Dupont, "Phase transformation and welding of Eglin Steel" Steel Founders of America Technical and Operating Conference, paper 3.7, Chicago, IL, December 14, 2012.

[8] M.F. Dilmore, A.J. Armstrong, M.L. Green, M.L. Hughes, "Development of Eglin Steel for Hard Target Warhead Case Applications," 6th Joint Classified Bombs/Warheads & Balistics Symposium. Monterey: Air Force Research Laboratory Munitions Directorate, (2003).

[9] R. Russo, B. Baker, N. Dutton, K. Torres, S. E. Jones "TAYLOR CYLINDER TEST REDUCTION USING A ONE-DIMENSIONAL THEORY," ASME Pressure Vessels and Piping Division Conference, (pp. 1-6) Chicago, (2008).

[10] W.P. Hatch, J. "CORRELATION OF TOUGHNESS BETWEEN H-PLATE AND CHARPY IMPACT TESTS," WATERTOWN: WATERTOWN ARESENAL LABORATORIES, (1959).

[11] A. O'Loughlin, E. Martinez, K. Peaslee, and S. Lekakh, "Effects of Steel Processing on Property Variation in Eglin Steel (ES-1)" Materials Science &Technology 2010 Conference & Exhibition.

[12] R. Abrahams, P.Lynch, R.Voigt, "Processing & Composition of High Strength Cast Steel," 2009 SFSA Technical & Operating Conference.

[13] P. Lynch, R. Abrahams, R. Voigt, "Hot Isostatic Pressing and Homogenization of High Strength Steel Investment Castings," Investment casting Institute, 58th Technical Conference and Equipment Expo 2011.

[14] A. O'Loughlin, K. D. Peaslee and D. C. Van Aken, "Development of High Strength (200ksi) Cast Steel Alloy," 2011 SFSA technical & Operating Conference.

[15] M.C. McGrath and D.C. Van Aken, "On the Crystallography of Peritectic Austenite and the Role of Primary Ferrite in High Manganese and Aluminum Steels," Int. J. Metalcasting vol. 6, Issue 3, pp. 35-50 (2012).

[16] R.A. Hardin and C. Beckermann, "Effect of Porosity on Deformation, Damage, and Fracture of Cast Steel," Metall. Mater. Trans. A44, (2013) pp. 5316-5332.

[17] W.C. Leslie. "The Physical Metallurgy of Steels", Hemisphere Publishing Co. (1981).

[18] G. R. Speich, H. Hu and R.L. Miller, "Effect of Preferred Orientation and Related Metallurgical Parameters on Mechanical Properties and Ballistic Performance of High-Hardness Steel Armor" Monroeville: United States Steel Corporation. (1974)

# APPENDIX A

# CLASSIFICATION RULES FOR NONMETALLIC INCLUSION ANALYSIS

Classification of porosity and nonmetallic inclusions conducted during this research was performed by first using the Gibbs free energy minimization model of the thermodynamic software FactSage for the given chemistry range of Eglin Steel and determining what inclusions maybe present with in the steel. After review of the predicted inclusions a cursory scan of selected samples using a PICA 1020 ASPEX SEM with backscatter electron detector was used to determine location and compositional information of inclusions within the selected samples. Finally comparison of optical microscope, scanning electron microscope, and the thermodynamic software information was made in order to generate a set of rules by which the automated feature analysis software with in the PICA 1020 ASPEX SEM may correctly classify inclusions found in Eglin steel. After each scan a review of the data was conducted in order to determine any outliers and a determination was made both on composition and micrograph comparison to correctly classify that outlier. Table A1 lists the classification rules generated to correctly classify individual inclusions with in Eglin Steel.

Table A 1- Post-acquisition analysis rules for inclusion and porosity analysis in Eglin Steel

| | Fe | Mn | S | Ca | C | Al | Si | Ti |
|---|---|---|---|---|---|---|---|---|
| Porosity | >= 80 | | | | | | | |
| MnS | | >30 | >15 | <20 | <10 | | | |
| CaS | | <20 | >20 | >30 | <10 | | | |
| MnS-CaS | | >15 | >20 | >15 | <10 | | | |
| CaAL2O4 | | <20 | <20 | >15 | <10 | >20 | <20 | |
| MnSiO3 | | >20 | <20 | <20 | <10 | <20 | >10 | |
| MnAlSiO | | >20 | <20 | <20 | <10 | >18 | >10 | |
| CaSiO3 | | <20 | <20 | >20 | <10 | <20 | >10 | |
| MnO-Al2O3 | | >25 | <20 | <20 | <10 | >25 | <20 | |
| CaO-MnO | | >25 | <20 | >25 | <10 | <20 | <20 | |
| Complex (MnO-Al2O3-SiO2) | | | | | <10 | >2 | >2 | |
| Al2O3 | | | | | <10 | >25 | | |
| MnO-Al2O3 | | >30 | <20 | | <10 | | | |
| CaO | | | <20 | >30 | <10 | | | |
| TiN | | | | | <10 | | | >40 |
| Other Oxides | | | <10 | | <10 | | | |
| Other Oxisulfides | | | >5 % <10 | | <10 | | | |
| Other Sulfides | | | >10 | | <10 | | | |
| Unclassified | | | | | <10 | | | |
| Porosity witd Diammond Paste | | | | | >=40 | | | |

# APPENDIX B

# EVALUATING CHEMICAL HOMOGENEITY IN THE PERFORMANCE OF EGLIN STEEL

# Evaluating Chemical Homogeneity in the Performance of Eglin Steel

T. O. Webb

Department of Materials Science and Engineering, Missouri University of Science and Technology, Rolla, MO

D. C. Van Aken, S. N. Lekakh

Department of Materials Science and Engineering, Missouri University of Science and Technology, Rolla, MO

## ABSTRACT

Elevated temperature homogenization was explored to improve the toughness of cast Eglin steel. Homogenization times were calculated using secondary dendrite arm spacing; however, the primary trunk spacing was found to be the rate controlling distance parameter for complete homogenization. Sufficient evidence is available to specify a normalization temperature for Eglin steel above 2100°F (1149°C) to eliminate persistent alloy carbides of the type $M_{23}C_6$ and fully homogenize the carbon content. Alloy homogeneity did not improve significantly either Charpy V-notch energy or dynamic fracture toughness. Charpy V-notch toughness at -40°F (-40°C) were less than half of the 30 ft-lb (41 J) goal for the homogenization study. Normalization at temperatures above 2100°F (1149°C) appear to promote MnS coarsening as a result of increased MnS solubility. Upon cooling the MnS in solution precipitates as a fine dispersion. The Eglin steels obtained for this study had higher inclusion and porosity contents as compared to previously tested cast Eglin

steels. It may be concluded that steel homogeneity is a secondary consideration to casting porosity and cleanliness.

## INTRODUCTION

Eglin steel was developed by the U.S. Air Force and Ellwood National Forge Company as a cost-effective, ultrahigh strength steel for use in armament, aerospace, and commercial applications[1,2]. Eglin steel has been successfully substituted for high alloy steels, such as AF1410 and HP-9-4-20/30, to produce the casing for "bunker buster" bombs where penetration of concrete barriers and rock at high velocity (>1000 ft/sec) is desired[3]. Unlike AF1410 and HP-9-4-20/30, Eglin steel is low nickel (nominal 1 wt.%) and contains no cobalt. Furthermore, Eglin steel is a Stage I tempered steel consisting of a lath martensitic microstructure (see Figure 1) with intra-lath ε-carbides. In the Stage I tempered condition, Eglin steel will produce a yield strength ranging from 180 to 190 ksi and an ultimate tensile strength of 240 to 250 ksi. The low ratio of yield to ultimate strength indicates extensive work hardening during plastic deformation and this contributes to the toughness of the steel under impact conditions. Eglin steel is designated as ES-1 when produced as a wrought product and CES when it is cast.

Alloy segregation is prevalent in most cast and wrought Eglin steel products with chromium, tungsten, and molybdenum segregating to interdendritic regions as shown in Figure 1(b).

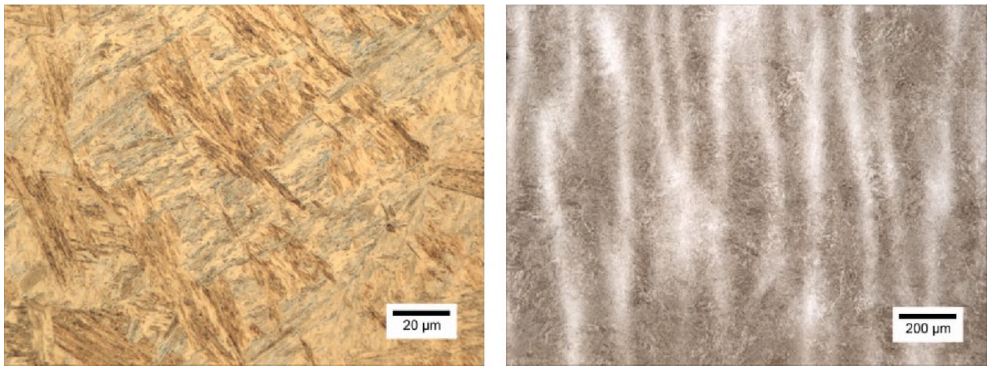


*(a)* *(b)*

Figure 1. Optical microscope images of wrought Eglin steel (ES-1). (a) Optical image of the Stage I tempered lath martensitic microstructure of ES-1 (b) Optical image of forged ES-1 showing the remnant alloy segregation from solidification. The light etching regions in (b) are higher in chromium, tungsten and molybdenum. 2% nital etch.

Many investigations have been performed to understand the role of heat treatment, steel cleanliness, and the role of persistent alloy carbides such as $M_{23}C_6$ in the notched impact strength of ES-1. Both nonmetallic inclusions and alloy carbides contribute to void nucleation and fracture by microvoid coalescence. In a study by O'Loughlin et al.[4] a weak correlation between the Charpy V-notch (CVN) energy at -40°F (-40°C) and steel cleanliness was obtained for ES-1. These results are shown in Figure 2 and to obtain CVN energies of at least 15 ft-lbs (20 J) the nonmetallic inclusion content should be less than 9 inclusions/ $mm^2$ and have an inclusion coverage less than 73 $\mu m^2/mm^2$.

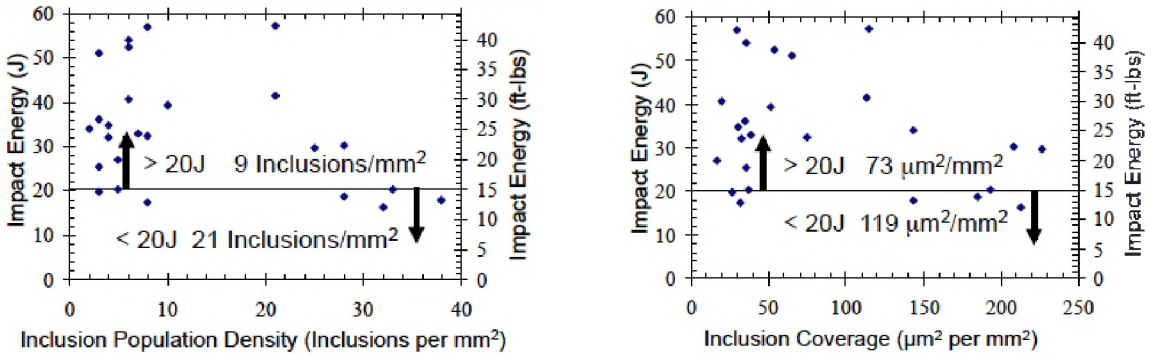


*(a)* *(b)*

Figure 2. Results of Charpy V-notch impact energy at -40°F (-40°C) for 31 different heats of wrought Eglin steel obtained from a variety of steel suppliers. Automated feature analysis was used to quantify the inclusion content by (a) areal density and (b) inclusion coverage (volume fraction). Results taken from reference[4].

The same steels shown in Figure 2 were evaluated with respect to persistent carbide content as shown in Figure 3. It should be noted that the presence of persistent carbides is dependent upon austenitization temperature prior to quench hardening and the results shown in Figure 3 are from a wide variation in heat treat processing. However, samples with CVN energies greater than 15 ft-lbs (20 J) were those steels with less than 542 carbides/mm$^2$. It has been shown by Abrahams et al.[5] that high austenitizing temperatures greater than 1850°F (1010°C) are critical in the heat treatment of ES-1 to prevent the loss of notch toughness resulting from these persistent alloy carbides.

Persistent carbide dissolution will be dependent upon segregation during solidification. Segregation of chromium and tungsten are of particular importance, since these elements are strong $M_{23}C_6$ carbide formers and have diffusivities that require high temperatures and extended time during normalization to effectively homogenize the steel.

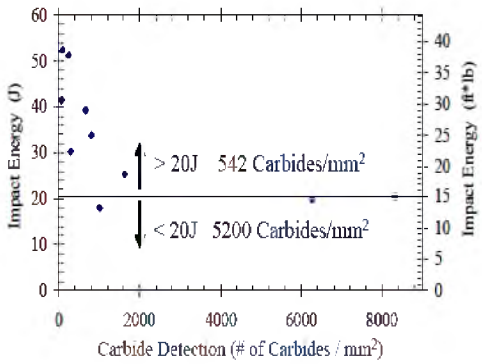


Figure 3. A comparison of CVN impact energy measured at -40°F (-40°C) against detectable carbides greater than 0.2 μm in diameter for wrought Eglin steel. Automated feature analysis was used to quantify the carbide content by areal density. Results taken from reference[4].

Homogenization of carbon will also depend upon the presence of persistent carbides. Figure 4 shows a schematic illustration of why persistent carbides inhibit carbon redistribution. Figure 4(a) shows a normalization temperature for which the nominal alloy should be in a single phase region

of austenite. However, the segregated (both carbon and alloy) interdendritic region is in a two-phase (austenite plus carbide) equilibrium for which the austenite composition is limited by the presence of the carbide. Figure 4(b) illustrates that the dissolution and redistribution of solute (both carbon and alloy) is dependent upon completely dissolving the carbide. The region of austenite and carbide will narrow with time, but the composition gradient is fixed by the the two phase equilibrium.

Porosity is also detrimental to high strength cast steels and studies have shown that hot isostatic pressing (HIP) will improve ductility and CVN impact energy[6,7]. Both studies show that the average yield and ultimate strengths of cast Eglin steel are unaffected by HIP, but elongation to failure, reduction in area, and Charpy V-notch energies are increased. O'Laughlin et al.[7] quantified the change in porosity with HIP treatment of CES and these results are provided in Figures 5 and 6. The dominant inclusion types in both cast Eglin steels were $MnSiO_3$, MnS and MnO with varying amounts of $Al_2O_3$ between the two heats. An increase in $Al_2O_3$ inclusions was observed with increasing aluminum from 0.008 wt.% in Heat #1 to 0.014 wt.% in Heat #2. In contrast, the porosity was higher for Heat #1 than for Heat #2. Nitrogen contents were measured and Heat #1 had 88.1 ppm nitrogen versus 120 ppm for Heat #2. Oxygen contents were 76.2 ppm and 60.3 ppm, respectively. As a result of HIP, the porosity as measured by particle coverage was lowered by 88.5% and the average diameter of the pore was reduced to below 3 μm, which is approximately twice the size of pores observed in the ES-1 product[7]. This reduction in porosity produced an increase in elongation to failure from 7% (40.7% reduction in area) to 13.3% (61.3% reduction in area) and improved -40°F (-40°C) CVN energy from 19.7 ft-lbs (26.7J) to 27 ft-lbs (36.6J).

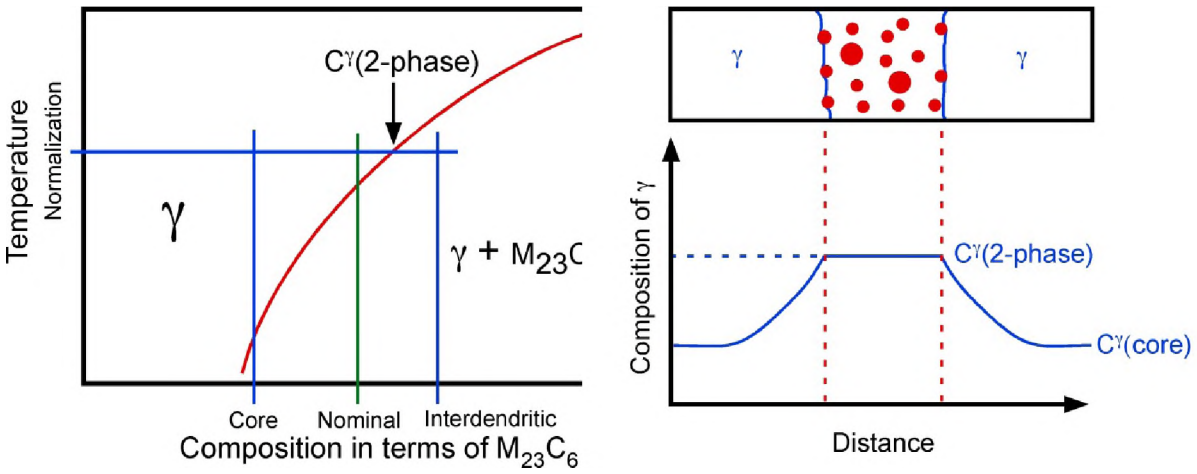


*(a)* *(b)*

Figure 4. A schematic illustration of how the redistribution of solute is affected by (a) a two-phase equilibrium in the alloy rich interdendritic region and (b) the effect of the two-phase equilibrium restricting the composition of the austenite (γ).

The goal of the study presented here was to examine the role of chemical homogeneity on the properties of cast Eglin steel with the aim of improving the CVN impact energy to greater than 30 ft-lbs (40 J) at -40°F (-40°C). Thermodynamic modeling was used to predict dissolution of $M_{23}C_6$ carbides and computational fluid dynamic models were used to predict secondary dendrite arm spacing and subsequent homogenization times. The homogenization model was checked using $M_{23}C_6$ carbide density precipitated by an intercritical anneal as a proxy for alloy homogeneity. Tensile testing, Dynamic Fracture Toughness testing, and Charpy V-notch impact testing at -40°F (-40°C) were used to evaluate the CES as a function of the degree of homogenization. Inclusion and porosity measurements were also used to differentiate the properties reported.

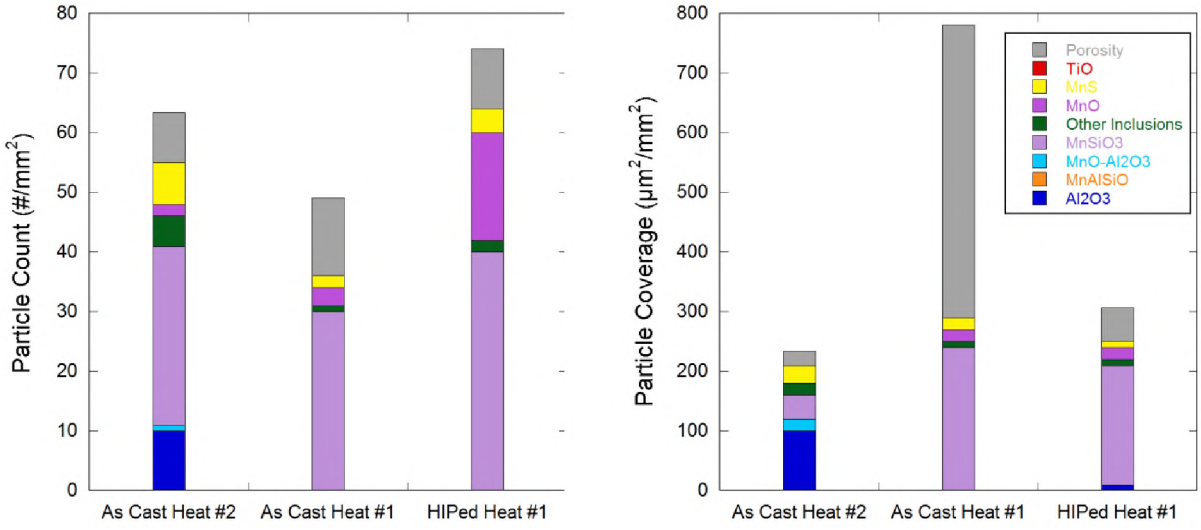


*(a)* *(b)*

Figure 5. Inclusion analysis of cast Eglin Steel using automated feature analysis as reported in reference[7]. The dominant inclusion type in the cast Eglin steel was $MnSiO_3$ with some MnS and MnO. Heat #2 had higher aluminum content, 0.014 wt.% vs. 0.008 wt.%, than Heat #1 and produced a higher concentration of $Al_2O_3$ inclusions. Also shown is the effect of hot isostatic pressing (HIP) on microporosity. (a) density of inclusions and pores measured as an areal density (b) particle coverage or volume fraction of inclusions and pores.

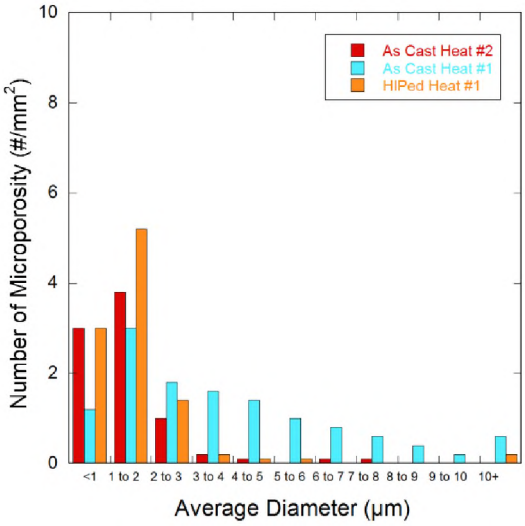


Figure 6. Histogram of pore size for data in Figure 5. Pore size distribution shows a growth in density of pores smaller than 2 µm in diameter and a dramatic decrease in the pore density for pores greater than 3 µm in diameter.

## EXPERIMENTAL PROCEDURES

The CES used in this study was induction melted using the SPAL process (liquid argon drip cover) and tapped into a ladle. Pouring temperature was between 2850°F (1566°C) and 2880°F (1582°C). Liquid metal was lip poured from the ladle through a Foseco 4in x 6in (101.6 mm x152.4mm) Kalpur sleeve and filter directly into a phenolic urethane mold. Mold geometry for the 12in x 12in x 1in (305mm x 305mm x 25.4mm) plate is shown in Figure 7. All test coupons were taken from the cast plate as shown in Figure 8. Standard keel blocks were not poured.

Optical emission spectrometry was used for chemical analysis of the cast Eglin steel. Carbon and sulfur were measured using a LECO CS6000; oxygen and nitrogen were measured using a LECO TC 500. The complete chemical analysis is shown in Table I.

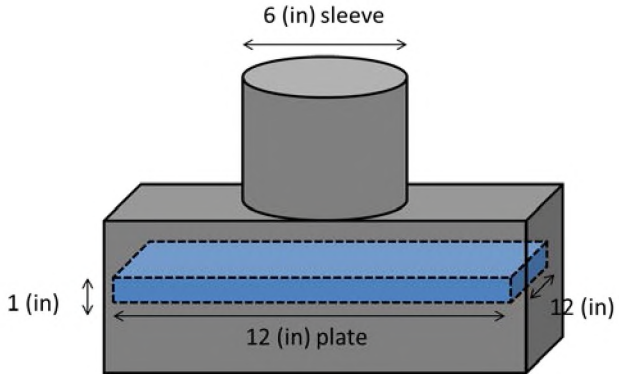


Figure 7. Schematic drawing of CES mold configuration used to cast the plate.

Test specimens were heat treated using the schedule shown in Table II. The minimum normalization temperature for homogenization was determined using FactSage software to determine the solvus temperature for $M_{23}C_6$ in the segregated microstructure and assuming a Scheil-Gulliver segregation model. The thermodynamic minimization algorithm predicts that 20 to 25% of the $M_{23}C_6$ carbides contain tungsten and the remainder are $(Cr, Fe)_{23}C_6$. Complete dissolution of the interdendritic carbide will occur at 2100°F (1149°C) for a nominal tungsten in the range of 0.5 wt.% to 1.0 wt.% (see Figure 9). Redistribution of carbon and alloy during the normalization hold is expected to lower the carbide solvus temperature and inhibit precipitation of new $M_{23}C_6$ carbides during subsequent austenitization and hardening.

Each specimen was double bagged for each austenitization heat treatment using treated stainless steel to inhibit decarburization. Flat "dog bone" shaped tensile bars 7.9in x .29in x .79in (200mm x 7.2mm x 20mm) were cut from the cast plate using a band saw and machined by milling to within +0.02in (0.5mm) on each face of the tensile specimen. Both of the surfaces were then ground to a final dimension of 0.29±0.002in (7.2±0.06mm) using a precision surface grinder after the hardening operation. Tensile gage profiles were machined using a custom routing table, fixture, and carbide tooling to meet ASTM E8 specification.

Table I - Composition of cast Eglin steel used in homogenization study

| **Element (wt%)** | **C** | **Mn** | **Si** | **Cr** | **Ni** | **Mo** | **W** | **V** | **Cu** | **P** | **S** | **Ca** | **N** | **Al** | **O** |
|---|---|---|---|---|---|---|---|---|---|---|---|---|---|---|---|
| **ES-1 (Patent)** | 0.16 - 0.35 | 0.85 Max | 1.25 Max | 1.50 - 3.25 | 5.00 Max | 0.55 Max | 0.70 - 3.25 | 0.05 - 0.30 | 0.50 Max | 0.015 Max | 0.012 Max | 0.02 Max | 0.14 Max | 0.05 Max | |
| **CES Spokane** | 0.276 | 0.62 | 0.98 | 2.73 | 1.01 | 0.42 | 0.94 | 0.11 | 0.046 | 0.016 | 0.009 | | 0.011 | 0.001 | 0.0061 |

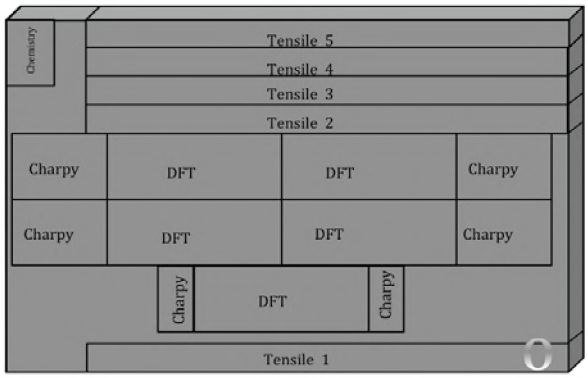


Figure 8. Schematic drawing of CES cast plate showing approximate locations from which test specimens were removed.

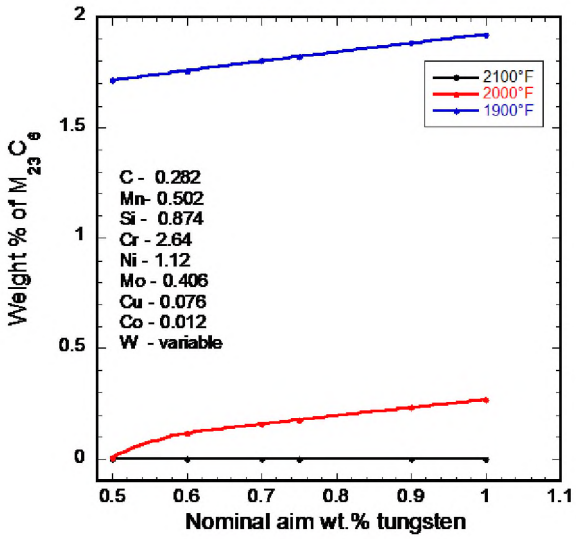


Figure 9. The plot shows the weight percent of carbide predicted using the composition of the last 15-20% liquid using a Scheil-Gulliver segregation model and the nominal CES alloy composition. The nominal tungsten composition was used as the independent variable (x-axis).

All dynamic fracture toughness (DFT) test bars were made from standard Charpy sized samples measuring 0.39in x 0.39in x 2.17in (10mm x 10mm x 55mm). Bars were first machined by milling to within +0.009in (+0.25mm) of the final dimensions and then each of the four surfaces were ground to produce a final dimension of 0.39±0.002in (10±0.05mm) using a precision surface grinder.

Ground DFT bars were notched using a 0.012in (0.31mm) thick diamond-wafering blade and pre-cracked in 3-point bending (R = 0.1) to a total initial crack length ($a_0$) of between 0.18in and 0.22in (4.5mm and 5.5mm) as per ASTM E1820-11, section 7.4.2.

Table II- Heat treatment schedule for homogenization study

| **Sample designation** | **Normalization** | **Austenitization** | **Tempering** |
|---|---|---|---|
| **Baseline** | 1 hr. at 2000°F (1093°C) | 1 hr. at 1900°F (1038°C) | 4 hrs. at 375°F (191°C) |
| **2 hrs. at 2250°F** | 2 hrs. at 2250°F (1232°C) | 1 hr. at 1900°F (1038°C) | 4 hrs. at 375°F (191°C) |
| **4 hrs. at 2250°F** | 4 hrs. at 2250°F (1232°C) | 1 hr. at 1900°F (1038°C) | 4 hrs. at 375°F (191°C) |
| **6 hrs. at 2250°F** | 6 hrs. at 2250°F (1232°C) | 1 hr. at 1900°F (1038°C) | 4 hrs. at 375°F (191°C) |
| **11 hrs. at 2250°F** | 11 hrs. at 2250°F (1232°C) | 1 hr. at 1900°F (1038°C) | 4 hrs. at 375°F (191°C) |

Fatigue loading was incrementally reduced during pre-cracking, as per section 7.4.5 of ASTM E1820-11, to avoid large plastic strain fields that might affect measurement of the fracture toughness. Finished DFT bars were fractured at room temperature using a Tinius Olson model 84 Charpy pendulum impact machine outfitted with an MPM instrumented striker. The load vs. displacement data was used to estimate the dynamic fracture toughness ($K_{ID}$) using the single specimen technique developed by Schindler[8]. All CES specimens behaved in an elastic-fracture manner. The maximum load recorded during impact was used as $P_Q$ and the crack length, a, was measured after fracture using optical microscopy. The average crack length was determined by using the nine point method described in section 8.5.3 of ASTM E1820-11 with the exception that the original crack length was not heat tinted prior to fracture. The toughness, $K_Q$, was calculated using section A3.5.2 of ASTM E399-08. The reported value of $K_{ID}$ is the calculated value $K_Q$. A complete description of the test procedure and methods for the analysis of the data may be obtained from a reading of Schindler[8].

## RESULTS

### MODELING of HOMOGENIZATION

Computational fluid dynamics software, Fluent, was used to model the casting process using parameters appropriate for both no-bake sand and investment casting of steel. From these studies the local solidification time was determined relative to the casting wall thickness. The secondary dendrite arm spacing was then determined using two different empirical models based upon local solidification time. It should be noted that the Bower et al.[9] work is based upon aluminum solidification and the Pierer et al. work is for steel and includes a dependence upon carbon content[10]. Results shown in Figure 10 for Pierer et al. are for a 0.27 wt.%C steel. The Bower et al. work

would represent the lower bound of expected secondary dendrite arm spacing and is included for comparison only.

Alloy segregation profiles were calculated using thermodynamic optimization software for both an equilibrium model (Table III) and a Scheil-Gulliver segregation model (Table IV). Results show a partitioning of carbon and alloy to the interdendritic liquid. These composition profiles were then used in a computational fluid dynamics model consisting of an assembly of close packed spheres. Diffusivity of Cr, W and Mo were used to calculate homogenization rate, since these elements are involved in the formation of $M_{23}C_6$ carbides. Tungsten was determined to be the limiting diffusion rate. Table V contains the pertinent parameters for calculating the diffusion coefficients used in the computational fluid dynamics model for homogenization and Figure 11 shows the calculated diffusivity for a range of temperatures typically used for austenitization. The distance between spheres was chosen as the secondary dendrite arm spacing as determined from Figure 10(c) using the Pierer et al. trend for the 0.27 wt.%C steel. For a one inch (25.4mm) casting wall thickness the secondary arm spacing is expected to be 70μm for a no-bake sand mold casting. Figure 12 shows the expected tungsten composition as a function of time for various homogenization temperatures. Results on the standard Eglin steel composition shows that complete homogenization is impractical at typical austenitizing temperatures below 2000°F (1093°C). Reasonable agreement with the homogenization model was obtained when applied to a one inch round casting. Figure 13 shows a microstructural comparison of a baseline CES heat treatment and a homogenized CES bar using 11 hours at 2250°F (1232°C). The microstructural comparison in Figure 13 was performed using a Jominy end-quench bar that was austenitized at 1900°F (1038°C) after the homogenization heat treatment.

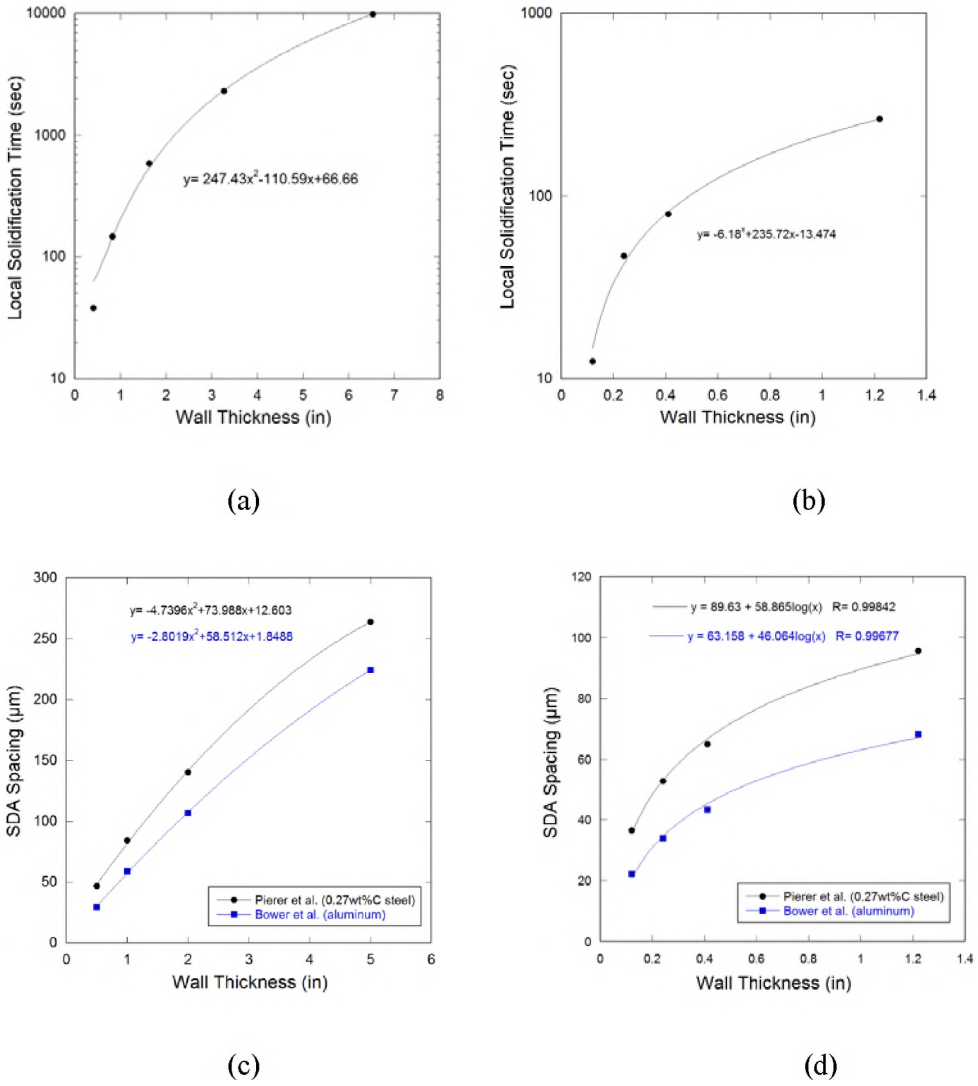


Figure 10. Computational fluid dynamics was used to calculate the local solidification time as a function of casting wall thickness for (a) no-bake sand and (b) an investment shell mold with a 1740°F (950°C) preheat. Empirical models were then used to calculate the secondary dendrite arm spacing based upon casting wall thickness (local solidification time) for (c) no-bake sand and (d) an investment shell with a 1740°F (950°C) preheat. Bower et al. [9] is for solidification of aluminum and represents a lower bound to the expected secondary dendrite arm spacing. Pierer et al. is for steel and is adjusted for a carbon content of 0.27wt.% [10].

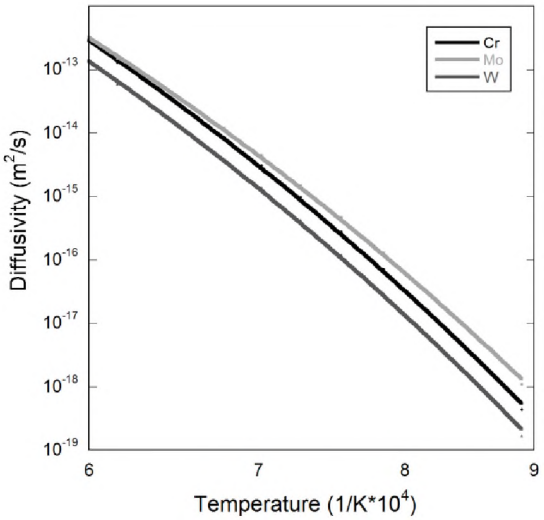


Figure 11. Calculated coefficients of solute diffusion as a function of temperature using the parameters in Table V.

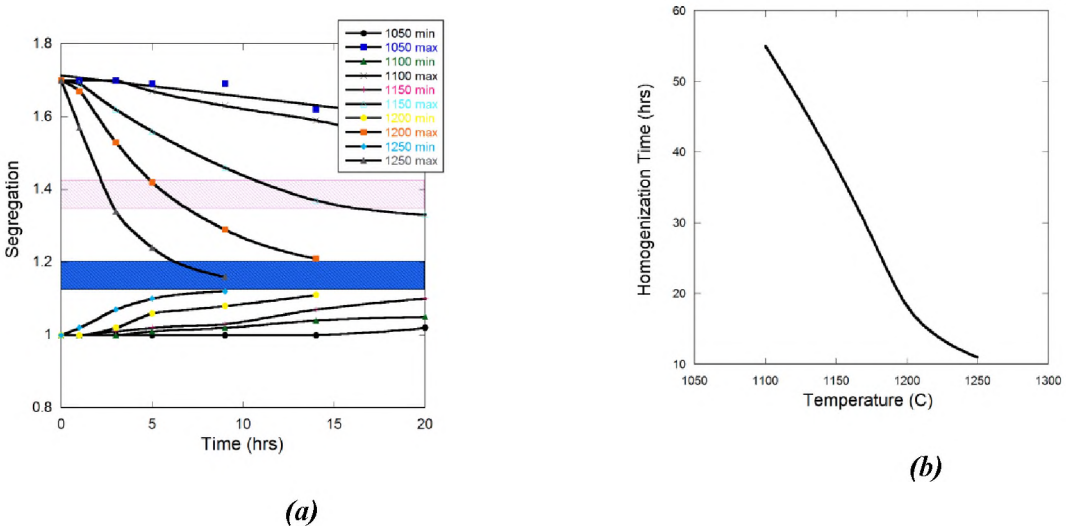


Figure 12. (a) Homogenization of segregated tungsten based upon a secondary dendrite arm (SDA) spacing of 70μm. Pink and blue areas indicate partial (50%) and 90% homogenization. (b) Plot of times required to obtain 90% reduction in the interdendritic segregation. At 2280°F (1250°C) homogenization to 90% of the base chemistry would take more than 11 hours and a 50% reduction would take 2.75 hours.

Table III- Equilibrium thermodynamic prediction of liquid composition with solidification.

| Temperature | Liquid % | C wt. % | Cr wt. % | W wt. % | Mo wt. % | V wt.% |
|---|---|---|---|---|---|---|
| 2732°F (1500°C) | 100 | 0.27 | 2.60 | 1.00 | 0.40 | 0.10 |
| 2696°F (1480°C) | 98 | 0.27 | 2.60 | 1.00 | 0.40 | 0.10 |
| 2678°F (1470°C) | 75 | 0.34 | 2.67 | 1.06 | 0.44 | 0.11 |
| 2660°F (1460°C) | 50 | 0.42 | 2.80 | 1.30 | 0.54 | 0.13 |
| 2642°F (1450°C) | 30 | 0.51 | 2.86 | 1.47 | 0.63 | 0.15 |
| 2624°F (1440°C) | 17 | 0.62 | 2.93 | 1.65 | 0.72 | 0.17 |

Table IV - Scheil-Gulliver segregation model prediction of liquid composition with solidification.

| Temperature | Liquid % | C wt. % | Cr wt. % | W wt. % | Mo wt. % | V wt. % |
|---|---|---|---|---|---|---|
| **2732°F (1500°C)** | **100** | **0.27** | **2.60** | **1.00** | **0.40** | **0.10** |
| **2696°F (1480°C)** | **100** | **0.27** | **2.60** | **1.00** | **0.40** | **0.10** |
| **2678°F (1470°C)** | **76** | **0.34** | **2.67** | **1.06** | **0.44** | **0.11** |
| **2660°F (1460°C)** | **55** | **0.42** | **2.76** | **1.20** | **0.50** | **0.12** |
| **2624°F (1440°C)** | **32** | **0.60** | **2.95** | **1.50** | **0.66** | **0.16** |
| **2588°F (1420°C)** | **21** | **0.78** | **3.11** | **1.83** | **0.81** | **0.20** |

Table V- Diffusion parameters for Cr, Mo, and W solute in iron[11].

| **Crystal structure** | | **Cr** | **Mo** | **W** |
|---|---|---|---|---|
| **BCC** | $D_0$ in $m^2/s$ | $2.4 \times 10^{-4}$ | $7.85 \times 10^{-5}$ | $1.57 \times 10^{-4}$ |
| | Q in kJ/mole | 239.8 | 226 | 243.5 |
| **FCC** | $D_0$ in $m^2/s$ | $6.27 \times 10^{-6}$ | $3.6 \times 10^{-6}$ | $1.3 \times 10^{-5}$ |
| | Q in kJ/mole | 252.3 | 239.8 | 267.4 |

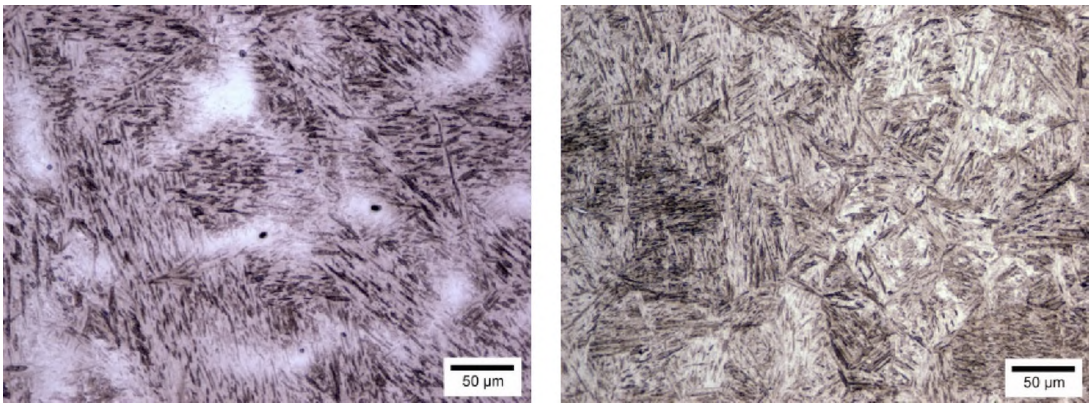


***(a)*** ***(b)***

Figure 13. Optical micrographs from Jominy end-quench CES at J30 (1/16in). (a) Baseline CES normalized at 2000°F (1093°C) for one hour and end-quenched from 1900°F (1038°C). Quenched hardness was 45 HRC. (b) Baseline CES homogenized for 11 hours at 2250°F (1232°C) to obtain ~90% reduction in segregation. The homogenized specimen was end-quenched from 1900°F (1038°C) and produced a quenched hardness of 47 HRC. 2% nital etch.

In an effort to validate the degree of homogenization obtained, an intercritical heat treatment at 1380°F (750°C) for 100 hours was used on previously hardened bars to evaluate carbide size and distribution relative to the normalization temperature and time at 2250°F (1232°C). Alloy carbides of $M_{23}C_6$ form during the intercritical anneal and serve as a proxy for the distribution of Cr, W, and Mo. Figure 14 shows the carbide distribution as determined using a scanning electron microscope equipped with automated feature analysis software. It should be noted that the minimum detectable carbide diameter is approximately 0.4μm. Differences in secondary dendrite arm spacing were related to where the sample was taken from the casting. For example, the minimum SDAS is shown in Figure 14(a) and this specimen came from the casting edge. A more quantitative measure of the carbide distribution is provided in Figures 15 (a) and (b). Regions were selected manually that were representative of the dendrite core and interdendritic region. Figure 15(a) shows that the volume fraction initially decreased with increasing normalization temperature: plot of 0 hours is really one hour at 2000°F (1093°C) and 2 hours is at 2250°F (1232°C). Increasing time at 2250°F (1232°C) shows a steady increase in carbide volume fraction. Figure 15(b) shows the difference in volume fraction from an average of the core and interdendritic regions.

Carbide particle density and particle diameter were then determined over a large representative region containing both the core and interdendritic regions and these results are shown in Figure 16. Carbide density changes erratically between $1.5x10^4$ and $4.5x10^4$ particles/mm$^2$ and this may represent the uncertainty in area selection. In general, the carbide size decreased as the normalization temperature is increased from the 0 hour specimen heated to 2000°F (1093°C) to the 2 hour specimen heated to 2250°F (1232°C) and this may reflect that the alloy carbide was not completely dissolved at 2000°F (1093°C) and simply coarsened during the intercritical anneal. Thus in general, both a higher volume fraction and larger average diameter would be expected after

intercritical annealing when persistent alloy carbides remain after normalization. Upon heating to 2250°F (1232°C) for two hours a minimum in both the volume fraction and alloy carbide diameter is obtained. Subsequent increases in both volume fraction and carbide size occurs with further time at 2250°F (1232°C) and this may be a result of tungsten redistribution.

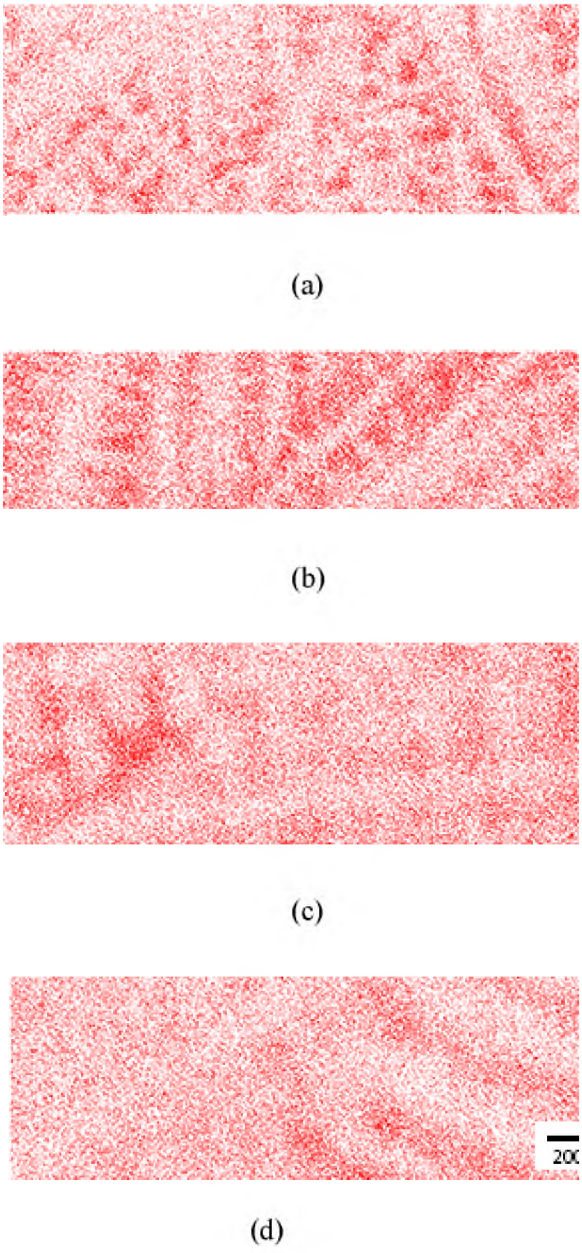


Figure 14. Carbide particle maps obtained by automated feature analysis software showing the carbide distribution change with homogenization heat treatment. Figure (a) represents the baseline heat treatment where the CES has been normalized for one hour at 2000°F (1093°C). Figure (b) was normalized at 2250°F (1232°C) for 2 hours, (c) 6 hours at 2250°F (1232°C) and (d) 11 hours at 2250°F (1232°C). All of the specimens were subsequently austenitized at 1900°F (1038°C) for one hour, quench hardened in water, tempered 4 hours at 375°F (191°C), and annealed for 100 hours at an intercritical temperature of 1382°F (750°C) to precipitate and coarsen the alloy carbides. All images were taken at the same magnification.

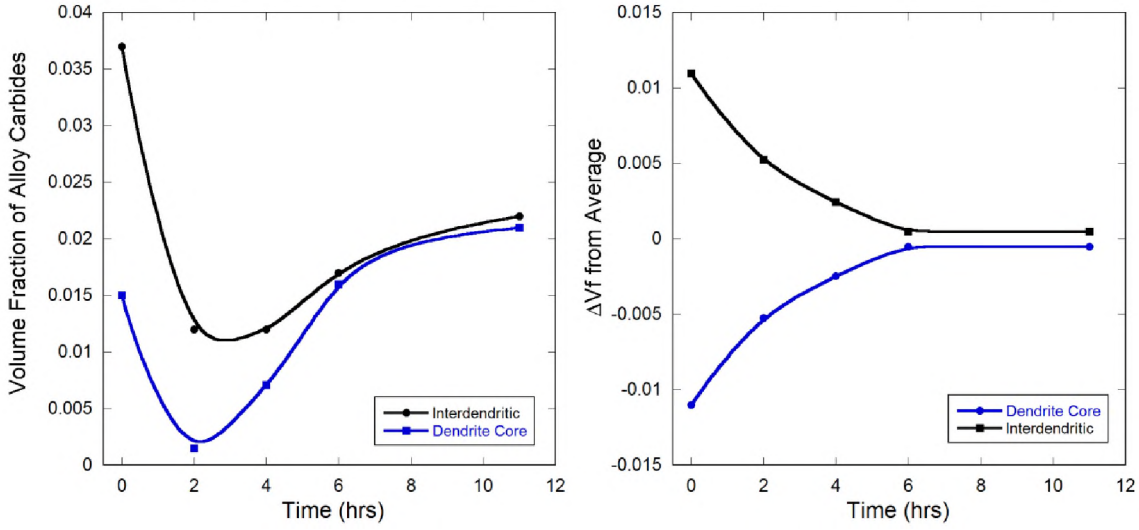


*(a)* *(b)*

Figure 15. Carbide volume fraction was measured using the automated feature analysis program to evaluate the distribution of tungsten and chromium after normalization. Alloy carbides, $M_{23}C_6$, were used as a proxy for solute distribution. (a) Volume fraction of alloy carbides in the interdentritic and dendritic areas as a function of normalization time (b) Deviation in volume fraction from average volume fraction of carbides in interdentritic and dendritic core areas as a function of normalization time.

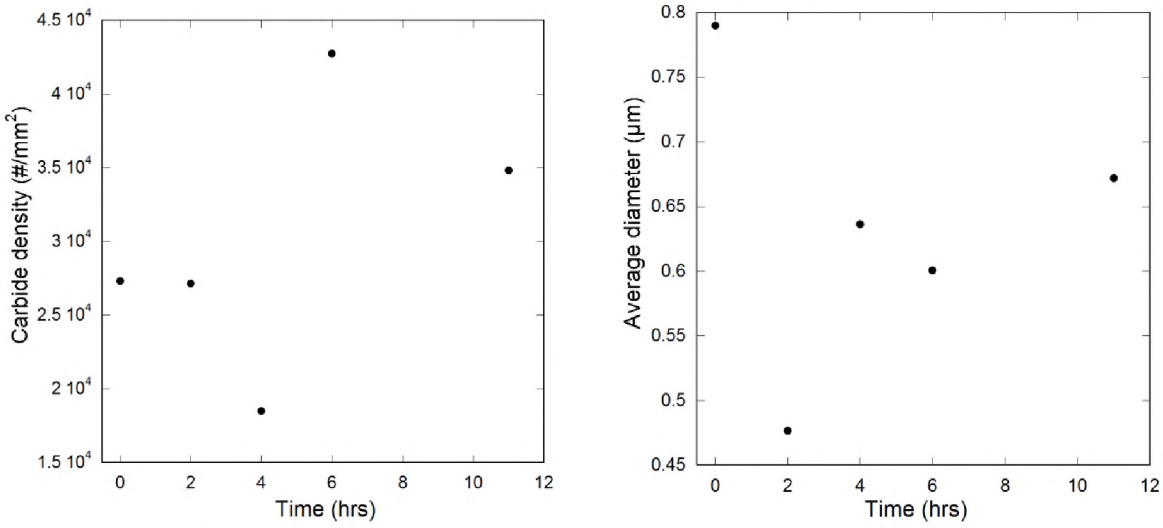


*(a)* *(b)*

Figure 16. Carbide density and average size as measured using an automated feature analysis software. (a) Number density of carbides as a function of homogenization time. (b) Average diameter of carbides as a function of normalization time. It should be noted that the minimum diameter that can be measured is 0.4 μm.

HOMOGENIZATION EFFECTS UPON TENSILE PROPERTIES, DYNAMIC FRACTURE TOUGHNESS AND CVN IMPACT ENERGY

Single sample tensile test results are reported in Table VI. Ultimate tensile strengths were limited by poor ductility. The baseline heat treatment for the CES produced typical values for yield strength, ultimate tensile strength, and elongation to failure as reported by O'Laughlin et al. for CES materials; however, the percent reduction in area was approximately half that previously reported[7]. Figure 17 shows the failed test bars.

*(a)*

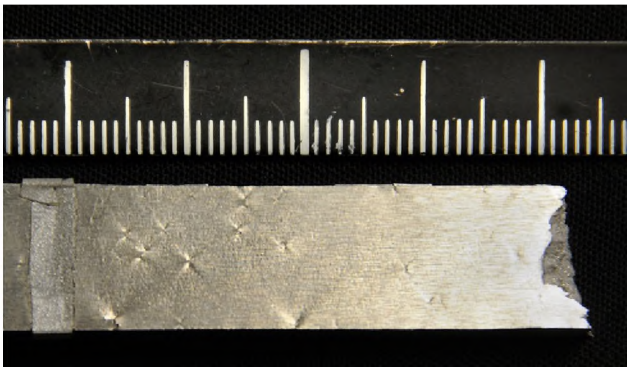

*(b)*

Figure 17. (a) Broken tensile bars of CES. Localized necking associated with casting porosity was observed in the low elongation to failure specimens. An example of the localized necking is shown in (b) for the 4 hour homogenized tensile bar that failed at 2.9%.

Table VI- Tensile results for homogenized cast Eglin steel

| CES sample | Tensile bar location in Figure 8 | Young's modulus in GPa | 0.2% offset yield strength in ksi (MPa) | Ultimate tensile strength in ksi (MPa) | Elongation (%) | Reduction in area (%) | Rockwell hardness C-scale (68%CL) |
|---|---|---|---|---|---|---|---|
| **Baseline*** | 5 | 208 | 197 (1360) | 247 (1700) | 7.6 | 22.7 | 45.4±0.5 |
| **2 hrs @ 2250°F** | 1 | 218 | 193 (1330) | 226 (1560) | 8.2 | 20.3 | 44.4±0.5 |
| **4 hrs @ 2250°F** | 3 | 201 | 197 (1360) | 235 (1620) | 2.9 | 5.3 | 43.2±1.1 |
| **6 hrs @ 2250°F** | 4 | 208 | 188 (1300) | 236 (1630) | 6.5 | 18.4 | 42.0±0.7 |
| **11 hrs @ 2250°F** | 2 | 233 | 180 (1240) | 207 (1430) | 1.4 | 2.6 | 43.6±1.1 |

* Baseline sample slipped in grip after yielding and test was restarted. Total strain to failure is the strain measured during the retest

Automated feature analysis was performed on the baseline, 4 hr, and 6 hr at 2250°F (1232°C) samples to ascertain the cleanliness of the cast plate and determine the cause of the poor reduction in area observed in the tensile samples. Results are shown in Figure 18. The average of the three measurements produced an inclusion count of 298 particles/mm$^2$ with an average inclusion coverage of 1241 μm$^2$/mm$^2$. The highest porosity count was observed in the 4 hr at 2250°F (1232°C) sample with 154 pores/mm$^2$, and an average pore diameter of 1.1 μm. The 6 hr at 2250°F specimen had the largest average pore diameter of 1.51 μm. In general, the 4 hr at 2250°F (1232°C) sample had more numerous and smaller inclusions and pores. A frequency histogram of pore size is shown in Figure 19. Both the 4 hr and the 6 hr tensile bar had a significant number of pores

greater then 5 μm in diameter. Examples of these large pores are shown in the secondary electron images of the fracture surfaces shown in Figure 20 for the 11 hr and 4 hr tensile test bars. Fracture was dominated by microvoid coalescence with predominance of MnS particles nucleating the voids.

A total of 6 DFT specimens were tested per heat treatment, with the exception of the 6 hr normalization heat treatment in which 9 specimens were tested. While no statistically significant trend can be claimed from instrumented impact measurements, a small increase from 92.9 MPa $m^{1/2}$ to 96.5 MPa $m^{1/2}$ in dynamic fracture toughness with normalization time at 2250°F (1232°C) was observed, see Table VII. Results for the 6 hr normalization treatment did not follow the expected trend as shown in Figure 21, and an additional 3 specimens were tested to verify the low value obtained.

A total of 4 Charpy V-notch specimens were tested for each heat treatment, with the exception of the baseline heat treatment, which had 2 specimens. CVN tests performed at -40°F (-40°C) show a similar trend with both normalization temperature and time held at 2250°F (1232°C), see Table VIII. However, the measured values fall below the cast Eglin steel goal of 30ft-lbs (41J) at -40°F (-40°C), but come close to the 16ft-lbs (22J) minimum for Class 1 rolled homogeneous armor (RHA).

Anomalous values were observed for the 6 hour normalization in all testing as shown in Tables VI, VII, VII and Figure 21. This may be accounted for through sample cleanliness as shown in Figure 22 and specifically in Figure 23 showing a frequency histogram of MnS inclusion diameter for the various normalization heat treatments. In general, there is an increase in MnS particle count with the increase in normalization temperature and there appears to be an increase in average diameter of the MnS inclusion with time at 2250°F (1232°C). The average of the 5 measurements produced

an inclusion count of 79 MnS particles/mm$^2$ with an average MnS coverage of 262 μm$^2$/mm$^2$. The highest MnS count was observed in the 11 hr at 2250°F (1232°C) sample with 109 MnS particles/mm$^2$, but the average diameter was the least of the five measurements (1.37 μm). The baseline specimen had the largest average MnS diameter of 1.75 μm. In general, the 11 hr at 2250°F (1232°C) sample had more numerous and smaller MnS inclusions.

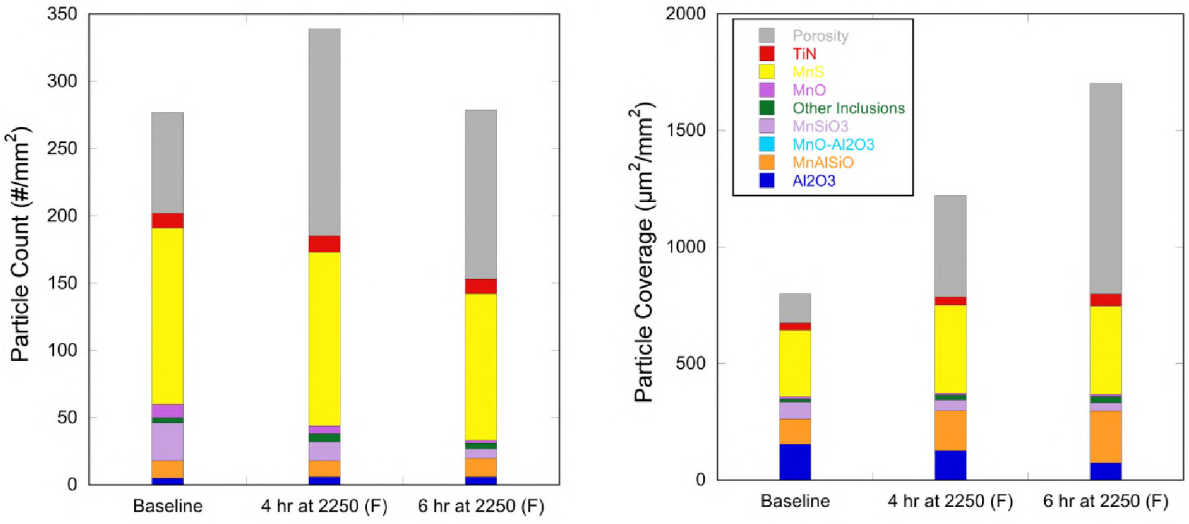


*(a)* *(b)*

Figure 18. Automated feature analysis for CES tensile bars. Samples came from the grip section of the test bars. (a) Density of inclusions and pores measured as an areal density. (b) Area fraction of inclusions and pores.

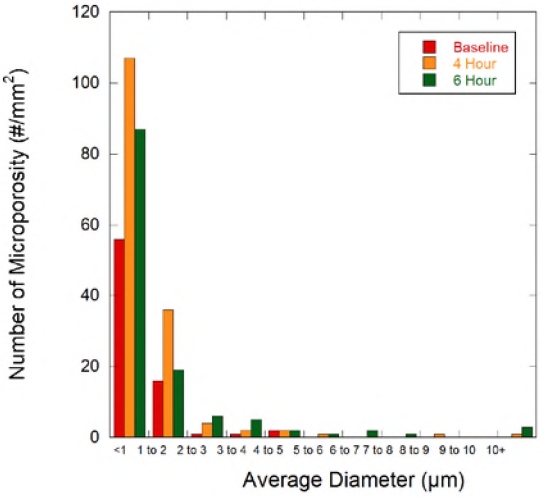


Figure 19. Pore size distribution for tensile bars.

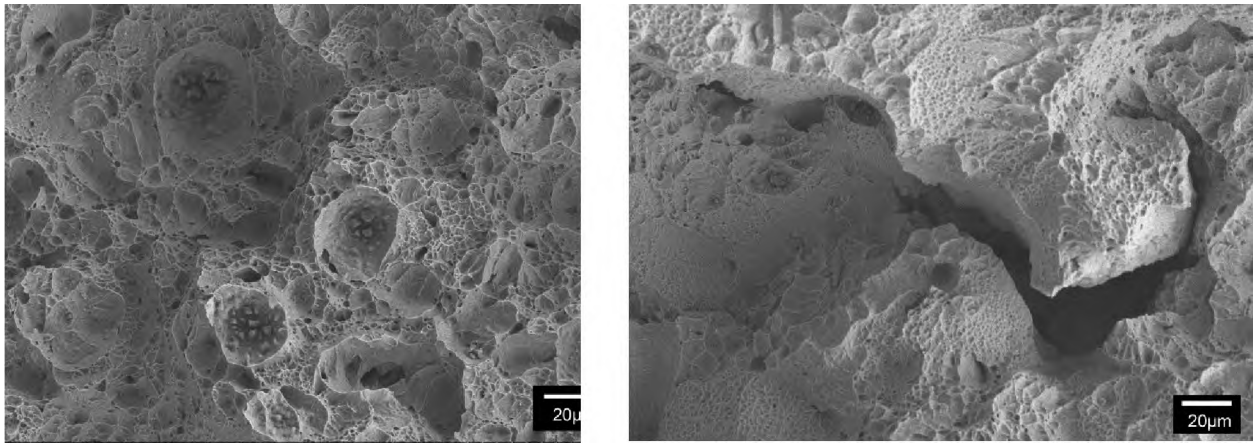


***(a)*** ***(b)***

Figure 20. Secondary electron images of tensile bar fracture surfaces normalized for (a )11 hours, and (b) 4 hours. Low values for % elongation to failure and reduction in area may be explained by pores greater than 5 µm and the large number density of MnS and TiN particles.

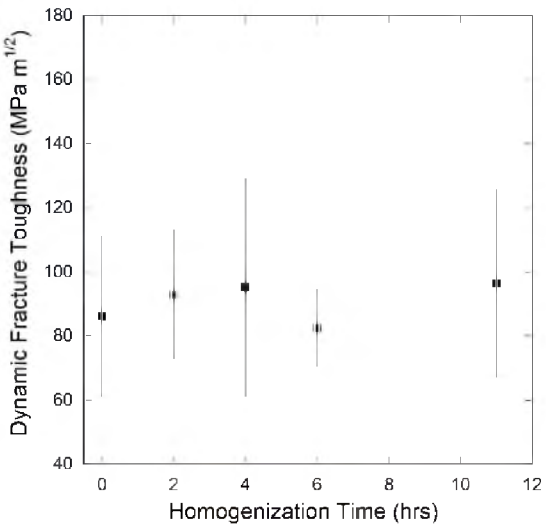


Figure 21. Instrumented Charpy impact test results showing the effect of homogenization time upon dynamic fracture toughness. The sample at time zero is the baseline heat treatment where the material was normalized one hour at 2000°F (1093°C). All samples were hardened from 1900°F (1038°C) after one hour at temperature and tempered four hours at 375°F (191°C). 3 Additional samples were tested for the 6 hour homogenization heat treatment to verify the low value obtained. Uncertainties are calculated at the 95% confidence level.

Table VII- Effect of elevated temperature normalization on dynamic fracture toughness

| | **$K_{ID}$ min (MPa $m^{1/2}$)** | **$K_{ID}$ max (MPa $m^{1/2}$)** | **Average ± 95%CL (MPa $m^{1/2}$)** | **Hardness Rockwell C (68% CL)** |
|---|---|---|---|---|
| **Baseline** | 64.7 | 113 | 86.2 ± 25 | 48.7 ± 1.4 |
| **2 hrs at 2250°F** | 78.9 | 109 | 92.9 ± 20 | 49.4 ± 0.3 |
| **4 hrs at 2250 °F** | 83.1 | 122 | 95.2 ± 34 | 49.2 ± 0.6 |
| **6 hrs at 2250°F** | 62.6 | 100 | 82.6 ± 12 | 47.8 ± 0.4 |
| **11 hrs at 2250°F** | 80.4 | 133 | 96.5 ± 29 | 45.5 ± 0.9 |

Table VIII- Effect of elevated temperature normalization on -40°F (-40°C) Charpy V-notch energy

| | **CVN min ft-lb (J)** | **CVN max ft-lb (J)** | **Average ± 95% CL ft-lb (J)** | **Hardness Rockwell C (95% CL)** |
|---|---|---|---|---|
| **Baseline** | 9.9 (13.4) | 13.4 (18.2) | 11.6 (15.7) | 48.7 ± 2.3 |
| **2 hrs at 2250°F** | 12.8 (17.4) | 15.8 (21.4) | 14.0 ± 6.9 (19.0 ± 9.4) | 47.5 ± 2.1 |
| **4 hrs at 2250°F** | 13.1 (17.8) | 15.7 (21.3) | 13.7 ± 4.6 (18.6 ± 6.2) | 48.4 ± 2.0 |
| **6 hrs at 2250°F** | 10.3 (14) | 12.2 (16.5) | 10.9 ± 2.7 (14.8 ± 3.7) | 48.0 ± 2.0 |
| **11 hr at 2250°F** | 13.2 (17.9) | 16.4 (22.2) | 15.4 ± 4.9 (20.9 ± 6.6) | 47.8 ± 1.9 |

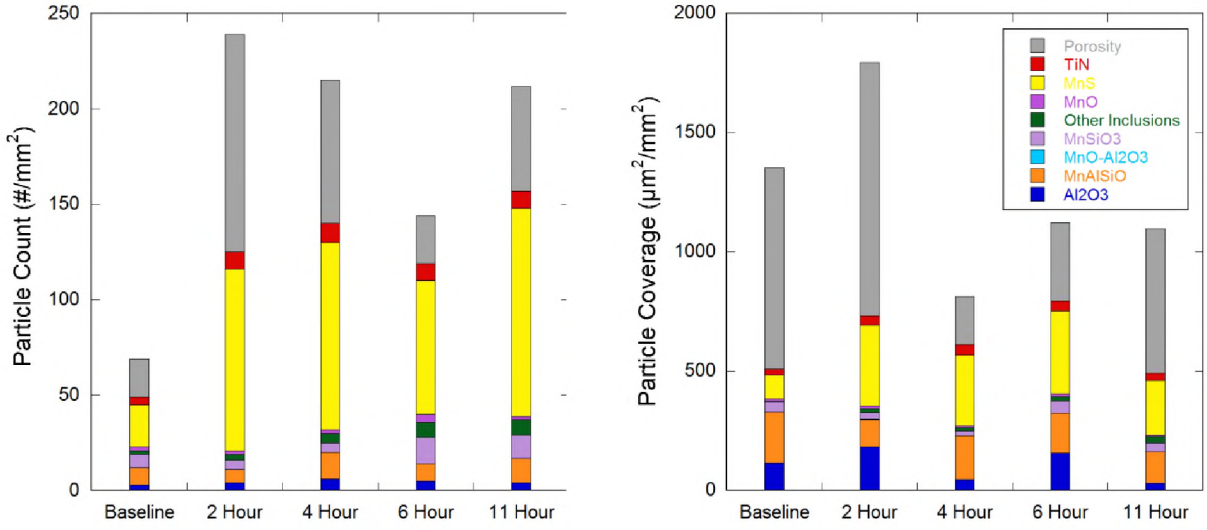


Figure 22. Automated feature analysis for CES DFT bars. (a) Density of inclusions and pores measured as an areal density. (b) Area fraction of inclusions and pores.

**DISCUSSION**

This study shows that homogenization of Eglin steel can be evaluated using an intercritical anneal to precipitate $M_{23}C_6$ carbides as a proxy for the redistribution of alloy. Alloy rich regions produce a greater number and volume fraction of carbides, which can be mapped using a scanning electron microscope and automated feature analysis software. As shown in Figure 14, these carbide maps are very effective visually in characterizing the degree of homogenization. After 11 hours at 2250°F (1232°C) the segregation between the secondary dendrite arms has been removed. However, there is clearly a longer characteristic diffusion length associated with the primary dendrite trunk spacing that is still visible, which was not accounted for in the homogenization

model used in this study. Full homogenization of the cast Eglin steel would take much longer and the benefits of such a treatment appear to be limited.

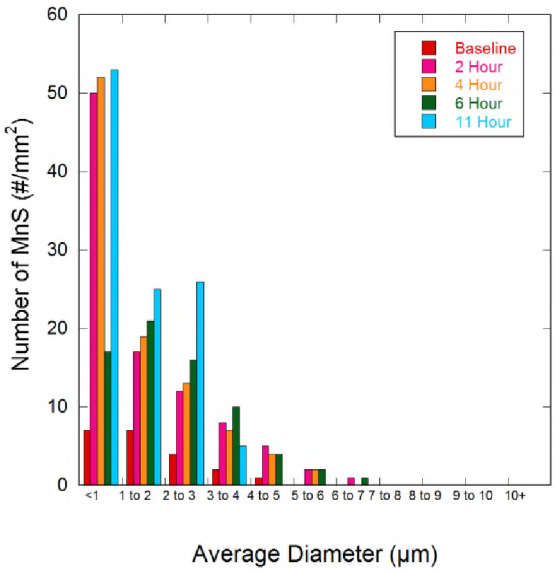


Figure 23. A frequency histogram of MnS particle diameter showing a trend of increasing MnS size with time at 2250°F (1232°C) for a size range of 1 to 4 µm.

The single specimen tensile tests were of little value in examining the benefits of homogenization. Yield strengths appear to decrease continuously as does the hardness (see Table VI) and this may be a result of carbon loss during extended times at 2250°F (1232°C). Ultimate tensile strength and ductility were interrelated; low ultimate strengths are attributed to premature necking as a result of

large pores greater than 5 μm in size as shown in Figure 19 and the evidence of large pores associated with fracture as shown in Figure 20. Both dynamic fracture toughness and Charpy V-notch impact energies show a trend towards higher values with increasing degree of homogeneity; however, it is difficult to argue that this increase is statistically significant. The greatest increase in toughness, either CVN or DFT, occurs as a result of increasing the normalization temperature from 2000°F (1093°C) to 2250°F (1232°C). The increased toughness may be the result of $M_{23}C_6$ carbide dissolution as predicted in Figure 9. However, it should be noted that Richie[12] observed a similar trend for dynamic fracture toughness of 4340 steel.

Richie[12] reports that the fracture toughness of 4340 steel increases and the CVN impact energy decreases with increasing austenitizing temperature (see Figure 24). This may explain the observed difference between the baseline CES and the materials homogenized at 2250°F (1232°C) as shown in Figure 21. Richie explains this divergent behavior between fracture toughness, either $K_{IC}$ or $K_{ID}$, and CVN impact energy with increasing austenitization temperature in terms of the notch acuity. For measures of fracture toughness, the sharp notch created by fatigue cracking has a plastic process zone comparable to the lath martensite bundle size and the tempered microstructure would control the ductile fracture. Cleavage fracture is controlled by the crystallographic misorientation of adjacent lath bundles. An increase in fracture toughness might be expected when the scale of these lath bundles are greater than the plastic process zone of the notch, which would be encouraged by grain growth at higher austenitizing temperatures. The larger notch radius of the CVN test is more sensitive to grain size.

Additional dynamic fracture toughness results taken from unpublished research at MS&T for cast Eglin steel with nominal composition from two different industrial suppliers is shown in Figure 25, which compares materials normalized at different temperatures for one to two hours, subsequently hardened from 1900°F (1038°C) and tempered for four hours at 375°F (191°C). Again, a slight

increase in dynamic fracture toughness is obtained for each supplier as the normalization temperature is increased. Again, these results may simply reflect the complete dissolution of the $M_{23}C_6$ carbides at the higher temperature and the similar increase in CVN impact energy supports the carbide dissolution explanation.

Low CVN notch impact energies observed in this study can be explained by the high inclusion and porosity content of the casting. As previously noted by O'Laughlin et al.[4], inclusion densities greater than 9 particles/mm$^2$ and inclusion coverage greater than 73 μm$^2$/mm$^2$ will generally have CVN -40°F (-40°C) energies less than 15ft-lbs (20J) and that was certainly the case here for the inclusion contents measured for the tensile bars (see Figure 18) and the DFT bars (see Figure 22). It should also be noted that TiN has been shown to decrease dynamic fracture toughness in HY130 cast steels[13].

It may be argued that the dynamic fracture toughness results shown in Figure 21 are statistically the same for the specimens normalized at 2250°F (1232°C), since the $M_{23}C_6$ carbides were dissolved for each time. An increase in dynamic fracture toughness can be argued then for increasing the normalization temperature from 2000°F (1093°C) to a temperature greater than 2100°F (1149°C) to fully dissolve the $M_{23}C_6$ carbide.

The DFT results reported in both Figure 21 and Figure 25 support the carbide dissolution hypothesis for improving DFT as does the CVN data shown in Table VIII. It may also be argued that there is an increase in toughness as a result of MnS coarsening. It is well known that elevated temperature heat treatment can result in the phenomena known as "overheating" where MnS is dissolved at the elevated temperature and precipitated upon prior austenite grain boundaries when cooled. Figure 26 shows the susceptibility of steel to embrittlement based upon sulfur and phosphorus content[14].

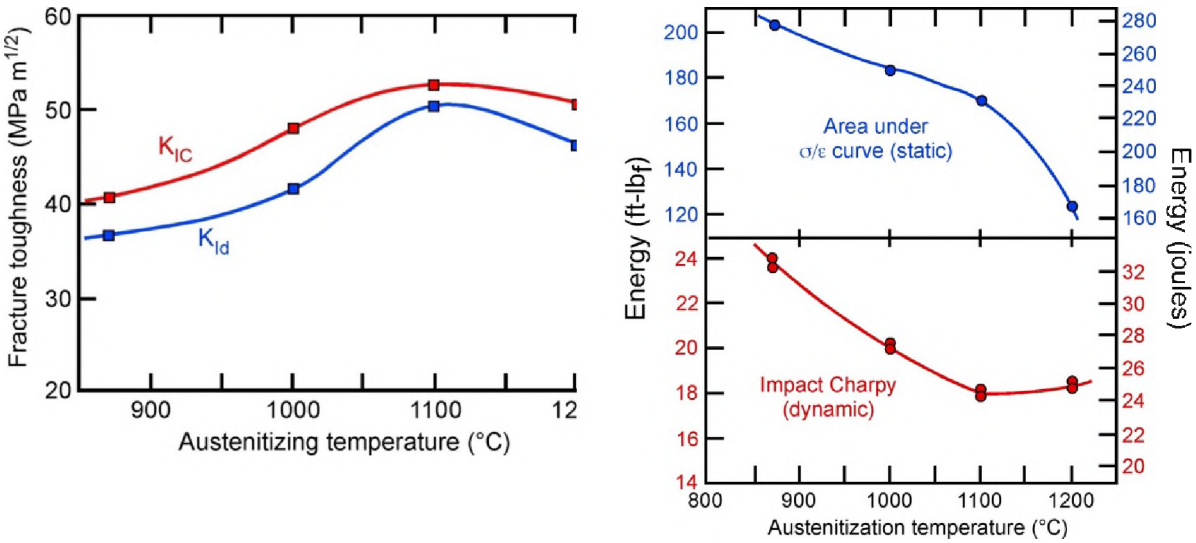


*(a)*

*(b)*

Figure 24. A comparison of (a) fracture toughness and (b) CVN impact energy with austenitizing temperature showing that increasing the hardening temperature may increase the observed toughness, but decrease the notch toughness. This figure also shows that dynamic fracture toughness, $K_{ID}$, follows a similar trend as the quasi-static test for $K_{IC}$, but is lower. Figure redrawn from work presented by Richie[12].

For cast Eglin steel, normalization temperatures above 2100°F (1149°C) becomes questionable. From Figure 18 and Figure 22 it should be noted that the MnS appear more prevalent after elevated temperature normalization. This may be a result of coarsening of the MnS to a size that is detectable by the automated feature analysis software. Figure 23 shows that indeed the size shifts towards larger diameters with time held at 2250°F (1232°C).

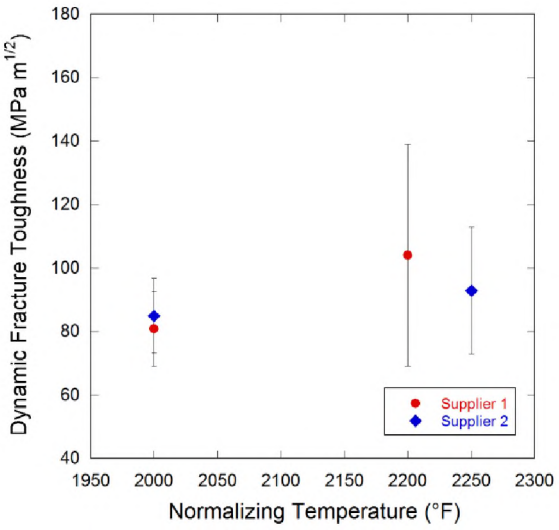


Figure 25. Influence of normalization temperature on the dynamic fracture toughness for standard cast Eglin steel produced by two suppliers. In general, an increase in toughness with increasing normalization temperature is observed for each steel casting producer and the combined data suggests that an optimum temperature for normalization may occur above 2000°F (1093°C). Three different heats are shown: two from Supplier 1 and one from Supplier 2. Uncertainties are calculated at the 95% confidence level. Results in figure taken from unpublished research of the authors.

Coarsening would be facilitated by the greater solubility of MnS at the higher temperature and subsequent austenitization for hardening may mitigate the embrittlement predicted by Figure 26. The persistence of a high MnS number density in the less than 1 μm size range supports a overheating hypothesis as does the increase in number density for the 1 to 4 μm diameter sulfides

with increasing time during the elevated normalization temperature as shown in Figure 23. The sudden increase in MnS count between the baseline heat treatment and the elevated temperature may also be explained by coarsening of preexisting MnS inclusions that were of a size less than 0.5 μm in diameter, which is below the detection threshold of the automated feature analysis. Upon further coarsening, the average MnS inclusion diameter would increase and the number density decrease. However, the high number density of MnS in the 11 hour heat treatment suggests that the MnS is precipitated upon cooling during normalization.

It would be expected that a decreasing number density and an increasing average particle diameter would produce a larger distance between MnS particles and produce an increase in fracture toughness. As shown by Bartlett et al. the increasing distance between inclusions produces an increase in DFT for HY130 cast steels[13]. However precipitation of a fine MnS distribution along prior austenite grain boundaries would be expected to affect CVN results more than DFT as a result of the notch acuity effect. This was observed to some extent in Table VIII. Thus, the initial improvement in DFT and CVN are related to the elimination of persistent carbides as a result of normalizing above the solvus temperature of the persistent carbides. However, overheating can occur in CES at temperatures that would be required for a commercial practice of homogenization. The minimal observed property improvements do not warrant austenitization temperatures above the carbide solvus temperature.

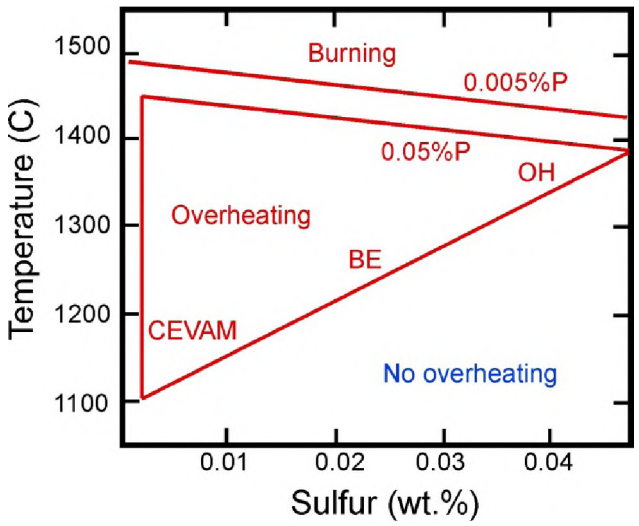


Figure 26. Susceptibility to MnS embrittlement designated as either overheating or burning. Concern might exist for cast Eglin steel when heat treated above 1150°C or 2100°F. Figure redrawn from work presented by Hale and Nutting[15]. CEVAM=consumable electrode vacuum arc melting, BE=basic electric, OH=open hearth.

## CONCLUSIONS

In summary, the melt processing and casting of Eglin Steel remains a critical issue. Sulfur and phosphorus levels should be minimized to reduce MnS inclusions and potential overheating issues. Sufficient evidence was presented to specify a normalization temperature above 2100°F (1149°C) to eliminate persistent alloy carbides of the type $M_{23}C_6$ and fully homogenize the carbon content. Homogenization for extended time does not appear necessary to obtain good fracture toughness. Subsequent austenitization can be performed at 1900°F (1038°C) prior to quenching provided the carbides have been completely dissolved at the elevated normalization temperature.

## ACKNOWLEDGEMENTS

This work has been supported under the Steel Founders' Society of America (SFSA) program on Casting and Advanced Steel Technology that has been funded by the Army Research Laboratory under the provisions of cooperative agreement W911NF-12-2-0033. The authors are grateful for steel castings supplied by both Mr. Rod Grozdanich at Spokane Industries and Mr. Rick Boyd formerly of Nova Precision Castings and for optical emission spectroscopy results provided by Mr. Don Denney at American Cast Iron Pipe Co. (ACIPCo). The authors also gratefully acknowledge the Army Research Office Defense University Research Instrumentation Program (award number W911NF-08-1-0267) for financial support in buying the ASPEX-PICA 1020 SEM that was used for automated feature analysis.

## REFERENCES

1. J. Paules, M. Dilmore and K. Handerhan, "Development of Eglin Steel – A New, ultrahigh-Strength Steel for Armament and Aerospace Applications," Materials Science and Technology – AIST 2005 Vol. 2, pp 13-24.
2. M. Dilmore and J.D. Ruhlman, Eglin Steel - A Low Alloy High Strength Composition. United States Patent Publication: US7537727.
3. M.F. Dilmore, A.J. Armstrong, M.L. Green and M.L. Hughes, "Development of Eglin Steel for Hard Target Warhead Case Applications (U)," 6th Joint Classified Bombs/Warheads & Ballistics Symposium, Monterey, California, 2-5 June 2003.

4. A. O'Loughlin, E. Martinez, K. Peaslee, and S. Lekakh, "Effects of Steel Processing on Property Variation in Eglin Steel (ES-1)" Materials Science &Technology 2010 Conference & Exhibition.
5. R. Abrahams, P.Lynch, R.Voigt, "Processing & Composition of High Strength Cast Steel," 2009 SFSA Technical & Operating Conference.
6. P. Lynch, R. Abrahams, R. Voigt, "Hot Isostatic Pressing and Homogenization of High Strength Steel Investment Castings," Investment casting Institute, 58th Technical Conference and Equipment Expo 2011.
7. Andrew O'Loughlin, Kent D. Peaslee and David C. Van Aken, Development of High Strength (200ksi) Cast Steel Alloy," 2011 SFSA technical & Operating Conference.
8. Schindler, H.J. "Estimation of the Dynamic J-R Curve from a Single Impact Bending Test". Mechanisms and Mechanics of Damage and Failure: proceedings of the 11th ECF, (1996).
9. T.F. Bower, H.D. Brody, and M.C. Flemings, "Measurement of Solute Solidification in Dendritic Solidification," Trans. AIME vol. 236 (1966) pp. 624-634.
10. R. Pierer, and C. Bernhard, "On the influence of carbon on secondary dendrite arm spacing in steel," J. Mater. Sci. vol. 43 (2008) pp. 6938-6943.
11. P.J. Alberry and C.W. Haworth, "Interdiffusion of Cr, Mo, and W in Fe," Metal Sci vol. 8 (Dec. 1974) pp. 407-412.
12. R.O. Richie ASM conference proceedings, What Does the Charpy Test Really Tell Us? , (1978) pp. 54-73.
13. L.N. Bartlett, A. Dash, D.C. Van Aken, V.L. Richards, and K.D. Peaslee, Dynamic Fracture Toughness of High Strength Cast Steels," AFS Trans vol.120, (2012) pp. 469-486.
14. G.E. Hale and J. Nutting, "Overheating of low alloy steels," International Metals Reviews vol. 29 (1984), pp.273-298.

## VITA

Terrell O. Webb, Jr. is a Florida native who came to Rolla for his PhD. in the spring of 2012. He received his Masters of Science in Geological Engineering and a certificate of Military Geological Engineering from Missouri University of Science and Technology in the spring of 2011. He also holds an Associate of Arts in Military Science from Marion Military Institute, and a Bachelor of Science in Engineering Technologies from the University of West Florida. During his graduate studies he served as treasurer/secretary for the international professional and academic honor society for the materials science and engineering Alpha Sigma Mu. He received his Ph.D. in Metallurgical Engineering from Missouri University of Science and Technology in December 2015 under the supervision of Dr. David Van Aken.